APL Quantum

RESEARCH ARTICLE | SEPTEMBER 22 2025

Dynamics of time-modulated quantum systems via integrated Lindblad and Maxwell–Bloch equations

Special Collection: Quantum Dynamics in Theory, Numerics and in Experimental Research

Achiles F. da Mota ; Mohammad Mojtaba Sadafi ; Wei-Chi Chiu ; Bernardo Barbiellini ;
Michael N. Leuenberger ; Arun Bansil ; Hossein Mosallaei ✉

APL Quantum 2, 036107 (2025)
https://doi.org/10.1063/5.0271171

AIP Publishing

APL Quantum ARTICLE pubs.aip.org/aip/apq

Dynamics of time-modulated quantum systems via integrated Lindblad and Maxwell–Bloch equations

Cite as: APL Quantum 2, 036107 (2025); doi: 10.1063/5.0271171
Submitted: 15 March 2025 • Accepted: 4 September 2025 •
Published Online: 22 September 2025

View Online Export Citation CrossMark

Achiles F. da Mota,[1,2] **Mohammad Mojtaba Sadafi,**[1] **Wei-Chi Chiu,**[3,4] **Bernardo Barbiellini,**[3,4,5] **Michael N. Leuenberger,**[3,4,6] **Arun Bansil,**[3,4] **and Hossein Mosallaei**[1,a)]

AFFILIATIONS

[1] Department of Electrical and Computer Engineering, Northeastern University, Boston, Massachusetts 02115, USA
[2] Department of Electrical Engineering, University of Brasília (UnB), 70910-900 Brasilia, Brazil
[3] Physics Department, Northeastern University, Boston, Massachusetts 02115, USA
[4] Quantum Materials and Sensing Institute, Northeastern University, Burlington, Massachusetts 01803, USA
[5] Department of Physics, School of Engineering Science, LUT University, 34, FI-53850 Lappeenranta, Finland
[6] NanoScience Technology Center, Department of Physics, and College of Optics and Photonics (CREOL), University of Central Florida, Orlando, Florida 32826, USA

Note: This paper is part of the APL Quantum Special Topic on Quantum Dynamics in Theory, Numerics and in Experimental Research.

[a)] **Author to whom correspondence should be addressed:** h.mosallaei@northeastern.edu

ABSTRACT

Time-modulated quantum electrodynamics (TM-QED) investigates the dynamic interactions between quantum emitters (QEs) and photonic systems with temporally varying properties, allowing for unprecedented control over light–matter interactions. This paper presents a framework for employing TM-QED in dynamic systems by coupling the Gorini–Kossakowski–Sudarshan–Lindblad equation with the time-Floquet method and Mie theory. The proposed approach enables the study of QEs interacting with dynamically modulated photonic structures, focusing on the dynamic control of the density of states and coupling between frequency harmonics. Unlike traditional static photonic environments, our approach enables active manipulation of emission properties post-fabrication, offering new avenues for quantum control. By leveraging time modulation, we demonstrate the generation of frequency harmonics, enhanced spontaneous emission rates, and control over the radiation of quantum emitters. We also demonstrate how plasmonic resonances enhance light–matter interactions, resulting in optimized spectral properties. Time modulation offers a fourth dimension in optimizing quantum structures, which can be utilized to manipulate emission properties post-fabrication actively. Finally, understanding the dynamics of harmonic coupling in QE's states can help improve quantum sensing, single-photon sources, and read-out.

I. INTRODUCTION

In the past few years, intensive research has been dedicated to studying new approaches to efficiently control the emission of quantum emitters (QEs) with applications as diverse as lasers, LEDs, quantum sensors, quantum communication systems;[1,2] single-photon-sources;[3] free-space optical communications; and others.[4,5] The most efficient way of controlling the emission of QEs (such as quantum dots, quantum wells, and fluorescence molecules) is by engineering their photonic density of states (PDoS) since it affects the QE emission properties, namely, spontaneous emission rate (Γ), radiated power (Q), quantum efficiency (η), and radiation pattern (D) or scattering (S). According to the Fermi golden rule, enhancing the PDoS increases the probability for the QE to decay, allowing a faster decay rate Γ. The ratio between Γ and the emission rate in free space (Γ_0) is known as the Purcell factor (P).[6,7] Thus, manipulating P is crucial for several applications since it implies controlling the QE lifetime and modulation speed. The most common approach for managing its properties is placing the QE close to or inside resonant photonic structures, such as photonic crystal cavities,[8] dielectric nanoholes,[9] nano-antennas, or hyperbolic metamaterials (HMM).[5,10] In addition, spatially periodic media, such as photonic crystals and metasurfaces, are also effective in engineering the local density of electromagnetic states and controlling the spontaneous emission of QEs.[11–13] By analogy with spatial periodicity, temporal modulation can be introduced into photonic systems, adding a new degree of freedom to the design paradigm and enabling control over both the spatial and spectral characteristics of QE radiation. Nonetheless, after the fabrication, the system is static, and radiation manipulation can only be achieved by changing QE's excitation parameters.

Time-modulated systems have emerged as a promising area in quantum electrodynamics, particularly in applications involving the manipulation of coherence and thermal radiation at the nanoscale.[14–18] When integrated with photonic structures, these systems enable spatial and temporal control over radiated wave properties.[19,20] For example, in near-field regimes, time modulation can influence thermal radiation coherence and allow dynamic control of emission rates, offering new avenues for controlling light–matter interactions and spontaneous emission processes.[21–25] In Ref. 23, the authors used frequency-modulated optical transitions for spectral engineering of single-photon emission. They demonstrate that a two-level system modulated faster than its optical lifetime can produce single photons with a tunable spectrum. Moreover, it has also been shown that the spatial coherence of thermal radiation can be controlled using time-modulated photonic systems that support surface polaritons (SPPs).[25–28] Micro- and nano-particles composed of plasmonic materials can support geometrical, or Mie type, resonances that not only enhance light–matter interactions for a more profound impact of time modulation but also enable control over key features such as directionality and orbital or spin angular momentum.[29–31] A time-modulated structure allows for controllable energy transfer between different frequencies (change of the photon momentum), enabling new correlations between frequency components.

Open quantum systems can be described using one of the general forms of the Markovian master equation,[31–35] the Gorini–Kossakowski–Sudarshan–Lindblad (GKSL) equation to model the dynamics of the quantum states, where spontaneous emission is considered via a Lindblad superoperator.[32] Quantum field theoretical methods have been employed to study light–matter interactions in complex photonic systems, such as the quantum-optical description of emitter–plasmon coupling and polaritonic modes in metallic nanostructures,[33] electrochemically switchable multimode strong coupling in plasmonic nanocavities,[34] and the control of strong light–matter coupling in hybrid plasmonic–dielectric environments.[35] The interaction between the QE and the electric field can be modeled under dipolar approximation, which can be coupled to time-varying fields. In a multi-level system, the QE interacts with a time-modulated electric field, which introduces multiple harmonics into the system, leading to intricate coherence effects and harmonic generation. Unlike previous studies that model the quantum emitter as a classical dipole, where the emitter is treated as a point source with a fixed polarizability or dipole moment,[36–38] our approach provides a quantum-mechanical treatment by directly solving the general form of the Markovian master equation. In classical dipole models, the quantum dynamics of the emitter, such as population transfer and coherence between states, are not explicitly captured and the feedback between the emitter and its environment is treated in a simplified. Some studies have coupled GKSL-like quantum dynamics with static electromagnetic solvers to capture the quantum-classical interaction better.[39–41] However, our study integrates a time-modulated Floquet–Mie framework with GKSL formalism, enabling the modeling of quantum emitters embedded in dynamically varying photonic structures. This enables us to investigate how the time modulation of the environment directly affects quantum coherence, sideband generation, and frequency-selective emission, capabilities that surpass those achievable by traditional static or classical models. In the case of a three-level system, the interaction is also notable as it involves transitions between multiple energy states with distinct frequencies.

In this work, we present a comprehensive framework for modeling and analyzing time-modulated quantum electrodynamics (TM-QED) in dynamic systems by coupling the GKSL equations with an adequate electromagnetic formalism. Several methods exist for coupling quantum systems with electromagnetic fields.[39–41] In Refs. 28 and 29, the authors developed a finite-difference time domain (FDTD)-style algorithm that uses a photon wave-function in the spin-1 Dirac formulation to directly discretize space and time, tracking the spatio-temporal field evolution at the level of single-photon states coupled to the quantum dot in a fully quantized description, which allows for tracking of the Heisenberg uncertainty principle during the spontaneous emission of a single photon. The time-floquet Mie theory is not a direct time-domain solver such as FDTD, i.e., it does not perform time stepping. Instead, it describes the coupling of a quantum emitter to the classical electromagnetic field using Mie theory,[42,43] enabling the calculation of dipolar emission, the Purcell factor, and quantum coherence in systems where quantum emitters interact with dynamically modulated plasmonic structures. While Tafur and Leuenberger's FDTD-based method can also describe time-modulated electromagnetic systems, it does not incorporate decoherence or dissipative mechanisms and becomes computationally expensive for low modulation speeds. Meanwhile, the quantized photon's spontaneous emission is defined as a coherent process in Refs. 28 and 29; here, we describe the spontaneous (radiative) decay of the quantum emitter employing the incoherent transition rate in the Lindblad-type equations. Previous studies have shown that periodically driven open quantum systems governed by Markovian dynamics can be described within the Lindblad formalism using a Floquet-based approach, where the Lindblad master equation admits a time-periodic solution due to the Floquet structure of the Liouvillian superoperator[44,45] In this sense, the proposed approach enables the calculation of dipolar emission, Purcell factor, and quantum coherence in systems where quantum emitters interact with dynamically modulated photonic structures. We demonstrate how time modulation can couple harmonic frequencies, enhance spontaneous emission rate, and provide real-time control over emission dynamics. Furthermore, as an illustrative example, we explore the role of resonant plasmonic effects in amplifying light–matter interactions and propose optimization strategies for frequency-selective emission using the proposed formalism. Our approach enables optimizing time-modulated systems by incorporating the coupling between quantum emitters (QEs) and their environment. This allows for targeted enhancements, such as increasing the Purcell factor and improving overall emission efficiency, as in Ref. 28, while facilitating control over the interaction dynamics within complex quantum photonic structures. Ranging from classical to quantum mechanical descriptions,[46,47] our paper offers a comprehensive understanding together with a theoretical framework for studying the interaction of an open quantum system with temporally modulated electromagnetic fields.

II. TIME-MODULATED QUANTUM EMITTER

For the proposed modeling, we consider an N-level ($|n\rangle$ where the ith state has energy $\hbar\omega_i$. To model the quantum states of the emitter, we resort to the open form of one of the general form of the Markovian master equation, which is the Lindbladian or GKSL equation in the Lindblad form,[44,45,48–50]

$$\frac{d\hat{\rho}(t)}{dt} = \frac{i}{\hbar}\big[\hat{\rho}(t), \hat{H}\big] + \mathcal{L}_\gamma \hat{\rho}(t), \tag{1}$$

where $\hat{\rho}$ is the density operator, $\hat{H}$ is the Hamiltonian, and $\mathcal{L}_\gamma$ denotes a superoperator accounting for dissipative processes such as spontaneous emission, under the assumption of negligible memory effects (i.e., Markovian evolution). Under the dipolar approximation, the semi-classical light–atom interaction Hamiltonian and $\hat{H}$ can be written, respectively, as

$$\begin{aligned} \hat{H} &= \hat{H}_{atom} + \hat{H}_{atom:field}(t) \\ &= \sum_i \hbar\omega_i |i\rangle\langle i| + \sum_{i\neq j} |i\rangle \frac{\hbar}{2}\hat{d}_{ij}\cdot \mathbf{E}(\vec{r},t)\langle j| e^{\mathrm{j}\omega_{ij}t}, \end{aligned} \tag{2}$$

$$\mathcal{L}_\gamma \hat{\rho}(t) = \sum_{i,j} \gamma_{ij}\Big(\Big[\hat{\sigma}_{ij}, \hat{\rho}\hat{\sigma}_{ij}^{\dagger}\Big] + \Big[\hat{\sigma}_{ij}\hat{\rho}, \hat{\sigma}_{ij}^{\dagger}\Big]\Big), \tag{3}$$

where $\omega_{ij} = \omega_i - \omega_j$, $\hat{d}_{ij}$ is the dipolar operator, $\hat{H}_{atom}$ takes into account the atom/system response, $\hat{H}_{atom:field}$ is the dipolar approximation of the atom/field interaction, $\mathbf{E}(\mathbf{r},t)$ is the electric field, γ_{ij} is the dumping frequency between ith and jth levels, and $\hat{\sigma}_{ij}$ is the ladder operator. Considering a time-modulated electric field, $\mathbf{E}(\mathbf{r},t)$ can be written as

$$\mathbf{E}(\mathbf{r},t) = \sum_{i\neq j}\left(\sum_n E_{ij}^n e^{\mathrm{j}\left(\overrightarrow{k_{ij}^n}\,\vec{r} - \omega_{ij}^n t\right)} \boldsymbol{\varepsilon}_{\mathbf{ij}}^{\mathbf{n}}\right), \tag{4}$$

where i and j are related to the transition between the states, $\omega_{ij}^n = \omega_{ij} + \Delta_{ij} + n\omega_m$ is the frequency related to the ω_{ij} transition, ω_m is the modulation frequency, Δ_{ij} stands for the frequency shift, E_{ij}^n is the nth harmonic electric field amplitude, and $\boldsymbol{\varepsilon}_{\mathbf{ij}}^{\mathbf{n}}$ is the versor of the electric field. To solve the linear system, we can resort to the Floquet-eigen solutions of (1),

$$\rho(t) = \sum_n \sum_m A_m B_{n,m} \rho^{m,n} e^{\lambda_m t + \mathrm{j} n\omega_m t}, \tag{5}$$

where λ_m represents the complex quasienergies (Floquet–Liouville exponents), $B_{n,m}$ is the associated element of the eigenvector, and A_m is the eigenvector amplitude. In this sense, by truncating the number of time-harmonics from $-M$ to M, Eq. (1) can be rewritten as a matrix,

$$\frac{d\rho_M(t)}{dt} = \mathbf{M}\rho_M(t), \tag{6}$$

where $\rho_M(t) = \big[\rho_M^{-M}; \rho_M^{-M+1}; \ldots; \rho_M^{0}; \ldots; \rho_M^{M}\big]$, and ρ_M^n corresponds to the nth time-harmonic and is equal to $\rho_M^n = [\rho_{11}^n; \rho_{22}^n; \ldots; \rho_{NN}^n; \rho_{12}^n; \ldots; \rho_{1N}^n; \rho_{21}^n; \ldots \rho_{N,N-1}^n]$, with $\rho_{i,j}^n$ being the nth harmonic of $\hat{\rho}_{ij}$. $\mathbf{M}$ is defined as an $N^2(2M + 1)$ square matrix obtained by resorting to (1)–(3). We provide the full formalism for two and three level systems in the supplementary material. After calculating the density of states, we can exploit the dipolar approximation to calculate the dipolar transition moment from level i to j, as follows:[51,52]

$$\begin{aligned} \mathbf{p_{ij}}(t) &= \mu_{ij}\rho_{ij}\boldsymbol{\varepsilon} e^{-\mathrm{j}\omega_{ij}t} \\ &= N_{emi}\mu_{ij}\left(\sum_n \sum_m A_m B_{n,m} \rho_{ij}^{m,n} e^{(\lambda_m + \mathrm{j}(\omega + n\omega_m))t}\right)\boldsymbol{\varepsilon}_{\mathbf{ij}}^{\mathbf{n}}, \end{aligned} \tag{7}$$

in which N_{emi} is the number of quantum emitters. Moreover, in (7), the term with frequency $\omega_{ij} + \omega + n\omega_m$ is not considered due to the high frequency. Another important consideration is that as $t \to \infty$, modes with real parts vanish, leaving only purely imaginary eigenvalues. Therefore, we only need to consider purely imaginary eigenvalues in the steady-state analysis. Since $\hat{\rho}(t)$ is written by its eigenvalues Eq. (5), the condition $\frac{d\hat{\rho}(t)}{dt} \to 0$ means that each state population harmonic converges to a different steady state and the emission and population of each state remain time-modulated although in a steady state. Having calculated the dipolar moments, we can couple the QE to the electrodynamic system, as presented in Fig. 1. In the proposed system, the electric field at the QE position is the composition of the incident electric field $[\mathbf{E_i}(\mathbf{r},t)]$ with the electric field generated by the interaction with the nearby structures $[\mathbf{E_r}(\mathbf{r},t)]$, considering the QE itself also radiates and generates electric field $[\mathbf{E_{QE}}(\mathbf{r},t)]$, as can be seen in Fig. 1(a). In this sense,

$$\vec{\mathbf{E}}(\mathbf{r},t) = \mathbf{E_i}(\mathbf{r},t) + \mathbf{E_{QE}}(\mathbf{r},t) + \mathbf{E_r}(\mathbf{r},t). \tag{8}$$

Using dipolar approximation, the radiation of the QE can be written as a dipolar emission, where the dipole moment is given in Eqs. (7) and (8). In (9), $\mathbf{E_r}(\mathbf{r},t) = \mathbf{E_r^i}(\mathbf{r},t) + \mathbf{E_r^{QE}}(\mathbf{r},t)$ is a contribution of the structure interacting with the incident light $\mathbf{E_r^i}(\mathbf{r},t)$ and the $\mathbf{E_r^{QE}}(\mathbf{r},t)$. Both can be calculated using conventional time-modulated solvers, such as time-modulated rigorous coupled wave (RCWA) analysis;[53] time-modulated discrete dipole approximation (DDA);[54] and the time-Floquet Mie theory[42,55] and time varying crystals theory.[56] It is worth noting that the total $\mathbf{E}(\mathbf{r},t)$ depends on the states to calculate the dipolar approximation, while the states need the Electric field, which can be seen in the QE energy levels shown in Fig. 1(b). In this sense, we make use of the Newton–Raphson[57] algorithms to converge the density of states, which provides the exact same electric field necessary to produce $\mathbf{p_{ij}}(t)$. After the calculations, we can compute the scattering properties of the time-modulated QE, as the example shown in Fig. 1(c). A chart of the procedure can be seen in Fig. 2, where we start by calculating the background electric fields $\mathbf{E_i}(\mathbf{r},t)$ and $\mathbf{E_r^i}(\mathbf{r},t)$, and computing the density of states ρ along with the dipole moments $\mathbf{p_{ij}}$.

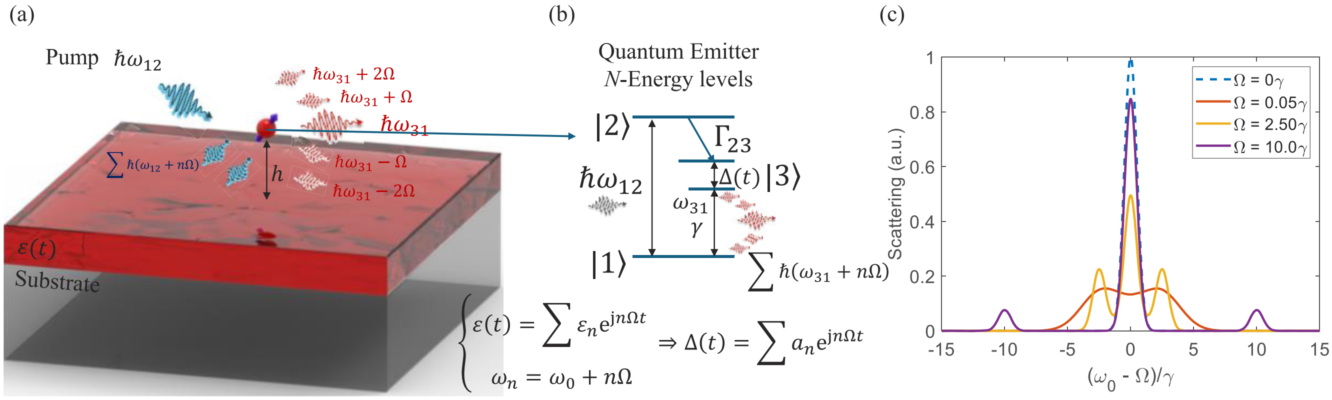

FIG. 1. (a) Schematic of a quantum emitter (QE) interacting with a time-modulated structure (the red slab above the substrate), where the total electric field $\mathbf{E}(\mathbf{r},t)$ at the QE is a sum of the incident field $\mathbf{E}_\mathrm{i}(\mathbf{r},t)+\mathbf{E}_\mathrm{r}^\mathrm{i}(\mathbf{r},t)$, the field radiated by the $\mathbf{E}_\mathrm{QE}(\mathbf{r},t)+\mathbf{E}_\mathrm{r}^\mathrm{QE}(\mathbf{r},t)$, and the field reflected by the structure. (b) Energy-level diagram of the QE, showing transitions influenced by the modulated electric field, crucial for achieving steady-state solutions. (c) Scattering spectrum as a function of frequency detuning, illustrating the impact of modulation strength Ω on the emission profile.

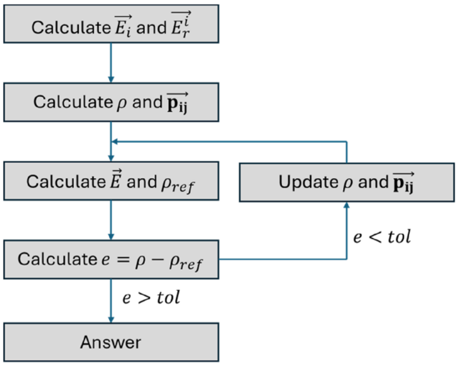

FIG. 2. Flow chart illustrating the iterative procedure to achieve the steady-state solution of the time-modulated QE system.

With this information, we capture the total electric field radiated by the QE and reflected by the structure [as shown in Fig. 1(a)] and calculate the new ρ_{ref}. In sequence, with the error $e=\rho-\rho_{ref}$ (note that all states levels need to converge) being smaller than a defined tolerance *tol*, the present state is correct; otherwise, we use the Newton method to calculate the new ρ and perform another interaction until the approach converges. It is also important to highlight that, in our model the coupling between harmonics originates from the electric fields that excite the time-harmonic components in the QE state. In this context, the energy exchange between harmonics is governed by the properties of the time-modulated material, which changes the photon momentum and, consequently, their frequencies. Hence, the QE is excited by different electric field harmonics Eq. (4), and each harmonic operates as a detuned excitation for the QE.

III. POLARIZABILITY ANALYSIS

To validate our approach, we calculate the polarizability of a two- and three-level quantum system, considering a low-power regime. Under these considerations, the nth harmonic of the polarizability of a two-level system can be calculated as

$$\alpha_n(\omega)=\frac{2d_{12}^2}{\hbar}\frac{1}{\left[(\omega-n\omega_m)^2-\omega_{12}^2+j\Gamma_{12}(\omega-n\omega_m)\right]},\qquad(9)$$

where ω is the excitation light angular frequency. By considering $\omega_0=\omega_{12}$, $\Gamma_{12}=\Gamma/20$, and $\omega_m=\omega_0/5$, the real (solid lines) and imaginary (dashed lines) α_n for a two-level system can be seen in Fig. 3(a) for $n=(-2,2)$ [energy levels shown as an inset in Fig. 3(b)]. As illustrated, polarizability is related to a Lorentzian-shaped curve, as expected and demonstrated in other studies,[58] which is verified in our formalism. Moreover, we also calculate the ratio between coherent and spontaneous emission, given by $\rho_{12}\rho_{12}^*/\rho_{22}$[51] when all harmonics of the excitation have the same amplitude, as shown in Fig. 3(b). As can be seen, time modulation decreases the coherence of a two-level system since some photons decay out of coherence in different harmonics.

For a V-shaped three-level system polarizability, we considered $\omega_{13}=2\omega_{12}$, $\Gamma_{12}=\Gamma_{13}=\Gamma_{23}/20=\omega_{13}/100$, $\omega_m=\omega_{13}/5$, and finally, the Rabi frequency $\Omega_{12}=2\Omega_{13}$. Ω_{12} excites the electrons to the 2-level, which decays non-radiatively to 3-level. Finally, the radiative decay from level 2 to 1 is stimulated by an external time-modulated electric field, with equal harmonic amplitudes. As a consequence, each frequency harmonic can be associated by a polarizability α_n that relates the excitation with the emission of the QE. The real (solid lines) and imaginary (dashed lines) α_n are given in Fig. 3(c) for $n=(-2,2)$ [energy levels shown as an inset in Fig. 3(d)], and as expected, the polarizability has a Lorentzian shape for all harmonics. When subjected to a time-modulated electric field, the quantum emitter will emit at frequencies corresponding to all harmonics, with varying amplitudes depending on the detuning. For a three-level system, it is considerably more challenging to obtain coherence since it needs to invert the population on E_3. However, introducing time-modulation helps with coherence, as shown in Fig. 3(d). It is important to note that when a time-modulated electric field excites the QEs with different time harmonics, the QEs behave as multiple

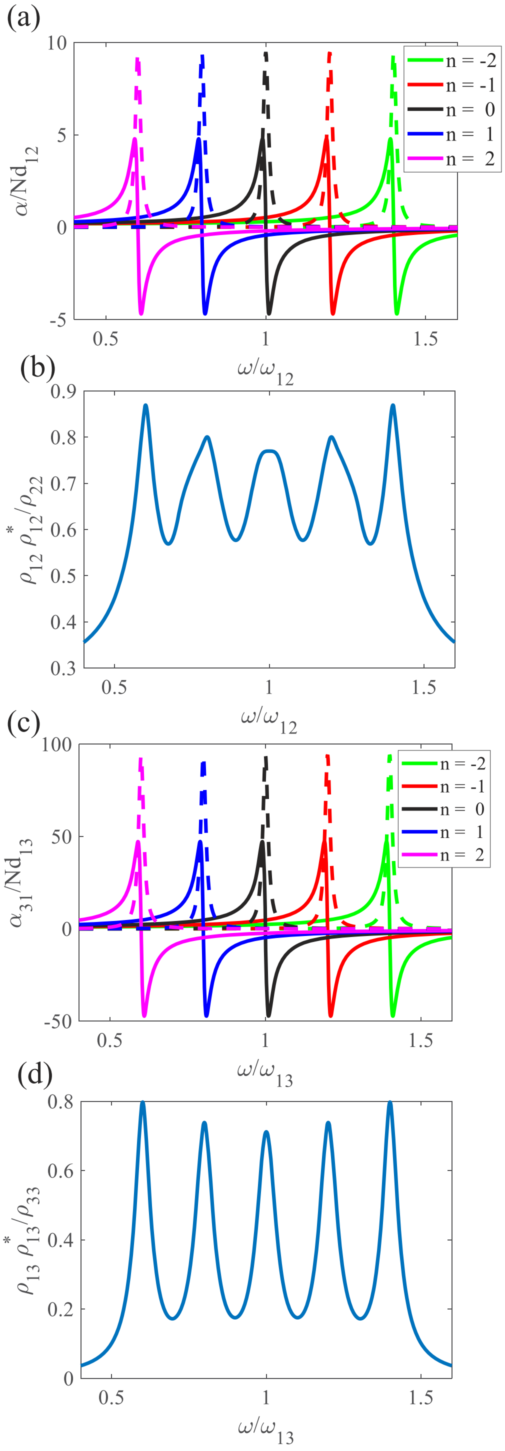

FIG. 3. Panels (a) and (c) show real (solid lines) and imaginary (dashed lines) α_n for two- and three-level systems, respectively, for $n = (-2, 2)$. The coherent and spontaneous emission ratio, given by $\rho_{12}\rho_{12}^*/\rho_{22}$ (b) and $\rho_{13}\rho_{13}^*/\rho_{33}$ (d) when all harmonics of the excitation have the same amplitude for two- and three-level systems.

dipoles oscillating at distinct frequencies, each corresponding to a specific harmonic. This occurs because polarizability is defined separately for each frequency harmonic, leading to a multi-frequency dipolar response. Moreover, each frequency harmonic corresponds to a different transition pathway in the three-level system, highlighting the role of time modulation in redistributing energy across multiple transitions and enhancing the overall control of the system. This effect allows for controlled energy exchange between different harmonics, leading to a tunable emission spectrum that can be engineered by adjusting the modulation frequency and amplitude.

IV. COUPLING QE WITH TM-QED

After calculating the polarizability of QEs, the next step to demonstrate the application of the proposed modeling is to place a 3 nm diameter V-shaped three-level quantum dot close to two time-modulated spheres with radii a and distanced $2d$ from each other, as shown in Fig. 4. In this example, the QE characteristics are chosen as $\lambda_{12} = 785$ nm, $\lambda_{13} = 850$ nm, $\Gamma_{12} = \Gamma_{13} = \Gamma_{23}/4 = 5 \times 10^{11}$ Hz, and $d_{12} = d_{13} = 10^{-30}$ cm. The quantum dot radius is embedded in a $d_{particle} = 2$ nm diameter silica sphere with a density of QE set as 10^{-23} cm^{-3}. Since the particle diameter is much smaller than the wavelength ($\mathrm{d}_{\mathrm{particle}}/\lambda_{13} = 0.0023$, well below the Rayleigh limit[59]), we considered a dipolar emission, as shown in Fig. 4. The time modulated sphere has an arbitrary permittivity $\varepsilon(t) = \varepsilon_r(1 + \delta \cos \omega_m t)$, where $\varepsilon_r = -4$, $\delta = 0.1$, and it is illuminated by a plane wave of 1 W/m^2 at λ_{12} with an electric field along the vector connecting the spheres center and operating at the weak coupling regime. It is important to notice that formalism can be adapted to various parameter choices, and the system is chosen to represent practical structures such as nano-antennas and metasurfaces close to QEs. To accommodate these scenarios, one needs to adjust the electromagnetic solver, which may involve using methods such as time-modulated DDA. Moreover, it is worth noting that our choice of material in this work is entirely arbitrary, allowing the focus on the proposed theoretical formalism, neglecting the effects of material properties, such as dispersion. One can obtain results for any specific material and toward a goal of interest, depending on the availability of materials. Nonetheless, various mechanisms such as acousto-optic[60,61] and free-carrier density modulation[62,63] can be employed to realize temporally modulated electromagnetic systems. In particular, indium tin oxide, titanium nitrate, and graphene have been used in combination with a plasmonic metasurface to demonstrate space–time modulation at optical and THz frequencies experimentally.[64–66]

Before exploring the time modulation (assuming $\delta = 0$), we use time-floquet Mie theory[42] to calculate the electric field at the quantum emitter (QE) position, providing the initial input for the iterative approach illustrated in Fig. 2. The Floquet–Mie framework used in this work builds upon a previously validated formalism, which was benchmarked against FDTD simulations and adiabatic limit comparisons, as detailed in Ref. 43. Using this framework combined with the model proposed in this manuscript, we calculated the dipolar emission at λ_{13} and the average emission $|\mathbf{p}_{13}(t)|$. Figures 5(a)–5(c) illustrate the Purcell factor (considering the emission), ρ_{33} and $\rho_{13}\rho_{13}^*/\rho_{33}$, for varying sphere radii and distances

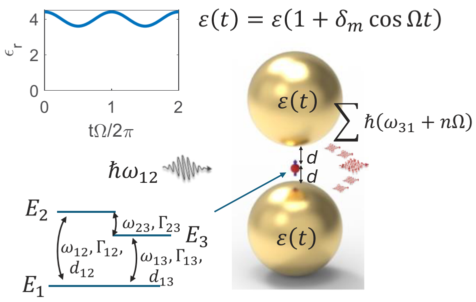

FIG. 4. Schematic of the proposed system. The 3 nm diameter V-shaped three-level quantum dot is placed between two time-modulated spheres with radius a and distanced $2d$.

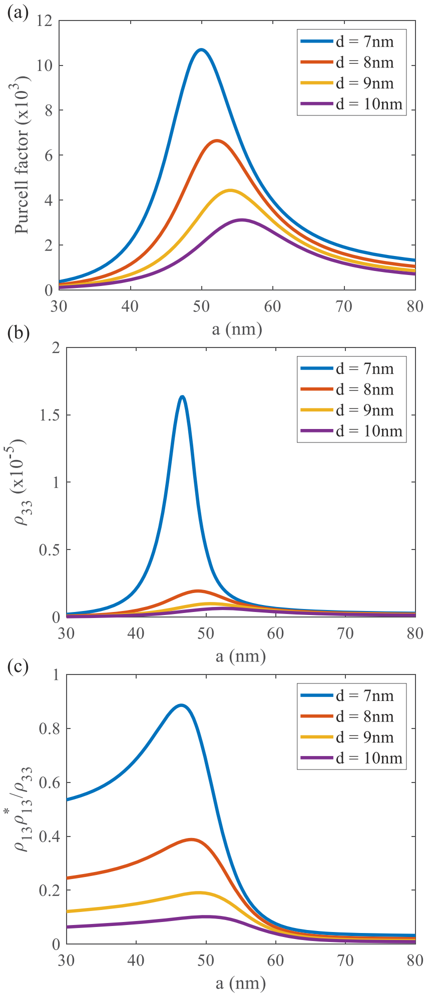

FIG. 5. Purcell factor (a) ρ_{33} (b) and $\rho_{13}\rho_{31}^*/\rho_{33}$ (c) for different sphere radius and distances from the QE.

or RCWA. Moreover, between the QE and the spheres. As observed, closer proximity of the spheres to the QE enhances the Purcell factor due to intensified plasmonic resonances in the spheres. A stronger electric field increases the Rabi frequency, resulting in higher ρ_{33}. Notably, a strong resonance is achieved for a sphere radius $a = 50$ nm and $d = 7$ nm, as shown in Figs. 5(a) and 5(b), as observed by the high Purcell factor shown in Fig. 5(a). These parameters ($a = 50$ nm and $d = 7$ nm) optimize the system for enhanced spontaneous emission and provide a platform for controlling emission via time modulation. Note that the scattering properties of the metallic nanospheres used in the model were validated using Mie theory and FDTD simulations (see the supplementary material), confirming that they operate strictly within the electric dipole regime, which supports coupling through localized surface plasmon resonances that can be used to enhance the interaction of the structure with the QE. Moreover, the high Purcell indicates strong coupling between the quantum emitter and the surrounding structure, resulting in a more efficient energy transfer into the desired frequency harmonics. Moreover, in terms of emission, enhancing the Purcell factor is directly related to the QE lifetime,[7] resulting in faster modulation speeds that can be employed in telecommunications.

For the time-modulated scenario, we explore different modulation frequencies, $\omega_m = 4$, 7, 10, and 14 Γ_{23}. Figure 6 shows the total power dissipated by the QE (P) normalized by the free-space power of the 23 transitions, $P_0 = d_{13}^2\omega_{13}^4/(4\pi\varepsilon_0 c^3)$ in Figs. 6(a)–6(e), the total radiated power (P_{rad}) in Figs. 6(f)–6(j), and[42] ρ_{33} in Figs. 6(k)–6(o) for the first two positive and negative frequency harmonics. The incident plane wave with frequency ω_{12} interacts with the time-modulated sphere system, generating harmonics that excite the QE. Moreover, the harmonics also contribute to exciting the QE, as can be seen by the harmonic excitation at Fig. 6(c), where for $n = \pm 1, \pm 2$, the harmonics generated by the structure at ω_{12} act to excite the QE.

In addition, the time-modulated Rabi frequency influences the electron population flux between levels 2 and 3, resulting in an oscillating population ρ_{33}, as shown by the harmonics in Figs. 6(k)–6(o). It is important to note that the population levels remain small due to the adoption of low-power excitation lasers. This choice has been made as the main focus of the work is on the development and validation of formalism, and since the system operates in the linear regime, increasing the excitation power would increase the population densities without altering the underlying dynamics. For completeness, we include simulations under higher-power excitation conditions and the population of ρ_{22} in the supplementary material.

The modulated population of ρ_{33} reflects the flux in which the electrons decay to level 1, as evidenced by the harmonics of the emission P in Figs. 6(a)–6(e). While most dissipated power is concentrated at the fundamental harmonic, the energy level oscillations cause the QE to emit photons at sideband harmonic frequencies.

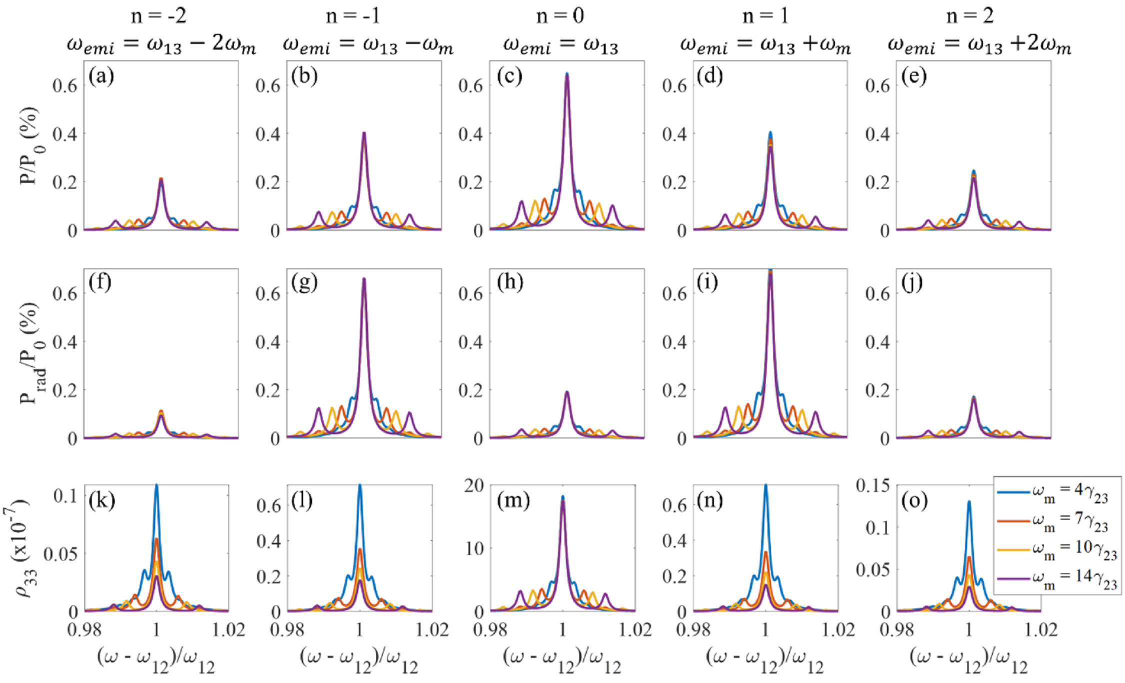

FIG. 6. Panels (a)–(e) show the normalized total dissipated power P/P_0, panels (f)–(j) show total radiated power P_{rad}/P_0 (k)–(n), and panels (k)–(o) show the excited state population ρ_{33}, for $n = 0, \pm1, \pm2$ and $\omega_m = 4\gamma_{23}$, $7\gamma_{23}$, $10\gamma_{23}$, and $14\gamma_{23}$.

Interestingly, the time-modulated system converts energy from the fundamental frequency to +1 and −1 harmonics, as evidenced by the higher radiated power at sidebands in Figs. 6(g) and (i) compared to the fundamental frequency shown in Fig. 6(h). Although the time modulation in this system is symmetric, optimization could enable power conversion to specific sidebands or frequencies. Notably, the quantum emitter (QE) excitation by a time-modulated field induces power dissipation across multiple frequency harmonics, which cannot be accurately captured when modeling the QE as a classical dipole. By incorporating time modulation into our quantum-mechanical framework, we introduce a new degree of freedom for controlling both the emission spectrum and radiative energy transfer of the QE, enabling dynamic spectral shaping through the proposed model.

In summary, we demonstrate that harmonic emission of quantum emitters (QEs) can be effectively excited and manipulated through their interaction with time-modulated (TM) systems. In addition, we show that the fundamental emission of the QE can be converted into specific sideband harmonics by carefully controlling the modulation of the sphere's permittivity. Unlike previous approaches that treat the emitter and environment separately, our framework inherently couples the QE dynamics with the time-modulated electromagnetic field, where the sidebands effectively act as additional energy levels, enabling new transition pathways and enhancing emission control. By exploring alternative modulation schemes, it is possible to enhance further and optimize the conversion efficiency of the radiated emission, offering a powerful tool for precise control over quantum light emission. Furthermore, by integrating this approach with arrays of nano-antennas, such as metasurfaces, not only can harmonic energy transfer be controlled but it also enables directional photon routing through beamforming. These results highlight the potential of time-modulated systems for advanced emission control.

It is important to emphasize that while previous *studies* have experimentally demonstrated time-modulated photonic structures, our work focuses predominantly on establishing a framework for coupling quantum emitter (QE) emission with dynamically modulated environments, which can be employed for any of these systems. The development and implementation of more practical time-modulated structures, such as plasmonic antennas or TMD, will be explored in future studies. In this context, promising material platforms include indium tin oxide (ITO), titanium nitride (TiN), doped silicon, and graphene, which have been experimentally shown to enable space–time modulation at optical and terahertz frequencies[64–66] and whose voltage-tunable permittivity allows for the realization of realistic and versatile designs, including at the permittivity regime presented here.

V. CONCLUSION

In conclusion, these results provide insights into the Markovian dynamics of open quantum systems interacting with time-modulated photonic structures, revealing how periodic modulation affects emission properties, coherence, and population transfer. We demonstrated that time modulation generates frequency harmonics that modify the system's energy levels, enabling the QE to radiate across multiple bands. By coupling the GKSL equation with the Floquet–Mie theory, we developed a robust approach to analyze the dipolar emission and Purcell factor in time-modulated systems. We also demonstrated that the emitted power of the quantum emitter (QE) can be decoupled from the total radiated power of the QE-TM system, highlighting how the time-modulated (TM) system enables energy transfer from the fundamental harmonic to higher-order harmonics. By optimizing the modulation parameters, it becomes possible to control the coupling to specific harmonics, effectively tuning the energy of the radiated photons. Furthermore, integrating this approach with arrays of nano-antennas, such as metasurfaces, enables active manipulation of emission properties post-fabrication, such as directional photon routing, opening new possibilities for tunable photonic devices and enhanced control over quantum and classical light sources. We provided a framework for designing time-modulated structures tailored for qubits, quantum transduction, and photonic systems. By utilizing the proposed system, it is possible to control the Purcell effect across different harmonics, allowing for modulation of emission lifetimes at multiple frequencies. The integration of tunable metasurfaces, time-modulated materials, and high-Q resonances provides a framework for advancements in photonic devices, with possible applications in quantum networks, secure communication, and high-speed data processing.

SUPPLEMENTARY MATERIAL

The supplementary material presents the full deduction for a two- and V-shaped 3-level system.

ACKNOWLEDGMENTS

This work was supported by the National Science Foundation through the Expand-QISE Award No. NSF-OMA-2329067 and benefited from the resources of Northeastern University's Advanced Scientific Computation Center, the Discovery Cluster, the Massachusetts Technology Collaborative Award No. MTC-22032, and the Quantum Materials and Sensing Institute.

AUTHOR DECLARATIONS

Conflict of Interest

The authors have no conflicts to disclose.

Author Contributions

Achiles F. da Mota: Conceptualization (equal); Data curation (equal); Investigation (equal); Methodology (equal); Validation (equal); Writing – original draft (equal); Writing – review & editing (equal). **Mohammad M. Sadafi**: Conceptualization (equal); Investigation (equal); Methodology (equal); Validation (equal); Visualization (equal); Writing – original draft (equal); Writing – review & editing (equal). **Wei-Chi Chiu**: Investigation (equal); Methodology (equal); Validation (equal); Writing – original draft (equal); Writing – review & editing (equal). **Bernardo Barbiellini**: Investigation (equal); Methodology (equal); Validation (equal); Writing – original draft (equal); Writing – review & editing (equal). **Michael N. Leuenberger**: Investigation (equal); Methodology (equal); Validation (equal); Writing – review & editing (equal). **Arun Bansil**: Funding acquisition (equal); Investigation (equal); Methodology (equal); Supervision (equal); Validation (equal); Writing – original draft (equal); Writing – review & editing (equal). **Hossein Mosallaei**: Conceptualization (equal); Formal analysis (equal); Funding acquisition (equal); Investigation (equal); Methodology (equal); Project administration (equal); Supervision (equal); Validation (equal); Writing – original draft (equal); Writing – review & editing (equal).

DATA AVAILABILITY

The data that support the findings of this study are available within the article and its supplementary material.

REFERENCES

[1] W. Zhang, D. S. Ding, Y. B. Sheng, L. Zhou, B.-S. Shi, and G. C. Guo, "Quantum secure direct communication with quantum memory," Phys. Rev. Lett. **118**, 220501 (2017).

[2] S.-K. Liao *et al.*, "Satellite-to-ground quantum key distribution," Nature **549**, 43 (2017).

[3] C. Shang, M. De Gregorio, Q. Buchinger, M. Meinecke, P. Gschwandtner, A. Pfenning, T. Huber-Loyola, S. Hoefling, and J. E. Bowers, "Ultra-low density and high performance InAs quantum dot single photon emitters," APL Quantum **1**, 036115 (2024).

[4] A. F. da Mota and H. Mosallaei, "Enhanced quantum efficiency and Purcell factor of incoherent light-emitting source modulators coupled with nanoantennas: DDA modeling and optimization," J. Opt. Soc. Am. B **40**, 94 (2023).

[5] A. F. d. Mota, A. Martins, H. Ottevaere, W. Meulebroeck, E. R. Martins, J. Weiner, F. L. Teixeira, and B.-H. V. Borges, "Semianalytical model for design and analysis of grating-assisted radiation emission of quantum emitters in hyperbolic metamaterials," ACS Photonics **5**, 1951 (2018).

[6] A. N. Poddubny, P. A. Belov, P. Ginzburg, A. V. Zayats, and Y. S. Kivshar, "Microscopic model of Purcell enhancement in hyperbolic metamaterials," Phys. Rev. B **86**, 035148 (2012).

[7] E. M. Purcell, "Spontaneous emission probalities at radio frequencies," Phys. Rev. **69**, 37 (1946).

[8] M. Kamandar Dezfouli, R. Gordon, and S. Hughes, "Modal theory of modified spontaneous emission of a quantum emitter in a hybrid plasmonic photonic-crystal cavity system," Phys. Rev. A **95**, 013846 (2017).

[9] N. Michieli, B. Kalinic, C. Scian, T. Cesca, and G. Mattei, "Emission rate modification and quantum efficiency enhancement of Er^{3+} emitters by near-field coupling with nanohole arrays," ACS Photonics **5**, 2189 (2018).

[10] A. F. Mota, A. Martins, J. Weiner, F. L. Teixeira, and B.-H. V. Borges, "Constitutive parameter retrieval for uniaxial metamaterials with spatial dispersion," Phys. Rev. B **94**, 115410 (2016).

[11] R. Sprik, B. A. v. Tiggelen, and A. Lagendijk, "Optical emission in periodic dielectrics," Europhys. Lett. **35**, 265 (1996).

[12] K. Busch and S. John, "Photonic band gap formation in certain self-organizing systems," Phys. Rev. E **58**, 3896 (1998).

[13] M. Jeong, B. Ko, C. Jung, J. Kim, J. Jang, J. Mun, J. Lee, S. Yun, S. Kim, and J. Rho, "Printable light-emitting metasurfaces with enhanced directional photoluminescence," Nano Lett. **24**, 5783 (2024).

[14] H. Barati Sedeh, H. Mohammadi Dinani, and H. Mosallaei, "Optical nonreciprocity via transmissive time-modulated metasurfaces," Nanophotonics **11**, 4135 (2022).

[15] C. Caloz and Z.-L. Deck-Leger, "Spacetime metamaterials—Part II: Theory and applications," IEEE Trans. Antennas Propag. **68**, 1583 (2020).

[16] N. Engheta, "Four-dimensional optics using time-varying metamaterials," Science **379**, 1190 (2023).

[17] E. Galiffi, R. Tirole, S. Yin, H. Li, S. Vezzoli, P. A. Huidobro, M. G. Silveirinha, R. Sapienza, A. Alù, and J. B. Pendry, "Photonics of time-varying media," Adv. Photonics **4**, 014002 (2022).

[18] H. Moussa, G. Xu, S. Yin, E. Galiffi, Y. Ra'di, and A. Alù, "Observation of temporal reflection and broadband frequency translation at photonic time interfaces," Nat. Phys. **19**, 863 (2023).

[19] A. Ganfornina-Andrades, J. E. Vázquez-Lozano, and I. Liberal, "Quantum vacuum amplification in time-varying media with arbitrary temporal profiles," Phys. Rev. Res. **6**, 043320 (2023).

[20] J. B. Pendry and S. A. R. Horsley, "QED in space–time varying materials," APL Quantum **1**, 020901 (2024).

[21] M. F. Picardi, K. N. Nimje, and G. T. Papadakis, "Dynamic modulation of thermal emission—A tutorial," J. Appl. Phys. **133**, 111101 (2023).

[22] S. A. R. Horsley and J. B. Pendry, "Quantum electrodynamics of time-varying gratings," Proc. Natl. Acad. Sci. U. S. A. **120**, e2302652120 (2023).

[23] D. M. Lukin *et al.*, "Spectrally reconfigurable quantum emitters enabled by optimized fast modulation," npj Quantum Inf. **6**, 80 (2020).

[24] A. D. White, R. Trivedi, K. Narayanan, and J. Vučković, "Enhancing superradiance in spectrally inhomogeneous cavity QED systems with dynamic modulation," ACS Photonics **9**, 2467 (2022).

[25] R. Yu and S. Fan, "Manipulating coherence of near-field thermal radiation in time-modulated systems," Phys. Rev. Lett. **130**, 096902 (2023).

[26] J. M. Pitarke, V. M. Silkin, E. V. Chulkov, and P. M. Echenique, "Theory of surface plasmons and surface-plasmon polaritons," Rep. Prog. Phys. **70**, 1 (2006).

[27] V. H. Nguyen and B. H. Nguyen, "Quantum field theory of interacting plasmon–photon system," Adv. Nat. Sci.: Nanosci. Nanotechnol. **6**, 025010 (2015).

[28] M. Bernardi, J. Mustafa, J. B. Neaton, and S. G. Louie, "Theory and computation of hot carriers generated by surface plasmon polaritons in noble metals," Nat. Commun. **6**(1), 7044 (2015).

[29] X. Fan, W. Zheng, and D. J. Singh, "Light scattering and surface plasmons on small spherical particles," Light: Sci. Appl. **3**, e179 (2014).

[30] J. Olmos-Trigo, D. R. Abujetas, C. Sanz-Fernández, J. A. Sánchez-Gil, and J. J. Sáenz, "Optimal backward light scattering by dipolar particles," Phys. Rev. Res. **2**, 13225 (2020).

[31] M. M. Sadafi, M. Taghavi, A. F. da Mota, and H. Mosallaei, "Optical manipulation of nanoparticles: A selective excitation approach using highly focused orbital angular momentum beams," Adv. Photonics Res. **4**, 2200224 (2023).

[32] L. Hayati, C. Lane, B. Barbiellini, A. Bansil, and H. Mosallaei, "Self-consistent scheme for optical response of large hybrid networks of semiconductor quantum dots and plasmonic metal nanoparticles," Phys. Rev. B **93**, 245411 (2016).

[33] R. Frank, "Coherent control of Floquet-mode dressed plasmon polaritons," Phys. Rev. B **85**, 195463 (2012).

[34] W. J. Zhou, Y. W. Lu, J. F. Liu, R. Liu, L. K. Ang, O. Hess, and L. Wu, "Spatiospectral localized modal coupling for room-temperature quantum coherence protection," Nanophotonics **14**, 885 (2025).

[35] Y. Yang, R. Chikkaraddy, Q. Lin, D. D. A. Clarke, D. Wigger, J. J. Baumberg, and O. Hess, "Electrochemically switchable multimode strong coupling in plasmonic nanocavities," Nano Lett. **24**, 238 (2024).

[36] S. Huang, T. Ming, Y. Lin, X. Ling, Q. Ruan, T. Palacios, J. Wang, M. Dresselhaus, and J. Kong, "Ultrasmall mode volumes in plasmonic cavities of nanoparticle-on-mirror structures," Small **12**, 5190 (2016).

[37] A. E. Krasnok, A. P. Slobozhanyuk, C. R. Simovski, S. A. Tretyakov, A. N. Poddubny, A. E. Miroshnichenko, Y. S. Kivshar, and P. A. Belov, "An antenna model for the Purcell effect," Sci. Rep. **5**, 12956 (2015).

[38] A. F. da Mota, A. Martins, J. Weiner, P. Courteille, E. R. Martins, and B.-H. V. Borges, "Design and analysis of nanopatterned graphene-based structures for trapping applications," Phys. Rev. B **102**, 085415 (2020).

[39] F. P. Bonafé, E. Ilke Albar, S. T. Ohlmann, V. P. Kosheleva, C. M. Bustamante, F. Troisi, A. Rubio, and H. Appel, "Full minimal coupling Maxwell-TDDFT: An *ab initio* framework for light-matter phenomena beyond the dipole approximation," Phys. Rev. B **111**, 085114 (2025).

[40] M. Ruggenthaler, J. Flick, C. Pellegrini, H. Appel, I. V. Tokatly, and A. Rubio, "Quantum-electrodynamical density-functional theory: Bridging quantum optics and electronic-structure theory," Phys. Rev. A **90**, 012508 (2014).

[41] Z. Maleki and T. Naseri, "A theoretical study of quantum coherence and plasmon-enhanced diffraction in practical hybrid systems including semiconductor quantum dots and metallic nanoparticles," J. Opt. **26**, 105202 (2024).

[42] M. M. Sadafi, A. F. da Mota, and H. Mosallaei, "Dynamic control of light scattering in a single particle enabled by time modulation," Appl. Phys. Lett. **123**, 101702 (2023).

[43] M. M. Sadafi, A. F. da Mota, and H. Mosallaei, "Time-varying Mie resonators for real-time manipulation of quantum emitter radiation," Phys. Rev. B **111**, 125419 (2025).

[44] T. Mori, "Floquet states in open quantum systems," Annu. Rev. Condens. Matter Phys. **14**, 35 (2023).

[45] A. Schnell, A. Eckardt, and S. Denisov, "Is there a Floquet Lindbladian?," Phys. Rev. B **101**, 100301 (2020).

[46] P. Sheng, *Introduction to Wave Scattering, Localization and Mesoscopic Phenomena* (Springer, Berlin/Heidelberg, 1995).

[47] R. J. Glauber and M. Lewenstein, "Quantum optics of dielectric media," Phys. Rev. A **43**, 467 (1991).

[48] V. Gorini, A. Kossakowski, and E. C. G. Sudarshan, "Completely positive dynamical semigroups of N-level systems," J. Math. Phys. **17**, 821 (1976).

[49] F. Campaioli, J. H. Cole, and H. Hapuarachchi, "Quantum master equations: Tips and tricks for quantum optics, quantum computing, and beyond," PRX Quantum **10**, 020202 (2024).

[50] T. Becker, L.-N. Wu, and A. Eckardt, "Lindbladian approximation beyond ultraweak coupling," Phys. Rev. E **104**, 014110 (2021).

[51] Ph. W. Courteille, *Quantum Mechanics Applied to Atoms and Light* (Universidade de São Paulo, 2024).

[52] M. Sukharev and A. Nitzan, "Optics of exciton-plasmon nanomaterials," J. Phys.: Condens. Matter **29**, 443003 (2017).

[53] S. Inampudi, M. M. Salary, S. Jafar-Zanjani, and H. Mosallaei, "Rigorous space-time coupled-wave analysis for patterned surfaces with temporal permittivity modulation [invited]," Opt. Mater. Express **9**, 162 (2019).

[54] M. M. Salary, S. Jafar-Zanjani, and H. Mosallaei, "Nonreciprocal optical links based on time-modulated nanoantenna arrays: Full-duplex communication," Phys. Rev. B **99**, 045416 (2019).

[55] T. X. Hoang, D. Leykam, and Y. Kivshar, "Photonic flatband resonances in multiple light scattering," Phys. Rev. Lett. **132**, 043803 (2024).

[56] M. M. Asgari, P. Garg, X. Wang, M. S. Mirmoosa, C. Rockstuhl, and V. Asadchy, "Theory and applications of photonic time crystals: A tutorial," Adv. Opt. Photonics **16**, 958 (2024).

[57] F. Casella and B. Bachmann, "On the choice of initial guesses for the Newton–Raphson algorithm," Appl. Math. Comput. **398**, 125991 (2021).

[58] V. Asadchy, A. G. Lamprianidis, G. Ptitcyn, M. Albooyeh, Rituraj, T. Karamanos, R. Alaee, S. A. Tretyakov, C. Rockstuhl, and S. Fan, "Parametric Mie resonances and directional amplification in time-modulated scatterers," Phys. Rev. Appl. **18**, 054065 (2022).

[59] C. Craig Bohren and D. Huffman, *Absorption and Scattering of Light by Small Particles* (Wiley, 1998), Vol. 1.

[60] G. Gantzounis, N. Papanikolaou, and N. Stefanou, "Nonlinear interactions between high-Q optical and acoustic modes in dielectric particles," Phys. Rev. B **84**, 104303 (2011).

[61] I. E. Psarobas, N. Papanikolaou, N. Stefanou, B. Djafari-Rouhani, B. Bonello, and V. Laude, "Enhanced acousto-optic interactions in a one-dimensional phoxonic cavity," Phys. Rev. B **82**, 174303 (2010).

[62] M. M. Salary, S. Farazi, and H. Mosallaei, "A dynamically modulated all-dielectric metasurface doublet for directional harmonic generation and manipulation in transmission," Adv. Opt. Mater. **7**, 1900843 (2019).

[63] R. Sabri, M. M. Salary, and H. Mosallaei, "Single sideband suppressed carrier modulation with spatiotemporal metasurfaces at near-infrared spectral regime," J. Lightwave Technol. **40**, 3802 (2022).

[64] J. Sisler, P. Thureja, M. Y. Grajower, R. Sokhoyan, I. Huang, and H. A. Atwater, "Electrically tunable space–time metasurfaces at optical frequencies," Nat. Nanotechnol. **19**(10), 1491 (2024).

[65] V. W. Brar, M. C. Sherrott, M. S. Jang, S. Kim, L. Kim, M. Choi, L. A. Sweatlock, and H. A. Atwater, "Electronic modulation of infrared radiation in graphene plasmonic resonators," Nat. Commun. **6**, 7032 (2015).

[66] Y. J. Lu, R. Sokhoyan, W. H. Cheng, G. Kafaie Shirmanesh, A. R. Davoyan, R. A. Pala, K. Thyagarajan, and H. A. Atwater, "Dynamically controlled Purcell enhancement of visible spontaneous emission in a gated plasmonic heterostructure," Nat. Commun. **8**, 1631 (2017).

RESEARCH ARTICLE | SEPTEMBER 09 2025

Impurity-induced counter skin-effect and linear modes in the Hatano–Nelson model

Special Collection: Quantum Dynamics in Theory, Numerics and in Experimental Research

Nico G. Leumer ; Dario Bercioux

APL Quantum 2, 036105 (2025)
https://doi.org/10.1063/5.0270893

APL Quantum ARTICLE pubs.aip.org/aip/apq

Impurity-induced counter skin-effect and linear modes in the Hatano–Nelson model

Cite as: APL Quantum 2, 036105 (2025); doi: 10.1063/5.0270893
Submitted: 13 March 2025 • Accepted: 17 August 2025 •
Published Online: 9 September 2025

Nico G. Leumer[1,a) and **Dario Bercioux**[1,2,b)

AFFILIATIONS

[1] Donostia International Physics Center (DIPC), Manuel de Lardizbal 4, 20018 San Sebastián, Spain
[2] IKERBASQUE, Basque Foundation for Science, Plaza Euskadi 5, 48009 Bilbao, Spain

Note: This paper is part of the APL Quantum Special Topic on Quantum Dynamics in Theory, Numerics and in Experimental Research.

[a)] **Author to whom correspondence should be addressed:** nico.leumer@dipc.org
[b)] **Electronic mail:** dario.bercioux@dipc.org

ABSTRACT

Non-reciprocal lattice systems are among the simplest non-Hermitian systems, exhibiting several key features absent in their Hermitian counterparts. In this study, we investigate the Hatano–Nelson model with impurity and unveil how the impurity influences the intrinsic non-Hermitian skin effect of the system. We present an exact analytical solution to the problem under open and periodic boundary conditions, irrespective of the impurity's position and strength. Numerical simulations thoroughly validate this exact solution. Our analysis reveals a distinctive phenomenon where a specific impurity strength, determined by the non-reciprocal hopping parameters, induces a unique skin state at the impurity site. This impurity state exhibits a skin effect that counterbalances the boundary-induced skin effect, a phenomenon we term the *impurity-induced counter skin-effect*. These findings offer insights into the dynamics of non-Hermitian systems with impurities, elucidating the complex interplay between impurities and the system's non-reciprocal nature. We propose a possible implementation of this system for a non-Hermitian discrete-time quantum walk, and we demonstrate that an impurity-induced counter skin-effect also exists in multi-band models.

I. INTRODUCTION

In 1996, Hatano and Nelson[1] demonstrated that a simple tight-binding model with non-reciprocal hopping terms can lead to unexpected localization effects of the bulk wavefunctions. This one-band model features anisotropic nearest-neighbor couplings and was originally proposed to study localization transitions in superconductors. One of the most intriguing consequences of this model is the appearance of a dramatic accumulation of eigenstates at the system boundaries when open boundary conditions (OBCs) are imposed—a phenomenon now known as the *non-Hermitian skin effect* (NHSE).[2] In contrast, under periodic boundary conditions (PBCs), the eigenstates remain extended throughout the bulk, a discrepancy that highlights the breakdown of the conventional bulk-boundary correspondence.[3] The NHSE fundamentally arises from the non-reciprocal nature of the hopping terms, which break certain symmetries (e.g., parity $\mathcal{P}$) in the system. Typically, the effect is observed in non-Hermitian systems that exhibit a winding of the energy spectrum in the complex plane.[4–8] One of the main characteristics of systems displaying the NHSE is their extreme sensitivity to boundary conditions: even minor variations in boundary couplings can lead to significant changes in both the spectrum and the localization properties of the eigenstates;[8,9] this peculiarity is at the basis of various proposals for the detection of weak signals.[10,11] The phenomenology of the NHSE has recently been extended to non-Hermitian systems with flatbands[12–14] and fractal lattices.[15]

Recent experimental implementations of the Hatano–Nelson model have been demonstrated in various platforms, including topolectrical circuits,[16] ring resonators using a synthetic frequency dimension,[17] multi-terminal quantum Hall devices,[18] mechanical continuous systems,[19] and photonic time-multiplexed resonators.[20] Moreover, the NHSE has been verified in a wide range of experimental setups, from optical waveguide arrays[21] to cold-atom platforms.[22]

An additional peculiarity of the non-Hermitian system is that the left and the right eigenstates are different. This leads to a fundamental question of how to evaluate physical observables in a quantum mechanical framework. The statistical interpretation of quantum mechanics fundamentally depends on the choice of metric, which is typically not unique and must be handled with care—especially regarding left and right eigenvectors—when deriving physical conclusions, as highlighted in studies of quasi-Hermitian Hamiltonians.[23] A possible solution to this problem is the implementation of the so-called *biorthogonal* formulation of quantum mechanics, thereby setting the metric implicitly.[23–25] Here, the left and the right eigenstates are orthogonalized to each other, and physical observables are defined as an expectation value over the left and right eigenstates. This construction ensures that observable quantities (probabilities and mean values) are independent of the arbitrary overall phase between left/right eigenvector pairs. Within this formulation, the NHSE cancels since it is the opposite for left and right eigenstates. This complete treatment of non-Hermitian systems within the biorthogonal quantum mechanics differs from the Lindblad master equation formulation in which an effective non-Hermitian Hamiltonian arises as an effective description of dissipation.[25,26] We emphasize that the eigenvectors of the associated Lindbladian generally lack physical meaning. We note in passing that some recent work suggests that the NHSE is not robust to fluctuations when treated within the Lindblad master equation approach.[27]

The localization associated with the NHSE can compete with other similar phenomena, such as the Anderson localization[28] and the Wannier–Stark localization.[29] In the former case, the interplay can lead to the appearance of an asymmetric Anderson localization characterized by a finite winding number and by two Lyapunov exponents[30] and to chiral currents.[31] In the latter case, the interplay between the NHSE and the Wannier–Stark localization leads to rich entanglement dynamics and phase transitions,[32] with the NHSE being more robust to external driving by an electric field.[33]

It is well known that single impurities or defects in a tight-binding model can act similarly to boundaries, modifying the local density of states and potentially introducing localized modes. In the context of the Hatano–Nelson model, this observation naturally raises the question of how impurities affect the NHSE. Under PBC, where the NHSE is absent and the bulk states remain extended, impurities can create an *internal* boundary that traps states, effectively mimicking the localization typically observed at the system edges under OBC. Several studies have explored this phenomenon, showing that even a single impurity can lead to a substantial reorganization of the eigenstate distribution, with the degree of localization depending sensitively on the impurity strength.[34–40] Moreover, the interplay between impurity-induced localization and the inherent non-reciprocal hopping—which drives the NHSE under OBC—can give rise to competing localization mechanisms. Such competition may, in certain parameter regimes, result in a cancellation of the skin effect for modes localized around the impurity. In our work, we investigate this delicate balance and its implications for the spectral properties of non-Hermitian systems.

In this paper, we investigate the impact of a single impurity in the Hatano–Nelson model under open boundary conditions. We show that the competition between the NHSE at the physical boundaries and at the impurity site can lead to a cancellation of the skin effect for the impurity mode. We refer to this phenomenon as the *impurity-induced counter skin-effect* (ICSE). The remainder of this paper is organized as follows: In Sec. II, we present the Hatano–Nelson model with impurities and outline the solution method. In Sec. III, we discuss our results for impurities of various strengths for PBC and OBC, including the emergence of a linear mode and the ICSE. At the end of Sec. III, we present a possible implementation of the ICSE for a biased quantum walk. Finally, in Sec. IV, we summarize our findings and offer perspectives for implementation in the framework of the non-Hermitian quantum walk.

II. MODEL AND FORMALISM

In the following, we will consider the Hatano–Nelson model[1] in the presence of an onsite impurity. This one-dimensional, non-reciprocal, non-Hermitian model is characterized by hopping amplitudes different for the left (L) and right (R) hopping directions. The model Hamiltonian reads

$$\hat{H}_l = \sum_{j=1}^{N-1} \left(t_\mathrm{L}\, c_j^\dagger c_{j+1} + t_\mathrm{R}\, c_{j+1}^\dagger c_j\right) + \delta\, c_l^\dagger c_l, \tag{1}$$

where $t_{\mathrm{L,R}} \in \mathbb{C}\backslash\{0\}$ are the two different hopping amplitudes, and $\delta \in \mathbb{C}$ is the impurity strength that can be placed on any lattice site $l \in \{1, \ldots, N\}$. In the previous Hamiltonian, c_j $(c_j^\dagger)$ represents the single-particle creation (annihilation) operators for a particle at site n. We present a sketch of the system in Figs. 1(a) and 1(b) for OBC and PBC, respectively. The hopping terms could be fixed as $t_\mathrm{R} = te^{g}$ and $t_\mathrm{L} = te^{-g}$ with $g = 1/2\ln(t_\mathrm{R}/t_\mathrm{L})$ and $t \in \mathbb{R}$; this choice would permit us to use t as a scale of energy but would not allow us to have a negative product $t_\mathrm{L}t_\mathrm{R}$ in Eq. (3).

Analytically, we obtained right (left) hand eigenvectors ψ_R (ψ_L) from Eq. (1) by solving a recursive formula of their respective entries. Since non-reciprocal hopping connects only nearest neighbors, the recursion consists of only three terms, i.e., it is of "Fibonacci" type,[41–50] and solutions follow similarly to $\delta = 0$ as superpositions of left/right moving contributions modulated by an overall exponential localization due to the non-Hermitian skin effect.[27,35,36,51] In addition, in the language of standard 1D scattering theory,[52] the eigenvector equation provides a continuity condition that connects left/right moving solutions before and after the impurity. Respective superposition coefficients, required to obtain the eigenvector itself, are found from the applied boundary condition, either OBC or PBC. Yet, energy and associated wavevectors k_n have still to be found from the (transcendental) quantization constraint—see Eq. (4) in Sec. III. A full analytical Fibonacci-type solution is presented in the supplementary material. Furthermore, we have verified our analytical results by considering numerical routines with infinite precision,[53] since it is well known that machine precision may cause faulty data. In the supplementary material, we show that this issue also depends on the solver/routine applied.

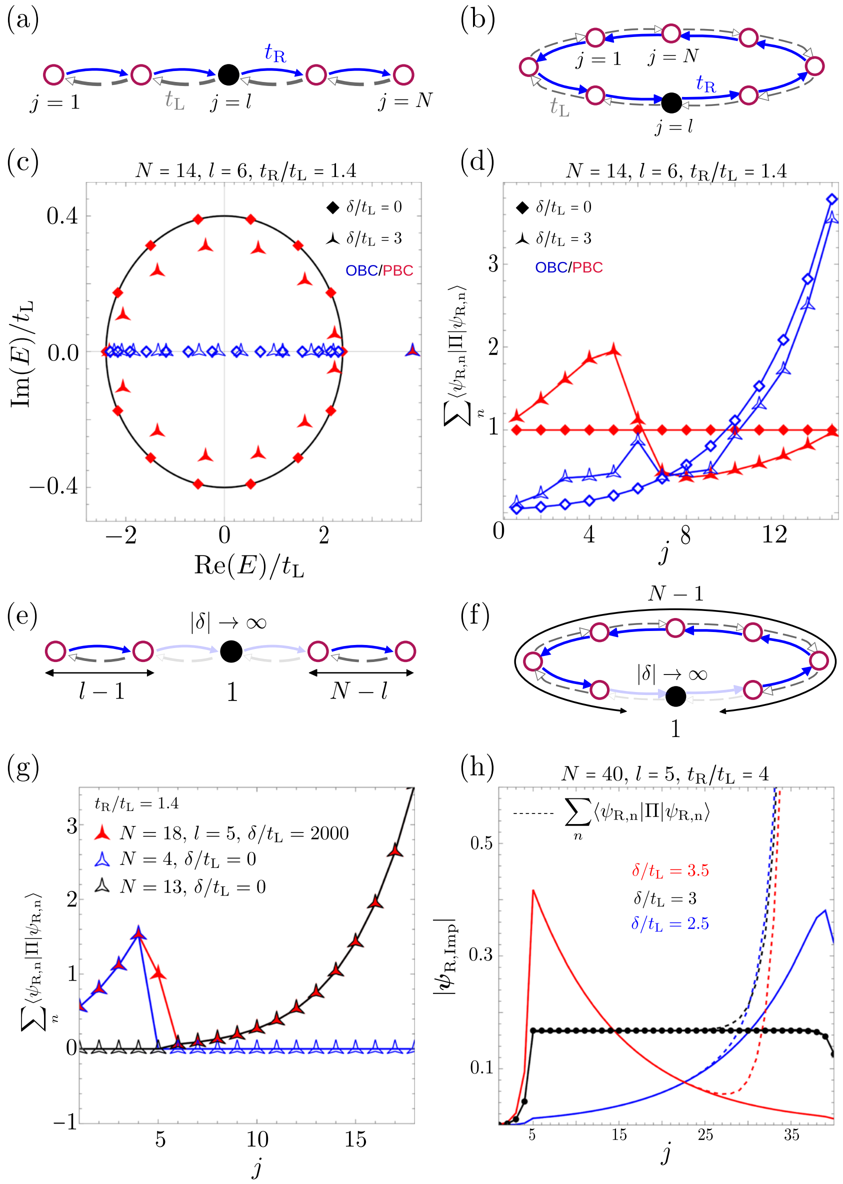

FIG. 1. Hatano–Nelson model with impurity: spectrum, NHSE, and impurity mode. [(a) and (b)] Sketch of the system under OBC (PBC), non-reciprocal hopping $t_{L,R}$, and onsite impurity δ (•). (c) Energy eigenvalues for $\delta/t_L = 0$ ($\delta/t_L = 3$) shown as ⋄ (⅄) under PBC (OBC) in red (blue). Black line: Bloch spectrum from Eq. (2) for $N \to \infty$. (d) NSHE effect for right-hand eigenvectors [same color/markers as in (c)] in agreement with Ref. 35. [(e) and (f)] Effective chain fragmentation in the limit $|\delta| \to \infty$ for OBC (PBC). (g) The NHSE emerges at the intermediate boundary, i.e., the impurity, due to the chain fragmentation at large δ. Red: full model for $N = 18$, $l = 5$, and OBC. Blue/black: chain fragments with $N - l = 13$, $l - 1 = 4$ sites, $\delta = 0$, and OBC. (h) Competing localization effects on $\psi_{R,\,Imp}$ caused by NHSE and onsite impurity $\delta \neq 0$ for fixed $N = 40$, $l = 5$, and $t_R/t_L = 4$. Strong (weak) impurities shown in red (blue) overcome (underlie) the NHSE. Intermediate values of δ may cause a compensation (black), resulting in a near flat profile of $\psi_{R,Imp}$ to one site of the impurity. Dashed lines show the NHSE and block dots mark our analytic approximation for $\psi_{R,Imp}$. Discussion in the main text. All data are obtained by exact diagonalization. In panels (d) and (g), the projector Π is defined as $\Pi \equiv \Pi_n = \sum_\alpha |e_{\alpha,n}\rangle\langle e_{\alpha,n}|$, where $\Pi \equiv \Pi_n = \sum_\alpha |e_{\alpha,n}\rangle\langle e_{\alpha,n}|$ is an eigenstate of the system.

III. RESULTS

We start analyzing the spectral properties of the Hatano–Nelson model by considering impurities of various strengths δ. We will also show the appearance of out-of-band transition, linear modes, and the ICSE. For completeness, we will consider the cases both with PBC and OBC. A sketch of our model is presented in Figs. 1(a) and 1(b) under OBC and PBC, respectively.

A. Limiting cases in δ

The Hamiltonian comprises two important and complementary limits concerning the impurity strength that read $\delta = 0$ and $|\delta| \to \infty$. In the former case, Eq. (1) reduces to the well-known Hatano–Nelson model, and under PBC, its spectrum reads

$$E(q_n) = (t_\mathrm{L} + t_\mathrm{R})\cos(q_n d) + \mathrm{i}(t_\mathrm{L} - t_\mathrm{R})\sin(q_n d) \tag{2}$$

with $q_n d = 2n\pi/N$ and $n = 1, \ldots, N$. It winds around the origin in the complex plane whenever the hopping amplitudes differ, i.e., $t_\mathrm{L} \neq t_\mathrm{R}$—cf. Fig. 1(c), red ⋄. In contrast, under OBC, the spectrum reads

$$E(k_n) = 2\sqrt{t_\mathrm{L} t_\mathrm{R}}\cos(k_n d) \tag{3}$$

with $k_n d = n\pi/(N+1)$, $n = 1, \ldots, N$, and it resides on the real (imaginary axis) if $t_\mathrm{L} t_\mathrm{R} > 0$ ($t_\mathrm{L} t_\mathrm{R} < 0$) as shown by the blue ⋄ in Fig. 1(c). Predicted by the spectral winding for PBC, all right-hand energy eigenstates of Eq. (1) under OBC pile up toward the right (left) chain's end in case of $t_\mathrm{R}/t_\mathrm{L} > 1$ ($t_\mathrm{R}/t_\mathrm{L} < 1$), as shown in Fig. 1(d)—this represents the non-Hermitian skin effect.

We consider, then, the second interesting limit, $|\delta| \to \infty$. Although hopping $t_\mathrm{L,R}$ still connects all neighboring sites, the chain effectively splits into various *fragments*, three in the case of OBC with lengths $l-1$, 1, and $N-l$ and two for PBC with length 1 and $N-1$, as illustrated in Figs. 1(e) and 1(f), respectively. The reason for this is similar to the tunneling effect in textbook quantum mechanics in that the impurity acts as a potential barrier $V(j)$, i.e., that the energy difference $V(j=l) - V(j \neq l) = \delta$ does not support hybridization between regions of different onsite energies.[38] Indeed, the eigenvector equation from Eq. (1) explicitly displays an additional OBC at the impurity position for all states from the various fragments with $N-1$ sites for PBC and $l-1$, $N-l$ sites for the OBC case. The single exception is the impurity mode $\psi_\mathrm{R,imp}$. This state has an energy $E \simeq \delta$ and is trapped at the impurity site.

In Fig. 1(g), we show the NHSE found from Eq. (1) for $\delta/t_\mathrm{L} = 2000$, $l = 5$, $t_\mathrm{R}/t_\mathrm{L} = 1.4$, and $N = 18$ in red. Since the impurity strength is the dominant energy scale, the illustrated data mimic the scenario of $|\delta| \to \infty$. In this regard, blue and black points correspond to the impurity-free Hatano–Nelson chains for $t_\mathrm{R}/t_\mathrm{L} = 1.4$ and respective lengths of $l - 1 \equiv 4$ and $N - l \equiv 13$ sites. The perfect match of blue/red (black/red) data points on the sites $j = 1, 2, 3, 4$ ($j = 6, \ldots, 18$) showcases that the impurity realizes OBC, i.e., the chain effectively fragments. At $j = l = 5$, only the trapped impurity mode (red) contributes, such that the NHSE assumes unity.

Finally, in Fig. 1(h), we show the competition between the exponential localization of the impurity and the NHSE, shown in red and blue, respectively. For a specific value of δ, the two localization lengths nearly cancel on the impurity site (black), causing a nearly flat profile. This effect is the impurity-induced counter skin-effect, and we shall discuss it further below.

B. Generic δ and quantization condition for OBC

Generally, the case of finite (complex) δ can be understood as an interplay between the two extreme limits discussed above, and it manifests in the quantization condition of wavevectors kd associated with energy E. In the case of OBC, Eq. (3) still holds with $k_n d$ being the (complex) solutions of

$$\frac{\delta}{\sqrt{t_\mathrm{L} t_\mathrm{R}}}\,\frac{\sin(k_n d\, l)}{\sin(k_n d)}\,\frac{\sin[k_n d(N-l+1)]}{\sin(k_n d)} = \frac{\sin[k_n d(N+1)]}{\sin(k_n d)}. \tag{4}$$

Notice that at $\delta = 0$, Eq. (4) reduces to the known quantization condition $\sin[k_n d(N+1)] = 0$ for the impurity-free Hatano–Nelson chain consisting of N connected sites. Dividing Eq. (4) by $\delta \neq 0$ and assuming that $\delta \to \pm\infty$, we have $\sin(k_n d\, l) = 0$ and $\sin[k_n d(N-l+1)] = 0$. Since the two constraints generally yield two distinct sets of solutions k_n for arbitrary N and l, Eq. (4) explicitly manifests the chain's fragmentation into two sub-chains of $l-1$ and $N-l$ sites, respectively. This limit extends to complex δ, as can be seen by using the polar form $\delta = |\delta| e^{i\phi_\delta}$. In addition, the real part of solutions $\mathrm{Re}(k_n d) \in [-\pi/2, \pi/2)$ may be restricted to the first Brillouin zone, exploiting the periodicity of the sin functions. Because the sign inversion $\delta \to -\delta$ in Eq. (4) is always counteracted by the shift $k_n d \to k_n d + \pi$, the spectrum only reverses its sign when the impurity does.

Since the wavevector quantization condition under PBC also displays the chain's fragmentation for $|\delta| \to \infty$ explicitly, Figs. 1(c) and 1(d) can be understood as follows: In Fig. 1(d), eigenvectors of Eq. (1) under PBC (OBC) signal the emergence of the NHSE at the impurity site—cf. ⅄. This is accompanied by a change of the associated eigenvalues shown in Fig. 1(c). Although energies under PBC and $\delta \neq 0$ still wind around the origin of the complex plane, the ellipses flatten and shrink. This behavior is clear when $|\delta| \to \infty$, since the fragmentation of the system is equivalent to having OBC, i.e., the spectrum becomes purely real (imaginary) whenever $t_\mathrm{L} t_\mathrm{R} > 0$ ($t_\mathrm{L} t_\mathrm{R} < 0$). Similarly, the spectrum of Eq. (1) and OBC rearranges itself on the real (imaginary) axis for finite δ in order to properly display the energies of the eigenvalues of the chain fragments.

C. Out-of-band transition and linear modes

We notice that under OBC and sufficiently strong but finite δ, the energy spectrum of Eq. (1) is not restricted to $(-2\sqrt{t_\mathrm{L} t_\mathrm{R}}, 2\sqrt{t_\mathrm{L} t_\mathrm{R}})$ as illustrated by Fig. 1(c). Here, we observe the appearance of a state at energy $E \approx \delta > t_\mathrm{R}$ for both OBC/PBC beyond the band's extremes. This corresponds to the impurity mode $\psi_\mathrm{R,imp}$, whose energy is typically $E_\mathrm{Imp} \simeq \delta$, besides a small correction due to hybridization with neighboring sites. Generally, E_Imp corresponds to a complex wavevector kd such that $\psi_\mathrm{R,imp}$ localizes exponentially around the impurity depending on the precise value of δ.

An exact solution for $\psi_\mathrm{R,imp}$ (in all parameter regimes), and following our analytical approach, requires merely the knowledge of the associated kd. However, the transcendental character of Eq. (4) prohibits an exact solution, except in certain limiting cases, such as the out-of-band transition—here, the impurity mode energy lies beyond the band limits. Since we can continuously change parameters from $\delta = 0$ to sufficiently large values, we can identify a critical value δ_c for which the impurity modes energy equals one extreme of the band, i.e., $E_\mathrm{Imp} = \pm 2\sqrt{t_\mathrm{L} t_\mathrm{R}}$ under OBC. For this specific case, the dispersion relation demands $kd = 0, \pi$ for the associated wavevector. Therefore, the critical value

$$\frac{\delta_{\mathrm{c}}}{\sqrt{t_{\mathrm{L}} t_{\mathrm{R}}}} = \pm \frac{N+1}{l(N+1-l)} \tag{5}$$

of δ follows from Eq. (4), at which the oscillatory part of $\psi_{\mathrm{R,\,Imp}} = (\alpha_1, \ldots, \alpha_l, \gamma_{l+1}, \ldots \gamma_N)^{\mathrm{T}}$ adopts a linear shape,[54]

$$\frac{\alpha_j}{\alpha_1} = \left[\pm\sqrt{\frac{t_{\mathrm{R}}}{t_{\mathrm{L}}}}\right]^{j-1} j, \tag{6a}$$

$$\frac{\gamma_j}{\alpha_1} = l\left[\pm\sqrt{\frac{t_{\mathrm{R}}}{t_{\mathrm{L}}}}\right]^{j-1} \frac{j-N-1}{l-N-1}, \tag{6b}$$

with $j \in \{1, \ldots, N\}$ and l being the impurity position. The positive sign belongs to $k_n d = 0$, whereas the negative one belongs to $k_n d = \pi$. Notice also that α_1 adopts the role of the normalization constant.

In Fig. 2(a), we show $|\psi_{\mathrm{R,imp}}|$ obtained numerically with infinite precision for $\delta = \delta_{\mathrm{c}}$, $l = 10$, $N = 20$, and fixed $t_{\mathrm{L}} t_{\mathrm{R}} = 2$. In the Hermitian case $t_{\mathrm{L}} = t_{\mathrm{R}}$ (black), we witness a linear shape peaked at the impurity position $j = l = 10$. In case of anisotropic hopping $t_{\mathrm{L}} \neq t_{\mathrm{R}}$, the NHSE localizes $|\psi_{\mathrm{R,imp}}|$ toward the right (left) end whenever $t_{\mathrm{R}} > t_{\mathrm{L}}$ $(t_{\mathrm{R}} < t_{\mathrm{L}})$, as Eq. (6) suggests that the exponential dominates locally over the linear term. The results for lhs eigenvectors $|\psi_{\mathrm{L,imp}}|$ (dashed) follow from those of $|\psi_{\mathrm{R,imp}}|$ by mutual exchange of $t_{\mathrm{L}} R$.

In Fig. 2(b), we show $|\psi_{\mathrm{R,imp}}|$ for $|\delta/\delta_{\mathrm{c}}| > 1$ $(|\delta/\delta_{\mathrm{c}}| < 1)$ in dotted (dashed) lines, while the solid ones belong to $|\delta/\delta_{\mathrm{c}}| = 1$. When δ exceeds the critical value δ_{c}, the linear shape is altered into an exponential one, and $|\psi_{\mathrm{R,\,imp}}|$ localizes toward the impurity. In gray (black), we show the case of an impurity at an edge (bulk) site $l = 1$ $(l = 10)$. Similarly, we have an oscillatory behavior of $|\psi_{\mathrm{R,imp}}|$ for $|\delta/\delta_{\mathrm{c}}| < 1$. In addition, the impurity modes' profile is sensitive to the smallest changes in δ when the impurity resides close to the chain's edges.

The actual dependence of δ_{c} on the various parameters is intrinsically intriguing. In terms of the impurity's position l, δ_{c} is the product of two hyperbolas with poles at $l = 0, N+1$; that means beyond the chain's terminal sites, as illustrated in Fig. 2(c). Hence, the largest value $|\delta_{\mathrm{c}}/\sqrt{t_{\mathrm{L}} t_{\mathrm{R}}}|$ is $1 + 1/N$ for $l = 1, N$, while placing the impurity close to the center of the chain $l = N/2$ gives $(N+1)/(N^2/4+4)$, a vanishingly small contribution for longer chains $N \to \infty$.

This is an interesting property, in particular since the rhs of Eq. (5) is formed by real quantities, i.e., the out-of-band transition survives the Hermitian limit $\delta \in \mathbb{R}$, $t_{\mathrm{L}} = t_{\mathrm{R}}^*$ of the model. That implies that the transition from $|\delta_{\mathrm{c}}/\delta| < 1$ to $|\delta_{\mathrm{c}}/\delta| > 1$ can be caused by rearranging the sites. For example, in state-of-the-art scanning tunneling microscope experiments, atoms can be placed in a controlled manner on substrates, i.e., the chain of atoms may be broken into two pieces as sketched in Fig. 2(d). This allows the control of the out-of-band transition even in the case that δ cannot be changed directly.

D. Impurity induced counter skin effect

The ISCE results from a nearly perfect cancellation of exponential localizations due to the impurity and the NHSE, as shown in black in Fig. 1(h). We obtain that the necessary impurity strength to observe it is

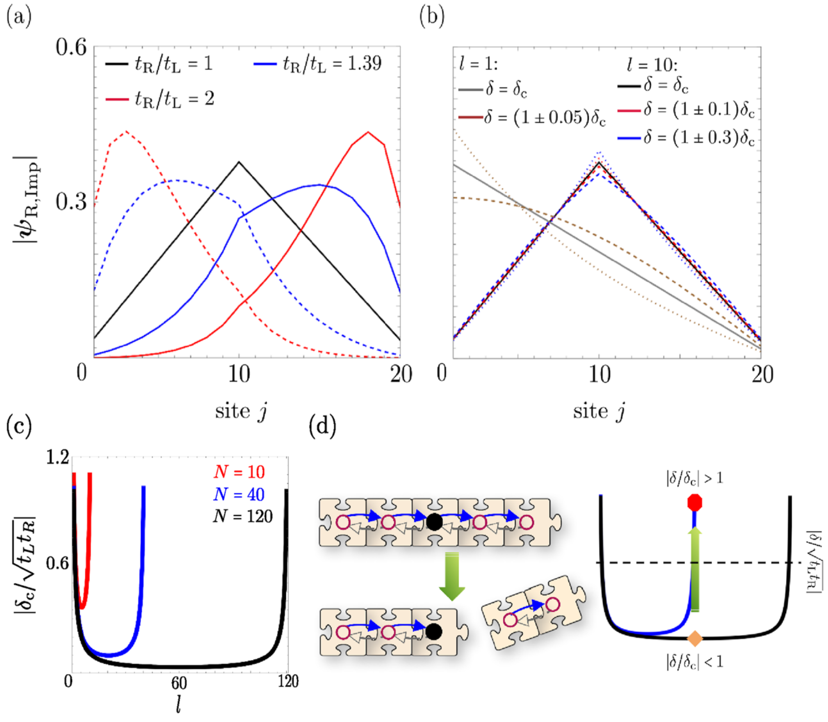

FIG. 2. Linear mode and its stability. (a) Due to its exponential dependence, tuning the ratio $t_{\mathrm{R}}/t_{\mathrm{L}}$ alters $\psi_{\mathrm{R,\,Imp}}$'s profile (black) significantly. Data shown belong to $l = 10$, $\delta = \delta_{\mathrm{c}}$, and $t_{\mathrm{L}} t_{\mathrm{R}} = 2$ fixed. Dashed lines belong to $\psi_{\mathrm{L,Imp}}$. (b) Modifying δ around δ_{c} yields minor (significant) changes for $l = N/2$ $(l = 1)$, comparing the blue/red (brown) lines with the black (gray) one. Dotted (dashed) curves indicate increased (reduced) δ for $t_{\mathrm{R}}/t_{\mathrm{L}} = 1$. In the two panels, we have used $N = 20$. (c) δ_{c} as a function of impurity position l for different system sizes $N = 10, 40, 120$. (d) Removing impurity-free sites may cause a transition from $|\delta/\delta_{\mathrm{c}} > 1|$ to $|\delta/\delta_{\mathrm{c}} < 1|$ even if the impurity strength is constant and cannot be controlled.

$$\delta = \pm(t_\mathrm{R} - t_\mathrm{L}) \tag{7}$$

when the impurity is not placed too close to the chain's terminal sites; cf. the supplementary material. We start by considering the case in which the impurity is placed in the center of the chain and discuss the correction caused by placing the impurity close to the terminal sites later.

To verify the computational results (with infinite precision) and also to deepen our understanding of the phenomenon, we opt for an analytic approximation for $\psi_{\mathrm{R,\,imp}}$. Although our exact formulas for all eigenstates allow for exact results, they require the knowledge of the states' energy or the associated wavevector kd. Due to the complexity of Eq. (4), we choose instead to approximate the energy directly. Thus, we return to the eigenvector equation from Eq. (1), cf. the supplementary material, that describes the spatial change of $\psi_{\mathrm{R,Imp}} = (\alpha_1, \ldots, \alpha_l, \gamma_{l+1}, \ldots \gamma_N)^\mathrm{T}$ behind the impurity, i.e., $\gamma_{l+1}, \ldots, \gamma_N$, and apply the phenomenological constraint of a flat profile: $\gamma_{l+1} = \ldots = \gamma_N = \mathrm{const}$. That fixes the states' total energy to be $E = \pm(t_\mathrm{L} + t_\mathrm{R})$ for $\delta = \pm(t_\mathrm{R} - t_\mathrm{L})$, which is very close to the actual numerical values. Using our approximated energy, Eq. (3) for kd, and the exact formulas for eigenstates, the approximated state is shown by the black dots in Fig. 1(h), thus confirming all computational data.

Concerning the localization strength of the impurity, we find $\kappa d = \operatorname{arccosh}[(t_\mathrm{L} + t_\mathrm{R})/(2\sqrt{t_\mathrm{L} t_\mathrm{R}})]$ using Eq. (3), $E = t_\mathrm{R} + t_\mathrm{L}$ and $kd \to \mathrm{i}\kappa d$ to properly account for the non-real wavevector under sufficient δ and $t_\mathrm{R} > t_\mathrm{L} > 0$. On the basis of our assumptions, the argument of the function arccosh is positive and larger than one; thus, exploiting the relation to the natural logarithm permits us to obtain the length scale $1/\kappa = 2d/\ln(t_\mathrm{R}/t_\mathrm{L})$. We observe that $1/\kappa$ is identical to the localization L imposed by the NHSE, which can be extracted from Eq. (SE7) of the supplementary material. We conclude that both effects can cancel depending on the impurity's position l at a given $t_\mathrm{R}/t_\mathrm{L}$.

In the supplementary material, we further examine the energy dependence of $\psi_{\mathrm{R,Imp}}$ when the ICSE is present. Moreover, as the ratio $t_\mathrm{R}/t_\mathrm{L}$ increases, the ICSE becomes progressively flatter—resulting in a less pronounced decay, as shown by the black curve in Fig. 1(h). Finally, the ICSE can also manifest to the left of the impurity; in this case, a ratio $t_\mathrm{R}/t_\mathrm{L} < 1$ is required to shift the NHSE toward the opposite end.

To conduct a more in-depth study on the ICSE, we evaluate the following gradient of the impurity mode:

$$D_x(\psi_\mathrm{R}) := \frac{|\psi_{\mathrm{R},l}| - |\psi_{\mathrm{R},l+x}|}{x} \tag{8}$$

between sites l and $l + x$ as a function of t_L, t_R, and δ using exact numerical results. For the largest possible range of impurity positions l, we show data for only $x = \pm 1$. Since D_x may be small due to exponential localization effects of either the NHSE or the impurity, we improve the resolution by interpreting $\mathcal{D}_\pm = \ln\left(10^{-5} + |D_{\pm 1}(\psi_{\mathrm{R,Imp}})|\right)$. In addition, to explore the full range of $t_\mathrm{L}R$, we introduce

$$\Delta(\delta, t_\mathrm{L}, t_\mathrm{R}) = \begin{cases} \delta, & t_\mathrm{L} t_\mathrm{R} > 0, \\ \mathrm{i}\delta, & t_\mathrm{L} t_\mathrm{R} < 0. \end{cases} \tag{9}$$

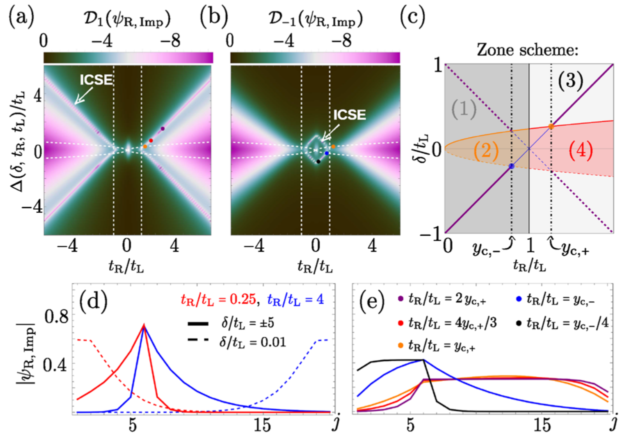

FIG. 3. ICSE phase diagram: $\mathcal{D}_{\pm 1} = \ln\left(10^{-5} + |D_{\pm 1}(\psi_{\mathrm{R,Imp}})|\right)$ vs $t_\mathrm{R}/t_\mathrm{L}$ and Δ. (a) ICSE (purple/white lines) confirms the linear relation $\delta = \pm(t_\mathrm{R} - t_\mathrm{L})$, $t_\mathrm{R}/t_\mathrm{L} > 0$ ($\mathrm{i}\delta = \pm(t_\mathrm{R} - t_\mathrm{L})$, $t_\mathrm{R}/t_\mathrm{L} < 0$) for $t_\mathrm{R}/t_\mathrm{L} > 1$ ($t_\mathrm{R}/t_\mathrm{L} < -1$). (b) For $t_\mathrm{R}/t_\mathrm{L} < 1$, the ICSE exists as well, but detection requires $\mathcal{D}_{-1}$. (c) The phase diagram consists of four distinct sub-areas: (1), (2), (3), and (4). (d) Spatial profile of $|\psi_{\mathrm{R,\,Imp}}|$ in (1)–(4). (e) Impurity mode along the ICSE line $\delta/t_\mathrm{L} = t_\mathrm{R}/t_\mathrm{L} - 1$. For discussion, see the main text. All data were obtained from exact diagonalization for $N = 20$, $l = 6$.

This approach preserves the spectrum of Eq. (1) for all $t_\mathrm{L} t_\mathrm{R}$, since the appearing complex phases in Eq. (4) cancel. Since the spectrum of Eq. (1) inverts its sign in case δ does, the shown data for the gradient are symmetric with respect to the horizontal and vertical axes.

The results for the gradient for the impurity mode are shown in Fig. 3(a) for $x = +1$ and in Fig. 3(b) for $x = -1$ with $N = 20$, $l = 6$. Note that vertical dashed lines correspond to $t_\mathrm{L} = t_\mathrm{R}$. On the top/bottom center (dark green), the gradient registers that $\psi_{\mathrm{R,imp}}$ is exponentially localized at the impurity site l, while on the center left/right $\mathcal{D}_\pm$ (deep purple) reflects the pileup due to the NHSE. Supporting data are presented in Fig. 3(d). In between both regimes and in agreement with Eq. (7), resides the ICSE, forming the separated and mostly purple *chevron* pointing to the right and to the left in Fig. 3(a) and a diamond shape in Fig. 3(b) with detailed data in Fig. 3(e).

The sketch in Fig. 3(c) illustrates the different parameter areas inside Figs. 3(a) and 3(b). Zones (1) and (3) correspond to values of $|\delta/\delta_\mathrm{c}| > 1$, i.e., $\psi_{\mathrm{R,imp}}$ exponentially localizes at the impurity, with NHSE toward the left (right) end of the chain in (1) [(3)]. Similarly, in areas (2) and (4), we have $|\delta/\delta_\mathrm{c}| < 1$, and $|\delta/\delta_\mathrm{c}| = 1$ marks the boundary between (1), (2) and (3), (4), respectively. In purple, we show the parameter constraint for the ICSE—cf. Eq. (7). Since exponential localizations due to NHSE and impurity need to compensate for the ICSE, the latter actually resides only on the purple lines within regions (1) and (3). The transition points $y_\mathrm{c}, \pm$ follow from Eqs. (5) and (7), and the explicit formula is given in the supplementary material. Physically, $y_\mathrm{c}, \pm$ give limits for $t_\mathrm{R}/t_\mathrm{L}$ beyond which we expect the ICSE.

The colored spots in Figs. 3(a) and 3(b) refer to the states shown in Fig. 3(e). For $t_\mathrm{R}/t_\mathrm{L} = 2y_{\mathrm{c},+}$ (purple), the flat profile of $|\psi_{\mathrm{R,imp}}|$ reflects clearly the ICSE, which is preserved until $t_\mathrm{R}/t_\mathrm{L} = 4y_{\mathrm{c},+}/3$ (red). In between $t_\mathrm{R}/t_\mathrm{L} = y_{\mathrm{c},+}$ (orange) and $t_\mathrm{R}/t_\mathrm{L} = y_{\mathrm{c},-}$ (blue), the

ICSE is absent and, due to $t_R/t_L < 1$, the NHSE now localizes $\psi_{R,\mathrm{imp}}$ toward the right end of the chain. For sufficiently small $t_R/t_L = \gamma_{c,-}/4$ (black), the ICSE re-emerges.

Concerning impurities on edge sites, i.e., $l = 1, N$, the ICSE does exist, but for adapted impurity strength, i.e., Eq. (7) is no longer valid since it was derived from a bulk constraint in the absence of OBC. Instead, we find the linear relationship $\delta = t_R$ ($\delta = t_L$) for $l = 1$ ($l = N$) for sufficient t_L/t_R. We show supporting data in the supplementary material. In the case of impurities on the first/last few sites, the value of δ seems to transition between the respective two conditions. In the supplementary material, we show the ICSE for a multi-band model; in particular, we consider the non-reciprocal SSH model.[55]

E. Application: Quantum Walk

In this section, we demonstrate how our findings can be implemented within the framework of a discrete-time quantum walk (DTQW) under non-Hermitian dynamics. Quantum walks generalize classical random walks by incorporating essential quantum features such as superposition and interference.[56,57] In a classical random walk, a particle moves through position space with fixed probabilities at each step. In contrast, in a quantum walk, the walker evolves coherently, exploring multiple paths simultaneously. The resulting interference of probability amplitudes—constructive or destructive—leads to markedly different behavior: in particular, the variance of the walker's position grows quadratically with the number of steps, as opposed to the linear scaling observed in classical walks.[58,59]

The Hilbert space for the DTQW is constructed as the tensor product,

$$\mathcal{H} = \mathcal{H}_P \otimes \mathcal{H}_C, \tag{10}$$

where $\mathcal{H}_P$ denotes the position space spanned by $\{|x\rangle : x \in \mathbb{Z}\}$ and $\mathcal{H}_C \cong \mathbb{C}_2$ is the two-dimensional coin (or internal) space. Each basis element $|x\rangle \otimes |c\rangle$ (with $c = \mathrm{R, L}$) represents the walker at position x with coin state $|c\rangle$.

A single step of the DTQW is defined by the unitary (or, in our case, non-unitary) evolution operator,

$$U = S\,(\mathbb{I} \otimes C), \tag{11}$$

where $\mathbb{I}$ is the identity operator in the walker subspace, C is the coin operator acting on $\mathcal{H}_C$, and S is the conditional shift operator acting on the combined space.

In the case of a Hermitian evolution of the DTQW, the coin operator can be defined as

$$C = \frac{1}{\sqrt{2}}\begin{pmatrix} 1 & 1 \\ 1 & -1 \end{pmatrix} \tag{12}$$

which is known in the literature as either the *unbiased coin* operator[60] or the Hadamard coin operator.[61] Later in this work, we generalize this by introducing *biased* coin operators—where the amplitude for moving left or right differs—thereby laying the foundation for realizing a nonreciprocal, impurity-free analog of the Hatano–Nelson model in the DTQW framework.

The shift operator in Eq. (11) is defined as

$$S = \sum_x \left(|x+1\rangle\langle x| \otimes |R\rangle\langle R| + |x-1\rangle\langle x| \otimes |L\rangle\langle L|\right), \tag{13}$$

where $|R\rangle$ and $|L\rangle$ denote the coin states corresponding to right and left moves, respectively, and after t steps, the walker is

$$|\psi(t)\rangle = U^t |\psi(0)\rangle. \tag{14}$$

The Hatano–Nelson model can be effectively mapped onto a non-Hermitian DTQW. In this correspondence, the Hamiltonian's non-reciprocal hopping amplitudes are encoded in the coin or shift operations of the quantum walk, thereby reproducing the essential features of biased and non-Hermitian dynamics. We adopt the following mapping, where the coin operator is defined as

$$C = \begin{pmatrix} \sqrt{r} & \sqrt{1-r} \\ \sqrt{1-\ell} & -\sqrt{\ell} \end{pmatrix} \tag{15}$$

in the left/right coin basis, with r and ℓ representing the transition probabilities for the walker to move to the right and left, respectively, satisfying $r, \ell \in [0, 1]$. These coin parameters can be identified with the hopping amplitudes in the Hatano–Nelson model via the associations $t_R \sim \ell$ and $t_L \sim r$, such that the non-reciprocal character of the original model is captured through asymmetry in the quantum walk's internal dynamics. In the continuum limit, this asymmetry manifests as a biased derivative term, representing a net drift induced by the imbalance, thus mirroring the non-Hermitian transport behavior characteristic of the Hatano–Nelson model.[62]

The presence of an impurity in a DTQW can significantly alter the interference landscape and, thus, reshape the evolution of the walker. Several schemes exist for implementing such impurities, all premised on locally modifying the coin operator introduced in Eq. (15). In the most straightforward scenario, we apply a scaling factor γ_{imp} exclusively at the designated impurity location,

$$C^{\mathrm{M}_1}_{\mathrm{imp}} = \gamma_{\mathrm{imp}}\, C\delta_{n,n_{\mathrm{imp}}}, \tag{16}$$

with n_{imp} being the position of the impurity and $\gamma_{\mathrm{imp}} \in [0, 1]$.[63] This implementation directly modifies the walker time evolution, transforming it into a position-dependent one. The mismatch in coin parameters acts like a scattering center. A walker incident on the impurity can be partially reflected and transmitted, much like encountering a potential barrier. Depending on the degree of mismatch, localized states may form near the impurity. These localized modes can lead to resonant scattering, where the walker's amplitude becomes temporarily trapped. Due to the non-unitary DTQW and its inherently non-reciprocal nature ($r \neq \ell$), the impurity can accentuate directional biases in propagation. The case where $\gamma_{\mathrm{imp}} \approx 1$ represents a negligible impurity, meaning the walker evolves nearly undisturbed. In contrast, when $\gamma_{\mathrm{imp}} \approx 0$, the impurity acts as a strong barrier, effectively splitting the Hilbert space into two disconnected regions: one accessible to the left of the impurity and another beyond it. In the extreme limit $\gamma_{\mathrm{imp}} = 0$, the walker is completely blocked from accessing the downstream region. Interestingly, when $\gamma_{\mathrm{imp}} \approx \ell - r$, destructive interference at the impurity can give rise to a mode that remains dynamically localized at the defect site

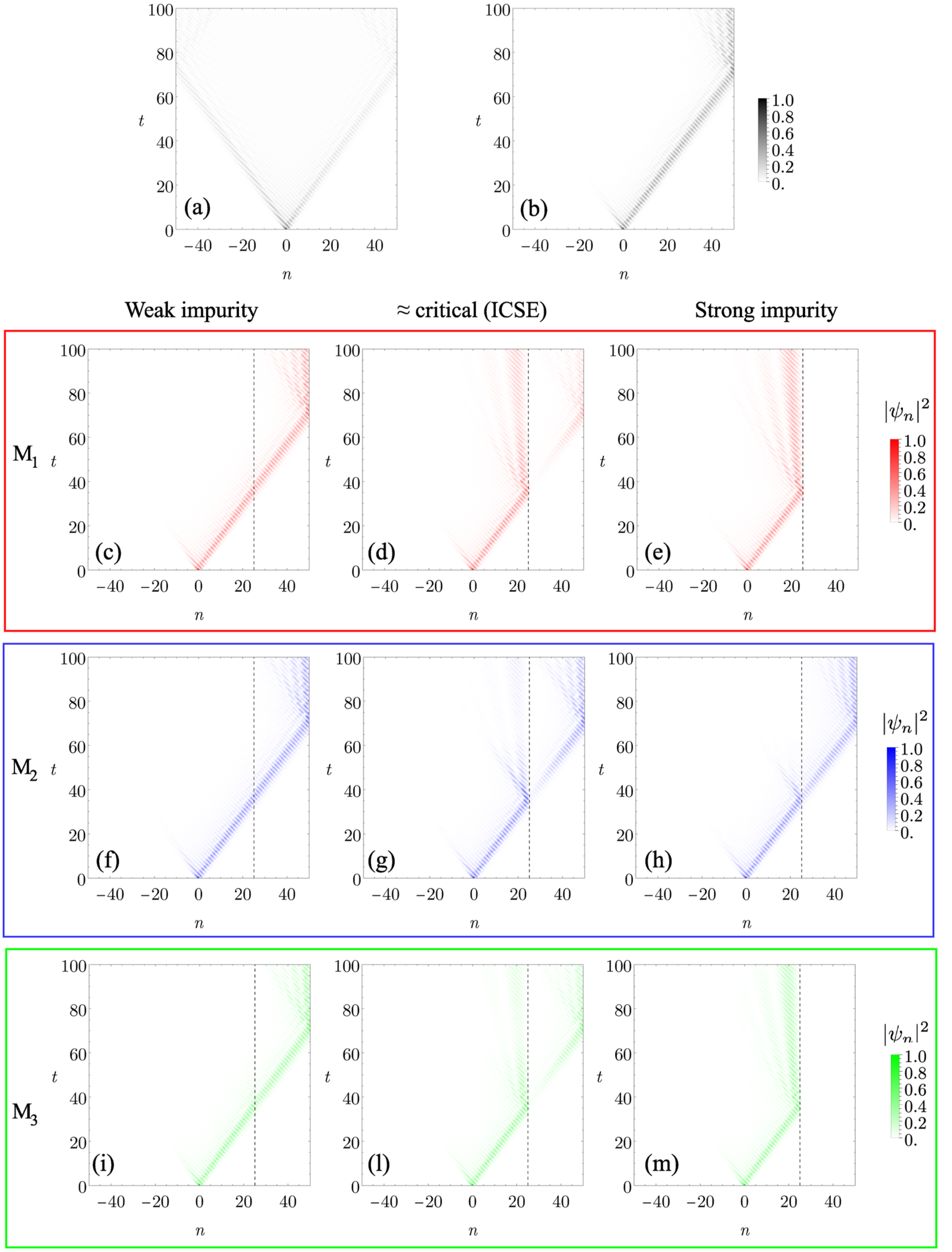

FIG. 4. Quantum Walk: (a) case of unbiased coin and (b) case of biased coin with $r = 0.6$ and $\ell = 0.45$. Cases of impurity M_1 in Eq. (16) for $\gamma_{\mathrm{imp}} = 6\gamma_{\mathrm{c}}$ in (c), $\gamma_{\mathrm{imp}} = \gamma_{\mathrm{c}}$ in (d), and $\gamma_{\mathrm{imp}} = \gamma_{\mathrm{c}}/10$ in (e) with $\gamma_{\mathrm{c}} = \ell - r$. Cases of impurity M_2 in Eq. (17): $\phi = \pi/20$ in (f), $\phi = \pi$ in (g), and $\phi = \pi/2$ in (h). Cases of impurity M_3 in Eq. (18) for $\gamma_{\mathrm{L}} = \gamma_{\mathrm{L}}^{\mathrm{c}}$ and $\gamma_{\mathrm{R}} = \gamma_{\mathrm{R}}^{\mathrm{c}}$ in (i), $\gamma_{\mathrm{L}} = 13\gamma_{\mathrm{L}}^{\mathrm{c}}/10$ and $\gamma_{\mathrm{R}} = \gamma_{\mathrm{R}}^{\mathrm{c}}/10$ in (l), and $\gamma_{\mathrm{L}} = \gamma_{\mathrm{L}}^{\mathrm{c}}/10$ and $\gamma_{\mathrm{R}} = \gamma_{\mathrm{R}}^{\mathrm{c}}/1000$ in (m). Respective critical values read $\gamma_{\mathrm{L}}^{\mathrm{c}} = 1.1r$ and $\gamma_{\mathrm{R}}^{\mathrm{c}} = 0.99\ell$. For the panels (c)–(m), the impurity is placed at $n_{\mathrm{imp}} = 25$.

throughout the evolution—this behavior mirrors the impurity-ICSE observed in the Hatano–Nelson model.

A different approach to include the presence of the impurity consists of multiplying the coin operator in Eq. (15) by a phase factor $\mathrm{e}^{\mathrm{i}\phi}$,

$$C^{\mathrm{M}_2}_{\mathrm{imp}} = \mathrm{e}^{\mathrm{i}\phi} C \delta_{n,n_{\mathrm{imp}}}, \tag{17}$$

with $\phi \in [0, 2\pi)$.[64–66] The extra phase modifies the interference pattern of the DTQW. This can result in shifts in the positions of constructive and destructive interference, altering the probability distribution of the walker, and can additionally modify interference pathways in the DTQWca. While its magnitude remains unity—unlike the amplitude-defect case in Eq. (16)—a phase-only defect cannot create a strong barrier that fragments the walker's Hilbert space. Instead, it affects walker dynamics by altering interference patterns. In particular, when the phase parameter is $\phi \approx 0$, the impurity is effectively weak; at $\phi \approx \pi/2$, it induces strong *phase* scattering yet does not fragment the network; and at $\phi = \pi$, it produces behavior reminiscent of the ICSE, with a localized mode forming due to destructive interference at the defect. However, none of these regimes result in Hilbert-space fragmentation.

Finally, we can modify the coin operator to include an asymmetric gain or loss at the impurity site.[67] This is obtained by adjusting the coin operator at the impurity site as

$$C^{\mathrm{M}_3}_{\mathrm{imp}} = \begin{pmatrix} \sqrt{\gamma_{\mathrm{R}}} & 0 \\ 0 & \sqrt{\gamma_{\mathrm{L}}} \end{pmatrix} \cdot C \delta_{n,n_{\mathrm{imp}}}, \tag{18}$$

where γ_{R} and γ_{L} are the gain/loss factors, with one possibly greater than one and the other less than 1. In turn, motion to the right might be amplified (if $\gamma_{\mathrm{R}} > 1$) while the motion to the left is attenuated (if $\gamma_{\mathrm{L}} < 1$), i.e., the procedure accentuates the inherent non-reciprocity of the Hatano–Nelson model. In addition, this model of impurity as the one in Eq. (16) allows for Hilbert-space fragmentation when the gain/loss factors γ_{R} and γ_{L} are both small and highly imbalanced. If their ratio remains close to unity, the impurity remains weak. However, an extreme imbalance causes the impurity to act as a strong barrier, effectively dividing the walker's accessible regions—at the limit, the walker cannot cross into the downstream fragment. Interestingly, when the ratio satisfies $\frac{\gamma_{\mathrm{R}}}{\gamma_{\mathrm{L}}} = \frac{\ell}{r}$, destructive interference at the defect site generates a dynamically localized mode—a hallmark of the ICSE.

In Fig. 4, we present a comprehensive visualization of the DTQW phenomena discussed throughout this work. In Fig. 4(a), we present the case of the unbiased coin, where the walker develops the characteristic probability bimodal distribution during time evolution. In Fig. 4(b), we present the case of the biased coin with $r/\ell \approx 0.75$, in which the bimodal symmetry is disrupted due to directional bias. In Figs. 4(c)–4(e), we present the case with a defect of type M_1 for three different strengths of the impurity γ_{imp}: weak, intermediate, and strong. Analogously, in Figs. 4(f)–4(h), we present results for the case of a defect of type M_2 for three different values of the phase factor characterizing this model. Finally, in Figs. 4(i)–4(m), we present results for the last model of disorder M_3, considering three different cases for the gain and loss coefficients. Crucially, in each set the middle panel exemplifies the ICSE-*like* regime, where a walker mode becomes persistently localized near the impurity site, coexisting with bulk drift. This robust localized behavior is the DTQW counterpart to the ICSE described earlier.

IV. CONCLUSIONS

In this paper, we have studied the spectral properties of the Hatano–Nelson model with a generic impurity's position and strength. We have shown analytical solutions for both the periodic and open boundary conditions. For both cases, the associated wavevectors obey a transcendental constraint.

Interestingly, we have found that the strong impurity limit fixes the matching condition to open boundary conditions, causing the chain to fragment. Subsequently, the non-Hermitian skin effect emerges naturally under periodic boundary conditions, confirming earlier studies.[37,38] Under open boundary conditions, we uncovered that the impurity introduces a second length scale capable of competing against the non-Hermitian skin effect. This is explicit in the case of an infinitely strong impurity, where one mode (the impurity mode) is trapped at the impurity site despite the model's non-reciprocal hopping. For moderate impurity strength, this mode decays exponentially away from the impurity.

We investigated the parameter regions where the impurity dominates the impurity mode over the non-Hermitian skin effect. At the interface between the two regimes, we found the impurity-induced counter-skin effect, where the impurity mode becomes constant within one pristine subchain. We provided numerical and analytical evidence and demonstrated that the impurity-induced counter-skin effect may be identified from the non-Hermitian skin effect. We have verified the appearance of the ICSE in multi-band non-Hermitian models—see the supplementary material.

Our study may serve as a blueprint for the multi-impurity case. Supposing that they are placed at distinct sites $l_1, \ldots, l_n$ and have strengths $\delta_1, \ldots, \delta_n$, each impurity may induce its own localization strength in case a domain wall architecture ($\delta_1 = \ldots = \delta_n$ for neighboring sites) is prevented. The argument is obvious from the case $n = 2$, since $|\delta_1| \to \infty$ fragments the chain, one of which contains the second impurity. Now, $|\delta_2| \to \infty$ splits the fragment into pieces, traps a second state at l_2, and the argument may be continued for further impurities.

There are two conclusions to be drawn from this. First, placing an impurity on every second site is sufficient to isolate all sites from their respective neighbors for sufficient impurity strength. In turn, the NHSE vanishes.

Second, and following our discussion of the out-of-band transition for a single impurity, placing one at every site with sufficient strength, and at best with alternating signs, effectively destroys the band structure of the chain. Although the dispersion relation $E(kd)$ from the pristine case can be used together with a proper quantization condition, the state's energy is determined mainly by the local impurity, i.e., energy eigenvalues appear fully misplaced with respect to the dispersion relation due to generally complex wavevectors.

In the last part of this work, we have explored how the ICSE can manifest in a DTQW by incorporating three distinct impurity models—amplitude (M1), phase (M2), and gain/loss (M3) modifications. A central contrast between the DTQW and the original

Hatano–Nelson framework lies in the nature of the ICSE manifestation: in the Hatano–Nelson model, the ICSE appears as a localized impurity eigenmode that can be isolated in the system's spectrum, whereas in the DTQW, the inherently non-Hermitian, dynamic evolution precludes such static spectral isolation. Instead, one must scrutinize the full-time evolution of the walker's state ensemble to detect ICSE-like behavior. We argue that a reliable signature in this context is the emergence of a component that remains persistently localized around the impurity site, despite an overall biased drift. The sustained localization of such a state thus serves as a practical indicator of interference-driven cancellation of the biased coin and the realization of ICSE dynamics within the DTQW framework.

SUPPLEMENTARY MATERIAL

In the supplementary material, we derive the exact analytic formulas for all rhs and lhs eigenvectors of Eq. (1) under both OBC and PBC. We also discuss the numerical satisfaction of the quantization condition for OBC by comparing approaches with machine or infinite precision. In addition, we also provide additional data for the ICSE, such as the parameter dependence for impurities placed on terminal sites and the energy dependence of the impurity mode. Finally, we provide explicit evidence that the ICSE is also present in multi-band models.

ACKNOWLEDGMENTS

We acknowledge the interesting and fruitful discussions with Geza Giedke, Flore Kunst, Thomas Frederiksen, Shayan Edalatmanesh, and Carolina Martinez Strasser. This research was funded by the IKUR Strategy under the collaboration agreement between the Ikerbasque Foundation and DIPC on behalf of the Department of Education of the Basque Government. D.B. acknowledges the support from the Spanish MICINN-AEI through Project No. PID2020-120614GB-I00 (ENACT), the Transnational Common Laboratory *QuantumChemPhys*, and the Department of Education of the Basque Government through Project No. PIB 2023 1 0007 (STRAINER).

AUTHOR DECLARATIONS

Conflict of Interest

The authors have no conflicts to disclose.

Author Contributions

Nico G. Leumer: Conceptualization (equal); Data curation (equal); Formal analysis (equal); Funding acquisition (equal); Investigation (equal); Methodology (equal); Project administration (equal); Resources (equal); Software (equal); Supervision (equal); Validation (equal); Visualization (equal); Writing – original draft (equal); Writing – review & editing (equal). **Dario Bercioux**: Conceptualization (equal); Data curation (equal); Formal analysis (equal); Funding acquisition (equal); Investigation (equal); Methodology (equal); Project administration (equal); Resources (equal); Software (equal); Supervision (equal); Validation (equal); Visualization (equal); Writing – original draft (equal); Writing – review & editing (equal).

DATA AVAILABILITY

The data associated with the figures in this work are available via Zenodo at https://doi.org/10.5281/zenodo.17013433. The codes can be shared upon reasonable request.

REFERENCES

[1] N. Hatano and D. R. Nelson, "Localization transitions in non-Hermitian quantum mechanics," Phys. Rev. Lett. **77**, 570–573 (1996).

[2] S. Yao and Z. Wang, "Edge states and topological invariants of non-Hermitian systems," Phys. Rev. Lett. **121**, 086803 (2018).

[3] E. J. Bergholtz, J. C. Budich, and F. K. Kunst, "Exceptional topology of non-Hermitian systems," Rev. Mod. Phys. **93**, 015005 (2021).

[4] N. Okuma, K. Kawabata, K. Shiozaki, and M. Sato, "Topological origin of non-Hermitian skin effects," Phys. Rev. Lett. **124**, 086801 (2020).

[5] K. Zhang, Z. Yang, and C. Fang, "Correspondence between winding numbers and skin modes in non-Hermitian systems," Phys. Rev. Lett. **125**, 126402 (2020).

[6] X. Zhang, T. Zhang, M.-H. Lu, and Y.-F. Chen, "A review on non-Hermitian skin effect," Adv. Phys.: X **7**, 2109431 (2022).

[7] K. Zhang, Z. Yang, and C. Fang, "Universal non-Hermitian skin effect in two and higher dimensions," Nat. Commun. **13**, 2496 (2022).

[8] R. Lin, T. Tai, L. Li, and C. H. Lee, "Topological non-Hermitian skin effect," Front. Phys. **18**, 53605 (2023).

[9] R. Koch and J. C. Budich, "Bulk-boundary correspondence in non-Hermitian systems: Stability analysis for generalized boundary conditions," Eur. Phys. J. D **74**, 70 (2020).

[10] J. C. Budich and E. J. Bergholtz, "Non-Hermitian topological sensors," Phys. Rev. Lett. **125**, 180403 (2020).

[11] A. McDonald and A. A. Clerk, "Exponentially-enhanced quantum sensing with non-Hermitian lattice dynamics," Nat. Commun. **11**, 5382 (2020).

[12] C. Martínez-Strasser, M. A. J. Herrera, A. García-Etxarri, G. Palumbo, F. K. Kunst, and D. Bercioux, "Topological properties of a non-Hermitian quasi-1D chain with a flat band," Adv. Quantum Technol. **7**, 2300225 (2023).

[13] C. Martínez-Strasser, M. A. J. Herrera, A. García-Etxarri, G. Palumbo, F. K. Kunst, and D. Bercioux, "Correction to topological properties of a non-Hermitian quasi-1D chain with a flat band," Adv. Quantum Technol. **8**, 2400348 (2024).

[14] F. Yang and E. J. Bergholtz, "Anatomy of higher-order non-Hermitian skin and boundary modes," arXiv:2405.03750 [cond-mat.mes-hall] (2024).

[15] S. Manna and B. Roy, "Inner skin effects on non-Hermitian topological fractals," Commun. Phys. **6**, 10 (2023).

[16] T. Helbig, T. Hofmann, S. Imhof, M. Abdelghany, T. Kiessling, L. W. Molenkamp, C. H. Lee, A. Szameit, M. Greiter, and R. Thomale, "Generalized bulk–boundary correspondence in non-Hermitian topolectrical circuits," Nat. Phys. **16**, 747–750 (2020).

[17] K. Wang, A. Dutt, K. Y. Yang, C. C. Wojcik, J. Vučković, and S. Fan, "Generating arbitrary topological windings of a non-Hermitian band," Science **371**, 1240–1245 (2021).

[18] K. Ochkan, R. Chaturvedi, V. Könye, L. Veyrat, R. Giraud, D. Mailly, A. Cavanna, U. Gennser, E. M. Hankiewicz, B. Büchner *et al.*, "Non-Hermitian topology in a multi-terminal quantum Hall device," Nat. Phys. **20**, 395–401 (2024).

[19] A. Maddi, Y. Auregan, G. Penelet, V. Pagneux, and V. Achilleos, "Exact analog of the Hatano-Nelson model in one-dimensional continuous nonreciprocal systems," Phys. Rev. Res. **6**, L012061 (2024).

[20] M. Parto, C. Leefmans, J. Williams, R. M. Gray, and A. Marandi, "Enhanced sensitivity via non-Hermitian topology," Light: Sci. Appl. **14**, 6 (2025).

[21] S. Weidemann, M. Kremer, T. Helbig, T. Hofmann, A. Stegmaier, M. Greiter, and R. Thomale, "Topological funneling of light in non-Hermitian optical lattices," Science **368**, 202 (2020).

[22] Q. Liang, D. Xie, Z. Dong, H. Li, H. Li, B. Gadway, W. Yi, and B. Yan, "Dynamic signatures of non-Hermitian skin effect and topology in ultracold atoms," Phys. Rev. Lett. **129**, 070401 (2022).

[23] H. B. Geyer, W. D. Heiss, and F. G. Scholtz, "The physical interpretation of non-Hermitian Hamiltonians and other observables," Can. J. Phys. **86**, 1195–1201 (2008).

[24] D. C. Brody, "Biorthogonal quantum mechanics," J. Phys. A: Math. Theor. **47**, 035305 (2014).

[25] K. Sim, N. Defenu, P. Molignini, and R. Chitra, "Observables in non-Hermitian systems: A methodological comparison," Phys. Rev. Res. **7**, 013325 (2025).

[26] H. P. Breuer and F. Petruccione, *The Theory of Open Quantum Systems* (Oxford University Press, Great Clarendon Street, 2002).

[27] C. Ehrhardt and J. Larson, "Exploring the impact of fluctuation-induced criticality on non-Hermitian skin effect and quantum sensors," Phys. Rev. Res. **6**, 023135 (2024).

[28] F. Evers and A. D. Mirlin, "Anderson transitions," Rev. Mod. Phys. **80**, 1355 (2008).

[29] D. Emin and C. F. Hart, "Existence of Wannier-Stark localization," Phys. Rev. B **36**, 7353 (1987).

[30] H. Jiang, L.-J. Lang, C. Yang, S.-L. Zhu, and S. Chen, "Interplay of non-Hermitian skin effects and Anderson localization in nonreciprocal quasiperiodic lattices," Phys. Rev. B **100**, 054301 (2019).

[31] R. Sarkar, S. S. Hegde, and A. Narayan, "Interplay of disorder and point-gap topology: Chiral modes, localization, and non-Hermitian Anderson skin effect in one dimension," Phys. Rev. B **106**, 014207 (2022).

[32] H.-Z. Li, M. Wan, and J.-X. Zhong, "Fate of non-Hermitian free fermions with Wannier-Stark ladder," Phys. Rev. B **110**, 094310 (2024).

[33] A. Chakrabarty and S. Datta, "Fate of Wannier-Stark localization and skin effect in periodically driven non-Hermitian quasiperiodic lattices," Phys. Rev. B **111**, 174202 (2025).

[34] L. Li, C. H. Lee, and J. Gong, "Impurity induced scale-free localization," Commun. Phys. **4**, 42 (2021).

[35] Y. Liu, Y. Zeng, L. Li, and S. Chen, "Exact solution of the single impurity problem in nonreciprocal lattices: Impurity-induced size-dependent non-Hermitian skin effect," Phys. Rev. B **104**, 085401 (2021).

[36] C.-X. Guo, C.-H. Liu, X.-M. Zhao, Y. Liu, and S. Chen, "Exact solution of non-Hermitian systems with generalized boundary conditions: Size-dependent boundary effect and fragility of the skin effect," Phys. Rev. Lett. **127**, 116801 (2021).

[37] Y. Liu and S. Chen, "Diagnosis of bulk phase diagram of nonreciprocal topological lattices by impurity modes," Phys. Rev. B **102**, 075404 (2020).

[38] F. Roccati, "Non-Hermitian skin effect as an impurity problem," Phys. Rev. A **104**, 022215 (2021).

[39] P. Molignini, O. Arandes, and E. J. Bergholtz, "Anomalous skin effects in disordered systems with a single non-Hermitian impurity," Phys. Rev. Res. **5**, 033058 (2023).

[40] H. Spring, V. Könye, A. R. Akhmerov, and I. C. Fulga, "Lack of near-sightedness principle in non-Hermitian systems," SciPost Phys. **17**, 153 (2024).

[41] W. A. Webb and E. A. Parberry, "Divisibility properties of Fibonacci polynomials," Fibonacci Q. **7**, 457 (1969).

[42] V. E. Hoggatt, Jr. and C. T. Long, "Divisibility properties of generalized Fibonacci polynomials," Fibonacci Q. **12**, 113 (1974).

[43] M. Özvatan and O. K. Pashaev, "Generalized fibonacci sequences and Binet-Fibonacci curves," arXiv:1707.09151 (2017).

[44] N. G. Leumer, "On symmetric tetranacci polynomials in mathematics and physics," J. Phys. A: Math. Theor. **56**, 435202 (2023).

[45] N. Leumer, "Spectral and transport signatures of 1D topological superconductors of finite size in the sub- and supra-gap regime: An analytical study," Ph.D. thesis, University of Regensburg, Regensburg, 2021.

[46] N. Leumer, M. Grifoni, B. Muralidharan, and M. Marganska, "Linear and nonlinear transport across a finite Kitaev chain: An exact analytical study," Phys. Rev. B **103**, 165432 (2021).

[47] B. C. Shin, "A formula for Eigenpairs of certain symmetric tridiagonal matrices," Bull. Aust. Math. Soc. **55**, 249–254 (1997).

[48] S. Kouachi, "Eigenvalues and eigenvectors of tridiagonal matrices," Electron. J. Linear Algebra **15**, 115–133 (2006).

[49] N. Leumer, M. Marganska, B. Muralidharan, and M. Grifoni, "Exact eigenvectors and eigenvalues of the finite Kitaev chain and its topological properties," J. Phys.: Condens. Matter **32**, 445502 (2020).

[50] W.-C. Yueh, "Eigenvalues of several tridiagonal matrices," Appl. Math. E-Notes **5**, 210–230 (2005), see http://eudml.org/doc/51497.

[51] E. Edvardsson and E. Ardonne, "Sensitivity of non-Hermitian systems," Phys. Rev. B **106**, 115107 (2022).

[52] D. J. Griffiths and D. F. Schroeter, *Introduction to Quantum Mechanics* (Cambridge University Press, 2018).

[53] W. R. Inc., Mathematica, Version 14.0, Champaign, IL, 2024.

[54] Linear modes do exist also in the Hermitian Su-Schrieffer-Heeger model (and the Kitaev chain for absent onsite energy) of finite size and OBC.[45] This mode appears when a former in-gap mode enters the upper/lower band by sweeping the ratio of inter/intra- band hoppings. Here, the mode may be used to define the topological phase transition under OBC and for finite chain length.

[55] S. Lieu, "Topological phases in the non-Hermitian Su-Schrieffer-Heeger model," Phys. Rev. B **97**, 045106 (2018).

[56] Y. Aharonov, L. Davidovich, and N. Zagury, "Quantum random walks," Phys. Rev. A **48**, 1687 (1993).

[57] J. Kempe, "Quantum random walks: An introductory overview," Contemp. Phys. **44**, 307–327 (2003).

[58] A. Ambainis, E. Bach, A. Nayak, A. Vishwanath, and J. Watrous, "One-dimensional quantum walks," in *Proceedings of the 33rd ACM Symposium on Theory of Computing* (ACM Press, New York, 2001), p. 60.

[59] A. Nayak and A. Vishwanath, "Quantum walk on the line," arXiv:quant-ph/0010117 (2001).

[60] B. Tregenna, W. Flanagan, R. Maile, and V. Kendon, "Controlling discrete quantum walks: Coins and initial states," New J. Phys. **5**, 83 (2003).

[61] X. Qiang, S. Ma, and H. Song, "Quantum walk computing: Theory, implementation, and application," Intell. Comput. **3**, 0097 (2024).

[62] A. M. Childs, "Universal computation by quantum walk," Phys. Rev. Lett. **102**, 180501 (2009).

[63] L. I. da S Teles and E. P. M. Amorim, "Localization in quantum walks with a single lattice defect: A comparative study," Braz. J. Phys. **51**, 911 (2021).

[64] A. Wójcik, T. Łuczak, P. Kurzyński, A. Grudka, T. Gdala, and M. Bednarska-Bzdęga, "Trapping a particle of a quantum walk on the line," Phys. Rev. A **85**, 012329 (2012).

[65] Z. J. Li, J. A. Izaac, and J. B. Wang, "Position-defect-induced reflection, trapping, transmission, and resonance in quantum walks," Phys. Rev. A **87**, 012314 (2013).

[66] R. Zhang, P. Xue, and J. Twamley, "One-dimensional quantum walks with single-point phase defects," Phys. Rev. A **89**, 042317 (2014).

[67] K. Mochizuki, D. Kim, and H. Obuse, "Explicit definition of $\mathcal{PT}$ symmetry for nonunitary quantum walks with gain and loss," Phys. Rev. A **93**, 062116 (2016).

APL Quantum

REVIEW ARTICLE | JUNE 17 2025

Hot electron relaxation: A review of the two temperature model for ultrafast non-equilibrium phenomena in metals

Special Collection: Quantum Dynamics in Theory, Numerics and in Experimental Research

Navinder Singh

APL Quantum 2, 021502 (2025)
https://doi.org/10.1063/5.0262933

AIP Publishing

APL Quantum REVIEW pubs.aip.org/aip/apq

Hot electron relaxation: A review of the two temperature model for ultrafast non-equilibrium phenomena in metals

Cite as: APL Quantum 2, 021502 (2025); doi: 10.1063/5.0262933
Submitted: 3 February 2025 • Accepted: 3 June 2025 •
Published Online: 17 June 2025

Navinder Singh[a)]

AFFILIATIONS

Theoretical Physics Division, Physical Research Laboratory (PRL), Ahmedabad 380009, India

Note: This paper is part of the APL Quantum Special Topic on Quantum Dynamics in Theory, Numerics and in Experimental Research.

[a)] **Author to whom correspondence should be addressed:** navinder@prl.res.in

ABSTRACT

The famous Two-Temperature Model (TTM) used extensively in the investigations of energy relaxation in photo excited systems originated in the seminal work of Kaganov *et al.* [Sov. J. Exp. Theor. Phys. **4**, 173 (1957)]. The idea that with an ultrashort laser pulse a temporal (transient) state of electrons in a metal can be created, in which electrons after absorbing energy from the laser pulse heat up and their temperature becomes substantially greater than that of lattice, was originated in the work of Anisimov *et al.* [Sov. J. Exp. Theor. Phys. **39**, 375 (1974)]. The heated electron sub-system (hot electrons) loses its energy to phonon sub-system via electron–phonon scattering, and thermodynamic equilibrium re-establishes over a time scale of a few picoseconds in metals. This field saw great developments in the 1980s and 1990s with the advent of femtosecond pump–probe spectroscopy. From 2000 onward, focus shifted from non-equilibrium phenomena in simple metals to those in more complex systems including strongly correlated systems such as high Tc cuprate superconductors. P. B. Allen, Phys. Rev. Lett. **59**, 1460 (1987), revisits the calculations of KLT and rewrites the electron–phonon heat transfer coefficient α in terms of a very important parameter in the theory of superconductivity ($\lambda\langle\omega^2\rangle$). This has far reaching consequences; λ, a very crucial dimensionless electron–phonon coupling parameter for a given superconducting material, can be estimated by doing pump–probe experiments on it. By mid 1990s, it became clear that TTM is violated and is not a sufficient model to discuss non-equilibrium relaxation. Year 2000 onward, field saw the development of models that go beyond the original TTM. Very recently, the field has entered into the attosecond domain. In this article, the author attempts a concise account of the development of the TTM and, in addition, a recent possible revival of it in the attosecond domain.

I. INTRODUCTION

The idea of the two-temperature model of hot electron relaxation in metals originated in studies of radiation damage in metals caused by very high-energy ions when metals are exposed to such ions. It all started near the end of World War II in 1945, and such studies were carried out in the so-called “Laboratory No. 1” at the Ukrainian Physico-Technical Institute (UPTI) in Bazaliy *et al.*[1] This section was then headed by Akhiezer and Lifshitz, and Kaganov joined to work on these projects related to radiation damage in metals by high-energy ions, as well as other topics in metal physics.[2] For several years, the results were not announced (they were kept classified), and finally, some of the results were published in 1957.[3]

The understanding that originated from those studies can be expressed in the following way: It was pointed out that the damage in a metal caused by high-energy ions occurs through a series of cascade processes, and various relaxation processes are separated from each other in time. High-energy ions, as they penetrate into a metal, first transfer their energy to electrons, as electrons have much less specific heat than the lattice. Due to this, the electron sub-system heats up preferentially, and internal electron–electron scattering leads to a hot Fermi–Dirac distribution of electrons at an elevated temperature. This hot electron distribution then transfers its energy to the phonon sub-system via slower electron–phonon scattering. They argued that electron–electron relaxation is much faster (occurring on a sub-picosecond timescale) compared to electron–lattice relaxation (which occurs on a several-picosecond timescale). During the electron–phonon scattering, the electron distribution remains in an equilibrium Fermi–Dirac distribution but at an elevated temperature.

II. A BIT OF HISTORY

The first method used by them is a classical one in which radiation of sound waves by a fast moving electron through the lattice ("Cerenkov" radiation) is computed by considering excitation of vibrations of an elastic continuum (on the lines of a method developed by Landau[4]). The second method, which is fully quantum, is an extension of a beautiful set of calculations by Akhiezer and Pomeranchuk.[5] Akhiezer and Pomeranchuk considered the mechanism of spin–lattice relaxation in the context of the magnetic method of cooling and used the Bloch–Boltzmann kinetic equation. Kaganov, Lifshitz, and Tanatarov (Fig. 1) applied the Akhiezer–Pomeranchuk method for the computation of relaxation time between hot electrons and lattice. The idea of laser excitation of electrons was not there at that time. In fact, laser was not discovered at that time (it came only in 1960 due to investigations of Theodore Maiman and others). These authors considered non-equilibrium between electrons and lattice as arising due to the passage of high energy ions in metals and also when large current is passed through a metal, such that Ohm's law is violated.[3] In Sec. III, we review the Two-Temperature Model (TTM).

III. THE TWO-TEMPERATURE MODEL (TTM)

Kaganov–Lifshitz–Tanatarov (KLT)[3] assumed that after preferential heating, electrons quickly regain the Fermi–Dirac distribution (via electron–electron collisions), albeit at an elevated temperature (that is, "hot" Fermi–Dirac distribution),

$$f_k = \frac{1}{e^{\beta_e(\varepsilon_k-\varepsilon_F)}+1}, \quad \beta_e = \frac{1}{k_B T_e}, \tag{1}$$

where T_e is the temperature of the electron sub-system (greater than the lattice temperature T during the process of relaxation). ε_F is the Fermi energy. Free electron model $\varepsilon_k = \frac{\hbar^2 k^2}{2m}$ was assumed, where m is the mass of an electron and k is the magnitude of the electron wave-vector. For phonons, equilibrium Bose distribution was assumed,

$$n_q = \frac{1}{e^{\beta\hbar\omega_q}-1}, \quad \beta = \frac{1}{k_B T}, \tag{2}$$

where q is the magnitude of the wave-vector of an acoustic phonon mode (the Debye model was used for phonon sub-system) and $\omega_q = c_s q$, in which c_s is the sound speed for acoustic phonons. During the process of relaxation, T_e remains greater than T. Heat transfers from electron sub-system to phonon sub-system, and then, by the process of diffusion, it goes out to the substrate or environment.

Authors compute the amount of average energy transferred by electrons to lattice per unit volume and per unit time,

$$\bar{U} = \int d^3r \frac{d^3q}{(2\pi)^3} \dot{N}_q \hbar\omega_q. \tag{3}$$

Here, $\dot{N}_q$ is the rate at which phonons are generated with wave-vector q per unit volume. Each phonon carries energy of amount $\hbar\omega_q$. Thus, $\dot{N}_q\hbar\omega_q$ is the amount of energy transferred (per sec per unit volume) to phonon modes with wave vector lying in the range q to $q + dq$. For the computation of $\dot{N}_q$, they use the Bloch–Boltzmann equation,

$$\begin{aligned}\dot{N}_q = 2\int \frac{d^3k'}{(2\pi)^3} W_{k,k'} f_{k'}(1-f_k)[\,(n_q+1) \\ \times \delta(\varepsilon_{k'}-\varepsilon_k-\hbar\omega_q) - n_q\delta(\varepsilon_{k'}-\varepsilon_k+\hbar\omega_q)\,],\end{aligned} \tag{4}$$

$$W_{k,k'} = \frac{\pi U^2}{\rho V c_s^2}\omega_q, \qquad \mathbf{q} = \mathbf{k} - \mathbf{k}'. \tag{5}$$

Here, U is the electron–phonon coupling constant, ρ is the density of metal, V is the unit cell volume, c_s is the sound speed, and ω_q is the phonon frequency with wave-vector q. By using the expressions (1) and (2) for Fermi and Bose functions at different temperatures and by imposing the assumption $\varepsilon_F \gg k_B T_e \gg \hbar\omega_q$ (generally valid for metals), the above equation [Eq. (4)] can be written as

$$\dot{N}_q = \frac{m^2U^2\hbar\omega_q}{2\pi\hbar^4\rho V c_s}\frac{e^{\beta\hbar\omega_q}-e^{\beta_e\hbar\omega_q}}{(e^{\beta\hbar\omega_q}-1)(e^{\beta_e\hbar\omega_q}-1)}. \tag{6}$$

Technical details are given in Refs. 6 and 7. Using the Debye model for phonons, the average energy transferred by electrons to lattice per unit volume and per unit time [Eq. (3)] can be written as

$$\bar{U} = A\left\{\left(\frac{T_e}{T_D}\right)^5\int_0^{\frac{T_D}{T_e}}\frac{x^4dx}{e^x-1} - \left(\frac{T}{T_D}\right)^5\int_0^{\frac{T_D}{T}}\frac{x^4dx}{e^x-1}\right\}, \tag{7}$$

where $A = \frac{2m^2U^2(k_BT_D)^5}{(2\pi)^3\hbar^7\rho c_s^4}$. The above expression simplifies in the following special cases:

CASE A: In the low temperature limit $T, T_e \ll T_D$, the above expression gives

$$\bar{U} = B(T_e^5 - T^5), \qquad B = A\int_0^\infty \frac{x^4dx}{e^x-1}. \tag{8}$$

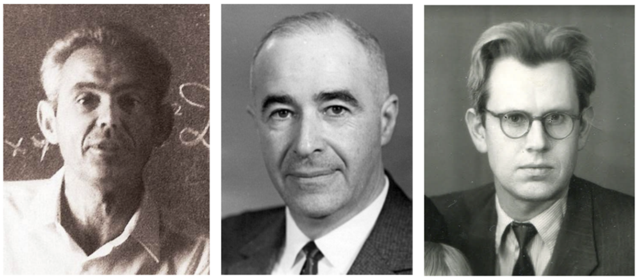
Moisey I. Kaganov (1921–2019)
Ilya M. Lifshitz (1917-1982)
L. V. Tanatarov (1929 - 2020)

FIG. 1. Through this article, the author pays his tribute to the pioneers of the two-temperature model. Image courtesy: Kaganov (from Bazaliy via personal communication); Lifshitz (Wikipedia commons); and Tanatarov [from Igor Tanatarov (grandson of Tanatarov) via personal communication].

In 2D, instead of T^5, it is T^4 behavior.[8] In a further sub-case $(T_e - T \ll T \ll T_D)$, we get

$$\bar{U} = \frac{2\pi^2}{3} \frac{mc_s^2 n}{\tau(T)} \frac{T_e - T}{T}. \tag{9}$$

CASE B: In the high temperature limit $T, T_e \gg T_D$, Eq. (7) leads to

$$\bar{U} = \alpha(T_e - T), \qquad \alpha = \frac{A}{4T_D}. \tag{10}$$

In a further sub-case $(T_e - T \ll T, T \gg T_D)$, we get

$$\bar{U} = \frac{\pi^2}{6} \frac{mc_s^2 n}{\tau(T)} \frac{T_e - T}{T}. \tag{11}$$

Here, $\frac{1}{\tau(T)}$ is the equilibrium relaxation rate due to electron–phonon scattering as it appears in the theory of resistivity of metals (in the Bloch–Grüeneisen formula).[9,10]

IV. TWO-TEMPERATURE MODEL (TTM) AND LASER EXCITATION

The idea of the study of TTM using laser excitation originated in 1973. Anisimov *et al.*[11] pointed out that when a metal surface is exposed to a picosecond laser pulse, emission current pulse (due to ejected electrons) from the surface of the metal is practically undelayed relative to the laser pulse. This is due to small specific heat of electrons leading to preferential heating of it, and during the course of the laser pulse (over picosecond time scales), electrons remain practically thermally insulated from the lattice. This preferential heating of electrons leads to thermionic emission current pulse. Thermionic emission occurs when kinetic energy of a small fraction of electrons in a heated metallic sample exceeds the work function of that metal such that they are able to escape from the metal surface. That is, the thermionic emission of electrons is possible because heat absorbed by electrons from the laser pulse remains in the electron sub-system for a short time scale of the order of picoseconds. They underlined that by measuring the thermionic emission over an extended timescale, electron–lattice relaxation kinetics can be investigated. Laser pulses at that time were not short enough (not in the femto-second regime), and the study of electron–phonon relaxation kinetics remained an open area of research for some time. It is interesting to re-visit their argument regarding separation of timescales.

The argument of the authors[11] that the energy absorbed from the laser pulse mostly remains trapped inside the electron subsystem over a picosecond timescale goes as follows: They refer to Eq. (9) in KLT paper[3] [Eq. (10) in Sec. III] and estimate the heat transfer coefficient α between electrons and lattice,

$$\bar{U} = \alpha(T_e - T), \qquad \alpha = \frac{m^2 U^2 (k_B T_D)^5}{2(2\pi)^3 \hbar^7 \rho c_s^4 T_D}. \tag{12}$$

They estimated the value of $\alpha \sim 10^{17}\,\mathrm{erg/cm^3/sec/deg}$. A typical heating time for phonons can be estimated as $\sim \frac{C_i}{\alpha}$, where C_i is the phonon heat capacity. It turns out that this time scale is of the order of 100 ps (this is an order of magnitude greater than the heating time for electrons, and it translates to the fact that electronic heat capacity is about two orders of magnitude smaller than that of the lattice). Those "hot" electrons, which are not ejected out due to thermionic emission, will transfer their energy to the lattice via electron–phonon scattering. Thus, the authors argued that the evolution of disequilibrium of electrons (or anomalous heating of electrons as called in the literature in the 1980s) can be studied. However, it turns out that picosecond laser pulses are not sufficient to observe the anomalous heating of the electrons. An experiment in 1983 made it clear [Sec. V].

However, this sets a foundation for future experiments with shorter pulses (fs) to study preferential heating of electron subsystem and subsequent electron–phonon relaxations kinetics.

V. FIRST EXPERIMENTS THAT SHOWED THAT ELECTRONS CAN BE SELECTIVELY EXCITED USING ULTRASHORT LASER PULSES

The first attempt to observe preferential heating of electrons (also called anomalous heating) was made by Eesley in 1983.[12] He used what is called Transient Thermomodulation Spectroscopy (TTMS), which is an early version of the pump–probe spectroscopy. He used 645 nm (1.92 eV) heating pulse (pump pulse) from a dye laser with a temporal width of 8 ps, and the sample used was a 400 nm copper film. The pump pulse heats up the electrons, and this further changes the reflectivity of the copper film. The changed reflectivity was measured by a time-delayed probe pulse of similar width (8 ps) but weaker intensity. The probe pulse was time delayed with respect to the pump pulse, and transient relative reflectivity change $(\Delta R/R)$ was measured as a function of the time delay between the pump pulse (heating pulse) and the probe pulse. Eesley argued that anomalous heating of the electron sub-system is observed.[12]

However, time resolution was very low (pulse width was 8 ps). The data were mostly affected by the equilibrium heating of the electrons (it turns out that electrons and lattice remained in equilibrium on the time scale probed), and the temperature difference between electrons and lattice was less than a few Kelvin! However, Eesley noticed the need for femto-second laser pulses to differentiate anomalous heating of the electron sub-system and to study the kinetics of the electron–phonon relaxation. We quote his words as follows:[12]

> "Extension of the technique into the femto-second regime should provide the capability to measure directly hot-electron relaxation times as a function of probe photon energy and as a function of both the transient and the equilibrium sample temperatures."

The first experimental observation of the anomalous heating (non-equilibrium electron distribution) came in 1984.[13] Fujimoto *et al.*, using 75-fs optical pulses, demonstrated that electrons can be selectively excited (anomalous heating) and the electron–phonon relaxation happens on a timescale of 1 ps. The authors observe thermally enhanced photoemission from a tungsten metal surface. The key to the observation of anomalous heating is that the transient electron heating due to the pump pulse enhances the photoemission signal induced by the second probe pulse. By varying the time delay between pump and probe pulses, time evolution of the selectively heated electron distribution can be studied. The estimated time scale for non-equilibrium electron distribution is found to be several hundred fs, and the electron–phonon coupling constant is estimated to be of the order of 10^{17} erg/cm^3/sec/K, which agrees with the estimate of Anisimov *et al.*[11]

The experiment of 1984[13] opened the floodgates for the studies of the anomalous heating of electrons in metals. Several results appeared in the late 1980s and early 1990s.[14–17]

As the field advanced, the questions asked also became sharper: On what time scale does the non-equilibrium electron distribution (non-Fermi–Dirac distribution) goes to the FD distribution via electron–electron scattering? How does the electron–phonon scattering affect the relaxation within the electron sub-system? Whether phonons always remain in equilibrium during the process of electron–phonon relaxation? etc.

In 1987, this field saw an extension in a very novel way (Sec. VI).

VI. USING ELECTRON–PHONON RELAXATION TO INVESTIGATE λ (AN IMPORTANT PARAMETER IN SUPERCONDUCTIVITY)

In 1987, Allen revisits the TTM problem posed by Kaganov *et al.* In a seminal work,[18] he generalizes the TTM in two important ways: (1) Instead of quadratic dispersion ($\varepsilon_k \propto k^2$) valid for simple metals (as used by KLT), Allen generalizes the KLT calculation for an arbitrary dispersion $\varepsilon(k)$, and (2) Allen expresses α [refer to Eq. (12)] in terms of a very important parameter used in superconductivity theory ($\lambda\langle\omega^2\rangle$),

$$\frac{dT_e}{dt} = \alpha(T - T_e), \qquad \alpha = \frac{3\hbar\lambda\langle\omega^2\rangle}{\pi k_B T_e}. \tag{13}$$

We briefly review this pioneering contribution. Allen uses the same set of physical assumptions as used by KLT as follows:

1. The electron–electron (Coulombic) scattering is effective in maintaining a local equilibrium distribution of electrons [Fermi–Dirac distribution at an elevated temperature (f_k)], and phonon–phonon (anharmonic) scattering is also assumed to be effective in maintaining a local Bose–Einstein distribution for phonons (n_q).
2. Energy relaxation from electron sub-system to phonon sub-system is due to electron–phonon scattering (no other scattering is present there).
3. Diffusion due to spatial inhomogeneities is not present.
4. Pump pulse is assumed to be a delta function in time (no light–matter interaction after $t = 0^+$).

The evolution of the distribution functions is given by the Bloch–Boltzmann–Peierls kinetic equations,

$$\begin{aligned}\frac{\partial f_k}{\partial t} = \frac{2\pi}{\hbar}\frac{1}{N_c}\sum_q |M_{kk'}|^2\big(f_{k'}(1-f_k)\big[\,(n_q+1)\delta(\varepsilon_{k'}-\varepsilon_k-\hbar\omega_q)\\ + n_q\delta(\varepsilon_{k'}-\varepsilon_k+\hbar\omega_q)\,\big] - f_k(1-f_{k'})\\ \times\big[\,(n_q+1)\delta(\varepsilon_k-\varepsilon_{k'}-\hbar\omega_q) + n_q\delta(\varepsilon_k-\varepsilon_{k'}+\hbar\omega_q)\big]\big),\end{aligned} \tag{14}$$

$$\begin{aligned}\frac{\partial n_q}{\partial t} = \frac{2\pi}{\hbar}\frac{1}{N_c}\sum_{k'} |M_{kk'}|^2 f_{k'}(1-f_k)\big[\,(n_q+1)\delta(\varepsilon_{k'}-\varepsilon_k-\hbar\omega_q)\\ - n_q\delta(\varepsilon_{k'}-\varepsilon_k+\hbar\omega_q)\,\big] + \frac{2\pi}{\hbar}\frac{1}{N_c}\sum_k |M_{kk'}|^2 f_k(1-f_{k'})\\ \times\big[(n_q+1)\delta(\varepsilon_k-\varepsilon_{k'}-\hbar\omega_q) - n_q\delta(\varepsilon_k-\varepsilon_{k'}+\hbar\omega_q)\big].\end{aligned} \tag{15}$$

The first equation in the above array gives the time evolution of the thermal occupancy of electrons in the kth state. The scattering of electrons from k' state to k state and vice versa along with the emission and absorption of phonons is written out, and the corresponding matrix element of scattering is given by $M_{kk'}$. N_c is the number of unit cells in the sample. The energy content of the electron sub-system and the phonon sub-system is given as

$$E_e(t) = 2\sum_k \varepsilon_k f_k(t) \simeq E_0 + \frac{1}{2}\gamma_e T_e^2(t), \tag{16}$$

$$E_l(t) = \sum_q \hbar\omega_q n_q \simeq 3N_a k_B T_l(t). \tag{17}$$

It can be easily verified that the total energy is conserved $\frac{d}{dt}(E_e(t) + E_l(t)) = 0$. Allen introduces the electron–phonon spectral function,

$$\alpha^2F(\varepsilon,\varepsilon',\Omega) \propto \sum_{k,k'} |M_{k,k'}|^2\delta(\omega_q-\Omega)\delta(\varepsilon_k-\varepsilon)\delta(\varepsilon_{k'}-\varepsilon'), \tag{18}$$

where $\mathbf{q} = \pm(\mathbf{k}-\mathbf{k}')$. By differentiating Eq. (16) with respect to time and after some relabeling of dummy variables in Eqs. (14) and (15) with some algebra,[18] one obtains

$$\frac{dE_e(t)}{dt} = 2\pi N_c N(\varepsilon_F)\int_0^\infty d\Omega\alpha^2F(\Omega)(\hbar\Omega)^2[n(\Omega,T_l) - n(\Omega,T_e)]. \tag{19}$$

Here, $n(\Omega, T_l)$ and $n(\Omega, T_e)$ are Bose functions at lattice temperature T_l and electron temperature T_e. Compare the above equation with Eqs. (6) and (7) of KLT. No quadratic form of the electronic dispersion is used. Furthermore, Allen introduces the moments of the electron–phonon spectral function,

$$\lambda\langle\omega^n\rangle = 2\int_0^\infty d\Omega\Omega^n\frac{\alpha^2F(\Omega)}{\Omega}. \tag{20}$$

In the high temperature limit $\frac{\hbar\Omega}{T_{l,e}} \ll 1$, the main equation [Eq. (19)], on keeping the leading order terms, leads to

$$\frac{dT_e(t)}{dt} = \alpha(T_l - T_e). \tag{21}$$

Here,

$$\alpha = \frac{3\hbar\lambda\langle\omega^2\rangle}{\pi k_B T_e}. \tag{22}$$

This is a very important result [compare Eqs. (21) and (22) with (12)]. The conclusion is that by doing pump–probe spectroscopy, a very crucial parameter needed in the theory of superconductivity $\lambda\langle\omega^2\rangle$ can be estimated!

It turns out that in 1990 (about three years after Allen's work[18]), in a very crucial experimental work,[19] Brorson and collaborators verified the predictions of Allen. The authors[19] performed systematic pump–probe measurements on thin films of Cu, Au, Cr, Ti, W, etc., and estimated the electron–phonon coupling constant λ using Allen's equation [Eq. (21)]. The agreement with other measurements of λ (such as tunneling) was excellent.[19]

These investigations showed that the basic assumptions in TTM are valid, and some sort of quasi-equilibrium exists in electronic sub-system and phononic sub-system after photo excitation, but further investigations unfolded a different story, and an apparent paradox arose in the field.

VII. EXPERIMENTS THAT SHOWED THAT TTM FAILS

The basic assumption of the TTM (thermalized Fermi–Dirac distribution at an elevated temperature) makes sense when the internal relaxation time of the non-thermal electron distribution (τ_{e-e}) is much less as compared to electron–phonon relaxation time τ_{e-ph} (that is, $\tau_{e-e} \ll \tau_{e-ph}$). Investigations in the early 1990s[20–23] showed that this is not true in general. In fact, it was estimated that a non-thermal electron distribution takes about 500 fs to relax to a hot Fermi–Dirac distribution, whereas $\tau_{e-ph} \sim 1$ ps (in the case of polycrystalline gold films). Thus, instead of two sub-systems, one must consider three sub-systems (Fig. 2).

In 1992, Fann and collaborators[20] used ultrafast photoemission spectroscopy (instead of transient reflectance spectroscopy). They used 400 fs visible (1.84 eV) heating pulse to create a non-thermal electron distribution in a gold film. For photoemission of this non-thermal distribution, they used 700 fs probe pulse. Although time resolution was low, they observed that, for time delays between pump (heating) pulse and probe pulse of 400 fs, electron distribution substantially differs from a hot Fermi–Dirac distribution (they carefully take into account density of state factors[20]). These observations clearly pointed to non-thermal electron distribution.

In another investigation by Sun and collaborators,[22] a different technique was used. They used transient reflectivity and transmissivity measurements in a pump–probe setup. The authors used 140 fs pump pulse in low fluence limit such that the electron temperature rise was only about 20 K. In addition, the pump pulse central wavelength was in the infrared regime so that only the intra-band excitation of electrons around the Fermi surface was probed. The probe pulse was 210 fs, and it was in the visible regime. The observed transient reflectivity and transmissivity showed fast rise time and slow decay time behavior (Fig. 3).

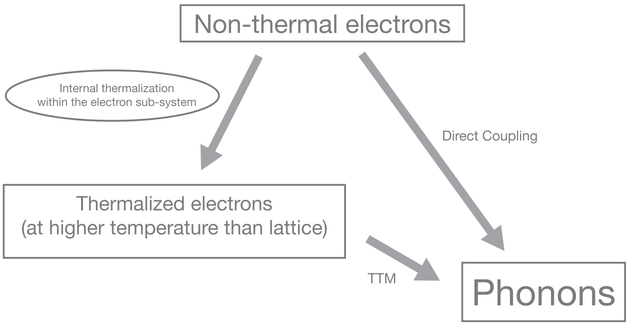

FIG. 2. Three sub-systems: (1) non-thermal (non-FD distributed electrons), (2) thermalized electrons (FD distributed electrons) at a higher temperature, and (3) phonon sub-system.

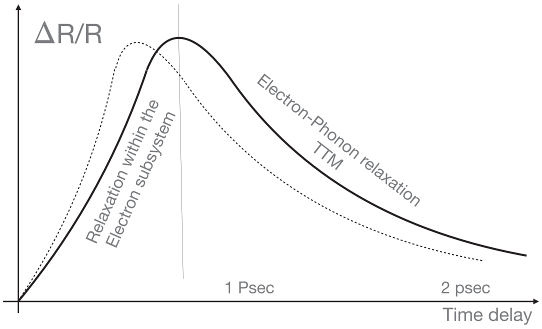

FIG. 3. Signatures of non-thermal electron distribution (schematic diagram. For original, refer to Ref. 22).

The authors first tried to reproduce the experimental data with the following single timescale (τ_{el-ph} only) response function:

$$S(t) = \Theta(t)\left(e^{-t/\tau_{e-ph}+\alpha}\right), \tag{23}$$

in which instantaneous thermalization of the electron gas is assumed, and only electron–phonon relaxation is incorporated using single relaxation time τ_{el-ph}. To account for the finite duration of the pulses, the response function was convoluted with measured pump–probe correlation function.[22] The resultant graph is given by the dotted line in Fig. 3. The agreement is very poor. Next, the authors included in the response function the rise time for a thermalized (hot) Fermi–Dirac distribution [that is, relaxation of a non-thermal electron distribution to thermalized (hot) Fermi–Dirac distribution],

$$S(t) = \Theta(t)\left(1 - e^{-t/\tau_{e-e}}\right)\left(e^{-t/\tau_{e-ph}+\alpha}\right). \tag{24}$$

This updated response function reproduced the data very well (both lines overlap very well, solid line in Fig. 3). From this, the authors estimated that non-thermal electrons take about 500 fs to relax to a thermalized electron distribution (hot Fermi–Dirac distribution).

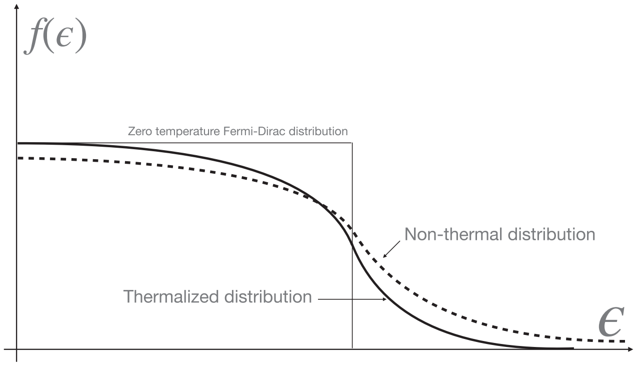

FIG. 4. Two schematic electron distributions: one is thermalized and the other is non-thermal.

These observations showed that the simple minded two-temperature model is not sufficient to address the real state of affairs in a photo excited metallic sample.

VIII. BEYOND TTM

In a pioneering experimental investigation in 1995 by Rogier Groeneveld and collaborators,[23] it is shown that electron distribution after photo-excitation remains a non-thermal (non-Fermi-Dirac) distribution on the time scale of electron–phonon relaxation. Thus, the assumption that non-equilibrium electrons reach to an equilibrium (hot Fermi–Dirac) distribution on a time scale much smaller than electron–phonon relaxation is found to be invalid (at least in the low fluence limit[23]). The authors used the expression

$$\Delta R(t) = (at + b)\Delta U_i(t) + c\Delta U_e(t), \tag{25}$$

which is based on the theory by Rosei.[24] Here, $\Delta R(t)$ is the change in reflectance. Time dependence of internal energies $(\Delta U_i, \Delta U_e)$ is given by the approximated coupled equations,

$$\frac{dU_e(t)}{dt} = \frac{d\left(\frac{1}{2}\gamma T_e^2\right)}{dt} = \gamma T_e \frac{dT_e}{dt} = -\alpha_{T_i}(T_e(t) - T_i(t)), \tag{26}$$

$$\frac{dU_i(t)}{dt} = \frac{d(C_i T_i)}{dt} = C_i \frac{dT_i}{dt} = \alpha_{T_i}(T_e(t) - T_i(t)). \tag{27}$$

By considering $T_e(0), a, b, c, \ \alpha_{T_i}$ as fitting parameters, a very good fit is obtained with experimentally determined reflectance up to 10 ps. Initial temperature of the ions $T_i(0)$ is an experimentally known quantity from the thermometer attached to the sample. It was found that the fitting parameters α_{T_i} and $T_e(0)$ were largely determined by initial relaxation (from 0.25 to 4 ps) and are decoupled from lattice parameters (a, b, c).

To make a tight comparison with the predictions of TTM, authors use its expression valid in the perturbative regime $T_e - T_i \ll T_i$ (valid in the given experimental setup),

$$\frac{dU_e(t)}{dt} = \frac{d\left(\frac{1}{2}\gamma T_e^2\right)}{dt} = \gamma T_e \frac{dT_e}{dt} = -\alpha T_i(T_e(t) - T_i(t)), \tag{28}$$

$$\frac{dU_i(t)}{dt} = \frac{d(C_i T_i)}{dt} = C_i \frac{dT_i}{dt} = \alpha T_i(T_e(t) - T_i(t)), \tag{29}$$

where

$$\alpha(T_i) = \frac{f(T_i)}{dT_i}, \quad f(T_i) = 4g_\infty (T/\Theta_D)^5 \int_0^{\frac{\Theta_D}{T}} \frac{x^4}{e^x - 1} dx. \tag{30}$$

TTM predicts that $\alpha(T_i) \simeq g_\infty$ when $T_i \gtrsim \Theta_D$. By fixing the lattice temperature at 300 K, which is greater than Debye temperature for gold ($\Theta_D = 170$ K), authors determine the coefficient g_∞ by the same fitting procedure. Now, one has all the information required to use TTM. However, when the lattice temperature was fixed at 100 K, authors found serious disagreement between the predictions of TTM and the experiment (refer to Fig. 4 in Ref. 23). The disagreement was seen at various fluence levels (still in the perturbative regime), and detailed discussions were presented on this aspect.[23] Authors went further and defined "instantaneous energy relaxation time,"

$$\tau_E(T_e, T_i) = \frac{U_e(\infty) - U_e(0)}{dU_e/dt}. \tag{31}$$

This time scale was obtained both from the experiment and from the TTM, and serious disagreements were found. In conclusion, TTM is found to be invalid in the low fluence limit (perturbative regime $T_e - T_i \ll T_i$). We notice that these investigations raise serious doubts on the validity of TTM. Disorder effects modify the relaxation mechanism by changing the phonon density of states and thus electron–phonon coupling. Groeneveld and collaborators used clean samples. Readers interested in disorder effects may refer to Refs. 25–27.

Next, in an important theoretical investigation in 2002,[28] Rethfeld and collaborators pointed out a very curious aspect of non-equilibrium electron relaxation in metals. They considered energy absorption from laser field, electron–electron thermalization, and electron–phonon thermalization, all within the full Boltzmann collision integrals approach without using any relaxation time approximation. Detailed calculations are done for the case of aluminum. The central result of this investigation can be expressed in the following way: For laser excitations near the damage threshold of the metal, the energy transfer from the non-equilibrium electrons to phonons can be expressed via the TTM, Eq. (10), even when the perturbed electron distribution is very far from the hot Fermi–Dirac distribution! However, in the regime of low laser excitation, relaxation is not according to TTM. It is much more delayed. It turns out that hot Fermi–Dirac distributed electrons are much more efficient in transferring energy to lattice than non-equilibrium distributed electrons. These theoretical and simulation results corroborate the experimental findings of Groeneveld and collaborators[23] in the perturbative regime.

These investigations have a clear message: In the perturbative regime, actual relaxation is slow as compared to that predicted by the TTM. It implies that electrons do not reach hot thermal equilibrium (Fermi–Dirac) distribution during the process of electron–phonon relaxation. If one assumes hot Fermi–Dirac distribution (like in TTM), we obtain mush faster relaxation in disagreement with the experiments.

IX. AN APPARENT PARADOX AND ITS RESOLUTION

If TTM fails, how is it possible that the investigations of Ref. 19 lead to a reasonably accurate estimate of the superconducting parameter λ introduced into TTM by Allen? Allen's extension is based on TTM.

It raises an apparent paradox! It turns out that in Ref. 19, the experiments were done in the strong fluence limit (not in the perturbative limit). In the strong fluence limit, the relaxation proceeds roughly according to TTM, as discussed in Ref. 28. However, in the strong fluence limit, there is no proof that electron distribution reaches a thermal distribution (FD distribution) on a timescale much shorter than that of electron–phonon relaxation. So, it seems quite surprising that the measured value of λ agrees very well with the estimated value of it (from Allen's generalization of TTM).

It also must be noted that—as far as the behavior of some average property of the electron gas is concerned—for a non-thermal electron distribution excited far from equilibrium and for a corresponding thermal distribution (that is, with the same energy content), the energy relaxation may be considered to follow roughly some similar behavior. To be concrete, consider two schematic

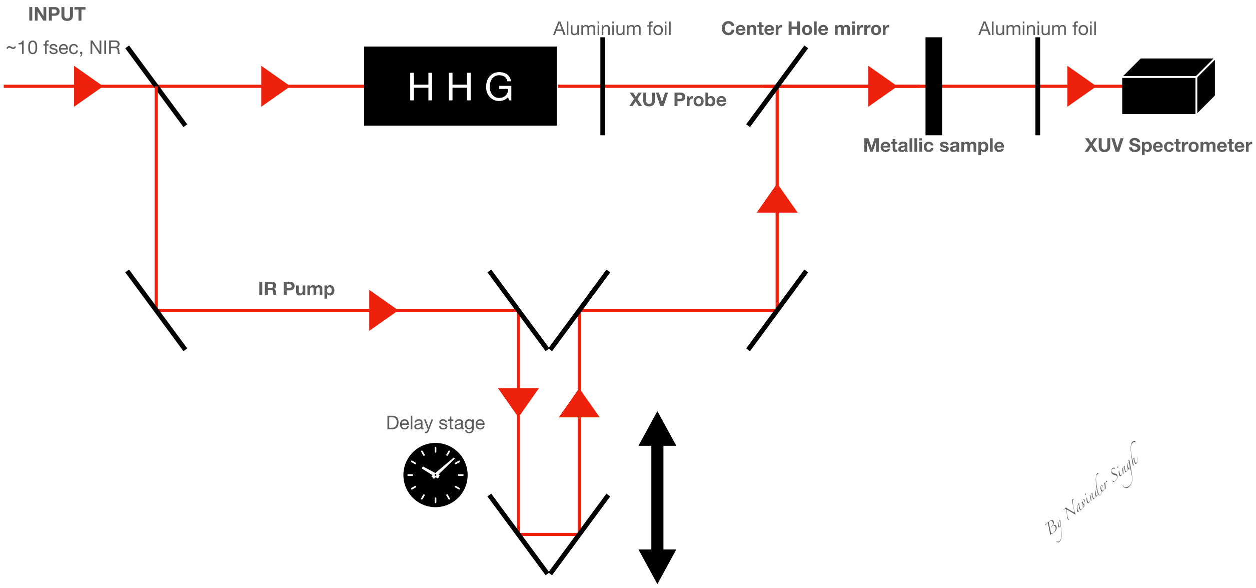

FIG. 5. A schematic ATAS setup.

non-equilibrium electron distributions, one thermal and other non-thermal (Fig. 4). In a thermal distribution, electron temperature can be defined, but $T_e > T$, whereas in a non-thermal distribution, electron temperature cannot be defined (however, energy content can be defined). There is more weight in the tail of the non-thermal distribution, but as far as some macroscopic parameter is concerned (such as λ introduced by Allen in TTM), the relaxation behavior of two distributions may be considered to be similar (without affecting the macroscopic results). However, as it stands, it is just a conjecture! Rigorous proofs, both experimental and theoretical, are much needed.

X. SUMMARY OF RELATED INVESTIGATIONS AFTER YEAR 2000

In this section, we briefly review some of the investigations, which attempt to address the problems of TTM and advance ideas and theories that go beyond it.

In year 2000, Del Fatti and collaborators[29] also show that the assumption of almost instantaneous thermalization of non-equilibrium electrons is not valid. Authors measured internal thermalization timescale for non-equilibrium electrons in silver films and found it to be of the order of 350 fs. This is somewhat smaller than that for gold films (~500 fs). This difference is ascribed to reduced electron–electron screening in silver films as compared to that in gold films. These experiments were also done in the perturbative limit and corroborate the results of Lagendijk and collaborators[23] (perturbative regime is defined as $T_e - T \ll T$. Pump fluences of tens of $\mu\mathrm{J/cm}^2$ typically lead to perturbative excitation of electrons in metals).

Next, it turns out that laser field also modifies the electron–phonon collision integral. In an important investigation,[30] Lugovskoy and Bray take into account this very effect (also known as the Gurzhi mechanism[31]). They also underlined the role of Umklapp electron–electron collisions. These two new inputs better accounted the experiments of Fann *et al.*[20,21] The authors also concluded that field modified electron–phonon scattering rate is higher than that for electron–electron scattering. This means that electron–electron scattering is not sufficient to establish equilibrium within the electron sub-system during the process of the electron–phonon relaxation.

In 2006, Carpene[32] extends the TTM by incorporating the initial non-thermal electron distribution within the relaxation time approximation. The author assumes the three temperature model (3TM): (1) a minority of non-thermal electrons, (2) majority of hot thermalized electrons, and (3) phonons. The non-thermal distribution (δ_{NT}) is assumed to decay via electron–electron scattering and electron–phonon scattering considered within the Relaxation Time Approximation (RTA),

$$\frac{\partial \delta_{NT}}{\partial \tau} = -\frac{\delta_{NT}}{\tau_{ee}} - \frac{\delta_{NT}}{\tau_{ep}}. \tag{32}$$

The author computes the energy transferred from non-thermal distribution to the thermal distribution. Thus, for thermal distribution of electrons, the non-thermal term (first term on the RHS of the above equation) acts like a heat source. Similarly, energy transferred to phonons from the non-thermal distribution (last term in the above equation) directly acts like a heat source for phonon distribution. Considering these physical features and by incorporating these into the original TTM, the author comes up with an updated TTM. Extensive numerical simulations exhibit marked deviations from TTM.

In 2017, Maldonado *et al.*[7] also considered the three temperature model (3TM) just like that considered by Carpene.[32] However, the phonon sub-system is analyzed in detail. In particular, phonon modes with frequency v and wave vector q are taken to be interacting via phonon–phonon interactions. Mode dependent "lattice temperature" is also defined. Phonon–phonon interactions then lead to equilibrium in the phonon sub-system (that is, the attainment of a single temperature for all modes). In addition, electronic and phononic heat capacities, electron–phonon, and phonon–phonon linewidths were calculated *ab initio* (using DFT). Extensive simulations for the system FePt showed that lattice takes about 20 ps to reach equilibrium! The 3TM developed by the authors gives a reasonable material dependent description of relaxation phenomena in a given material without the need of any fitting parameters.

Similarly, in the case of metal films, 3TM was introduced,[33] where two sub-systems of phonons were considered. One set of phonons remain within the film, and in the other, they cross the film–substrate boundary depending upon the angle of incidence. Thus, a concept of "leaky-phonons" is quite useful to study hot electron relaxation in metal films grown on substrates.

In 2017, TTM is extended to account for slow thermalization within the phonon sub-system in polar and non-polar semiconductors.[34] These calculations use electronic structure and phonon dispersion deduced from density functional theory, which is used as an input to the semi-classical Boltzmann equation. In these systems, electron–phonon and phonon–phonon interactions are very heterogeneous. It turns out that thermalization within the phonon sub-system (phonon–phonon interactions) acts like a "bottle-neck" (a limiting step) for electron–phonon thermalization. The "bottle-neck" effect originates because of the delay in phonon–phonon relaxation, which further leads to delayed energy transfer from electron sub-system to phonon sub-system. The system is most efficient in relaxing itself when both sub-systems quickly gain equilibrium within themselves (for more details, refer to Ref. 34). Due to this effect, a single exponential decay of the electron-temperature (due to electron–phonon relaxation within TTM) changes to multi-exponential decay of electron temperature in polar and non-polar semiconductors (due to above-mentioned heterogeneous interactions). This has very novel experimental consequences. Measurement of multi-exponential decay via pump–probe spectroscopy can provide a handle on the nature of heterogeneity of electron–phonon and phonon–phonon couplings and their spectral distributions. Refer also to Ref. 35 for non-equilibrium relaxation in semiconductors.

Very recently, Roulet and collaborators,[36] using state of the art technology of attosecond science and the method of Attosecond Transient extreme ultraviolet light Absorption Spectroscopy (ATAS), showed that time scales of relaxation of nascent electron distribution after optical pump pulse can be measured to the finest accuracy available today. In a basic ATAS setup (Fig. 5), a near IR pulse of $\sim 10 fs$ is divided into a weak pump pulse (that is further passed through a delay stage) and a stronger probe pulse. This probe part is an input to High Harmonic Generation (HHG) setup (involving argon gas). This generates a probe pulse in the XUV spectrum, which is passed through an aluminum foil to block visible and other lower frequency radiation. Both pump and probe pulses are combined again through a center-hole mirror and focused on a metallic sample under study. The transmitted radiation is send to an XUV spectrometer. For more details regarding ATAS experiments, readers may refer to Refs. 37 and 38. Novelty of this technique lies in the fact that at such a small time scale (below 50 fs), interference (perturbation) by phonons in the mechanism of relaxation of non-equilibrium electrons can be neglected. It is mainly about the electron–electron interactions. In fact, the authors, using ATAS, show that non-equilibrium electron relaxation time scales in Mg, Pt, Fe, and Co are of the order of 38, 15, 4.2, and 2.0 fs, respectively. It turns out that relaxation time scale matches remarkably well with the single electron lifetime given by the FLT,

$$\frac{1}{\tau} = A\left[(\pi k_B T_e)^2 + E^2\right] \simeq E^2. \tag{33}$$

Here, the coefficient A can be computed from the knowledge of EDOS and screened electron–electron scattering matrix element.[36] From the conditions of the experiment $k_B T_e \ll E$, the last approximation in the above equation follows.

It is quite counter-intuitive. Relaxation of a large number of non-equilibrium electrons is a many-body mechanism (should not be governed by single particle lifetime). But ATAS experiments and simple theory[36] demonstrate that relaxation can be rationalized within the single-particle effects and the FLT. In author's opinion, ATAS should be applied to a wider variety of materials where FLT is known to fail, such as strange metals. It will push the frontier in an entirely new direction.

The crucial aspect that the author would like to underline is this: if the electron–electron relaxation time scale is below 50 fs in metals (as it is for the case of Mg, Pt, Fe, Co, etc., via ATAS) and the electron–phonon relaxation time scale is in the range of ps, then, can one apply TTM to these systems? The answer is clearly yes! Then what about the investigations (with low resolution in the range of femto-seconds) of 1990s that showed TTM fails? In this author's opinion, all those old investigations should be re-visited with ATAS. Another crucial question would be the following: can one justify Allen's program with ATAS (that is, applicability of TTM)?

Recently, TTM and its generalizations and first-principles approaches that use the time-dependent Boltzmann equation have been applied to other very interesting systems such as graphene. In addition, coherent lattice dynamics and light-induced phase transitions have been studied. Interested readers may refer to Ref. 39 and to literature cited therein. A general treatment of non-equilibrium electron relaxation in quantum materials is provided in Ref. 40. Authors discuss relaxation due to Coulomb scattering, phonon scattering, and impurity scattering using Holstein–Hubbard model, and it is argued that clear separation of electron–electron relaxation or phonon–phonon scattering cannot be made. These processes run in parallel. Another recent trend is related to ultrafast control of quantum materials; interested readers can refer to Ref. 41.

XI. SUMMARY

The famous Two-Temperature Model (TTM) used extensively in the investigations of energy relaxation in photo-excited systems originated in the seminal work of Kaganov, Lifshitz, and Tanatarov (KLT) in 1957. Then, in 1974, Anisimov, Kapeliovich, and Perel'man pointed out that with an ultrashort laser pulse, a non-equilibrium state of electrons in metals can be created in which electron temperature is much greater than lattice temperature. This field experiences great developments in the 1980s and 1990s with the advent of femtosecond (fs) pump–probe spectroscopy. The first experimental proof of this preferential heating of electrons ("anomalous heating" as it was then known) after photo-excitation was provided by Fujimoto, Liu, Ippen, and Bloembergen in 1984. In 1987, Allen revisits the calculations of KLT and rewrites the electron–phonon heat transfer coefficient α in terms of a very important parameter in the theory of superconductivity ($\lambda\langle\omega^2\rangle$). This has far-reaching consequences. Doing a pump–probe experiment, λ for a given superconducting material can be estimated. However, as will be discussed in PART II of this review, the interpretation in the case of unconventional superconductors (such as cuprates) is non-trivial.

In the early 1990s, it became very clear that the basic assumptions of the TTM fail (internal relaxation time of the non-thermal electron distribution τ_{e-e} is not short as compared to electron–phonon relaxation time τ_{e-ph}, that is, $\tau_{e-e} \ll \tau_{e-ph}$). The first experimental proof of the non-equilibrium state of electrons (non-Fermi–Dirac distribution) was provided by several investigators, including Fann and Sun and their collaborators. From year 2000 and onward, focus has shifted from non-equilibrium phenomena in simple metals to those in strongly correlated systems such as high Tc cuprate superconductors and other unconventional superconductors. Very recently, with the advent of ATAS, we may be witnessing the coming back of TTM. But more investigations are needed. Some of the pressing issues are as follows: Why do, in the low fluence limit ($T_e - T \ll T$), experiments violate the predictions of the TTM? What are the roles played by the long wavelength excitations in the electron gas (like plasmons). Other issues include the use of ATAS in the study of time evolution of the effect of exchange interactions (at attosecond and femtosecond time scales) for magnetic metals near their critical points, and ATAS should be used to check whether FLT is violated in strange metals at the initial stages of non-equilibrium electron relaxation.

DEDICATION

The author dedicates this article to the loving memory of Professor N. Kumar (February 1, 1940–August 28, 2017) who guided the author through this field.

ACKNOWLEDGMENTS

The author is also grateful to Professor R. Srinivasan (of Mysuru) for helping the author with calculations, guidance, and many discussions related to several aspects of this field. He would also like to thank Yaroslaw Bazaliy and Igor Tanatarov for correspondence.

AUTHOR DECLARATIONS

Conflict of Interest

The author has no conflicts to disclose.

Author Contributions

Navinder Singh: Conceptualization (equal); Data curation (equal); Formal analysis (equal); Funding acquisition (equal); Investigation (equal); Methodology (equal); Project administration (equal); Resources (equal); Software (equal); Supervision (equal); Validation (equal); Visualization (equal); Writing – original draft (equal); Writing – review & editing (equal).

DATA AVAILABILITY

Data sharing is not applicable to this article as no new data were created or analyzed in this study.

REFERENCES

[1] Y. B. Bazaliy, O. S. Bakai, V. G. Bar'yakhtar, V. M. Loktev, and L. Yu, "To the memory of Moisei Isaakovych Kaganov," Ukr. J. Phys. **64**, 1154 (2019).

[2] This brief historical account is based on 2. For more details reader may refer to it and references therein.

[3] M. I. Kaganov, I. M. Lifshitz, and L. V. Tanatarov, "Relaxation between electrons and the crystalline lattice," Sov. J. Exp. Theor. Phys. **4**, 173 (1957).

[4] L. D. Landau, *Passage of Atomic Particles Through Matter Contribution to the Monograph of N. Bohr* (IIL, 1950).

[5] A. I. Akhiezer and I. Ya. Pomeranchuk, "On the thermal equilibrium between spins and crystal lattice," J. Phys. USSR **8**, 206 (1954).

[6] N. Singh, "Two-temperature model of non-equilibrium electron relaxation: A review," Int. J. Mod. Phys. B **24**, 1141 (2010).

[7] P. Maldonado, K. Carva, M. Flammer, and P. M. Oppeneer, "Theory of out-of-equilibrium ultrafast relaxation dynamics in metals," Phys. Rev. B **96**, 174439 (2017).

[8] N. Singh, "Relaxation between electrons and surface phonons of a homogeneously photoexcited metal film," Pramana **63**, 1083 (2004).

[9] N. Singh, *Electronic Transport Theories: From Weakly to Strongly Correlated Materials* (CRC Press, 2016).

[10] J. M. Ziman, *Electrons and Phonons* (OUP, 2001).

[11] S. I. Anisimov, B. L. Kapeliovich, and T. L. Perel'man, "Electron emission from metal surfaces exposed to ultrashort laser pulses," Sov. J. Exp. Theor. Phys. **39**, 375 (1974).

[12] G. L. Eesley, "Observation of nonequilibrium electron heating in copper," Phys. Rev. Lett. **51**, 2140 (1983).

[13] J. G. Fujimoto, J. M. Liu, E. P. Ippen, and N. Bloembergen, "Femtosecond laser interaction with metallic tungsten and nonequilibrium electron and lattice temperatures," Phys. Rev. Lett. **53**, 1837 (1984).

[14] G. R. Fleming and A. E. Siegman, "Ultrafast phenomena V," in *Proceedings of the Fifth Optical Society of America Topical Meeting, Snowmass, Colorado* (Springer, 1986).

[15] H. E. Elsayed-Ali, T. B. Norris, M. A. Pessot, and G. A. Mourou, "Time-resolved observation of electron-phonon relaxation in copper," Phys. Rev. Lett. **58**, 1212 (1987).

[16] R. W. Schoenlein, W. Z. Lin, J. G. Fujimoto, and G. L. Eesley, "Femtosecond studies of non-equilibrium electronic processes in metals," Phys. Rev. Lett. **58**, 1680 (1987).

[17] S. D. Brorson, J. G. Fujimoto, and E. P. Ippen, "Femtosecond electronic heat-transport dynamics in thin gold films," Phys. Rev. Lett. **59**, 1962 (1987).

[18] P. B. Allen, "Theory of thermal relaxation of electrons in metals," Phys. Rev. Lett. **59**, 1460 (1987).

[19] S. D. Brorson, A. Kazeroonian, J. S. Moodera, D. W. Face, T. K. Cheng, E. P. Ippen, M. S. Dresselhaus, and G. Dresselhaus, "Femtosecond room-temperature measurement of the electron-phonon coupling constant λ in metallic superconductors," Phys. Rev. Lett. **64**, 2172 (1990).

[20] W. S. Fann, R. Storz, H. W. K. Tom, and J. Bokor, "Direct measurement of nonequilibrium electron-energy distributions in subpicosecond laser-heated gold films," Phys. Rev. Lett. **68**, 2834 (1992).

[21] W. S. Fann, R. Storz, H. W. K. Tom, and J. Bokor, "Electron thermalization in gold," Phys. Rev. B **46**, 13592 (1992).

[22] C.-K. Sun, F. Vallee, L. Acioli, E. P. Ippen, and J. G. Fujimoto, "Femtosecond investigation of electron thermalization in gold," Phys. Rev. B **48**, 12–365 (1993).
[23] R. H. M. Groeneveld *et al.*, "Femtosecond spectroscopy of electron-electron and electron-phonon energy relaxation in Ag and Au," Phys. Rev. B **51**, 11433 (1995).
[24] R. Rosei, Phys. Rev. B **10**, 474 (1974).
[25] G. Bergmann, Phys. Rev. B **3**, 3797 (1971).
[26] S. J. Poon and T. H. Geballe, Phys. Rev. B **18**, 233 (1978).
[27] B. Keck and A. Schmid, J. Low Temp. Phys. **24**, 611 (1976).
[28] B. Rethfeld, A. Kaiser, M. Vicanek, and G. Simon, Phys. Rev. B **65**, 214303 (2002).
[29] N. Del Fatti, C. Voisin, M. Achermann, S. Tzortzakis, D. Christofilos, and F. Vallée, "Nonequilibrium electron dynamics in noble metals," Phys. Rev. B **61**, 16956 (2000).
[30] A. V. Lugovskoy and I. Bray, "Ultrafast electron dynamics in metals under laser irradiation," Phys. Rev. B **60**, 3279 (1999).
[31] R. N. Gurzhi, Sov. J. Exp. Theor. Phys. **6**, 451 (1958).
[32] E. Carpene, "Ultrafast laser irradiation of metals: Beyond the two-temperature model," Phys. Rev. B **74**, 024301 (2006).
[33] A. I. Bezuglyj and V. A. Shklovskij, "Kinetics of electron cooling in metal films at low temperatures and revision of the two-temperature model," J. Phys.: Condens. Matter **30**, 295001 (2018).
[34] S. Sadasivam, M. K. Y. Chan, and P. Darancet, "Theory of thermal relaxation of electrons in semiconductors," Phys. Rev. Lett. **119**, 136602 (2017).
[35] J.-A. Yang, S. Parham, D. Dessau, and D. Reznik, Sci. Rep. **7**, 40876 (2017).
[36] B. R. de Roulet, L. Drescher, S. A. Sato, and S. R. Leone, "Initial electron thermalization in metals measured by attosecond transient absorption spectroscopy," Phys. Rev. B **110**, 174301 (2024).
[37] A. Niedermayr *et al.*, Phys. Rev. X **12**, 021045 (2022).
[38] R. Locher *et al.*, Rev. Sci. Instrum. **85**, 013113 (2014).
[39] F. Caruso and D. Novko, "Ultrafast dynamics of electrons and phonons: From the two-temperature model to the time-dependent Boltzmann equation," Adv. Phys.: X **7**(1), 2095925 (2022).
[40] A. F. Kemper, O. Abdurazakov, and J. K. Freericks, Phys. Rev. X. **8**, 041009 (2018).
[41] A. de la Torre *et al.*, "Colloquium: Nonthermal pathways to ultrafast control in quantum materials," Rev. Mod. Phys. **93**, 041002 (2021).

APL Quantum

RESEARCH ARTICLE | JUNE 17 2025

Observation of photonic dynamics in dissipative quantum Rabi models

Special Collection: Quantum Dynamics in Theory, Numerics and in Experimental Research

Wen Ning ; Ri-Hua Zheng ; Jia-Hao Lü ; Ken Chen ; Xin Zhu; Fan Wu ; Zhen-Biao Yang ; Shi-Biao Zheng

APL Quantum 2, 026137 (2025)
https://doi.org/10.1063/5.0276914

AIP Publishing

APL Quantum ARTICLE pubs.aip.org/aip/apq

Observation of photonic dynamics in dissipative quantum Rabi models

Cite as: APL Quantum 2, 026137 (2025); doi: 10.1063/5.0276914
Submitted: 21 April 2025 • Accepted: 3 June 2025 •
Published Online: 17 June 2025

Wen Ning, Ri-Hua Zheng,[a] Jia-Hao Lü, Ken Chen, Xin Zhu, Fan Wu, Zhen-Biao Yang,[a] and Shi-Biao Zheng[a]

AFFILIATIONS

Fujian Key Laboratory of Quantum Information and Quantum Optics, College of Physics and Information Engineering, Fuzhou University, Fuzhou, Fujian 350108, China

Note: This paper is part of the APL Quantum Special Topic on Quantum Dynamics in Theory, Numerics and in Experimental Research.

[a] **Authors to whom correspondence should be addressed:** ruazheng@gmail.com, zbyang@fzu.edu.cn and t96034@fzu.edu.cn

ABSTRACT

The quantum Rabi model (QRM), composed of a qubit interacting with a quantized photonic field, is a cornerstone of quantum optics. The QRM with dominant unitary dynamics has been demonstrated in circuit quantum electrodynamics (QED) systems, but an open QRM with a strong photonic dissipation has not been experimentally explored. We here present the first experimental demonstration of such an open system in circuit QED, featuring a controlled competition between the coherent qubit-field interaction and the photonic dissipation. We map out the photon number distributions of the dissipative resonator for different coupling strengths in the steady state. We further observe the variation of the photon number during the system's evolution toward the steady state with fixed control parameters. The results demonstrate that the system's behavior is significantly modified by photonic dissipation.

The Quantum Rabi model (QRM), which describes the interaction between a qubit and a quantized field mode, lies at the heart of quantum optics.[1,2] It reduces to the well-known Jaynes–Cummings model (JCM)[3,4] in the rotating-wave approximation, which is valid when the qubit-photon interaction strength is much smaller than the frequency scale. When the coupling is comparable to the frequencies, the counter-rotating wave terms play a non-negligible role, resulting in a competition between the photonic creation and annihilation associated with the excitation or deexcitation of the qubit. This competition gives rise to the emergence of a cat-like state, where two coherent states of the field with opposite phases are entangled with the qubit's energy levels.[5–7] More intriguingly, it can exhibit a superradiant phase transition,[8–12] featuring a sharp increase in the photon number near the critical point. In addition to fundamental interest, the associated critical phenomena are useful for enhancement of the sensitivity in quantum metrology.[13–16]

Over the past few years, both the spectroscopic signatures[17,18] and dynamical behaviors of the QRM have been experimentally explored in different systems.[11,12,19–21] In most of these experiments, the qubit-photon coupling strength is much stronger than the system dissipation, so that the system evolution is dominated by the coherent dynamics. When the photonic decaying rate is comparable with the interaction strength, the system may display new effects, e.g., the dissipative phase transition.[22,23] Recently, the dissipative QRM was demonstrated in an ion-trap experiment,[24] where the phononic mode of a trapped ion, which was coupled to its electronic degree of freedom and subjected to an artificially engineered reservoir, mimicked the photonic mode of the original QRM. However, the open QRM with a naturally dissipative photonic mode has not been reported so far.

We here present a demonstration of such a dissipative QRM in a circuit quantum electrodynamics architecture, where a superconducting qubit is coupled to the microwave field stored in a lossy microwave resonator by an ac flux, which periodically modulates the qubit's frequency. This frequency modulation mediates a sideband interaction between the qubit and the resonator, with a controllable photonic swapping rate. A transverse drive transforms this JCM into a QRM with a non-negligible photonic dissipation rate. We investigate the photon-number distributions and average photon numbers for different effective coupling strengths after a long-time dynamics. We further track the system's evolution for fixed parameters. The results demonstrate that in each case, the photon number evolves toward a steady value without oscillations, in contrast to the unitary dynamics.

The dissipative QRM [intuitively seen in Fig. 1(a)] dynamics can be described by the master equation ($\hbar = 1$ hereafter, and the decoherence of the qubit is ignored)

$$\dot{\rho} = -i[H_{\text{Rabi}}, \rho] + \kappa a \rho a^{\dagger} - \frac{\kappa}{2}(a^{\dagger} a \rho + \rho a^{\dagger} a), \tag{1}$$

where ρ is the density matrix, a ($a^{\dagger}$) is the annihilation (creation) operator of the dissipative cavity mode with decay rate κ, and H_{Rabi} is the QRM Hamiltonian

$$H_{\text{Rabi}} = \frac{\Omega}{2}\sigma_y + \delta a^{\dagger} a + \eta \sigma_x (a + a^{\dagger}), \tag{2}$$

with effective frequencies Ω and δ of the qubit and cavity, respectively. Note that $\sigma_{x(y)}$ are the Pauli operators of the qubit under the ground and excited states basis $\{|g\rangle, |e\rangle\}$, and σ_y can be treated as σ_z here, after a simple representation transformation (see supplementary material, Sec. S1, for the details). A distinct feature of the current model is that the cavity decay rate $\kappa = 5$ MHz is close to the coupling strength $\eta \sim 2\pi \times 1$ MHz, resulting in a competition between the coherent QRM dynamics and incoherent photonic dissipation, further leading to a steady state with a stable photon number (see supplementary material, Sec. S2, for the detailed numerical simulation of system dynamics).

The experiment is carried out on an on-chip superconducting circuit,[25] where the lowest two energy levels of an Xmon constitute the qubit, while a lossy microwave resonator acts as the dissipative cavity [see Fig. 1(b)]. Typically, this dissipative resonator is used to measure the qubit population through dispersive interaction;[26,27] therefore, with frequency $\omega_r/(2\pi) = 6.656$ GHz, it is much higher than the qubit frequency $\omega_q/(2\pi) = 5.93$–5.996 GHz. We utilize Floquet technology to couple the qubit and resonator at the first sideband. Specifically, a periodical modulation, $\varepsilon \cos(\nu_1 t)$, is applied through the Z line of the qubit [see Fig. 1(b)], resulting in a series of frequency splittings. We adjust $\nu_1 = \omega_r - \omega_q$ to resonate the qubit and resonator at the first sideband with strength $\eta = \lambda J_1(\varepsilon/\nu_1)/2$ [$J_1(\cdot)$ the first kind Bessel function at the first order], where λ is the original interaction strength between the qubit and resonator. Furthermore, a transverse drive from the XY control line [see Fig. 1(b)], $\Omega_1 + i\Omega_2 \exp(i\nu_2 t)$, transforms the JCM to the QRM in Eq. (2) when $\nu_2 = 2\Omega_1 J_0(\varepsilon/\nu_1)$, with the effective frequency of resonator $\Omega/2 = \Omega_2 J_0(\varepsilon/\nu_1)/2$ (see supplementary material, Sec. S1, for the deviation). By adjusting ε and ν_1, we can gradually change the value of $\eta/(2\pi)$ from 0 to 1 MHz with fixed frequencies of the qubit and resonator $\Omega/(2\pi) = 1$ MHz and $\omega/(2\pi) = 0.18$ MHz. We first check the population oscillations of the dissipative QRM, realized with the choice $\varepsilon/(2\pi) = 56.7$ MHz, $\nu_1/(2\pi) = 708.7$ MHz, $\Omega_1/(2\pi) = 20$ MHz, and $\Omega_2/(2\pi) = 1$ MHz, corresponding to $\eta/(2\pi) = 0.8$ MHz.

The system starts from the ground state $|g\rangle_q \otimes |0\rangle_r$ (qubit's ground state and resonator's vacuum state). After a preset interaction time, both the longitudinal modulation and transverse driving are switched off so that the qubit is effectively decoupled from the dissipative resonator, as their detuning $(\omega_r - \omega_q)/(2\pi) \sim 700$ MHz is much larger than the coupling strength $\lambda/(2\pi) = 40$ MHz. Then the qubit's state can be read out. Figure 2 displays the measured population of the qubit's excited state. We note that the fast oscillations, with the period of about $2\pi/[2\Omega_1 J_0(\varepsilon/\nu_1)] = 25$ ns, are due to the transverse driving. In other words, the dissipative Rabi model is realized in the rotating framework at the frequency $2\Omega_1 J_0(\varepsilon/\nu_1)$,[12] but the results are measured in the laboratory framework. Consequently, the envelopes of these oscillations reflect the qubit dynamics of the effective dissipative QRM.[21] The upper and lower envelopes (solid

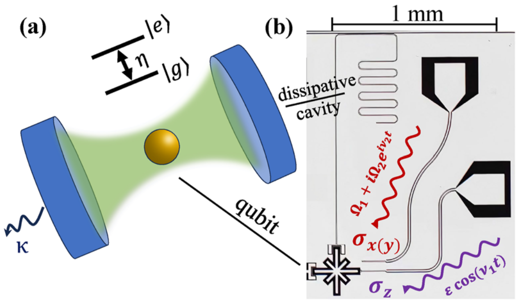

FIG. 1. Experimental setup diagram. (a) Schematic diagram of the dissipative QRM, including a two-level artificial atom coupling to the field mode stored in a dissipative cavity (decay rate $\kappa \sim \eta$). (b) On-chip demonstration of the dissipative QRM: optical micrograph of the superconducting circuit. The Xmon qubit is capacitively coupled to a dissipative resonator and an XY control line $[\sigma_{x(y)}]$, and inductively coupled to a Z control line (σ_z). In addition to the dissipative resonator, the qubit is controllably coupled to a bus resonator with a negligible dissipation rate (not shown here), which is used to bring the qubit to the ground state after the dissipative quantum Rabi dynamics, necessary for reading out the photon number of the dissipative resonator.

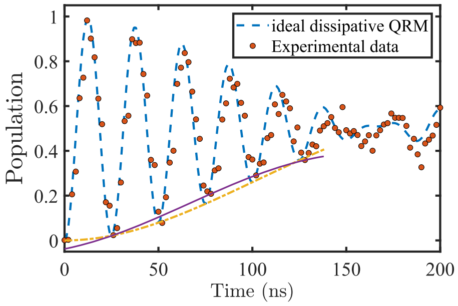

FIG. 2. Observation of the $|e\rangle$-state population evolution of the qubit. The effective dissipative Rabi model is realized for $\eta/(2\pi) = 0.8$, $\omega/(2\pi) = 0.18$, and $\Omega/(2\pi) = 0.5$ MHz. The system starts with the ground state. The lines and dots denote the numerical result for the ideal dissipative QRM [considering the transverse field rotating $2\Omega_1 J_0(\varepsilon/\nu_1)\sigma_x$] and the experimental result, respectively. The solid purple and black lines denote the lower and upper envelopes of the observed fast oscillations, respectively. These envelopes, respectively, starting from the qubit's ground and excited states, are in good agreement with the qubit dynamics of the effective dissipative QRM with the corresponding initial states (dashed–dotted lines).

lines) coincide with the qubit excitation-number evolutions, starting from the initial excited and ground states, respectively. These agreements confirm the validity of the engineered dissipative QRM. During the first several oscillatory periods, the experimental results are in good agreement with the simulation (line), confirming the validity of the approximations for deriving the effective dissipative QRM. With the elapse of time, the qubit becomes more and more affected by dephasing noise, which destroys the oscillatory signals but is not included in the effective model.

The photon number of the dissipative resonator is measured with the help of the qubit. To do so, it is necessary to first transfer the excitation of the qubit to the bus resonator through a swapping gate at the frequency of the bus resonator. Following this excitation transfer, the qubit is biased back to the original frequency, where a longitudinal modulation is applied to mediate a resonant sideband interaction with the dissipative resonator, described by a dissipative JCM. The photon number distributions can be inferred from the Rabi signals of the qubit. Figures 3(a) and 3(b), respectively, display the photon number distributions for $\eta/(2\pi) = 0.8$ and 0.9 MHz, measured after a 3-μs dynamics of the dissipative QRM with the initial state $(|g\rangle_q + |e\rangle_q) \otimes |0\rangle_c/\sqrt{2}$. The results imply that the populations of relatively large photon numbers increase with the effective coupling strength. For example, when $\eta/(2\pi) = 0.8$ MHz, the total population with three or more photons is 0.2684, which increases to 0.4044 for $\eta/(2\pi) = 0.9$ MHz.

Pushing one step further, we investigate the average photon number in the steady state of the dissipative QRM vs the effective coupling strength η. Figure 4(a) displays the results, all measured for the initial state $(|g\rangle_q + |e\rangle_q) \otimes |0\rangle_c/\sqrt{2}$, which evolves according to the dissipative QRM for an interaction time of 3 μs. As expected, with the increase of η, the average photon number monotonously increases. These experimental results coincide with the simulation (lines) very well. To confirm the system has well approached the steady state after 3 μs, we track the photon number evolutions within 3 μs. Figure 4(b) shows the photon number evolutions observed for different values of η. As expected, for each case the photon number almost remains unchanged from 2 to 3 μs, where the average growth rates of the photon number are 0.0033, 0.0056, 0.0116, 0.0113, and 0.0088 μs^{-1} for $\eta/(2\pi) = 0.2$, 0.4, 0.6, 0.8, and 1.0 MHz, respectively. This proves that the cavity dissipation (with rate $\kappa = 5$ MHz) plays an important role in the dynamics, making the system tend to a steady state, in stark contrast with the oscillatory pattern exhibited by the unitary QRM under the time-independent Hamiltonian. The results also demonstrate that the closer $\eta/(2\pi)$ is to 1 MHz, the larger the changing rate of the steady-state photon number with respect to η. Due to the limitation of system parameters, the QRM is realized with an effective frequency ratio of 5.6. With the improvement of this ratio, it is possible to observe the dissipative superradiant phase transition, which was predicted to occur at the critical point $\xi_c = \sqrt{1 + \kappa^2/(4\delta^2)}$[22] when this ratio approaches infinity.

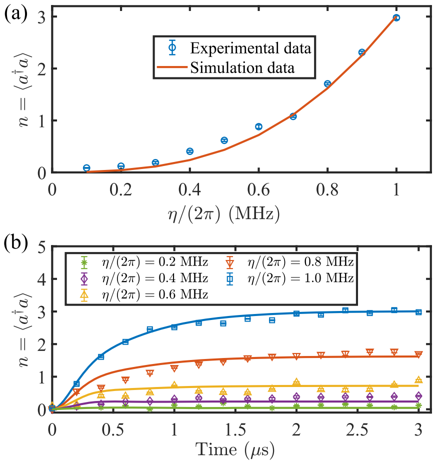

FIG. 4. Observation of the dissipative QRM dynamics. (a) Photon number n vs the QRM coupling $\eta/(2\pi)$. Each data point is measured at $t = 3$ μs under the dissipative QRM dynamics with corresponding coupling $\eta/(2\pi)$. (b) The variation of the photon number n during the dissipative QRM system's evolution toward the steady state with fixed coupling $\eta/(2\pi)$.

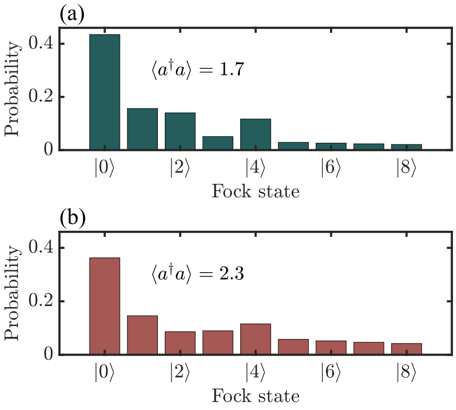

FIG. 3. Observed photon number distributions for $\eta/(2\pi) = 0.8$ MHz (a) and 0.9 MHz (b). For each case, the photon number distribution is obtained after dissipative QRM dynamics lasting for 3 μs. The result is measured with the qubit, whose excitation is transferred to the bus resonator after the quantum Rabi dynamics, following which it is coupled to the dissipative resonator to extract the photon-number populations. In (a), the measured N-photon populations for $N = 0$ to 8 are 0.4348, 0.1566, 0.1401, 0.0511, 0.1170, 0.0292, 0.0263, 0.0236, and 0.0213, respectively. In (b), the corresponding populations are 0.3629, 0.1460, 0.0866, 0.0898, 0.1156, 0.0579, 0.0521, 0.0469, and 0.0422, respectively.

In conclusion, we have demonstrated the dynamics of the dissipative QRM engineered with a frequency-tunable Xmon qubit, together with its readout resonator. The qubit-resonator interaction is mediated at the first upper sideband with respect to a frequency modulation applied to the qubit, which makes the photonic swapping rate tunable. Thanks to this tunability, a transverse microwave drive transforms this JCM into a QRM, with a strong photonic dissipation, in a rotated framework. The effective qubit frequency in the QRM is controlled by the amplitude of a second transverse drive. The observed evolution of the qubit excited state population shows fast oscillations, with the envelopes well agreeing with the qubit dynamics in the effective dissipative QRM. The photon number distribution of the resonator after a preset interaction time is extracted by re-initiating the sideband interaction and recording the Rabi signal, governed by dissipative JCM. The observed average photon number monotonically increases with the effective coupling-frequency ratio, tending toward a steady value after a long-time dynamics, which makes the dissipative QRM different from the unitary counterpart. The method can be extended to synthesize a dissipative Dicke model involving multiple qubits coupled to a decaying resonator, with a controllable effective coupling-frequency ratio. We plan to investigate the dissipative superradiant phase transition in such a model.

The supplementary material includes the engineering of the Rabi model with controlled unitary-dissipative competition, simulation of the system dynamics, realization of the quench process, observation of the photon number evolution during the quench process, and steady-state photon-number distributions.

This work was supported by the National Natural Science Foundation of China under Grant Nos. 12274080, 12474356, and 12475015, and the Innovation Program for Quantum Science and Technology under Grant No. 2021ZD0300200.

AUTHOR DECLARATIONS

Conflict of Interest

The authors have no conflicts to disclose.

Author Contributions

W.N. and R.H.Z. contributed equally to this work.

Wen Ning: Data curation (equal); Formal analysis (equal); Investigation (equal); Software (equal). **Ri-Hua Zheng**: Data curation (equal); Formal analysis (equal); Investigation (equal); Software (equal); Writing – review & editing (equal). **Jia-Hao Lü**: Data curation (equal); Visualization (equal). **Ken Chen**: Data curation (equal); Formal analysis (equal). **Xin Zhu**: Data curation (equal); Validation (equal). **Fan Wu:** Methodology (equal); Formal analysis (equal). **Zhen-Biao Yang**: Funding acquisition (equal); Project administration (equal); Supervision (equal); Writing – review & editing (equal). **Shi-Biao Zheng**: Conceptualization (equal); Funding acquisition (equal); Supervision (equal); Writing – original draft (equal).

DATA AVAILABILITY

The data that support the findings of this study are available within the article.

REFERENCES

[1] A. Frisk Kockum, A. Miranowicz, S. De Liberato, S. Savasta, and F. Nori, "Ultrastrong coupling between light and matter," Nat. Rev. Phys. **1**, 19 (2019).

[2] P. Forn-Díaz, L. Lamata, E. Rico, J. Kono, and E. Solano, "Ultrastrong coupling regimes of light-matter interaction," Rev. Mod. Phys. **91**, 025005 (2019).

[3] E. T. Jaynes and F. W. Cummings, "Comparison of quantum and semiclassical radiation theories with application to the beam maser," Proc. IEEE **51**, 89 (1963).

[4] B. W. Shore and P. L. Knight, "The Jaynes-Cummings model," J. Mod. Opt. **40**, 1195 (1993).

[5] S.-B. Zheng, "Preparation of motional macroscopic quantum-interference states of a trapped ion," Phys. Rev. A **58**, 761 (1998).

[6] E. Solano, G. S. Agarwal, and H. Walther, "Strong-driving-assisted multipartite entanglement in cavity QED," Phys. Rev. Lett. **90**, 027903 (2003).

[7] Y.-H. Chen, W. Qin, X. Wang, A. Miranowicz, and F. Nori, "Shortcuts to adiabaticity for the quantum Rabi model: Efficient generation of giant entangled cat states via parametric amplification," Phys. Rev. Lett. **126**, 023602 (2021).

[8] S. Ashhab, "Superradiance transition in a system with a single qubit and a single oscillator," Phys. Rev. A **87**, 013826 (2013).

[9] M.-J. Hwang, R. Puebla, and M. B. Plenio, "Quantum phase transition and universal dynamics in the Rabi model," Phys. Rev. Lett. **115**, 180404 (2015).

[10] L.-T. Shen, J.-W. Yang, Z.-R. Zhong, Z.-B. Yang, and S.-B. Zheng, "Quantum phase transition and quench dynamics in the two-mode Rabi model," Phys. Rev. A **104**, 063703 (2021).

[11] M.-L. Cai, Z.-D. Liu, W.-D. Zhao, Y.-K. Wu, Q.-X. Mei, Y. Jiang, L. He, X. Zhang, Z.-C. Zhou, and L.-M. Duan, "Observation of a quantum phase transition in the quantum Rabi model with a single trapped ion," Nat. Commun. **12**, 1126 (2021).

[12] R.-H. Zheng, W. Ning, Y.-H. Chen, J.-H. Lü, L.-T. Shen, K. Xu, Y.-R. Zhang, D. Xu, H. Li, Y. Xia, F. Wu, Z.-B. Yang, A. Miranowicz, N. Lambert, D. Zheng, H. Fan, F. Nori, and S.-B. Zheng, "Observation of a superradiant phase transition with emergent cat states," Phys. Rev. Lett. **131**, 113601 (2023).

[13] L. Garbe, M. Bina, A. Keller, M. G. A. Paris, and S. Felicetti, "Critical quantum metrology with a finite-component quantum phase transition," Phys. Rev. Lett. **124**, 120504 (2020).

[14] Y. Chu, S. Zhang, B. Yu, and J. Cai, "Dynamic framework for criticality-enhanced quantum sensing," Phys. Rev. Lett. **126**, 010502 (2021).

[15] J.-H. Lü, W. Ning, X. Zhu, F. Wu, L.-T. Shen, Z.-B. Yang, and S.-B. Zheng, "Critical quantum sensing based on the Jaynes-Cummings model with a squeezing drive," Phys. Rev. A **106**, 062616 (2022).

[16] X. Zhu, J.-H. Lü, W. Ning, F. Wu, L.-T. Shen, Z.-B. Yang, and S.-B. Zheng, "Criticality-enhanced quantum sensing in the anisotropic quantum Rabi model," Sci. China Phys. Mech. Astron. **66**, 250313 (2023).

[17] D. Lv, S. An, Z. Liu, J.-N. Zhang, J. S. Pedernales, L. Lamata, E. Solano, and K. Kim, "Quantum simulation of the quantum Rabi model in a trapped ion," Phys. Rev. X **8**, 021027 (2018).

[18] F. Yoshihara, T. Fuse, S. Ashhab, K. Kakuyanagi, S. Saito, and K. Semba, "Superconducting qubit–oscillator circuit beyond the ultrastrong-coupling regime," Nat. Phys. **13**, 44 (2017).

[19] F. Yoshihara, T. Fuse, Z. Ao, S. Ashhab, K. Kakuyanagi, S. Saito, T. Aoki, K. Koshino, and K. Semba, "Inversion of qubit energy levels in qubit-oscillator circuits in the deep-strong-coupling regime," Phys. Rev. Lett. **120**, 183601 (2018).

[20] N. K. Langford, R. Sagastizabal, M. Kounalakis, C. Dickel, A. Bruno, F. Luthi, D. J. Thoen, A. Endo, and L. DiCarlo, "Experimentally simulating the dynamics of quantum light and matter at deep-strong coupling," Nat. Commun. **8**, 1715 (2017).

[21] J. Braumüller, M. Marthaler, A. Schneider, A. Stehli, H. Rotzinger, M. Weides, and A. V. Ustinov, "Analog quantum simulation of the Rabi model in the ultra-strong coupling regime," Nat. Commun. **8**, 779 (2017).

[22] M.-J. Hwang, P. Rabl, and M. B. Plenio, "Dissipative phase transition in the open quantum Rabi model," Phys. Rev. A **97**, 013825 (2018).

[23] C. J. Zhu, L. L. Ping, Y. P. Yang, and G. S. Agarwal, "Squeezed light induced symmetry breaking superradiant phase transition," Phys. Rev. Lett. **124**, 073602 (2020).

[24] M.-L. Cai, Z.-D. Liu, Y. Jiang, Y.-K. Wu, Q.-X. Mei, W.-D. Zhao, L. He, X. Zhang, Z.-C. Zhou, and L.-M. Duan, "Probing a dissipative phase transition with a trapped ion through reservoir engineering," Chin. Phys. Lett. **39**, 020502 (2022).

[25] C. Song, S.-B. Zheng, P. Zhang, K. Xu, L. Zhang, Q. Guo, W. Liu, D. Xu, H. Deng, K. Huang, D. Zheng, X. Zhu, and H. Wang, "Continuous-variable geometric phase and its manipulation for quantum computation in a superconducting circuit," Nat. Commun. **8**, 1061 (2017).

[26] A. Blais, R.-S. Huang, A. Wallraff, S. M. Girvin, and R. J. Schoelkopf, "Cavity quantum electrodynamics for superconducting electrical circuits: An architecture for quantum computation," Phys. Rev. A **69**, 062320 (2004).

[27] A. Wallraff, D. I. Schuster, A. Blais, L. Frunzio, R.-S. Huang, J. Majer, S. Kumar, S. M. Girvin, and R. J. Schoelkopf, "Strong coupling of a single photon to a superconducting qubit using circuit quantum electrodynamics," Nature **431**, 162 (2004).

APL Quantum

RESEARCH ARTICLE | MAY 16 2025

Quantum dissipative dynamics of driven Duffing oscillator near attractors

Special Collection: Quantum Dynamics in Theory, Numerics and in Experimental Research

Wei Feng ; Lingzhen Guo

APL Quantum 2, 026124 (2025)
https://doi.org/10.1063/5.0267128

AIP Publishing

APL Quantum ARTICLE pubs.aip.org/aip/apq

Quantum dissipative dynamics of driven Duffing oscillator near attractors

Cite as: APL Quantum 2, 026124 (2025); doi: 10.1063/5.0267128
Submitted: 22 February 2025 • Accepted: 30 April 2025 •
Published Online: 16 May 2025

Wei Feng and Lingzhen Guo[a)]

AFFILIATIONS

Center for Joint Quantum Studies and Department of Physics, School of Science, Tianjin University, Tianjin 300072, China

Note: This paper is part of the APL Quantum Special Topic on Quantum Dynamics in Theory, Numerics and in Experimental Research.

[a)] **Author to whom correspondence should be addressed:** lingzhen_guo@tju.edu.cn

ABSTRACT

We investigate the quantum dissipative dynamics near the stable states (attractors) of a driven Duffing oscillator. A refined perturbation theory that can treat two perturbative parameters with different orders is developed to calculate the quantum properties of the Duffing oscillator near the attractors. We obtain the perturbative analytical results that go beyond the standard linearization approach for the renormalized level spacings, the orbital displacements, and the effective temperature near the classical attractor. Furthermore, we demonstrate that strong damping induces additional slight renormalization of level spacings and the Bose distribution together with dephasing. Our work provides new insights into the quantum dynamics of the driven Duffing oscillator and offers a theoretical framework that can be applied to related quantum systems near their stable states.

I. INTRODUCTION

The driven Duffing oscillator,[1] a paradigmatic model for various nonlinear mechanical systems and nonlinear optical phenomena, has fascinated physicists for a long time with its rich dynamical behaviors such as bistability, bifurcation, and chaotic trajectories. In recent years, the Duffing oscillator has received renewed attention, as the quantum regime of nanomechanical oscillators becomes experimentally accessible. The interplay between quantum effects, nonequilibrium dynamics, and nonlinear effects makes the driven Duffing oscillator a model with broad applicability across multiple domains, e.g., mechanical metrology,[2–5] chaotic dynamics,[6,7] cavity and circuit quantum electrodynamics,[8–11] nano- and opto-mechanics,[12–22] and cold atoms.[23–25] Notable examples include bifurcation-based quantum measurement devices, where the low- and high-amplitude states of bistability are entangled with the ground and excited states of qubits, respectively, enabling the analysis of the qubit states through the detection of classical signals.[26–30]

In practice, physical systems inevitably interact with their environment, leading to the decoherence of quantum states and dissipation of energy. The dissipative dynamics of driven Duffing oscillators have been extensively studied.[31,32] In the underdamped regime near a bifurcation point, a scaling law for the noise-induced escape from metastable states was established.[33] To the bottom of the well in a parametrically driven Duffing oscillator, it was identified that the energy dependence of the level spacings captured by the perturbative approach beyond linearization gives rise to a fine structure in the power spectrum.[34] It was also revealed that the quantum activation process has distinct temperature dependency compared to that for the quantum tunneling process.[35] The distinct transition rate scaling behaviors near bifurcation points were also revealed in the driven mesoscopic Duffing oscillator.[36] It was found that the bifurcation point is shifted by the quantum effect and a linear scaling behavior for the tunneling rate with the driving distance to the shifted bifurcation point.[37] Recent advances also showed that the quadrature squeezing can enhance the Wigner negativity in a Duffing oscillator, demonstrating a promising approach to generate nonclassical states in macroscopic mechanical systems.[38] For two Duffing oscillators coupled via nonlinear interactions, the stationary paired solutions and their dynamical stability were demonstrated.[16] In a coupled system consisting of a time-delayed Duffing oscillator (as a driver system) and a non-delayed Duffing oscillator (as a response system), the phenomenon of transmitted resonance was investigated.[39]

In this paper, we focus on investigating quantum dissipative dynamics near the attractors of a driven Duffing oscillator. We develop an effective quantum master equation that can address quantum fluctuations, thermal effects, damping, and dephasing in a unified framework. Our approach is essential to quantify the occupation of high levels near the bottom of the potential well by the quantum squeezing effects. We also demonstrate the effects of strong damping and dephasing on the system's dynamics, including level spacing renormalization and dephasing-modified Bose distributions. While prior studies within linearized frameworks have successfully captured phenomena such as effective temperatures,[34,40,41] the refined perturbation theory presented in our work goes beyond the standard linearization approach, allowing us to investigate the energy dependence of the level spacing, the orbital displacement, and the effective temperature. To address this, we develop a refined perturbation theory capable of treating two perturbative parameters with distinct orders, enabling a unified analysis of nonlinear and dissipative quantum effects near the attractors. By comparing our theoretical predictions with exact numerical simulations, we demonstrate the accuracy and utility of our proposed framework.

II. GENERAL THEORY

A. Model Hamiltonian

An extensive class of macroscopic physical systems, such as Josephson junctions and nanomechanical oscillators can be modeled by the Duffing oscillator in the presence of a periodic driving force, with the system Hamiltonian described by[42]

$$H_S(t) = \frac{p^2}{2m} + \frac{1}{2}m\Omega^2 x^2 - \gamma x^4 + F(t)x. \tag{1}$$

Here, parameter m (Ω) describes the mass (frequency) of the oscillator, γ gives the nonlinearity of the Duffing oscillator, and $F(t) = F_0(e^{i\nu t} + e^{-i\nu t})$ describes the periodical driving force with frequency ν. By switching to the rotating frame using the transformation $U(t) = \exp(-i\nu a^\dagger a t)$ with $a^\dagger$ (a) being the raising (lowering) operator and applying the rotating wave approximation (RWA), we obtain a time-independent Hamiltonian,

$$H = (\delta\omega + \chi)a^\dagger a + \chi(a^\dagger a)^2 + \epsilon(a^\dagger + a). \tag{2}$$

Here, parameter $\delta\omega = \hbar(\Omega - \nu)$ is the frequency detuning, $\chi = -3\gamma\hbar^2/2(m\Omega)^2$ is the scaled dimensionless nonlinearity, and $\epsilon = F_0\sqrt{\hbar/2m\Omega}$ is the scaled driving strength. We then introduce the position operator Q and momentum operator P in the rotating frame via

$$Q = \sqrt{\frac{\lambda}{2}}(a^\dagger + a), \quad P = i\sqrt{\frac{\lambda}{2}}(a^\dagger - a), \tag{3}$$

which satisfy the commutation relation

$$[Q, P] = i\lambda. \tag{4}$$

Here, the parameter $\lambda = -\chi/(4\Delta)$ is the dimensionless Planck constant that describes the quantumness of the system, i.e., the value of λ increases as the system approaches the quantum regime. Substituting operators Q and P back into the RWA Hamiltonian (2), we obtain

$$H/\Delta = \frac{1}{\lambda}\left(g + \frac{1}{4}\right) - \frac{1}{2} + \frac{\lambda}{4}, \tag{5}$$

where g is the quasienergy, given by

$$g = -(Q^2 + P^2 - 1)^2/4 + \sqrt{\beta}Q. \tag{6}$$

Here, the parameter $\beta = -f^2\chi/(2\Delta^3)$ is the scaled driving strength. Note that Eq. (6) is valid only for the soft nonlinearity $\chi > 0$. For the hard nonlinearity $\chi < 0$, the quasienergy is given by $g = (Q^2 + P^2 - 1)^2/4 - \sqrt{\beta}Q$.

B. Renormalized master equation

The characteristic behavior of the driven Duffing system is the *bistability* manifesting as two stable states: the low-amplitude state (LAS) and the high-amplitude state (HAS). As depicted in Fig. 1(a), these stable states correspond to the extrema in the quasienergy landscape, which are defined as the *attractors* in the phase space. The unstable state, known as the saddle point, is located on the separatrix, serving as the boundary dividing the basins of the attractors.

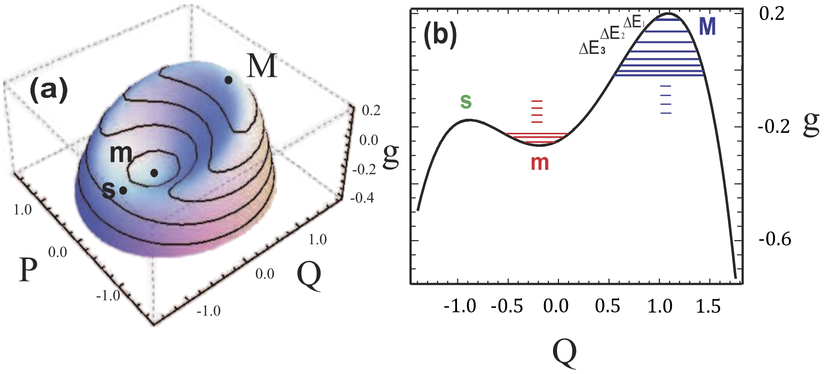

FIG. 1. (a) Quasienergy landscape in phase space of a driven Duffing oscillator. The extrema correspond to the high-amplitude stable state (M) and the low-amplitude stable state (m), while the saddle point (s) marks an unstable state. (b) Cross section of the quasienergy potential at $P = 0$. Quantum energy levels close to the maximum (M) and minimum (m) of the potential are depicted by blue and red lines, respectively. The unstable saddle point (s) is also indicated.

When the damping is present, the system evolves toward the nearby attractor if its initial state lies within the basin of the attractor. However, due to thermal noise, the system does not remain exactly on the attractor but forms a probability distribution within its basin of attraction. To describe the dissipative dynamics of our system, we employ the Lindblad form master equation,

$$\frac{d\rho}{dt} = -i[H,\rho] + \frac{\kappa}{2}\{(1+\bar{n})\mathcal{D}[a]\rho + \bar{n}\mathcal{D}[a^\dagger]\rho\}, \tag{7}$$

where $\mathcal{D}[\bullet]$ is the Lindblad operator defined as $\mathcal{D}[A]\rho \equiv 2A\rho A^\dagger - A^\dagger A\rho - \rho A^\dagger A$, $\bar{n}$ is the Bose–Einstein distribution, and κ is the damping strength.

To study the quantum dynamics near the bottom of each stable state, we first transform the system to the center of the attractor using the displacement operator,

$$D[\alpha] = e^{\alpha a^\dagger - \alpha^* a}, \tag{8}$$

with parameter α being a complex number. By defining the displaced density matrix $\tilde{\rho} = D[\alpha]^\dagger \rho D[\alpha]$, we obtain the following master equation:

$$\frac{d\tilde{\rho}}{dt} = -i\left[\tilde{H},\tilde{\rho}\right] + \frac{\kappa}{2}\{(1+\bar{n})\mathcal{D}[a]\tilde{\rho} + \bar{n}\mathcal{D}[a^\dagger]\tilde{\rho}\} + \left[\tilde{\alpha}^* a - \tilde{\alpha}a^\dagger, \tilde{\rho}\right], \tag{9}$$

with $\tilde{\alpha} = [\frac{1}{2}\kappa + i(\delta\omega + \chi + 2\chi|\alpha|^2)]\alpha + i\varepsilon$. By choosing α such that $\tilde{\alpha} = 0$, the master equation is simplified into

$$\frac{d\tilde{\rho}}{dt} = -[\tilde{H},\tilde{\rho}] + \frac{\kappa}{2}\{(1+\bar{n})\mathcal{D}[a]\tilde{\rho} + \bar{n}\mathcal{D}[a^\dagger]\tilde{\rho}\}, \tag{10}$$

with the renormalized Hamiltonian $\tilde{H}$ given by

$$\begin{aligned}\tilde{H} = {} & (\delta\omega + 4\chi|\alpha|^2)a^\dagger a + \chi(a^\dagger a)^2 + \chi(\alpha^{*2}a^2 + \alpha^2 a^{\dagger 2}) \\ & + 2\chi(\alpha a^{\dagger 2}a + \alpha^* a^\dagger a^2).\end{aligned} \tag{11}$$

We then introduce the squeezing operator

$$S(\xi) = e^{(\xi^* a^2 - \xi a^{\dagger 2})/2}, \tag{12}$$

which has the transformation property $S^\dagger a S = va + ua^\dagger$ with $v = \cosh(|\xi|)$ and $u = -\frac{|\xi|}{\xi}\sinh(|\xi|)$. By defining the squeezed density operator $\bar{\rho} = S^\dagger \tilde{\rho} S$, we transform the master equation of Eq. (10) into the following form:

$$\begin{aligned}\frac{d\bar{\rho}}{dt} = {} & -i[\bar{H},\bar{\rho}] + \frac{\kappa}{2}\{(1+\bar{N})\mathcal{D}[a]\bar{\rho} + \bar{N}\mathcal{D}[a^\dagger]\bar{\rho}\} \\ & + \frac{\kappa}{2}M(2a^\dagger\bar{\rho}a^\dagger - a^{\dagger 2}\bar{\rho} - \bar{\rho}a^{\dagger 2}) \\ & + \frac{\kappa}{2}M^*(2a\bar{\rho}a - a^2\bar{\rho} - \bar{\rho}a^2) - i[\bar{\xi}a^{\dagger 2} + \bar{\xi}^* a^2, \bar{\rho}],\end{aligned} \tag{13}$$

where $\bar{N} = \bar{n}|v|^2 + (1+\bar{n})|u|^2$ is the effective Bose distribution and $M = uv^*(2\bar{n}+1)$ is the squeezing number. The parameter $\bar{\xi}$ in the last term of Eq. (13) is given by

$$\bar{\xi} = [\delta\omega + 4\chi|\alpha|^2 + 2\chi(2|u|^2 + |v|^2)]v^* u + \chi(\alpha^{*2}u^2 + \alpha^2 v^{*2}).$$

By setting $\bar{\xi} = 0$, the renormalized master equation (13) is further simplified into

$$\begin{aligned}\frac{d\bar{\rho}}{dt} = {} & -i[\bar{H},\bar{\rho}] + \frac{\kappa}{2}\{(1+\bar{N})\mathcal{D}[a]\bar{\rho} + \bar{N}\mathcal{D}[a^\dagger]\bar{\rho}\} \\ & + \frac{\kappa}{2}M(2a^\dagger\bar{\rho}a^\dagger - a^{\dagger 2}\bar{\rho} - \bar{\rho}a^{\dagger 2}) + \frac{\kappa}{2}M^*(2a\bar{\rho}a - a^2\bar{\rho} - \bar{\rho}a^2).\end{aligned} \tag{14}$$

The final renormalized Hamiltonian $\bar{H}$ becomes

$$\bar{H} = \delta\bar{\omega}a^\dagger a + \bar{\chi}(a^\dagger a)^2 + 2\chi S^\dagger(\alpha a^{\dagger 2}a + \alpha^* a^\dagger a^2)S + \chi F, \tag{15}$$

with $F = 2(|v|^2 + |u|^2)(v^* u a^{\dagger 3}a + vu^* a^\dagger a^3) + (v^* u)^2 a^{\dagger 4} + (u^* v)^2 a^4$. The renormalized detuning $\delta\bar{\omega}$ and nonlinearity $\bar{\chi}$ are given by

$$\begin{cases}\delta\bar{\omega}/\delta\omega = (1 - 4\lambda|\alpha|^2)(|v|^2 + |u|^2) \\ \qquad\qquad -2\lambda(2|uv|^2 + |u|^4 + \alpha^{*2}uv + \alpha^2 u^* v^*), \\ \bar{\chi}/\delta\omega = -\lambda(|u|^4 + |v|^4 + 4|uv|^2),\end{cases} \tag{16}$$

with the displacement parameter α and the squeezing parameters u and v satisfying the following steady equations:

$$\begin{cases}0 = \left[\frac{\kappa}{2\delta\omega} + i(1 - \lambda - 2\lambda|\alpha|^2)\right]\alpha - i\sqrt{\frac{\beta}{2\lambda}}, \\ 0 = [1 - 4\lambda|\alpha|^2 - \lambda(4|u|^2 + 2|v|^2)]v^* u \\ \qquad -\lambda(\alpha^{*2}u^2 + \alpha^2 v^{*2}).\end{cases} \tag{17}$$

Here, we have introduced the dimensionless driving strength $\beta = 2\lambda(\varepsilon/\delta\omega)^2$.

C. Orders of perturbative parameters

To perform perturbation calculations for the renormalized Hamiltonian (15), we can choose the dimensionless Planck constant $\lambda = -\chi/(4\Delta)$ as the natural choice for the perturbation parameter. However, since the displacement parameter α is also a function of λ, it is subtle to properly organize the perturbative terms according to their respective orders. In fact, the Hamiltonian (15) should be written in different forms for different attractors. The stable state of the driven Duffing oscillator can be approximated as a coherent state $|\alpha\rangle$. By applying the variational principle in quantum mechanics, i.e., $\partial_\alpha\langle\alpha|H|\alpha\rangle = 0$, we obtain two solutions for the steady coherent number: a smaller one $|\alpha_l|^2 \approx \beta/(2\lambda)$ for the LAS and a larger one $|\alpha_h|^2 \approx 1/(2\lambda)$ for the HAS.

For the LAS, we sort the terms in the renormalized Hamiltonian (15) as follows:

$$\frac{\bar{H}^l}{\delta\omega} = h_0^l + \lambda h_\lambda^l + \beta h_\beta^l + \sqrt{\lambda\beta}h_{\lambda\beta}^l, \tag{18}$$

where the four terms on the right-hand side are given by

$$\begin{aligned} h_0^l &= (|v|^2 + |u|^2)a^\dagger a, \quad h_\lambda^l = -2(2|uv|^2 + |u|^4)a^\dagger a \\ &\quad - (|u|^4 + |v|^4 + 4|uv|^2)(a^\dagger a)^2 - F, \\ h_\beta^l &= -\frac{1}{\beta}[4\lambda|\alpha_l|^2(|v|^2 + |u|^2) + \lambda(2\alpha_l^{*2}uv + 2\alpha_l^2 u^* v^*)]a^\dagger a, \\ h_{\lambda\beta}^l &= -2\sqrt{\lambda/\beta}\, S^\dagger(\alpha_l a^{\dagger 2} a + \alpha_l^* a^\dagger a^2)S. \end{aligned} \tag{19}$$

Together with Eq. (17), we can now perform perturbative calculations near the bottom of the LAS. Given that the dimensionless driving strength β is also small, we consider the sum of the last three terms in the Hamiltonian of Eq. (18) as the perturbation term and calculate the desired quantities perturbatively.

For the HAS, as the coherent number $|\alpha_h|^2 \approx 1/(2\lambda)$ can be significantly large for $\lambda \ll 1$, a more careful sorting of the terms in the renormalized Hamiltonian of Eq. (15) is needed, along with the steady-state condition in Eq. (17), to ensure that terms of the same order are kept together. We introduce $\gamma = \sqrt{\lambda}$ as the perturbation parameter and rewrite the Hamiltonian as

$$\frac{\bar{H}^h}{\delta\omega} = h_0^h + \gamma h_1^h + \gamma h_2^h, \tag{20}$$

where the three terms on the right-hand side are

$$\begin{aligned} h_0^h &= [(1 - 4\lambda|\alpha_h|^2)(|v|^2 + |u|^2) - 2\lambda(\alpha_h^{*2}uv + \alpha_h^2 u^* v^*)]a^\dagger a, \\ h_1^h &= -\sqrt{\lambda}\, S^\dagger(2\alpha_h a^{\dagger 2} a + 2\alpha_h^* a^\dagger a^2 + \alpha_h a^\dagger + \alpha_h^* a)S, \\ h_2^h &= -2(2|uv|^2 + |u|^4)a^\dagger a - (|u|^4 + |v|^4 + 4|uv|^2)(a^\dagger a)^2 \\ &\quad - F - 2(2|u|^2 + |v|^2)(v^* u a^{\dagger 2} + u^* v a^2). \end{aligned} \tag{21}$$

To handle the perturbation orders coherently, we have rearranged the perturbation terms by removing those of order λ from the steady condition of Eq. (17) and incorporating them into the renormalized Hamiltonian. The coherent number α_h and u and v for the HAS are now determined by the revised steady condition

$$\begin{cases} \left[\dfrac{\kappa}{2\delta\omega} + i(1 - 2\lambda|\alpha_h|^2)\right]\alpha_h - i\sqrt{\dfrac{\beta}{2\lambda}} = 0, \\ (1 - 4\lambda|\alpha_h|^2)v^* u - \lambda(\alpha_h^{*2}u^2 + \alpha_h^2 v^{*2}) = 0. \end{cases}$$

The behavior near the bottom of the LAS is relatively simple and can be modeled using a harmonic oscillator. However, for the HAS, the nonlinear term $\chi(a^\dagger a)^2 \approx \chi|\alpha_h|^2$ becomes prominent, and the oscillator behaves as a highly squeezed coherent state. In Secs. III A and III B, we will apply our perturbative method to calculate the crucial quantities related to the HAS of the driven Duffing oscillator, namely, the level spacings, the orbital displacement, and the effective temperature in the vicinity of the HAS attractor.

III. RESULTS

A. Quantum dynamics of HAS

The quantum dynamics of the driven Duffing oscillator near the HAS attractor exhibit a rich interplay among nonlinearity, quantum fluctuations, and thermal noise. In this section, we discuss the quantum properties of the HAS using the renormalized master equation combined with a refined perturbation theory.

1. Level spacing

The nonlinear term $\chi(a^\dagger a)^2$ in the Hamiltonian, having the opposite sign to $\delta\omega$, results in a decrease in the level spacing $\Delta E_n = |E_{n+1} - E_n|$ as we approach the saddle point, as illustrated in Fig. 1(b). One can calculate the level spacings with standard perturbation theory by treating the sum of γh_1^h and γh_2^h in Eq. (20) as one perturbation term. However, it becomes a challenge to control the accuracy of the level spacings using the perturbative parameter. We find it necessary to distinguish between these two perturbative terms in the perturbation calculations to accurately determine the level spacing. To address this, we have developed a double perturbation theory framework that is particularly suited for the HAS Hamiltonian containing second-order small terms; see the details in Appendix A.

In Fig. 2, we compare our perturbation calculations with the exact numerical results obtained by diagonalizing the original Hamiltonian of Eq. (2). These results show an excellent agreement for energy levels near the bottom of the potential well. Under the zeroth-order perturbation approximation, the energy level spacing remains constant across all levels, similar to that of the harmonic oscillator. The second-order and fourth-order corrections provide accuracies up to $\gamma^2 = \lambda$ and $\gamma^4 = \lambda^2$, respectively. Higher-order perturbation calculations become necessary for levels farther from the bottom.

2. Orbital displacement

We denote the eigenstate of the renormalized Hamiltonian $\bar{H}$ as $|n'\rangle$, which is generally a superposition of harmonic oscillator eigenstates $|n'\rangle = |n\rangle + \sum_{k\neq n} \xi_{kn}|k\rangle$, where the superposition coefficients ξ_{kn} are provided in Appendix A. The eigenstate $|N\rangle$ of the original Hamiltonian (2) is related to that of the renormalized Hamiltonian

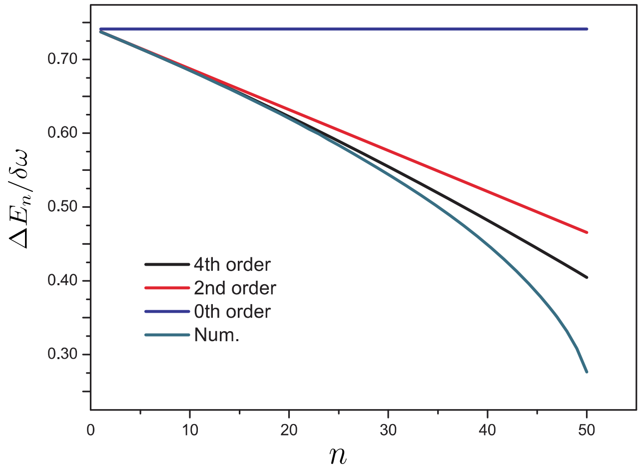

FIG. 2. Comparison of perturbation calculations and exact results for energy level spacing. The exact results (lowest curve) for level spacing $\Delta E_n = |E_{n+1} - E_n|$ are compared with the zeroth-order (constant spacing), the second-order (second highest line, $\gamma^2 = \lambda$) and the fourth-order (third highest line, $\gamma^4 = \lambda^2$) corrections. Excellent agreement is observed for low-level numbers near the potential well bottom, while higher-order corrections are required for large n. Parameters: $\lambda = 0.016$ and $\beta = 4/75$.

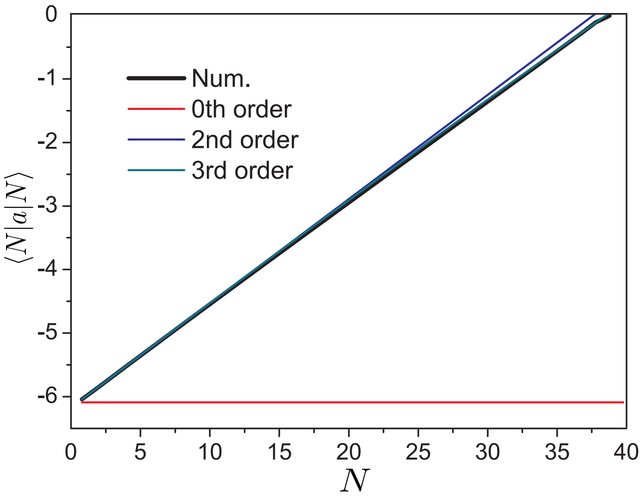

FIG. 3. Orbital displacement. The average position $\langle N|a|N\rangle$ of the energy level N illustrates the shift due to the quantum fluctuation. Under the harmonic approximation, $\langle N|a|N\rangle$ is a constant for every level (lowest line). Considering higher-order corrections, we observe changes in $\langle N|a|N\rangle$ across levels. Compared with the second-order perturbation result (highest line), the third-order result (second highest line) already aligns well with the exact one (bold line).

(15) via the relationship $|N\rangle = DS|n'\rangle$. The matrix element $\langle N|a|M\rangle$ for different levels $|N\rangle$ and $|M\rangle$ is then given by

$$\begin{aligned}\langle N|a|M\rangle &= \langle n'|S^{\dagger}D^{\dagger}aDS|m'\rangle = \langle n'|(va+u^{\dagger}+\alpha)|m'\rangle\\ &= v\langle n'|a|m'\rangle + u\langle m'|a|n'\rangle^{*} + \alpha\langle n'|m'\rangle. \end{aligned}\tag{22}$$

The matrix element $\langle N|a|N\rangle$ provides insight into the orbital displacement in the phase space. Under the harmonic approximation ($\xi_{kn}=0$), $\langle N|a|N\rangle$ remains a constant α for all levels. However, considering higher-order corrections, the orbital displacement $\langle N|a|N\rangle$ changes with the energy level, as depicted in Fig. 3. The perturbation results agree well with numerical calculations.

3. Effective temperature

Next, we calculate the stationary distribution over the levels of the HAS and the effective temperature near the bottom. It is important to note that the annihilation operator a is for the Fock state $|N\rangle$, which decreases the Fock state from a higher level to the next lower level $a|N\rangle = \sqrt{N}|N-1\rangle$. However, in our case, the eigenstate of quasienergy $|n\rangle$ is the superposition of Fock states $|N\rangle$. As a result, the annihilation operator a can either decrease or increase the state $|n\rangle$ even at zero temperature.

Under the assumption of weak damping ($\kappa \ll E_n - E_{n+1}$), the off-diagonal matrix elements on the state $|n\rangle$ are very small. Thus, we can only keep the diagonal elements. Here, we assume that the stationary density matrix is diagonal and denote the diagonal terms as $p_{n'} = \langle n'|\rho|n'\rangle$. The master equation (15) can be simplified into a balance equation,[43]

$$\frac{dp_{n'}}{dt} = \kappa\sum_{m'}\left(W_{n',m'}p_{m'} - W_{m',n'}p_{n'}\right),\tag{23}$$

where the transition rate from level $|m'\rangle$ to level $|n'\rangle$ ($m' \neq n'$) is given by

$$\begin{aligned}W_{n',m'} &= M\langle m'|a|n'\rangle^{*}\langle n'|a|m'\rangle^{*} + M^{*}\langle m'|a|n'\rangle\langle n'|a|m'\rangle\\ &\quad + (1+\bar{N})|\langle n'|a|m'\rangle|^{2} + \bar{N}|\langle m'|a|n'\rangle|^{2}.\end{aligned}\tag{24}$$

One can prove that the transition rate $W_{n',m'}$ for $n' \neq m'$ is equal to $|\langle N|a|M\rangle|^{2}$ calculated above in Eq. (22).

As can be seen from the above rate equation, even at zero temperature, the oscillator can make transitions to both lower and higher energy levels. In Fig. 4, we compare the stationary distribution obtained using our double perturbation theory with exact numerical results. To the lowest order, all superposition coefficients are zero. To the first order of $\sqrt{\lambda}$ (i.e., $\xi_{kn} = \sqrt{\lambda}\xi_{kn}^{(1)}$), there is no correction to the stationary distribution $p_{n'}$. Then, to the second order (i.e., $\xi_{kn} = \sqrt{\lambda}\xi_{kn}^{(1)} + \lambda\xi_{kn}^{(2)}$), we solve the balance equation (23) accordingly. Figure 4(b) illustrates the relative error $\Delta p_n/p_n$ in comparison with the exact numerical results, which shows that the discrepancy for low levels is mitigated by high-order perturbative calculations.

In the vicinity of the bottom, we can apply the harmonic approximation ($\xi_{kn}=0$). Under this approximation, the ratio of probabilities over adjacent levels is

$$\frac{p_{n'+1}}{p_{n'}} = \frac{W_{n'+1,n'}}{W_{n',n'+1}} = \frac{\bar{N}}{1+\bar{N}} = \frac{\bar{n}|v|^{2} + (1+\bar{n})|u|^{2}}{1+\bar{n}|v|^{2} + (1+\bar{n})|u|^{2}}.\tag{25}$$

We verify the relationship between $\ln(p_1/p_2)$ and the Bose distribution $\bar{n}$ in Fig. 5. The agreement between the analytical results from Eq. (25) and the exact numerical one is excellent.

For high levels, we can define the level-dependent effective temperature via

$$N_{eff}(n) \equiv p_{n+1}/(p_n - p_{n+1})$$

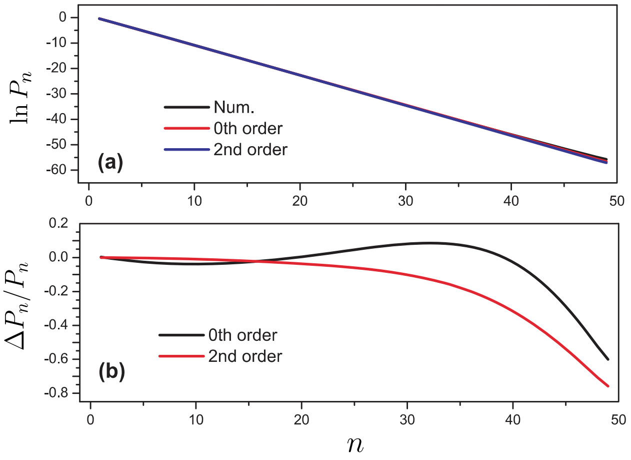

FIG. 4. Comparison of stationary probability distributions. (a) Comparison of the stationary probability distribution obtained through perturbation theory to zeroth-order (red line), second-order (blue line), and exact numerical simulations (black line). (b) Relative error $\Delta p_n/p_n$ in the stationary distribution obtained from perturbation theory compared to numerical results. The discrepancy increases for higher levels but remains less than 1.

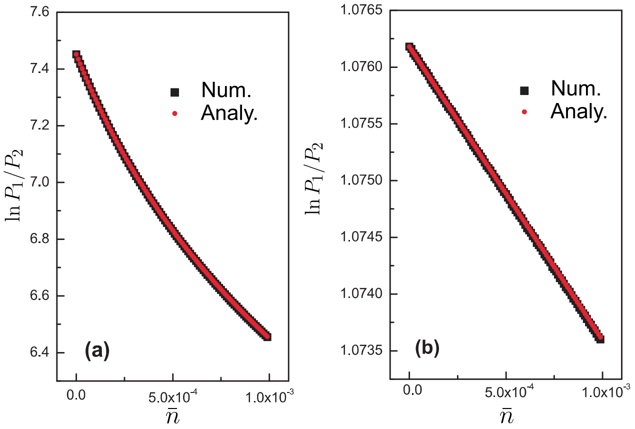

FIG. 5. Ratio of probabilities for the lowest levels in (a) the LAS and (b) HAS, plotted as a function of the Bose distribution $\bar{n}$. The agreement between the analytical results (black square dots) and the exact numerical results (red circle dots) is excellent.

for level $|n\rangle$. Figure 6 illustrates how N_{eff} varies from the lowest to higher levels. The zero-order term yields a constant effective temperature. When we include the correction up to the order of λ, the correction leads to changes in N_{eff}, showing a good agreement with the numerical results for levels near the bottom.

B. Strong damping and dephasing

In this section, we explore the dynamics and the stationary state of the system under conditions of strong damping and dephasing, which can significantly alter the behavior predicted by the weak damping approximation.

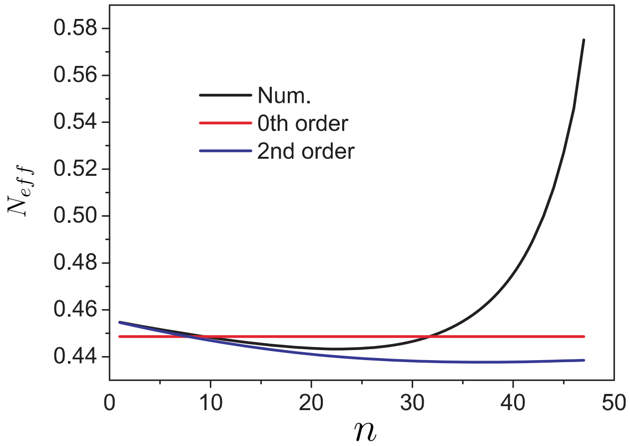

FIG. 6. Effective temperature of energy levels. The stationary probability distributions $N_{eff}(n)$ of level $|n\rangle$ obtained through perturbation theory to zeroth order (red line) and second order (blue line) are compared with the exact numerical simulations (black line). The zero-order effective temperature term gives a constant effective temperature. The second-order term results in changes in $N_{eff}(n)$, which are quite accurate for levels near the bottom.

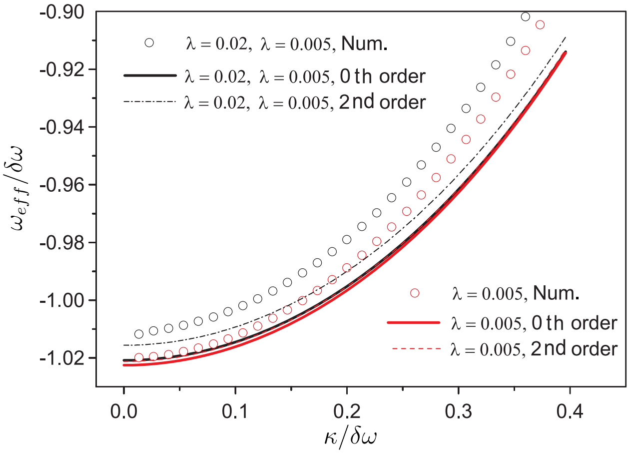

FIG. 7. Relationship between effective frequency $\omega_{eff} = \Delta E_1$ and damping strength κ. Results obtained from the emission spectrum method (circles), cf. Eq. (26), are compared with those from our perturbation theory (solid and dashed lines).

1. Strong damping

In the regime of strong damping, the harmonic approximation, which leads to the level spacing ΔE_n that is independent of damping, is no longer valid. Instead, the level spacing undergoes slight renormalization for strong damping. Such an effect can be observed through the emission spectrum $S(\omega)$, which represents the spectral density of photons emitted by the driven resonator and is given by

$$S(\omega) = 2\mathrm{Re}\int_0^\infty e^{-i\omega t}\,\mathrm{Tr}\,[a^\dagger e^{\mathcal{L}t}(a\rho_{\mathrm{st}})]\mathrm{d}t. \tag{26}$$

Our method inherently incorporates damping effects into the calculation of ΔE_n. For finite damping, the squeezing parameters u and v are complex numbers, determined by the steady-state conditions given in Eq. (22). Substituting these parameters into Eq. (20), we obtain the effective frequency $\omega_{eff} = \Delta E_1$. In Fig. 7, we compare the results obtained through the emission spectrum of Eq. (26) with those from our perturbation theory, demonstrating satisfactory consistency. The minor discrepancy arises primarily from higher-level spacings $\Delta E_n(n > 1)$, which are generally smaller than the first-level spacing ΔE_1. For more accurate results, the average of all level spacings should be considered in the calculations.

2. Dephasing

To incorporate dephasing, we introduce the dephasing term $\eta^{ph}\mathcal{D}[a^\dagger a]\rho$ into the master equation (7). For convenience, we define a generalized Lindblad operator $\mathcal{L}[A;B]\rho \equiv 2A\rho B - BA\rho - \rho AB$. In the spirit of the rotating wave approximation, we obtain the renormalized master equation for the displaced and squeezed density operator $\bar{\rho} = S^\dagger D^\dagger \rho D S$ (see the detailed derivation in Appendix B),

$$\begin{aligned}\frac{d\bar{\rho}}{dt} &= -i[\bar{H},\bar{\rho}] + \frac{\kappa}{2}\{(1+\tilde{N})\mathcal{D}[a]\bar{\rho} + \tilde{N}\mathcal{D}[a^\dagger]\bar{\rho}\} + \frac{\kappa}{2}M\,\mathcal{L}[a^\dagger;a^\dagger]\bar{\rho}\\ &\quad + \frac{\kappa}{2}M^*\,\mathcal{L}[a;a]\bar{\rho} + \eta^{ph}(|v|^2+|u|^2)^2\mathcal{D}[a^\dagger a]\bar{\rho}\\ &\quad + \eta^{ph}|uv|^2(\mathcal{D}[a^{\dagger 2}]\bar{\rho} + \mathcal{D}[a^2]\bar{\rho}),\end{aligned} \tag{27}$$

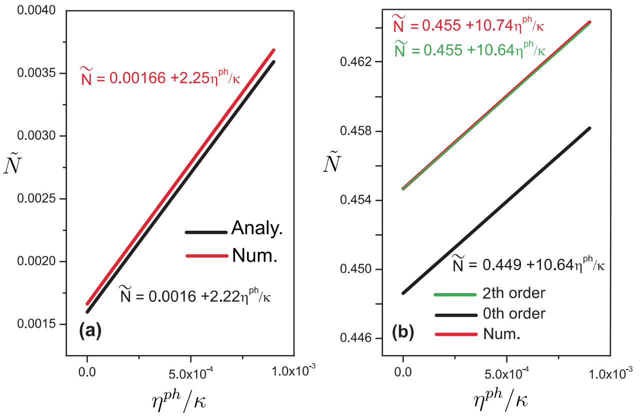

FIG. 8. Renormalized effective Bose distribution $\tilde{N}$ due to dephasing effects for (a) the LAS and (b) the HAS. We compare theoretical predictions from Eq. (28) with the exact numerical results and extract the linear relationships.

where the renormalized Bose distribution, affected by dephasing, is given by

$$\tilde{N} = \bar{N} + \frac{\eta^{ph}}{\kappa}|\alpha^* u + \alpha v^*|^2 = |u|^2 + \bar{n}(|u|^2 + |v|^2) + \frac{\eta^{ph}}{\kappa}|\alpha^* u + \alpha v^*|^2. \tag{28}$$

We verify our predictions for the renormalized Bose distribution by comparing them with exact numerical simulations according to the probabilities over the two lowest levels, specifically, $\tilde{N} = p_2/(p_1 - p_2)$. In Fig. 8, we plot and extract the renormalized Bose distribution as a function of dephasing, which demonstrates an excellent agreement between the numerical results and the analytical predictions given by Eq. (28) for both LAS and HAS.

IV. CONCLUSIONS

In this work, we have investigated the quantum dissipative dynamics of a driven Duffing oscillator near the bottoms of its stable states. We elucidated the intricate interplay among the nonlinearity, quantum fluctuations, and the influence of an external driving field. We formulated an effective quantum master equation that encompasses quantum and thermal fluctuations, strong damping, and dephasing within a unified framework. We have developed a refined perturbation approach to analyze the quantum dynamics near both the LAS and the HAS of the Duffing oscillator. While the LAS behavior can be approximated using a harmonic oscillator model, the HAS exhibits more complex behavior owing to significant nonlinear terms. Because of quantum fluctuations, even at zero temperature, higher energy levels near the bottom of the potential well are excited. We calculated the level spacing and effective temperature near the bottom of the HAS and compared them with numerical simulations, demonstrating the accuracy and utility of our proposed approach.

We also investigated the effects of strong damping and dephasing on the system's dynamics. We showed that the level spacing undergoes slight renormalization for strong damping, which can be observed through the emission spectrum. We derived the renormalized quantum master equation and analyzed the system's behavior affected by dephasing. Our work provides new insights into the quantum dynamics of driven Duffing oscillators, particularly near their stable states, and offers a theoretical framework that can be applied to related quantum systems under strong damping and dephasing conditions.

ACKNOWLEDGMENTS

This work was supported by the Natural Science Foundation of China (Grant No. 12475025).

AUTHOR DECLARATIONS

Conflict of Interest

The authors have no conflicts to disclose.

Author Contributions

The two authors contributed equally to this work.

Wei Feng: Conceptualization (equal); Data curation (equal); Formal analysis (equal); Funding acquisition (equal); Investigation (equal); Methodology (equal); Project administration (equal); Resources (equal); Software (equal); Supervision (equal); Validation (equal); Visualization (equal); Writing – original draft (equal); Writing – review & editing (equal). **Lingzhen Guo**: Conceptualization (equal); Data curation (equal); Formal analysis (equal); Funding acquisition (equal); Investigation (equal); Methodology (equal); Project administration (equal); Resources (equal); Software (equal); Supervision (equal); Validation (equal); Visualization (equal); Writing – original draft (equal); Writing – review & editing (equal).

DATA AVAILABILITY

The data that support the findings of this study are available within the article.

APPENDIX A: DOUBLE PERTURBATION THEORY

To effectively address Hamiltonians containing second-order perturbation terms, exemplified by the HAS in the driven Duffing oscillator, we develop a framework for double perturbation theory. This theory is specifically designed for systems where treating the second-order terms independently is essential for maintaining computational precision and obtaining physically meaningful results. Consider a Hamiltonian of the general form,

$$H = H_0 + \gamma H_1 + \gamma^2 H_2, \tag{A1}$$

where γ is a small parameter. In conventional perturbation theory, the terms $\gamma H_1 + \gamma^2 H_2$ are often treated as a single perturbation term. However, for the HAS of the driven Duffing system, this approach does not yield results with the necessary accuracy. Therefore, we introduce the concept of double perturbation theory, where the terms are handled separately.

The eigenvalues and eigenstates of H_0 are denoted as $\epsilon_n^{(0)}$ and $|\psi_n^{(0)}\rangle$, respectively, satisfying $H_0|\psi_n^{(0)}\rangle = \epsilon_n^{(0)}|\psi_n^{(0)}\rangle$. The exact eigenvalues and eigenstates of H are denoted as ϵ_n and $|\psi_n\rangle$, which can be expanded in powers of γ as

$$\begin{aligned}\epsilon_n &= \epsilon_n^{(0)} + \gamma\epsilon_n^{(1)} + \gamma^2\epsilon_n^{(2)} + \gamma^3\epsilon_n^{(3)} + \gamma^4\epsilon_n^{(4)} + o(\gamma^5),\\ |\psi_n\rangle &= |\psi_n^{(0)}\rangle + \gamma\sum_{k\neq n}\xi_{kn}^{(1)}|\psi_k^{(0)}\rangle + \gamma^2\sum_{l\neq n}\xi_{\mathrm{ln}}^{(2)}|\psi_l^{(0)}\rangle\\ &\quad + \gamma^3\sum_{m\neq n}\xi_{mn}^{(3)}|\psi_m^{(0)}\rangle + \gamma^4\sum_{p\neq n}\xi_{pn}^{(4)}|\psi_p^{(0)}\rangle + o(\gamma^5).\end{aligned} \tag{A2}$$

From the eigenvalue equation $H|\psi_n\rangle = \epsilon_n|\psi_n\rangle$, we can derive the following perturbative results order by order:

(1) to the order of $\gamma^0 = 1$: $H_0|\psi_n^{(0)}\rangle = \epsilon_n^{(0)}|\psi_n^{(0)}\rangle$;
(2) to the order of γ:

$$\gamma\left(\sum_{k\neq n}\epsilon_k^{(0)}\xi_{kn}^{(1)}|\psi_k^{(0)}\rangle + H_1|\psi_n^{(0)}\rangle\right) = \gamma\left(\sum_{k\neq n}\epsilon_n^{(0)}\xi_{kn}^{(1)}|\psi_k^{(0)}\rangle + \epsilon_n^{(1)}|\psi_n^{(0)}\rangle\right), \tag{A3}$$

which gives us the perturbative result to the first order,

$$\epsilon_n^{(1)} = \langle\psi_n^{(0)}|H_1|\psi_n^{(0)}\rangle,\ \xi_{kn}^{(1)} = \frac{1}{\epsilon_n^{(0)} - \epsilon_k^{(0)}}\langle\psi_k^{(0)}|H_1|\psi_n^{(0)}\rangle; \tag{A4}$$

(3) to the order of γ^2:

$$\begin{aligned}&\gamma^2\left(\sum_{l\neq n}\epsilon_l^{(0)}\xi_{\mathrm{ln}}^{(2)}|\psi_l^{(0)}\rangle + \sum_{k\neq n}\xi_{kn}^{(1)}H_1|\psi_k^{(0)}\rangle + H_2|\psi_n^{(0)}\rangle\right)\\ &\quad = \gamma^2\left(\sum_{l\neq n}\epsilon_n^{(0)}\xi_{\mathrm{ln}}^{(2)}|\psi_l^{(0)}\rangle + \sum_{k\neq n}\xi_{kn}^{(1)}\epsilon_n^{(1)}|\psi_k^{(0)}\rangle + \epsilon_n^{(2)}|\psi_n^{(0)}\rangle\right),\end{aligned} \tag{A5}$$

which gives us the second-order perturbative result,

$$\begin{aligned}\epsilon_n^{(2)} &= \sum_{k\neq n}\langle\psi_n^{(0)}|H_1|\psi_k^{(0)}\rangle\xi_{kn}^{(1)} + \langle\psi_n^{(0)}|H_2|\psi_n^{(0)}\rangle,\\ \xi_{\mathrm{ln}}^{(2)} &= \frac{1}{\epsilon_n^{(0)} - \epsilon_l^{(0)}}\Bigg(\sum_{k\neq n}\langle\psi_l^{(0)}|H_1|\psi_k^{(0)}\rangle\xi_{kn}^{(1)}\\ &\quad + \langle\psi_l^{(0)}|H_2|\psi_n^{(0)}\rangle - \epsilon_n^{(1)}\xi_{\mathrm{ln}}^{(1)}\Bigg);\end{aligned} \tag{A6}$$

(4) to the order of γ^3:

$$\begin{aligned}&\gamma^3\left(\sum_{m\neq n}\epsilon_m^{(0)}\xi_{mn}^{(3)}|\psi_m^{(0)}\rangle + \sum_{l\neq n}\xi_{\mathrm{ln}}^{(2)}H_1|\psi_l^{(0)}\rangle + \sum_{k\neq n}\xi_{kn}^{(1)}H_2|\psi_k^{(0)}\rangle\right)\\ &\quad = \gamma^3\Bigg(\sum_{m\neq n}\epsilon_n^{(0)}\xi_{mn}^{(3)}|\psi_m^{(0)}\rangle + \sum_{l\neq n}\epsilon_n^{(1)}\xi_{\mathrm{ln}}^{(2)}|\psi_l^{(0)}\rangle\\ &\quad + \sum_{k\neq n}\xi_{kn}^{(1)}\epsilon_n^{(2)}|\psi_k^{(0)}\rangle + \epsilon_n^{(3)}|\psi_n^{(0)}\rangle\Bigg),\end{aligned} \tag{A7}$$

which gives us the following perturbative result to the third order:

$$\begin{aligned}\epsilon_n^{(3)} &= \sum_{l\neq n}(\langle\psi_n^{(0)}|H_1|\psi_l^{(0)}\rangle\xi_{\mathrm{ln}}^{(2)} + \langle\psi_n^{(0)}|H_2|\psi_l^{(0)}\rangle\xi_{\mathrm{ln}}^{(1)}),\\ \xi_{mn}^{(3)} &= \frac{1}{\epsilon_n^{(0)} - \epsilon_m^{(0)}}\Bigg[\sum_{l\neq n}\Big(\langle\psi_m^{(0)}|H_1|\psi_l^{(0)}\rangle\xi_{\mathrm{ln}}^{(2)}\\ &\quad + \langle\psi_m^{(0)}|H_2|\psi_l^{(0)}\rangle\xi_{\mathrm{ln}}^{(1)}\Big) - \epsilon_n^{(1)}\xi_{mn}^{(2)} - \epsilon_n^{(2)}\xi_{mn}^{(1)}\Bigg];\end{aligned} \tag{A8}$$

and (5) to the order of γ^4:

$$\begin{aligned}&\gamma^4\left(\sum_{p\neq n}\epsilon_p^{(0)}\xi_{pn}^{(4)}|\psi_p^{(0)}\rangle + \sum_{m\neq n}\xi_{mn}^{(3)}H_1|\psi_m^{(0)}\rangle + \sum_{l\neq n}\xi_{\mathrm{ln}}^{(2)}H_2|\psi_l^{(0)}\rangle\right)\\ &\quad = \gamma^4\Bigg[\sum_{m\neq n}(\epsilon_n^{(0)}\xi_{mn}^{(4)} + \epsilon_n^{(1)}\xi_{mn}^{(3)} + \xi_{mn}^{(2)}\epsilon_n^{(2)} + \xi_{mn}^{(1)}\epsilon_n^{(3)})|\psi_m^{(0)}\rangle\\ &\quad + \epsilon_n^{(4)}|\psi_n^{(0)}\rangle\Bigg],\end{aligned} \tag{A9}$$

which gives us the following fourth order perturbative result:

$$\begin{aligned}\epsilon_n^{(4)} &= \sum_{l\neq n}(\langle\psi_n^{(0)}|H_1|\psi_l^{(0)}\rangle\xi_{\mathrm{ln}}^{(3)} + \langle\psi_n^{(0)}|H_2|\psi_l^{(0)}\rangle\xi_{\mathrm{ln}}^{(2)}),\\ \xi_{pn}^{(4)} &= \frac{1}{\epsilon_n^{(0)} - \epsilon_p^{(0)}}\Bigg[\sum_{l\neq n}(\langle\psi_p^{(0)}|H_1|\psi_l^{(0)}\rangle\xi_{\mathrm{ln}}^{(3)} + \langle\psi_p^{(0)}|H_2|\psi_l^{(0)}\rangle\xi_{\mathrm{ln}}^{(2)})\\ &\quad - \epsilon_n^{(1)}\xi_{pn}^{(3)} - \epsilon_n^{(2)}\xi_{pn}^{(2)} - \epsilon_n^{(3)}\xi_{pn}^{(1)}\Bigg].\end{aligned} \tag{A10}$$

Similar expressions can be derived for higher-order corrections.

For the high-amplitude state of the driven Duffing oscillator, the perturbative Hamiltonian is given by Eq. (20),

$$\frac{\bar{H}^h}{\delta\omega} = h_0^h + \gamma h_1^h + \gamma h_2^h, \tag{A11}$$

where the order parameter γ is $\sqrt{\lambda}$. The zeroth-order Hamiltonian

$$h_0^h = [(1 - 4\lambda|\alpha_h|^2)(|v|^2 + |u|^2) - 2\lambda(\alpha_h^{*2}uv + \alpha_h^2u^*v^*)]a^\dagger a \tag{A12}$$

corresponds to a harmonic oscillator, and the eigenstates $|\psi_k^{(0)}\rangle$ are simply the harmonic oscillator states $|k\rangle$ with eigenvalues

$$\epsilon_k^{(0)} = k[(1 - 4\lambda|\alpha_h|^2)(|v|^2 + |u|^2) - 2\lambda(\alpha_h^{*2}uv + \alpha_h^2u^*v^*)]. \tag{A13}$$

By calculating the matrix elements $\langle l|h_1^h|k\rangle$ and $\langle l|h_2^h|k\rangle$,

$$\begin{aligned}\langle l|h_1^h|k\rangle &= -2\sqrt{\lambda k}[\alpha_h|v|^2u^*(2k-1)+\alpha_h|u|^2u^*(k+1)+\alpha_h^*v|u|^2(2k+1)+\alpha_h^*v|v|^2(k-1)+(\alpha_h^*v+\alpha_hu^*)/2]\delta_{l,k-1}\\ &\quad -2\sqrt{\lambda(k+1)}[\alpha_h|u|^2v^*(2k+3)+\alpha_h|v|^2v^*k+\alpha_h^*u|v|^2(2k+1)+\alpha_h^*u|u|^2(k+2)+(\alpha_h^*u+\alpha_hv^*)/2]\delta_{l,k+1}\\ &\quad -2u^*v\sqrt{\lambda k(k-1)(k-2)}(\alpha_h^*v+\alpha_hu^*)\delta_{l,k-3}-2v^*u\sqrt{\lambda(k+1)(k+2)(k+3)}(\alpha_h^*u+\alpha_hv^*)\delta_{l,k+3},\\ \langle l|h_2^h|k\rangle &= -[2(2|uv|^2+|u|^4)k+(|u|^4+|v|^4+4|uv|^2)k^2]\delta_{l,k}-2u^*v\sqrt{k(k-1)}[k|u|^2+(k-1)|v|^2]\delta_{l,k-2}\\ &\quad -2v^*u\sqrt{(k+1)(k+2)}[(k+2)|u|^2+(k+1)|v|^2]\delta_{l,k+2}-(u^*v)^2\sqrt{k(k-1)(k-2)(k-3)}\delta_{l,k-4}\\ &\quad -(v^*u)^2\sqrt{(k+1)(k+2)(k+3)(k+4)}\delta_{l,k+4},\end{aligned}\tag{A14}$$

we can apply the double perturbation theory to obtain the desired perturbative results, such as level spacing and effective temperature, for the high-amplitude state, as detailed in the main text.

APPENDIX B: DEPHASING

This section presents the derivation of Eq. (27) in the main text. To incorporate dephasing, we introduce the dephasing term $\eta^{ph}\mathcal{D}[a^\dagger a]\rho$ into the master equation. For convenience, we define a generalized Lindblad operator $\mathcal{L}[A;B]\rho \equiv 2A\rho B - BA\rho - \rho AB$, which satisfies

$$\begin{aligned}\mathcal{D}[A]\rho &= \mathcal{L}[A;A^\dagger]\rho,\\ \mathcal{D}[A+B]\rho &= \mathcal{D}[A]\rho+\mathcal{D}[B]\rho+\mathcal{L}[A;B^\dagger]\rho+\mathcal{L}[B;A^\dagger]\rho,\\ \mathcal{L}[A;B+C]\rho &= \mathcal{L}[A;B]\rho+\mathcal{L}[A;C]\rho,\\ \mathcal{L}[A+B;C]\rho &= \mathcal{L}[A;C]\rho+\mathcal{L}[B;C]\rho,\\ (\mathcal{L}[A;B]\rho)^\dagger &= \mathcal{L}[B^\dagger;A^\dagger]\rho.\end{aligned}\tag{B1}$$

Utilizing these properties, we derive the transformed dephasing term under the action of the displacement and squeezing operators,

$$\begin{aligned}S^\dagger D^\dagger(\mathcal{D}[a^\dagger a]\rho)DS &= (|v|^2+|u|^2)^2\mathcal{D}[a^\dagger a]\bar\rho + |\alpha^*u+\alpha v^*|^2\Big(\mathcal{D}[a^\dagger]\bar\rho\\ &\quad + \mathcal{D}[a]\bar\rho\Big)+|uv|^2(\mathcal{D}[a^{\dagger 2}]\bar\rho+\mathcal{D}[a^2]\bar\rho)\\ &\quad + \mathcal{L}\bar\rho+(\mathcal{L}\bar\rho)^\dagger.\end{aligned}\tag{B2}$$

The term $\mathcal{L}\bar\rho$ includes various higher-order terms,

$$\begin{aligned}\mathcal{L}\bar\rho &= |uv|^2\mathcal{L}[a^{\dagger 2};a^{\dagger 2}]\bar\rho+|\alpha^*u+\alpha v^*|^2\mathcal{L}[a^\dagger;a^\dagger]\bar\rho\\ &\quad + v^*u(\alpha^*u+\alpha v^*)\mathcal{L}[a^{\dagger 2};a^\dagger]\bar\rho+vu^*(\alpha u^*+\alpha^*v)\mathcal{L}[a;a^2]\bar\rho\\ &\quad + v^*u(\alpha u^*+\alpha^*v)\mathcal{L}[a;a^{\dagger 2}]\bar\rho+vu^*(\alpha^*u+\alpha v^*)\mathcal{L}[a^2;a^\dagger]\bar\rho\\ &\quad + (|v|^2+|u|^2)\Big\{v^*u\mathcal{L}[a^\dagger a;a^{\dagger 2}]\bar\rho+vu^*\mathcal{L}[a^\dagger a;a^2]\bar\rho\\ &\quad + (\alpha^*u+\alpha v^*)\mathcal{L}[a^\dagger;a^\dagger a]\bar\rho+(\alpha u^*+\alpha^*v)\mathcal{L}[a;a^\dagger a]\bar\rho\Big\}.\end{aligned}\tag{B3}$$

In the spirit of the rotating wave approximation, we neglect the terms $\mathcal{L}\bar\rho$ and $(\mathcal{L}\bar\rho)^\dagger$ in Eq. (B2). Adding the dephasing term to the renormalized master equation, we obtain

$$\begin{aligned}\frac{d\bar\rho}{dt} &= -i[\bar H,\bar\rho]+\frac{\kappa}{2}\{(1+\tilde N)\mathcal{D}[a]\bar\rho+\tilde N\mathcal{D}[a^\dagger]\bar\rho\}+\frac{\kappa}{2}M\mathcal{L}[a^\dagger;a^\dagger]\bar\rho\\ &\quad +\frac{\kappa}{2}M^*\mathcal{L}[a;a]\bar\rho+\eta^{ph}(|v|^2+|u|^2)^2\mathcal{D}[a^\dagger a]\bar\rho\\ &\quad +\eta^{ph}|uv|^2(\mathcal{D}[a^{\dagger 2}]\bar\rho+\mathcal{D}[a^2]\bar\rho),\end{aligned}\tag{B4}$$

where the renormalized Bose distribution, affected by dephasing, is given by

$$\begin{aligned}\tilde N = \bar N+\frac{\eta^{ph}}{\kappa}|\alpha^*u+\alpha v^*|^2 &= |u|^2+\bar n(|u|^2+|v|^2)\\ &\quad +\frac{\eta^{ph}}{\kappa}|\alpha^*u+\alpha v^*|^2.\end{aligned}\tag{B5}$$

REFERENCES

[1] G. Duffing, "Erzwungene Schwingungen bei veränderlicher Eigenfrequenz und ihre technische Bedeutung," Ing.-Arch. **8**, 445 (1918).

[2] M. I. Dykman, *Fluctuating Nonlinear Oscillators: From Nanomechanics to Quantum Superconducting Circuits* (Oxford University Press, 2012).

[3] A. N. Cleland and M. L. Roukes, "Noise processes in nanomechanical resonators," J. Appl. Phys. **92**, 2758 (2002).

[4] R. Lifshitz and M. C. Cross, *Nonlinear Dynamics of Nanomechanical and Micromechanical Resonators* (Wiley Meinheim Press, 2008).

[5] M. Poot and H. S. J. van der Zant, "Mechanical systems in the quantum regime," Phys. Rep. **511**, 273 (2012).

[6] K. A. Krok, A. P. Durajski, and R. Szczęśniak, "The Abraham–Lorentz force and the time evolution of a chaotic system: The case of charged classical and quantum Duffing oscillators," Chaos **32**, 073130 (2022).

[7] P. K. Ghosh and P. Roy, "On regular and chaotic dynamics of a non-*PT*-symmetric Hamiltonian system of a coupled Duffing oscillator with balanced loss and gain," J. Phys. A: Math. Theor. **53**, 475202 (2020).

[8] J. Zhang, Y.-X. Liu, Ş. K. Özdemir, R.-B. Wu, F. Gao, X.-B. Wang, L. Yang, and F. Nori, "Quantum internet using code division multiple access," Sci. Rep. **3**, 2211 (2013).

[9] J. Choi, H. Hwang, and E. Kim, "Measurement-induced bistability in the excited state of a transmon," Phys. Rev. Appl. **22**, 054069 (2024).

[10] T. K. Mavrogordatos, G. Tancredi, M. Elliott, M. J. Peterer, A. Patterson, J. Rahamim, P. J. Leek, E. Ginossar, and M. H. Szymańska, "Simultaneous bistability of a qubit and resonator in circuit quantum electrodynamics," Phys. Rev. Lett. **118**, 040402 (2017).

[11] M. Boissonneault, J. M. Gambetta, and A. Blais, "Improved superconducting qubit readout by qubit-induced nonlinearities," Phys. Rev. Lett. **105**, 100504 (2010).

[12] P. Del'Haye, A. Schliesser, O. Arcizet, T. Wilken, R. Holzwarth, and T. J. Kippenberg, "Optical frequency comb generation from a monolithic microresonator," Nature **450**, 1214 (2007).

[13] T. J. Kippenberg, R. Holzwarth, and S. A. Diddams, "Microresonator-based optical frequency combs," Science **332**, 555 (2011).

[14] P. D. Drummond and M. Hillery, *The Quantum Theory of Nonlinear Optics* (Cambridge University Press, 2014).

[15] E. Bolandhemmat and F. Kheirandish, "Quantum dynamics of a driven parametric oscillator in a Kerr medium," Sci. Rep. **13**, 9056 (2023).

[16] F. Hellbach, D. De Bernardis, M. Saur, I. Carusotto, W. Belzig, and G. Rastelli, "Nonlinearity-induced symmetry breaking in a system of two parametrically driven Kerr-Duffing oscillators," New J. Phys. **26**, 103020 (2024).

[17] D. R. K. Massembele, P. Djorwé, A. K. Sarma, A.-H. Abdel-Aty, and S. G. N. Engo, "Quantum entanglement assisted via Duffing nonlinearity," Phys. Rev. A **110**, 043502 (2024).

[18] E. Buks and B. Yurke, "Mass detection with a nonlinear nanomechanical resonator," Phys. Rev. E **74**, 046619 (2006).

[19] R. Almog, S. Zaitsev, O. Shtempluck, and E. Buks, "Noise squeezing in a nanomechanical Duffing resonator," Phys. Rev. Lett. **98**, 078103 (2007).

[20] J. S. Ochs, D. K. J. Boneß, G. Rastelli, M. Seitner, W. Belzig, M. I. Dykman, and E. M. Weig, "Frequency comb from a single driven nonlinear nanomechanical mode," Phys. Rev. X **12**, 041019 (2022).

[21] A. Bachtold, J. Moser, and M. I. Dykman, "Mesoscopic physics of nanomechanical systems," Rev. Mod. Phys. **94**, 045005 (2022).

[22] E. Babourina-Brooks, A. Doherty, and G. J. Milburn, "Quantum noise in a nanomechanical Duffing resonator," New J. Phys. **10**, 105020 (2008).

[23] R. Artuso and L. Rebuzzini, "Effects of a nonlinear perturbation on dynamical tunneling in cold atoms," Phys. Rev. E **68**, 036221 (2003).

[24] H. Gothe, T. Valenzuela, M. Cristiani, and J. Eschner, "Optical bistability and nonlinear dynamics by saturation of cold Yb atoms in a cavity," Phys. Rev. A **99**, 013849 (2019).

[25] V. Parigi, E. Bimbard, J. Stanojevic, A. J. Hilliard, F. Nogrette, R. Tualle-Brouri, A. Ourjoumtsev, and P. Grangier, "Observation and measurement of interaction-induced dispersive optical nonlinearities in an ensemble of cold Rydberg atoms," Phys. Rev. Lett. **109**, 233602 (2012).

[26] J. S. Aldridge and A. N. Cleland, "Noise-enabled precision measurements of a Duffing nanomechanical resonator," Phys. Rev. Lett. **94**, 156403 (2005).

[27] I. Siddiqi, R. Vijay, F. Pierre, C. M. Wilson, M. Metcalfe, C. Rigetti, L. Frunzio, and M. H. Devoret, "RF-driven Josephson bifurcation amplifier for quantum measurement," Phys. Rev. Lett. **93**, 207002 (2004).

[28] I. Siddiqi, R. Vijay, M. Metcalfe, E. Boaknin, L. Frunzio, R. J. Schoelkopf, and M. H. Devoret, "Dispersive measurements of superconducting qubit coherence with a fast latching readout," Phys. Rev. B **73**, 054510 (2006).

[29] V. E. Manucharyan, E. Boaknin, M. Metcalfe, R. Vijay, I. Siddiqi, and M. Devoret, "Microwave bifurcation of a Josephson junction: Embedding-circuit requirements," Phys. Rev. B **76**, 014524 (2007).

[30] R. Vijay, M. H. Devoret, and I. Siddiqi, "Invited Review Article: The Josephson bifurcation amplifier," Rev. Sci. Instrum. **80**, 111101 (2009).

[31] Q.-M. Chen, M. Fischer, Y. Nojiri *et al.*, "Quantum behavior of the Duffing oscillator at the dissipative phase transition," Nat. Commun. **14**, 2896 (2023).

[32] A. D. Maris, B. Pokharel, S. G. Seshachallam, M. Z. R. Misplon, and A. K. Pattanayak, "Chaos in the quantum Duffing oscillator in the semiclassical regime under parametrized dissipation," Phys. Rev. E **104**, 024206 (2021).

[33] M. I. Dykman, I. B. Schwartz, and M. Shapiro, "Scaling in activated escape of underdamped systems," Phys. Rev. E **72**, 021102 (2005).

[34] M. I. Dykman, M. Marthaler, and V. Peano, "Quantum heating of a parametrically modulated oscillator: Spectral signatures," Phys. Rev. A **83**, 052115 (2011).

[35] M. I. Dykman, "Critical exponents in metastable decay via quantum activation," Phys. Rev. E **75**, 011101 (2007).

[36] L. Z. Guo, Z. G. Zheng, and X.-Q. Li, "Quantum dynamics of mesoscopic driven Duffing oscillators," Europhys. Lett. **90**, 10011 (2010).

[37] L. Guo, Z. Zheng, X.-Q. Li, and Y. Yan, "Dynamic quantum tunneling in mesoscopic driven Duffing oscillators," Phys. Rev. E **84**, 011144 (2011).

[38] C. A. Rosiek, M. Rossi, A. Schliesser, and A. S. Sørensen, "Quadrature squeezing enhances Wigner negativity in a mechanical duffing oscillator," PRX Quantum **5**, 030312 (2024).

[39] M. Coccolo and M. A. F. Sanjuán, "Transmitted resonance in a coupled system," Commun. Nonlinear Sci. Numer. Simul. **135**, 108068 (2024).

[40] V. Peano and M. Thorwart, "Quasienergy description of the driven Jaynes-Cummings model," Phys. Rev. B **82**, 155129 (2010).

[41] M.-A. Lemonde and A. A. Clerk, "Real photons from vacuum fluctuations in optomechanics: The role of polariton interactions," Phys. Rev. A **91**, 033836 (2015).

[42] I. Serban and F. K. Wilhelm, "Dynamical tunneling in macroscopic systems," Phys. Rev. Lett. **99**, 137001 (2007).

[43] M. Marthaler and M. I. Dykman, "Switching via quantum activation: A parametrically modulated oscillator," Phys. Rev. A **73**, 042108 (2006).

APL Quantum

RESEARCH ARTICLE | MAY 13 2025

Two recent theoretical advances with potential impact on quantum technology

Special Collection: Quantum Dynamics in Theory, Numerics and in Experimental Research

Hans Christian Öttinger

APL Quantum 2, 026121 (2025)
https://doi.org/10.1063/5.0268387

AIP Publishing

APL Quantum ARTICLE pubs.aip.org/aip/apq

Two recent theoretical advances with potential impact on quantum technology

Cite as: APL Quantum 2, 026121 (2025); doi: 10.1063/5.0268387
Submitted: 1 March 2025 • Accepted: 30 April 2025 •
Published Online: 13 May 2025

Hans Christian Öttinger[a)]

AFFILIATIONS

ETH Zürich, Quantum Center and Department of Materials, HCP F 43.1, CH-8093 Zürich, Switzerland

Note: This paper is part of the APL Quantum Special Topic on Quantum Dynamics in Theory, Numerics and in Experimental Research.

[a)] **Author to whom correspondence should be addressed:** hco@mat.ethz.ch. **URL:** https://polyphys.mat.ethz.ch/

ABSTRACT

Research aimed at elucidating the foundations of quantum theory can have a direct impact on quantum technology. Two examples illustrate this potential: (1) the coupling of quantum systems to arbitrary classical environments that can be described by irreversible thermodynamics. In the spirit of Dirac's replacement of classical Poisson brackets by commutators, a thermodynamically consistent coupling of quantum and classical systems can be obtained by quantization of the geometric structure of classical irreversible thermodynamics. (2) The stochastic bra-ket interpretation of quantum mechanics, which is obtained by unraveling density matrices in terms of bra-ket pairs of stochastic jump processes in Hilbert space. It offers an alternative realization of entanglement and avoids paradoxes by imposing severe but natural restrictions on the types of systems to which quantum mechanics can be applied.

I. INTRODUCTION

Any practical quantum device must interact with the classical world of our direct experience in some way. For instance, a quantum sensor needs some kind of display, and a quantum computer should presumably interface with a classical computer to achieve its full potential. A Hamiltonian coupling between quantum systems and their classical environment is expected to be the most effective method for transferring "results" gained by quantum sensors or computers. However, a detailed understanding of dissipative couplings between quantum and classical systems is also important, if only to minimize undesirable dissipative interactions.

The good news of the first part of this paper is that there exists a general thermodynamic framework for coupling quantum systems to their classical environments, which are assumed to evolve according to the laws of reversible and irreversible dynamics. This framework has been established by quantizing a geometric formulation of classical irreversible thermodynamics, offering a significant extension of the theory of open quantum systems.[1,2]

The development of new and improved quantum devices would undoubtedly benefit from a more intuitive understanding of quantum mechanics. In particular, entanglement, which embodies the holistic nature of quantum mechanics, is counterintuitive but crucial. In the standard approach, it leads to several well-known paradoxes. When a quantum system is divided into two subsystems, such as two particles or groups of particles, entanglement is the phenomenon that each subsystem cannot be described independently of the state of the other subsystem, even when the subsystems are separated by a large distance.

After 100 years of quantum mechanics, rather than adhering to dogmatism and relying solely on its mathematical framework, we should demand a convincing interpretation. Should we not consider the so-called measurement problem of quantum mechanics a potential obstacle for the advancement of quantum technology?[3–6]

At least Feynman was amusingly irritated when he began contemplating what quantum computers could be good for,[7] "we always have had a great deal of difficulty in understanding the worldview that quantum mechanics represents. At least I do, because I am an old enough man that I haven't got to the point that this stuff is obvious to me. Okay, I still get nervous with it . . . you know how it always is. every new idea, it takes a generation or two until it becomes obvious that there's no real problem. It has not yet become obvious to me that there's no real problem. I cannot define the real problem, therefore, I suspect there's no real problem, but I'm not sure there's no real problem."

The good news in the second part of this paper is that there exists a new interpretation of quantum mechanics, which offers a fresh perspective on entanglement and eliminates the paradoxes that arise in the standard approach to quantum mechanics.

II. DISSIPATIVE QUANTUM SYSTEMS

The emergence of irreversibility has been intensely investigated and heavily debated for ~150 years. Boltzmann's transport equation for rarefied gases[8] marks the first milestone in this development. It is an irreversible equation for the single-particle probability density in position and momentum space based on the collision laws obtained from the Hamiltonian dynamics of gas particles. It also implies an evolution equation for entropy. By the end of the 19th century, Boltzmann had clearly understood the probabilistic nature of the second law of thermodynamics, recognizing that violations would never be observed for macroscopic systems but could become noticeable in very small systems.

Fluctuation–dissipation relations[9–13] and projection-operator methods[14–18] played a significant role in advancing the field of irreversible thermodynamics. In the 1960s, the foundational principles for formulating linear irreversible thermodynamics were well-established and documented in a classical textbook.[19]

An elegant geometric formulation of classical nonequilibrium thermodynamics, initiated by Grmela[20,21] in 1984, has led to the so-called GENERIC framework (general equation for the nonequilibrium reversible–irreversible coupling):[22,23] Reversible dynamics is generated by energy via a Poisson bracket, whereas irreversible dynamics is generated by entropy via a dissipative bracket.

Understanding the emergence of irreversibility on the quantum level is expected to be considerably more challenging, certainly not easier than for classical systems. We aim to avoid limitations imposed by perturbation theory, simplistic models like reservoirs composed of harmonic oscillators, or approximations of unclear validity.

Lindblad formulated a quantum master equation for the density matrix of a dissipative quantum system based on the assumptions of linearity and complete positivity.[24] Grabert has used the projection-operator method to derive a quantum master equation that is nonlinear in the density matrix.[18,25] Both equations address the dissipative coupling of a quantum system to a bath. In many applications, the classical environment should not be limited to a heat bath. Ideally, the coupling of a quantum system to an arbitrary classical nonequilibrium system would be desirable.

A systematic framework for quantum systems in contact with finite quantum heat reservoirs has been established in a pioneering paper.[26] This approach elaborates the meaning of entropy production and sheds light on the emergence of irreversibility in the limit of large heat reservoirs. More recent developments are summarized in a broad collection of over 40 papers[27] and in a recent review article,[28] both of which emphasize fluctuation theorems and information-theoretic aspects while also addressing experimental achievements and practical applications.

The geometric structure of the GENERIC framework offers the opportunity to extend Dirac's approach to quantization from Hamiltonian to dissipative systems. Instead of deriving suitable master equations for dissipative quantum systems emerging from the reversible equations of quantum mechanics, a quantization procedure, in the spirit of replacing Poisson brackets by commutators, is applied to dissipative classical systems. As illustrated in Fig. 1, this idea eliminates the most challenging task of explaining the emergence of irreversibility at the quantum level.

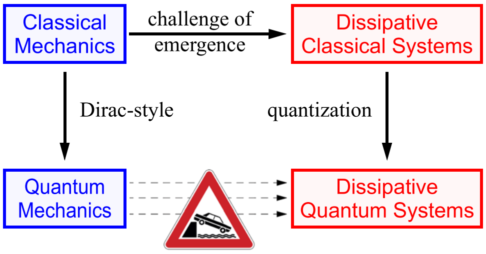

FIG. 1. Dirac-style quantization of dissipative classical systems for avoiding the challenging task of explaining the emergence of irreversibility at the quantum level.

As the von Neumann entropy is readily available as a generator of irreversible dynamics for quantum systems described by density matrices, one only needs to find a quantization rule for the dissipative bracket, analogous to Dirac's replacement of Poisson brackets with commutators.

This idea has been pursued in Ref. 29 and further formalized and generalized in Ref. 30. The argumentation and notation in those papers are very abstract because the emphasis is on the deep structural features of the procedure. Here, we offer a much simpler reformulation suitable for practical applications.

A. System and environment

The variables chosen to describe a quantum subsystem and its classical environment are summarized in Table I. In addition, energy and entropy as the generators of reversible and irreversible dynamics, respectively, are listed in this table.

The proper arena for quantum mechanics is provided by separable complete Hilbert spaces, which are complex vector spaces equipped with inner products.[31,32] Observables are self-adjoint linear operators on a Hilbert space $\mathscr{H}$. Here, we focus on the evolution of the density matrix ρ, also known as the statistical operator on $\mathscr{H}$. The density matrix characterizes the state of our quantum subsystem, and its time evolution determines the evolution of the averages $\langle A \rangle_\rho = \mathrm{tr}(\rho A)$ of all quantum observables A. This perspective corresponds to the Schrödinger picture, which we use throughout this letter.

TABLE I. Variables and the generators of reversible and irreversible dynamics for a quantum subsystem and its classical environment.

	Variables	Energy	Entropy
Quantum system	ρ on $\mathscr{H}$	$\langle H(x) \rangle_\rho$	$-k_\mathrm{B} \langle \ln \rho \rangle_\rho$
Classical environment	$x \in \mathscr{M}$	$E(x)$	$S(x)$

The discrete, continuous, or mixed set of variables x for the classical environment forms a manifold $\mathscr{M}$. Observables are functions or functionals on the manifold $\mathscr{M}$. For notational simplicity, we assume a discrete set of variables labeled by an index j or k. The modifications required for continuous sets of variables, in particular the proper generalization of matrices and partial derivatives, are explained in detail in Sec. 2 2 and Appendix C of Ref. 33.

Note that we allow the Hamiltonian $H(x)$ to depend on the variables of the environment, thereby introducing a reversible coupling of the quantum system and its environment. The appearance of classical external fields in the Hamiltonian of a quantum system is quite common, for example, a static magnetic field in the Schrödinger equation for discussing Larmor precession or the electromagnetic four-vector potential in the Pauli equation.

B. Quantization of dissipative structure

At the heart of quantizing the irreversible structure of nonequilibrium thermodynamics is the correlation of two Hilbert space operators A and B[29,30,34]

$$\langle A, B\rangle^{\alpha}_{\rho u} = \mathrm{tr}\Big(\rho^{1-u}\ \mathrm{i}[Q^{\dagger}_{\alpha}, A]\ \rho^{u}\ \mathrm{i}[Q_{\alpha}, B]\Big) + \mathrm{tr}\Big(\rho^{1-u}\ \mathrm{i}[Q^{\dagger}_{\alpha}, B^{\dagger}]\ \rho^{u}\ \mathrm{i}[Q_{\alpha}, A^{\dagger}]\Big), \tag{1}$$

in terms of the dimensionless operator Q_α, which is from a set of coupling operators labeled by α. The operators A and B are typically self-adjoint, whereas the coupling operators Q_α usually are not (for example, they can be creation and annihilation operators). The second trace term in the definition (1) has been added such that $\langle A, B\rangle^{\alpha}_{\rho u}$ becomes real, which is crucial for the coupling to a classical system.

The correlation $\langle A, B\rangle^{\alpha}_{\rho u}$ is closely related to the quantity introduced in Eq. (1) of Ref. 30. Note the symmetry

$$\langle A, B\rangle^{\alpha}_{\rho u} = \left\langle B^{\dagger}, A^{\dagger}\right\rangle^{\alpha}_{\rho u}, \tag{2}$$

and the positivity property

$$\left\langle A^{\dagger}, A\right\rangle^{\alpha}_{\rho u} \geq 0. \tag{3}$$

Moreover, an underlying joint convexity property follows from Lieb's theorem [see, for example, Eq. (2.120) of Ref. 1].

We further introduce the self-adjoint generalized free-energy operators

$$F^{u}_{\alpha}(x) = \frac{\partial E^{\mathrm{tot}}(x)}{\partial x} \cdot K^{u}_{\alpha}(x) \cdot \left\{ \frac{\partial S(x)}{\partial x}\, H(x) + \frac{\partial E^{\mathrm{tot}}(x)}{\partial x}\, k_{\mathrm{B}} \ln \rho \right\}, \tag{4}$$

where

$$E^{\mathrm{tot}}(x) = E(x) + \langle H(x)\rangle_{\rho}, \tag{5}$$

and the matrices $K^{\alpha}_{u}(x)$ associated with the coupling operators Q_α are assumed to be symmetric and positive semidefinite. The simplest dependence of these matrices on u is through a non-negative real prefactor $h_\alpha(u)$. We refer to the quantities $F^{u}_{\alpha}(x)$ as free energy operators because they are combinations of the energy and entropy operators with relative weights proportional to dS and $-dE^{\mathrm{tot}}$.

C. Evolution equations

According to the quantization procedure proposed in Refs. 29 and 30, the evolution of the average $\langle A\rangle_{\rho}$ of an observable A of the quantum subsystem is governed by the first-order differential equation

$$\frac{d\langle A\rangle_{\rho}}{dt} = \frac{\mathrm{i}}{\hbar}\langle [H(x), A]\rangle_{\rho} - \frac{1}{\hbar}\sum_{\alpha} \int_{0}^{1} \left\langle F^{u}_{\alpha}(x), A\right\rangle^{\alpha}_{\rho u} du, \tag{6}$$

which actually constitutes the essence of the Dirac-style quantization procedure. The first term expresses reversible evolution, and the second term provides the dissipative coupling to the environment. In the reversible term, we clearly recognize the commutator that, according to Dirac, replaces the Poisson bracket of classical mechanics. The correlation in the second term constitutes the previously suggested replacement for the dissipative bracket in the generalization of Dirac's quantization procedure.[29,30,34]

The evolution of the classical environment is given by the first-order differential equations

$$\begin{aligned}\frac{dx}{dt} = {} & L(x) \cdot \frac{\partial E^{\mathrm{tot}}(x)}{\partial x} + M(x) \cdot \frac{\partial S(x)}{\partial x} \\ & + \frac{1}{\hbar}\sum_{\alpha} \int_{0}^{1} K^{u}_{\alpha}(x) \cdot \Big\{ \langle H(x), H(x)\rangle^{\alpha}_{\rho u} \frac{\partial S(x)}{\partial x} \\ & + k_{\mathrm{B}} \langle \ln \rho, H(x)\rangle^{\alpha}_{\rho u} \frac{\partial E^{\mathrm{tot}}(x)}{\partial x} \Big\}\, du.\end{aligned} \tag{7}$$

The first term describes reversible dynamics of the environment generated by the energy. The energy gradient is multiplied by the antisymmetric Poisson matrix $L(x)$, which is given by the symplectic matrix transformed to non-canonical coordinates. The Poisson bracket of two observables is obtained by multiplying the Poisson matrix from both sides with the gradients of the two arguments of the bracket.

The second term in Eq. (7) describes irreversible dynamics generated by the entropy gradient. The friction matrix $M(x)$ is assumed to be positive-semidefinite so that irreversible dynamics essentially follows the entropy gradient.

The remaining term represents the dissipative coupling between the quantum system and its environment. It is constructed such that the change in the energy of the quantum system, as obtained from Eq. (6) for $A = H(x)$, is compensated by the change in energy of the classical environment, as obtained by multiplying the evolution Eq. (7) with $\partial E^{\mathrm{tot}}(x)/\partial x$.

The following degeneracy relations are part of the GENERIC structure of classical nonequilibrium systems:

$$L(x) \cdot \frac{\partial S(x)}{\partial x} = 0, \qquad M(x) \cdot \frac{\partial E^{\mathrm{tot}}(x)}{\partial x} = 0. \tag{8}$$

They express the conservation of entropy by reversible dynamics and the conservation of energy by irreversible dynamics for any choice of the respective generators of the dynamics.

Equation (6) specifies the evolution of the averages of all quantum observables A evaluated with the density matrix ρ. It can be rewritten as an evolution equation for ρ, which we refer to as the thermodynamic or GENERIC quantum master equation

$$\frac{d\rho}{dt} = -\frac{i}{\hbar}[H(x),\rho] - \frac{1}{\hbar}\sum_{\alpha}\int_0^1 \Big\{\Big[Q_\alpha, \rho^{1-u}\,[Q_\alpha^\dagger, F_\alpha^u(x)]\,\rho^u\Big] + \Big[Q_\alpha^\dagger, \rho^u\,[Q_\alpha, F_\alpha^u(x)]\,\rho^{1-u}\Big]\Big\}\,du. \tag{9}$$

Note that the reversible evolution is governed by the commutator with the Hamiltonian, whereas the dissipative contribution possesses a double commutator structure involving coupling and free energy operators. The classical analog of a quantum master equation is a diffusion of the Fokker–Planck equation for the evolution of a probability density, incorporating first and second derivatives for the reversible and irreversible contributions, respectively.

The master Eq. (9) is our fundamental equation for open quantum systems. As a consequence of the definition (1), the second term in Eq. (9) is generally nonlinear in ρ. This nonlinearity of the irreversible contribution is caused by the noncommutativity of quantum observables and implies that, in general, our master equation cannot be of the popular Lindblad form (see, for example, Sec. 3 7 of Ref. 1 for a discussion of nonlinear quantum master equations). The specific conditions under which the GENERIC quantum master equation is linear in ρ are discussed in the Appendix.

Equations (7) and (9) describe the evolution of the state variables for the classical environment and the quantum system introduced in Table I. They represent the dissipative coupling of a quantum system to a general classical nonequilibrium system as its environment, achieved through Dirac-style quantization of the GENERIC framework. An additional reversible coupling is included in the dependence of the Hamiltonian $H(x)$ of the quantum system on the classical variables x.

D. Entropy production

With the evolution equation for all system variables at hand, we can now calculate the time-evolution of entropy,

$$\sigma = \frac{\partial S(x)}{\partial x}\cdot M(x)\cdot\frac{\partial S(x)}{\partial x} + \frac{2}{\hbar}\sum_{\alpha jk}\int_0^1 K^u_{\alpha jk}(x)\langle f_j(x), f_k(x)\rangle^\alpha_{\rho u}\,du, \tag{10}$$

with the generalized free-energy operators

$$f_j(x) = \frac{\partial S(x)}{\partial x_j}\,H(x) + \frac{\partial E^{\text{tot}}(x)}{\partial x_j}\,k_B\ln\rho. \tag{11}$$

Note that these operators $f_j(x)$ are closely related to the operators $F_\alpha^u(x)$ defined in Eq. (4).

The first term in Eq. (10) describes the entropy production in the classical environment. Note that only the symmetric part of the friction matrix $M(x)$ contributes to entropy production. An antisymmetric contribution to $M(x)$ would describe irreversible processes without entropy production. Historically, this possibility has been introduced by Casimir.[19,35] Recent examples of irreversible processes without entropy production include slip phenomena and the energy cascade in turbulence.[36]

The second term in Eq. (10) describes the entropy production associated with the dissipative coupling of the quantum system and its classical environment. Note that both contributions to the entropy production (10) are always non-negative. In a thermodynamic setting, this property is more relevant than the complete positivity assumed in Lindblad's approach.

E. Applications

The first derivation of a nonlinear quantum master equation of the type (9) for a quantum system coupled to a heat bath was achieved by using the projection-operator method.[18,25] The same type of nonlinear equation has been recovered from the quantization of GENERIC and illustrated for the examples of a two-level system and a damped harmonic oscillator.[34] The zero-temperature limit of the thermodynamic quantum master equation has been discussed in Ref. 37. In addition, heat transport in quantum spin chains has been discussed with this master equation.[38]

It has been shown that the nonlinear quantum master Eq. (9) leads to a biexponential decay, a realistic susceptibility profile, and ultralong coherence of a qubit, which is not limited by the energy relaxation time because complete positivity is not imposed.[39] It has been recognized that the thermodynamic quantum master equation, which is generally nonlinear, may be of the linear Davies–Lindblad type if the coupling operators Q_α are eigenoperators of the Hamiltonian of the quantum subsystem and the associated coupling matrices $K_u^\alpha(x)$ are chosen suitably (see Appendix).[30]

The powerful tool of stochastic unravelings[1] of quantum master equations for dissipative quantum systems in terms of stochastic jump processes in Hilbert space has been applied to nonlinear equations of the type (9). The nonlinearity can be produced by mean-field interactions in the stochastic jump process.[40] One- and two-process unravelings have been developed and tested in Ref. 41.

The dissipative coupling of a quantum system to a time-evolving environment has been explored in Ref. 42. Practical applications include vibrational relaxations in liquids,[43] where slower rotational and translational modes can be treated by classical thermodynamics and hydrodynamics, or the Marcus theory of electron transfer in molecular systems,[44] where the dielectric environment can be treated by classical thermodynamics and electrodynamics. Further applications include spin-selective radical-ion-pair reactions relevant to photochemistry and photosynthesis,[45] quantum dots exchanging energy with two heat baths,[46] the coupling of quantum systems to classical opto-electronic systems for the modeling of laser devices,[46] semi-classical drift-diffusion-reaction models for the transport of charge carriers in opto-electronic devices,[47] and coupled spin dynamics for a sensitivity enhancement of magnetic resonance imaging and spectroscopy.[48]

As a final application, we mention that quantum master Eq. (9) provides the foundations of dissipative quantum field theory [cf. Eq. (1.45) of Ref. 49]. In this approach, dissipative smearing regularizes quantum field theory at short distances. Some ontological implications of dissipative quantum field theory have been discussed in Ref. 50. The unraveling of the quantum master equation leads to a new simulation technique for quantum field theory, where the simulation time corresponds to real time. In this context, it has been realized that it is natural to treat interactions as stochastic jumps.

Efficient simulations based on unravelings, in which the interactions of reversible quantum systems are treated as stochastic jumps, have been developed and tested in Refs. 51 and 52. This reformulation naturally leads to a new interpretation of quantum mechanics,[53] which is discussed in Sec. III.

III. STOCHASTIC BRA-KET INTERPRETATION OF QUANTUM MECHANICS

It is desirable for an interpretation of quantum mechanics to be based on quantum field theory. For example, in the hydrogen atom, the electron and the proton do not really interact through the static, classical Coulomb potential appearing in the Schrödinger equation, but rather through the exchange of photons.

At any given time, a hydrogen atom consists of an electron, a proton, and a number of photons mediating electromagnetic interactions between the charged particles. As the proton is no longer considered a fundamental particle, one might prefer to say that a hydrogen atom consists of an electron, three quarks, and a number of photons and gluons mediating electromagnetic and strong interactions. In any case, the hydrogen atom has a well-defined content of fundamental particles at any given time. These remarks should clarify that the usual quantum mechanical treatment of the hydrogen atom is a semi-classical approximation involving static classical interactions at a distance. An illustrative toy version of a quantum field theoretical calculation illustrates how bound states can be treated on a more fundamental level.[54] The comparison to quantum mechanics is based on the Fourier transformation of the wave functions from position to momentum space.

In contrast to wave functions or density matrices, which describe the properties of an ensemble of hydrogen atoms, stochastic unravelings of density matrices allow us to describe individual atoms. We thus gain a new perspective on both quantum mechanics and quantum technology. The idea that any quantum system has a well-defined particle content suggests that, at any given time, the system can be described by a multiple of a Fock space base vector.[49,55,56]

A. Idea of unravelings

Inspired by the discussion of the hydrogen atom, our goal is to reformulate the equations of reversible quantum mechanics in terms of stochastic jump processes, where interactions are treated as discrete collision events. Therefore, we need a splitting of the full Hamiltonian into free and interacting contributions, $H = H^{\text{free}} + H^{\text{int}}$. We further assume that there exists a distinguished basis of orthonormal eigenstates $|m\rangle$ of the free Hamiltonian H^{free}, which are labeled by the natural number m. The corresponding eigenvalues of H^{free} are given by E_m. Finally, we assume that the strict superselection rule of quantum field theory is inherited by quantum mechanics, meaning the state of the quantum system at any time t is described by a complex multiple of some base vector $|m_t\rangle$. No superpositions between different base vectors are allowed.

With an unraveling in terms of two stochastic processes, $|\phi\rangle_t$ and $|\psi\rangle_t$, in Hilbert space, we wish to reproduce the density matrix ρ_t evolving according to the von Neumann equation, which is the reversible part of the quantum master Eq. (9) for a quantum system without any dissipative coupling to the environment, by the following expectation evaluated on the probability space of the jump processes:

$$\rho_t = E\big(|\phi\rangle_t\langle\psi|_t\big), \tag{12}$$

where we use Dirac's bra-ket notation for state vectors (kets) and their duals (bras). The use of the dyadic product in Eq. (12) is motivated by the task of constructing a tensor from the stochastic state vectors in Hilbert space. The expectation $E(\cdot)$ can be thought of as an average over the trajectories of the jump processes.

With the representation (12), the average of a quantum observable A can be obtained as an expectation of stochastic matrix elements,

$$\langle A\rangle_\rho = \text{tr}(\rho_t A) = E\big(\langle\psi|_t A|\phi\rangle_t\big). \tag{13}$$

This expectation of a bilinear form of stochastic states provides the average of any observable A. Their stochastic nature arises from spontaneous quantum jumps occurring at random times. In the stochastic averaging procedure, nontrivial phase effects and entanglement can arise from this bra-ket formulation. The representation of quantum observables by linear operators on a Hilbert space suggests that there are two sides or aspects associated with every observable A, which, according to Eq. (13), are expressed by the two processes of the unraveling.

B. Stochastic jump process

The strict superselection rule, which states that linear combinations of different base vectors do not correspond to physical states, reduces the enormous number of possible stochastic jump processes $|\phi\rangle_t$ and $|\psi\rangle_t$. It naturally guides us to a construction of piecewise continuous trajectories with interspersed jumps among basis vectors for the two independent, identically distributed stochastic processes. The following unique stochastic jump process has been constructed in Ref. 53.

1. Free evolution between jumps

If the system between the times t' and t is represented by a multiple of the base vector $|m\rangle$, the complex prefactor oscillates in time and leads to an overall phase shift given by $-E_m(t-t')/\hbar$.

2. Random jumps

If the system is represented by a multiple of the base vector $|m\rangle$, a positive rate parameter r_m characterizes an exponentially decaying probability density for a jump to occur in time. If a jump occurs at time t, a transition from $c_t\,|m\rangle$ to a new state at time $t+$ is determined by the following stochastic jump rule:

$$c_t\,|m\rangle \to c_t\, f_{lm}|l\rangle \text{ with probability } p_{lm} = \frac{|\langle l|H^{\text{int}}|m\rangle|}{\sum_{l'}|\langle l'|H^{\text{int}}|m\rangle|}. \tag{14}$$

To reproduce the von Neumann equation, the rate parameters r_m and the weight factors f_{lm} have to be chosen such that the following conditions are satisfied:

$$i\hbar r_m(p_{lm}f_{lm} - \delta_{lm}) = \langle l|H^{\text{int}}|m\rangle. \tag{15}$$

The most general solution of these conditions is given by

$$f_{lm} = \frac{\hbar r_m\delta_{lm} - i\,\langle l|H^{\text{int}}|m\rangle)}{|\langle l|H^{\text{int}}|m\rangle|}\,S_m, \tag{16}$$

and

$$r_m = \frac{1}{\hbar S_m} \sum_l |\langle l|H^{\text{int}}|m\rangle|, \tag{17}$$

where S_m is a positive real parameter, possibly but not necessarily equal to 1. To find a criterion for the choice of the free parameter S_m, we look at the magnitudes of the weight factors f_{lm},

$$|f_{mm}| = R_m > S_m = |f_{lm}| \quad \text{for } l \neq m, \tag{18}$$

where R_m is defined by the first equation. If we chose $S_m = 1$, then $R_m > 1$ would lead to a total weight factor increasing exponentially in time along any trajectory of the jump process. We therefore prefer to choose $S_m < 1$ and $R_m > 1$, fine-tuned such that there occurs no exponential increase or decrease with time and the complex factors f_{lm} associated with jumps essentially introduce phase shifts,

$$R_m^{p_{mm}} \, S_m^{1-p_{mm}} = 1. \tag{19}$$

The unique values of S_m and R_m obtained from condition (19) are shown in Fig. 2 as functions of p_{mm}.

The stochastic bra-ket formulation of quantum mechanics offers a new interpretation of quantum mechanics. It may be considered an alternative to the currently favored interpretations: Bohmian mechanics,[57–61] the GRW approach,[62–64] and the many-worlds interpretation.[65,66]

C. Two processes: Quantum effects

For reversible quantum systems, the bra and ket processes evolve independently. If the initial conditions are also stochastically independent, the density matrix (12) can be rewritten in the factorized form

$$\rho_t = E(|\phi\rangle_t) E(\langle\psi|_t). \tag{20}$$

Since the stochastic processes $|\phi\rangle_t$ and $|\psi\rangle_t$ are identically distributed, this representation coincides with the density matrix associated with a solution of the Schrödinger equation. Despite the strong superselection rule, the averages $E(|\phi\rangle_t)$ and $E(|\psi\rangle_t)$ can be superposition states. These averages do not describe individual pure quantum systems, but they rather represent ensembles of pure quantum systems. The apparent superposition results from stochastic averaging over many individual quantum systems. For mixed states, the factorization (20) does not work.

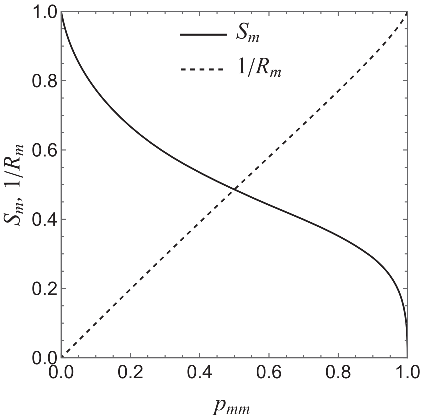

FIG. 2. Magnitude of the weight factors $S_m < 1$ and $R_m > 1$ of the stochastic bra-ket unraveling as a function of the probability p_{mm} for self-transitions. As the factor R_m associated with self-transitions is larger than 1, it is convenient to display its inverse. For $p_{mm} = 1/2$, one finds $S_m = 1/R_m = \sqrt{\sqrt{5} - 2} \approx 0.486 < 1/2$.

Note that a constant shift of the Hamiltonian H^{int} does not affect the von Neumann equation, but as it shifts the matrix elements $\langle m|H^{\text{int}}|m\rangle$, it affects the jump processes. Therefore, to obtain a unique unraveling, it is important to choose the zero of the interaction energy based on physical arguments.

If there is no natural choice for the zero of energy, one might choose the average energy to be zero. A disadvantage of this choice is that the Hamiltonian depends on the energy of the initial state. An advantage is that steady pure states are described by a time-independent $E(|\phi\rangle_t)$.

In Ref. 53, the usefulness of Eq. (20) is demonstrated in the context of the Einstein–Podolsky–Rosen experiment.[67–72] Entanglement arises from the averaging over independent individual states on the bra and ket sides. The wavelike behavior of quantum particles results from an interplay between the bra and ket vectors, as illustrated by the double-slit experiment.[53]

IV. SOME CONCLUDING REMARKS

We have shown how a theory of quantum dissipation can be developed by quantizing the geometry-based GENERIC framework of nonequilibrium thermodynamics. Thermodynamics is invaluable because it provides a sound language for science and engineering. According to Einstein's famous appraisal of thermodynamics,[73] "It is the only physical theory of universal content, which I am convinced that within the framework of applicability of its basic concepts will never be overthrown (for the special attention of those who are skeptics on principle)."

The geometric structure on which GENERIC is based should, whenever possible, be preserved in developing numerical methods for solving practical problems. For reversible equations, symplectic integrators that preserve the underlying Hamiltonian structure are known to be powerful numerical tools.[74,75] For classical dissipative systems, promising initial steps have been taken to reproduce the correct behavior of energy and entropy and to preserve the underlying bracket structure.[76–80] For dissipative quantum systems, the development of structure-preserving methods will be even more challenging, particularly when stochastic simulations are included.

The general reversible and irreversible coupling of quantum systems to classical environments is clearly a cornerstone of quantum technology. It is not only a key tool for simplifying or solving problems of practical importance, but it also offers a framework for discussing the measurement problem.

Even closer to the foundations of quantum mechanics is the stochastic bra-ket interpretation described in the second part of this paper. By eliminating the famous paradoxes from quantum mechanics through the application of a strict superselection rule, we may gain deeper intuition about the quantum world. The usual distinction between the classical and quantum worlds is not fundamental but rather a declaration of our lack of understanding and intuition, even after 100 years of quantum mechanics.

According to the bra-ket interpretation, two stochastic jump processes are required to describe an individual quantum system. According to Eq. (13), there are two sides or aspects of quantum variables: a bra and a ket side. The standard equations of quantum mechanics arise after averaging over ensembles of individual systems. The stochastic bra-ket interpretation provides a new quantum reality with a novel implementation of entanglement.

Realism is nice to have for engineers, as well as for down-to-earth scientists and philosophers. In the words often attributed to Max Planck, "When you change the way you look at things, the things you look at change." An alternative interpretation of quantum mechanics invites new ways of thinking and new questions to be asked, such as: Is a piecewise linear trajectory of a free particle between collisions a valid concept? How close in space and time must the bra and ket trajectories be to contribute to a local measurement? Do particles cease to exist if their bra and ket trajectories move so far apart that they cannot be detected by any local measurement? Should the corresponding loss of particles be compensated by the simultaneous creation of bra and ket vectors in all possible momentum states? Is there a mechanism for bra and ket vectors to stay spatially close, say by favoring momenta in properly selected directions during collisions or by an attractive bra-ket interaction? Can the bra and ket processes describing individual quantum systems be manipulated separately, say by magnetic fields?

A promising tool for addressing these questions is generalized versions of double-slit experiments,[81,82] where the electrons of the bra and ket processes always pass through specific slits, but the bra and ket versions of the electrons might pass through different slits.[53] By varying slit widths and analyzing high-precision intensity profiles, one could investigate whether interfering spherical waves arise uniformly along slits (according to the Huygens–Fresnel principle) or only by interactions at the edges. With configurations involving more than two slits, possibly arranged in multiple layers, one could try to find out whether the bra and ket electrons pass through well-defined slits or sequences of slits. While time-resolved experiments would provide valuable insights into path lengths, they likely remain beyond current technological capabilities.

The possibility of describing individual quantum systems, rather than ensembles, opens up opportunities for novel applications, although—or perhaps precisely because—these individual systems are subject to the intrinsic randomness of quantum mechanics. This might be relevant in the context of electronic or optical devices that exhibit shot noise. For quantum computers, it might be possible to simulate random variables rather than probability densities. The interplay between the bra and ket aspects of the world may also be key to understanding the transition from particle-wave duality to classical behavior.[83]

Advances in the foundations of quantum theory may be valuable for making progress in quantum technology. However, this is by no means a one-way street. The development of quantum devices, conversely, helps us to develop experience with and eventually intuition for quantum mechanics. The challenge of solving urgent practical problems may provide a stronger driving force for progress than the intellectual desire to understand what holds the world together at its core. Curiosity-driven research sometimes leads to curiosities and aberrations. In any case, quantum physics must become classical!

AUTHOR DECLARATIONS

Conflict of Interest

The author has no conflicts to disclose.

Author Contributions

Hans Christian Öttinger: Conceptualization (equal); Writing – original draft (equal); Writing – review & editing (equal).

DATA AVAILABILITY

Data sharing is not applicable to this article as no new data were created or analyzed in this study.

APPENDIX: LINEAR THERMODYNAMIC QUANTUM MASTER EQUATIONS

Elaborating on the ideas of Ref. 30, we here determine the conditions under which the GENERIC master Eq. (9) becomes linear. The identity

$$\frac{d}{du}\left(\rho^{1-u} A\, \rho^{u}\right) = \rho^{1-u} [A, \ln \rho]\, \rho^{u}, \tag{A1}$$

when used in the definition (1), leads to

$$\begin{aligned}\langle \ln \rho, A\rangle^{\alpha}_{\rho u} = &-\frac{d}{du}\mathrm{tr}\Big(\rho^{1-u}\, Q^{\dagger}_{\alpha}\, \rho^{u}\, [Q_{\alpha}, A]\Big)\\ &+\frac{d}{du}\mathrm{tr}\Big(\rho^{u} Q_{\alpha}\, \rho^{1-u}\, [Q^{\dagger}_{\alpha}, A^{\dagger}]\Big).\end{aligned} \tag{A2}$$

For some weight function $h(u)$, after an integration by parts, we obtain

$$\begin{aligned}\int_0^1 h(u)\langle \ln \rho, A\rangle^{\alpha}_{\rho u}\, du = &\int_0^1 \frac{dh(u)}{du}\Big\{\Big\langle \rho^{-u} Q^{\dagger}_{\alpha}\rho^{u}[Q_{\alpha}, A]\Big\rangle_{\rho}\\ &-\Big\langle \rho^{-u}[Q^{\dagger}_{\alpha}, A^{\dagger}]\rho^{u} Q_{\alpha}\Big\rangle_{\rho}\Big\} du\\ &+h(0)\Big\langle Q^{\dagger}_{\alpha}[Q_{\alpha}, A]\Big\rangle_{\rho}\\ &-h(1)\Big\langle [Q_{\alpha}, A] Q^{\dagger}_{\alpha}\Big\rangle_{\rho}\\ &+h(1)\Big\langle Q_{\alpha}[Q^{\dagger}_{\alpha}, A^{\dagger}]\Big\rangle_{\rho}\\ &-h(0)\Big\langle [Q^{\dagger}_{\alpha}, A^{\dagger}] Q_{\alpha}\Big\rangle_{\rho}.\end{aligned} \tag{A3}$$

The nonlinear integral part of the entropy-generated contribution must be canceled by the energy-generated contribution

$$\begin{aligned}&\int_0^1 h(u)\langle H(x), A\rangle^{\alpha}_{\rho u}\, du\\ &\quad = -\int_0^1 h(u)\Big\{\Big\langle \rho^{-u}[Q^{\dagger}_{\alpha}, H(x)]\rho^{u}[Q_{\alpha}, A]\Big\rangle_{\rho}\\ &\qquad + \Big\langle \rho^{-u}[Q^{\dagger}_{\alpha}, A^{\dagger}]\rho^{u}[Q_{\alpha}, H(x)]\Big\rangle_{\rho}\Big\} du.\end{aligned} \tag{A4}$$

To see the conditions for cancellation more clearly, we rewrite the generalized free-energy operators (4) as

$$F_\alpha^u(x) = \frac{\partial E^{\text{tot}}(x)}{\partial x} \cdot K_\alpha^u(x) \cdot \frac{\partial S(x)}{\partial x} \, [\, H(x) + T_\alpha(x) \, k_{\text{B}} \ln \rho], \tag{A5}$$

with the "temperature"

$$T_\alpha(x) = \frac{\frac{\partial E^{\text{tot}}(x)}{\partial x} \cdot K_\alpha^u(x) \cdot \frac{\partial E^{\text{tot}}(x)}{\partial x}}{\frac{\partial E^{\text{tot}}(x)}{\partial x} \cdot K_\alpha^u(x) \cdot \frac{\partial S(x)}{\partial x}}. \tag{A6}$$

If we want $T_\alpha(x)$ to be independent of u for all choices of the generators $E^{\text{tot}}(x)$ and $S(x)$ of reversible and irreversible dynamics of the classical environment, $K_\alpha^u(x)$ must depend on an overall factor of u that cancels out in the definition (A6). For a cancellation of the integral terms in Eqs. (A3) and (A4) to arise, the dependence of $K_\alpha^u(x)$ on u must be exponential,

$$K_\alpha^u(x) = \hat{K}_\alpha(x) \, e^{-\beta_\alpha u}. \tag{A7}$$

If we further assume that the operators Q_α are eigenoperators of the Hamiltonian $H(x)$

$$[Q_\alpha, H(x)] = \hbar\omega_\alpha Q_\alpha, \quad [Q_\alpha^\dagger, H(x)] = -\hbar\omega_\alpha Q_\alpha^\dagger, \tag{A8}$$

the condition for the cancellation of the nonlinear integral terms in the GENERIC quantum master equation becomes

$$\beta_\alpha = \frac{\hbar\omega_\alpha}{k_{\text{B}} T_\alpha(x)}. \tag{A9}$$

If the Hamiltonian $H(x)$ actually depends on x, we also expect the coupling operators and their frequencies introduced in Eq. (A8) to depend on x. The final linear quantum master equation of the GENERIC type is given by the linear part of Eq. (A3),

$$\begin{aligned} \frac{d\rho}{dt} = &-\frac{\mathrm{i}}{\hbar}[H(x), \rho] - \frac{k_{\text{B}}}{\hbar} \sum_\alpha \frac{\partial E^{\text{tot}}(x)}{\partial x} \cdot \hat{K}_\alpha(x) \cdot \frac{\partial E^{\text{tot}}(x)}{\partial x} \\ &\times \Big[Q_\alpha^\dagger Q_\alpha \rho - 2 Q_\alpha \rho Q_\alpha^\dagger + \rho Q_\alpha^\dagger Q_\alpha \\ &+ e^{-\beta_\alpha} \Big(Q_\alpha Q_\alpha^\dagger \rho - 2 Q_\alpha^\dagger \rho Q_\alpha + \rho Q_\alpha Q_\alpha^\dagger \Big) \Big]. \end{aligned} \tag{A10}$$

Note that for

$$\rho_\alpha \propto \exp\left\{ -\frac{H(x)}{k_{\text{B}} T_\alpha(x)} \right\}, \tag{A11}$$

the α contribution to dissipation in Eq. (A10) vanishes, as can be verified by using

$$Q_\alpha \rho_\alpha = e^{-\beta_\alpha} \rho_\alpha Q_\alpha, \quad Q_\alpha^\dagger \rho_\alpha = e^{\beta_\alpha} \rho_\alpha Q_\alpha^\dagger. \tag{A12}$$

REFERENCES

[1] H.-P. Breuer and F. Petruccione, *The Theory of Open Quantum Systems* (Oxford University Press, Oxford, 2002).

[2] U. Weiss, *Quantum Dissipative Systems*, *Series in Modern Condensed Matter Physics*, 3rd ed. (World Scientific, Singapore, 2008), Vol. 13.

[3] P. K. Feyerabend, "Problems of microphysics," in *Frontiers of Science and Philosophy*, *University of Pittsburgh Series in the Philosophy of Science No. 1*, edited by R. G. Colodny (University of Pittsburgh Press, Pittsburgh, 1962), pp. 189–283.

[4] D. Z. Albert, *Quantum Mechanics and Experience* (Harvard University Press, Cambridge, MA, 1992).

[5] T. Maudlin, "Three measurement problems," Topoi **14**, 7–15 (1995).

[6] J. A. Barrett, "Entanglement and disentanglement in relativistic quantum mechanics," Stud. Hist. Philos. Sci. B **48**, 168–174 (2014).

[7] R. P. Feynman, "Simulating physics with computers," Int. J. Theor. Phys. **21**, 467–488 (1982).

[8] L. Boltzmann, "Weitere Studien über das Wärmegleichgewicht unter Gasmolekülen," Wien. Ber. **66**, 275–370 (1872).

[9] H. Nyquist, "Thermal agitation of electric charge in conductors," Phys. Rev. **32**, 110–113 (1928).

[10] H. B. Callen and T. A. Welton, "Irreversibility and generalized noise," Phys. Rev. **83**, 34–40 (1951).

[11] R. Kubo, M. Toda, and N. Hashitsume, *Nonequilibrium Statistical Mechanics*, *Statistical Physics*, 2nd ed. (Springer, Berlin, 1991), Vol. 2.

[12] H. C. Öttinger, M. Peletier, and A. Montefusco, "A framework of nonequilibrium statistical mechanics. I. Role and types of fluctuations," J. Non-Equilib. Thermodyn. **46**, 1–13 (2021).

[13] A. Montefusco, M. Peletier, and H. C. Öttinger, "A framework of nonequilibrium statistical mechanics. II. Coarse-graining," J. Non-Equilib. Thermodyn. **46**, 15–33 (2021).

[14] R. Zwanzig, "Memory effects in irreversible thermodynamics," Phys. Rev. **124**, 983–992 (1961).

[15] H. Mori, "Transport, collective motion, and Brownian motion," Prog. Theor. Phys. **33**, 423–455 (1965).

[16] H. Mori, "A continued-fraction representation of the time-correlation functions," Prog. Theor. Phys. **34**, 399–416 (1965).

[17] B. Robertson, "Equations of motion in nonequilibrium statistical mechanics," Phys. Rev. **144**, 151–161 (1966).

[18] H. Grabert, *Projection Operator Techniques in Nonequilibrium Statistical Mechanics* (Springer, Berlin, 1982).

[19] S. R. de Groot and P. Mazur, *Non-Equilibrium Thermodynamics*, 2nd ed. (Dover, New York, 1984).

[20] M. Grmela, "Particle and bracket formulations of kinetic equations," in *Fluids and Plasmas: Geometry and Dynamics*, *Contemporary Mathematics No. 28*, edited by J. E. Marsden (American Mathematical Society, Providence, Rhodes Island, 1984), pp. 125–132.

[21] M. Grmela, "Bracket formulation of dissipative fluid mechanics equations," Phys. Lett. A **102**, 355–358 (1984).

[22] M. Grmela and H. C. Öttinger, "Dynamics and thermodynamics of complex fluids. I. Development of a general formalism," Phys. Rev. E **56**, 6620–6632 (1997).

[23] H. C. Öttinger and M. Grmela, "Dynamics and thermodynamics of complex fluids. II. Illustrations of a general formalism," Phys. Rev. E **56**, 6633–6655 (1997).

[24] G. Lindblad, "On the generators of quantum dynamical semigroups," Commun. Math. Phys. **48**, 119–130 (1976).

[25] H. Grabert, "Nonlinear relaxation and fluctuations of damped quantum systems," Z. Phys. B: Condens. Matter **49**, 161–172 (1982).

[26] M. Esposito, K. Lindenberg, and C. Van den Broeck, "Entropy production as correlation between system and reservoir," New J. Phys. **12**, 013013 (2010).

[27] *Thermodynamics in the Quantum Regime: Fundamental Aspects and New Directions*, *Fundamental Theories of Physics No. 195*, edited by F. Binder, L. A. Correa, C. Gogolin, J. Anders and G. Adesso (Springer, Cham, 2018).

[28] G. T. Landi and M. Paternostro, "Irreversible entropy production: From classical to quantum," Rev. Mod. Phys. **93**, 035008 (2021).

[29] H. C. Öttinger, "The geometry and thermodynamics of dissipative quantum systems," Europhys. Lett. **94**, 10006 (2011).

[30] D. Taj and H. C. Öttinger, "Natural approach to quantum dissipation," Phys. Rev. A **92**, 062128 (2015).

[31] P. A. M. Dirac, *The Principles of Quantum Mechanics*, *International Series of Monographs on Physics*, 4th ed. (Oxford University Press, Oxford, 1981), Vol. 27.

[32] L. I. Schiff, *Quantum mechanics*, *International Series in Pure and Applied Physics*, 3rd ed. (McGraw-Hill, New York, 1968).

[33] H. C. Öttinger, *Beyond Equilibrium Thermodynamics* (Wiley, Hoboken, 2005).

[34] H. C. Öttinger, "Nonlinear thermodynamic quantum master equation: Properties and examples," Phys. Rev. A **82**, 052119 (2010).

[35] H. B. G. Casimir, "On Onsager's principle of microscopic reversibility," Rev. Mod. Phys. **17**, 343–350 (1945).

[36] H. C. Öttinger, "Irreversible dynamics, Onsager–Casimir symmetry, and an application to turbulence," Phys. Rev. E **90**, 042121 (2014).

[37] H. C. Öttinger, "Zero-temperature limit of thermodynamic quantum master equations," Phys. Rev. A **98**, 012131 (2018).

[38] M. Borrelli and H. C. Öttinger, "Dissipation in spin chains using quantized nonequilibrium thermodynamics," Phys. Rev. A **106**, 022220 (2022).

[39] J. Flakowski, M. Osmanov, D. Taj, and H. C. Öttinger, "Biexponential decay and ultralong coherence of a qubit," Europhys. Lett. **113**, 40003 (2016).

[40] H. C. Öttinger, "Stochastic process behind nonlinear thermodynamic quantum master equation. I. Mean-field construction," Phys. Rev. A **86**, 032101 (2012).

[41] J. Flakowski, M. Schweizer, and H. C. Öttinger, "Stochastic process behind nonlinear thermodynamic quantum master equation. II. Simulation," Phys. Rev. A **86**, 032102 (2012).

[42] M. Osmanov and H. C. Öttinger, "Open quantum systems coupled to time-dependent classical environments," Int. J. Thermodyn. **34**, 1255–1264 (2013).

[43] D. W. Oxtoby, "Vibrational relaxation in liquids," Annu. Rev. Phys. Chem. **32**, 77–101 (1981).

[44] V. May and O. Kühn, *Charge and Energy Transfer Dynamics in Molecular Systems* (Wiley-VCH, Weinheim, 2011).

[45] I. K. Kominis, "Radical-ion-pair reactions are the biochemical equivalent of the optical double-slit experiment," Phys. Rev. E **83**, 056118 (2011).

[46] A. Mielke, "On thermodynamical couplings of quantum mechanics and macroscopic systems," in *Mathematical Results in Quantum Mechanics*, edited by P. Exner, W. König and H. Neidhardt (World Scientific, Singapore, 2015), pp. 331–348.

[47] M. Kantner, A. Mielke, M. Mittnenzweig, and N. Rotundo, "Mathematical modeling of semiconductors: From quantum mechanics to devices," in *Topics in Applied Analysis and Optimisation, CIM Series in Mathematical Sciences*, edited by M. Hintermüller and J. F. Rodrigues (Springer, Cham, 2019), pp. 269–293.

[48] R. Levi, S. Masis, and E. Buks, "Instability in the Hartmann–Hahn double resonance," Phys. Rev. A **102**, 053516 (2020).

[49] H. C. Öttinger, *A Philosophical Approach to Quantum Field Theory* (Cambridge University Press, Cambridge, 2017).

[50] A. Oldofredi and H. C. Öttinger, "The dissipative approach to quantum field theory: Conceptual foundations and ontological implications," Eur. J. Philos. Sci. **11**, 18 (2021).

[51] R. Chessex, M. Borrelli, and H. C. Öttinger, "Fixed-point quantum Monte Carlo method: A combination of density-matrix quantum Monte Carlo method and stochastic unravellings," Phys. Rev. A **105**, 062803 (2022).

[52] R. Chessex, M. Borrelli, and H. C. Öttinger, "Dynamical triplet unraveling: A quantum Monte Carlo algorithm for reversible dynamics," Phys. Rev. A **106**, 022222 (2022).

[53] H. C. Öttinger, "Stochastic bra-ket interpretation of quantum mechanics," J. Phys. Commun. **8**, 105004 (2024).

[54] T. Pashby and H. C. Öttinger, "Quantum jump revival" (in press) (2025).

[55] V. Fock, "Konfigurationsraum und zweite Quantelung," Z. Phys. **75**, 622–647 (1932).

[56] P. Teller, *An Interpretive Introduction to Quantum Field Theory* (Princeton University Press, Princeton, 1995).

[57] D. Bohm, "A suggested interpretation of the quantum theory in terms of 'hidden' variables," Phys. Rev. **55**, 166–179 (1952).

[58] D. Dürr, S. Goldstein, and N. Zanghí, "Quantum equilibrium and the origin of absolute uncertainty," J. Stat. Phys. **67**, 843–907 (1992).

[59] M. Esfeld, M. Hubert, D. Lazarovici, and D. Dürr, "The ontology of Bohmian mechanics," Br. J. Philos. Sci. **65**, 773–796 (2014).

[60] D.-A. Deckert, M. Esfeld, and A. Oldofredi, "A persistent particle ontology for quantum field theory in terms of the Dirac sea," Br. J. Philos. Sci. **70**, 747–770 (2019).

[61] O. Passon, *Bohmsche Mechanik*, 2nd ed. (Harri Deutsch, Frankfurt, 2010).

[62] G. C. Ghirardi, A. Rimini, and T. Weber, "Unified dynamics for microscopic and macroscopic systems," Phys. Rev. D **34**, 470–491 (1986).

[63] J. S. Bell, "Are there quantum jumps?," in *Schrödinger, Centenary Celebration of a Polymath*, edited by C. W. Kilmister (Cambridge University Press, Cambridge, 1987), pp. 41–52.

[64] R. Tumulka, "A relativistic version of the Ghirardi–Rimini–Weber model," J. Stat. Phys. **125**, 825–844 (2006).

[65] H. Everett III, "'Relative state' formulation of quantum mechanics," Rev. Mod. Phys. **29**, 454–462 (1957).

[66] D. Wallace, *The Emergent Multiverse: Quantum Theory According to the Everett Interpretation* (Oxford University Press, Oxford, 2012).

[67] A. Einstein, B. Podolsky, and N. Rosen, "Can quantum-mechanical description of physical reality be considered complete?," Phys. Rev. **47**, 777–780 (1935).

[68] J. S. Bell, "On the Einstein Podolsky Rosen paradox," Phys. Phys. Fiz. **1**, 195–200 (1964).

[69] J. S. Bell, "On the problem of hidden variables in quantum mechanics," Rev. Mod. Phys. **38**, 447–452 (1966).

[70] S. J. Freedman and J. F. Clauser, "Experimental test of local hidden-variable theories," Phys. Rev. Lett. **28**, 938–941 (1972).

[71] A. Aspect, P. Grangier, and G. Roger, "Experimental realization of Einstein–Podolsky–Rosen–Bohm gedankenexperiment: A new violation of Bell's inequalities," Phys. Rev. Lett. **49**, 91–94 (1982).

[72] A. Aspect, "Bell's theorem: The naive view of an experimentalist," in *Quantum (Un)speakables: From Bell to Quantum Information*, edited by R. A. Bertlmann and A. Zeilinger (Springer, Berlin, 2002), pp. 119–153.

[73] A. Einstein, *Autobiographical Notes*, in *Albert Einstein: Philosopher–Scientist, the Library of Living Philosophers No. VII*, edited by P. A. Schilpp (The Library of Living Philosophers, Inc., Evanston, 1949), pp. 1–96.

[74] J. Moser, *Lectures on Hamiltonian Systems* (Memoirs of the American Mathematical Society, 1968), Vol. 81, pp. 1–60.

[75] J. M. Sanz-Serna and M. P. Calvo, *Numerical Hamiltonian Problems, Applied Mathematics and Mathematical Computation* (Chapman & Hall, London, 1994), Vol. 7.

[76] M. Krüger, M. Groß, and P. Betsch, "An energy-entropy-consistent time stepping scheme for nonlinear thermo-viscoelastic continua," Z. Angew. Math. Mech. **96**, 141–178 (2016).

[77] D. Portillo, J. C. García Orden, and I. Romero, "Energy-entropy-momentum integration schemes for general discrete non-smooth dissipative problems in thermomechanics," Int. J. Numer. Methods Eng. **112**, 776–802 (2017).

[78] M. Kraus and E. Hirvijoki, "Metriplectic integrators for the Landau collision operator," Phys. Plasmas **24**, 102311 (2017).

[79] H. C. Öttinger, "GENERIC integrators: Structure preserving time integration for thermodynamic systems," J. Non-Equilib. Thermodyn. **43**, 89–100 (2018).

[80] X. Shang and H. C. Öttinger, "Structure-preserving integrators for dissipative systems based on reversible-irreversible splitting," Proc. R. Soc. A **476**, 20190446 (2020).

[81] A. Zeilinger, R. Gähler, C. G. Shull, W. Treimer, and W. Mampe, "Single- and double-slit diffraction of neutrons," Rev. Mod. Phys. **60**, 1067–1073 (1988).

[82] Y. Aharonov, E. Cohen, F. Colombo, T. Landsberger, I. Sabadini, D. C. Struppa, and J. Tollaksen, "Finally making sense of the double-slit experiment," Proc. Natl. Acad. Sci. U. S. A. **114**, 6480–6485 (2017).

[83] S. V. Gantsevich, "Common sense and quantum mechanics," Ann. Math. Phys. **5**, 196–198 (2022).

APL Quantum

RESEARCH ARTICLE | APRIL 14 2025

Designer gapped and tilted Dirac cones in lateral graphene superlattices

Special Collection: Quantum Dynamics in Theory, Numerics and in Experimental Research

A. Wild ; R. R. Hartmann ; E. Mariani ; M. E. Portnoi

APL Quantum 2, 026107 (2025)
https://doi.org/10.1063/5.0251887

AIP Publishing

APL Quantum ARTICLE pubs.aip.org/aip/apq

Designer gapped and tilted Dirac cones in lateral graphene superlattices

Cite as: APL Quantum 2, 026107 (2025); doi: 10.1063/5.0251887
Submitted: 5 December 2024 • Accepted: 28 March 2025 •
Published Online: 14 April 2025

A. Wild,[1] R. R. Hartmann,[2] E. Mariani,[1] and M. E. Portnoi[1,a)]

AFFILIATIONS

[1] Physics and Astronomy, University of Exeter, Stocker Road, Exeter EX4 4QL, United Kingdom
[2] Physics Department, De La Salle University, 2401 Taft Avenue, 0922 Manila, Philippines

Note: This paper is part of the APL Quantum Special Topic on Quantum Dynamics in Theory, Numerics and in Experimental Research.

[a)] **Author to whom correspondence should be addressed:** m.e.portnoi@exeter.ac.uk

ABSTRACT

We show that a planar array of bipolar waveguides in graphene can be used to engineer gapped and tilted two-dimensional Dirac cones within the electronic band structure. The presence of these gapped and tilted Dirac cones is demonstrated through a superlattice tight-binding model and verified using a transfer matrix calculation. By varying the applied gate voltages, the tilt parameter of these Dirac cones can be controlled, and their gaps can be tuned to fall in the terahertz range. The possibility of gate-tunable gapped Dirac cones gives rise to terahertz applications via interband transitions and designer Landau level spectra, both of which can be controlled via Dirac cone engineering. We anticipate that our paper will encourage Dirac cone tilt and gap engineering for gate-tunable device applications in lateral graphene superlattices.

I. INTRODUCTION

The relativistic nature of graphene's charge carriers leads to its fascinating optical and electronic properties.[1,2] Its discovery opened the door to the exploration of relativistic physics in condensed matter systems. Indeed, the rise of graphene inspired the search for new designer materials with ultra-relativistic spectra, such as 8-*Pmmn* borophene. This theoretical material is predicted to contain two-dimensional (2D) tilted Dirac cones in its electronic band structure in the vicinity of the Fermi level.[3] With its discovery came an explosion of interest in the physics arising from tilted Dirac cones. These cones can either be gapped or gapless and come in three types: type-I (sub-critically tilted), type-II (super-critically tilted), or type-III (critically tilted).[4,5] Each geometry gives rise to spectacularly different optical,[6–10] transport,[11–13] and thermal properties[14–16] and more.[17–24] For device applications, it would be highly desirable to be able to switch between different types of tilted Dirac cones in a single system post-fabrication.

Currently, there is a dearth of practical, tunable electronic systems that exhibit 2D tilted Dirac cones. Several theoretical materials with specific lattice geometries have been predicted to support electronically tilted Dirac cones.[3,25–39] However, after synthesis, crystalline structures cannot be practically changed to tune the tilt or modify the gap of these cones. Rather than placing real atoms in a particular lattice configuration, we propose to approach the problem using artificial atoms, namely, bound states trapped inside graphene wells and barriers organized in a lateral superlattice.

In contrast to non-relativistic systems, both electrostatic wells and barriers in graphene support bound states. These bound states are localized about the center of the confining potentials, much like atomic orbitals in a crystal are centered about their lattice positions. The confined states of a well and barrier overlap, much like adjacent atomic orbitals. This overlap can be characterized by the hopping parameter in the famous tight-binding model. Unlike a real crystal, where the overlap between adjacent orbitals is fixed, the overlap between well and barrier functions can be completely controlled. This can be achieved by varying the height and depth of the confining potentials via their top-gate voltages. Hence, constructing a superlattice from wells and barriers in graphene mimics the band structure of an atomic lattice but with the advantage of a newfound

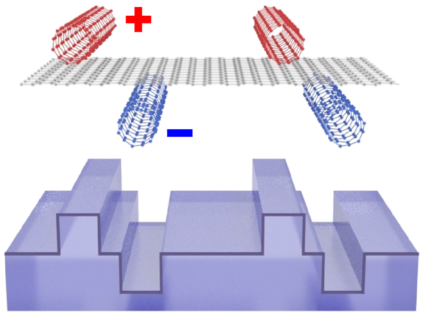

FIG. 1. Schematic of a planar array of bipolar waveguides in graphene created by carbon nanotubes gated with alternating polarity. The electrostatic potential created by the applied gate voltages is shown below. Please note that this schematic is not to scale; the proposed well/barrier separation is on the order of 50 nm and, thus, significantly larger than nanotube radii.

tunability. Thus, moving band structure engineering in condensed matter physics is in the same direction as optical control in designer metamaterials.[40]

In what follows, we show that a lateral superlattice comprised of repeating well and barrier pairs, i.e., a bipolar array (see Fig. 1), hosts gapped and tilted Dirac cones in the band structure. By varying the applied voltage profile of the superlattice, the tilt of these Dirac cones can be controlled and the bandgap can be tuned to energies corresponding to terahertz (THz) photons. By calculating the velocity matrix element in the vicinity of the gapped Dirac cones, we prove that the bipolar array in graphene will constitute a platform for tunable terahertz optics. While we demonstrate the existence of tunable tilted and gapped Dirac cones in the electronic band structure, we emphasize that these cones are satellites to a central gapless cone. In contrast to Dirac cones in pristine graphene, these central cones are anisotropic in momentum space, possessing elliptical isoenergy contours. Applying a magnetic field normal to the plane of the bipolar array creates a platform for gate-tunable Landau level spectra via Dirac cone engineering. Due to the presence of central gapless and satellite gapped Dirac cones, the Landau level spectra simultaneously contain features of massless and massive Dirac fermions.

II. MODEL

A lateral graphene superlattice can be modeled as an artificial crystal. While in a crystalline material, electrons hop between adjacent atomic orbitals; in a lateral superlattice, electrons hop between neighboring well and barrier sites. Thus, to calculate the band structure of a bipolar array in graphene, we shall use a simple nearest-neighbor tight-binding model.

Let us first consider one artificial atom (i.e., a square quantum well or barrier) in our superlattice. Although realistic top-gated structures in graphene generate smooth guiding potentials[41–43] (i.e., varying on a length scale much larger than the lattice constant), they can be modeled as square potentials with an effective depth and width. This is because the number of bound states in a potential is dictated by the product of its effective depth and width. It should be noted that in what follows, we consider sharp-but-smooth square potentials, i.e., we neglect inter-valley scattering. The effective one-dimensional matrix Hamiltonian for confined modes in a graphene waveguide can be written as

$$\left[\hat{H}_{\mathrm{G}} + U(x)\mathbb{I}\right]|\psi(x)\rangle = E|\psi(x)\rangle, \tag{1}$$

where $\hat{H}_{\mathrm{G}} = v_{\mathrm{F}}(\sigma_x \hat{p}_x + s_{\mathrm{K}}\sigma_y \hbar k_y)$, which acts on the spinor wavefunction defined in the standard basis of graphene sub-lattice Bloch sums $|\psi(x)\rangle = \psi_A(x)|\Phi_A\rangle + \psi_B(x)|\Phi_B\rangle$. The Pauli matrices are $\boldsymbol{\sigma} = (\sigma_x, \sigma_y, \sigma_z)$, the identity matrix is $\mathbb{I}$, the momentum operator is defined as $\hat{p}_x = -i\hbar\partial_x$, and k_y is a wavenumber corresponding to the motion along the waveguide. Here, the Fermi velocity in graphene is $v_{\mathrm{F}} \approx 10^6\ \mathrm{ms}^{-1}$, the energy eigenvalue is E, and the graphene valley index is $s_{\mathrm{K}} = \pm 1$. The square potential $U(x)$ is defined as

$$U(x) = \begin{cases} U, & |x| \le W/2, \\ 0, & \text{elsewhere}, \end{cases} \tag{2}$$

where W is the width of the potential and $U < 0$ for a well and $U > 0$ for a barrier. The eigenvalues of Eq. (1) can be obtained via the method outlined in Ref. 44. For zero-energy states ($E = 0$), the eigenvalue problem simplifies and the wavefunction takes on a simple form (see Appendix A)—these zero-energy well and barrier wavefunctions will be utilized later in this paper. In Fig. 2, we superimpose the energy spectra for various square wells and barriers. Each potential has the same width and contains only a few modes within. This occurs when the normalized product of the potential height and width ($|U|W/\hbar v_{\mathrm{F}}$) is of the order of unity. Indeed, few-mode smooth electron waveguides in graphene can be experimentally realized using carbon nanotubes as top-gates.[45]

As shown in Fig. 2, varying the potential strengths of the well and barrier results in differing group velocities at the crossing point.

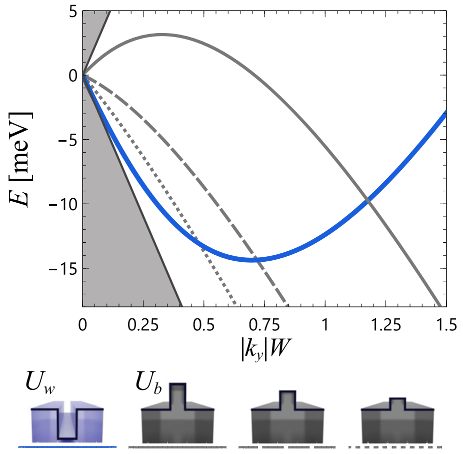

FIG. 2. Energy spectrum of confined states within a well of applied voltage $U = -120$ meV (blue) and three barriers of strengths 90 meV (gray solid), 60 meV (gray dashed), and 45 meV (gray dotted) in graphene—in each case the well/barrier width is $W = 15$ nm. The band dispersions are sketched in units of energy E in millielectron volts (meV) and wavevector associated with motion along the potentials k_y normalized by the well/barrier width. The formed band crossings are of type-I, type-III, and type-II, respectively. Tuning the barrier height and well depth changes the tilt of the band crossings. The gray regions contain continuum states outside of the guiding potentials.

Thus, the crossing formed by an isolated well and barrier can be switched between type-I, type-II, or type-III by simply changing the potential strength of the well and barrier. However, by superimposing the band dispersions of an isolated well and barrier, we have neglected any coupling between the two systems. When we bring the well and barrier closer together, the overlap between the barrier and well states leads to an anticrossing (pseudogap) appearing at the original band crossing [see Fig. 3(a)].[46] For bipolar waveguides created by carbon nanotube top-gates atop graphene, the pseudogap is of the order of several THz.[46,47] However, a single well and barrier does not constitute a macroscopic device, and for realistic THz applications, an important question must be answered: How is the band structure of a single bipolar waveguide modified when placed into a superlattice?

The Hamiltonian of a planar bipolar array $\hat{H}$ can be written as

$$\hat{H} = \hat{H}_{\mathrm{G}} + \sum_{j=1}^{N} \left[U_b(x - x_j) + U_w(x - x_j - a) \right], \tag{3}$$

where $U_b(x)$ and $U_w(x)$ are the individual barriers and wells [defined through Eq. (2)], centered at positions x_j and $x_j + a$, respectively, where $x_j = jL$ is a lattice vector, L is the width of the superlattice unit cell, and a is the distance between the centers of a well and barrier within the unit cell. Since the dispersion of any realistic guiding potential is determined by the product of the potential's depth and width, henceforth, we fix the width of all barriers and wells, W, to be the same. For square potentials, the well position within the unit cell must satisfy $a > W$, while the unit cell width must be larger than the sum of the well and barrier width, $L > 2W$.

One may envisage a bipolar array created by sandwiching a graphene sheet in between two planar arrays of nanotubes, with the top array gated at one polarity and the bottom array at the opposite polarity. The relative position of these two arrays (parameterized by a) will be fixed after device fabrication. In a realistic device, it will not be possible to align the two arrays exactly in such a way that each tube is equally separated; in general, the two arrays will be separated by some arbitrary distance ($a \neq L/2$). While we have highlighted the example of using carbon nanotubes to generate each well and barrier potential,[45] we note that our theory applies to any technique used to generate a one-dimensional periodic electrostatic potential to graphene, e.g., striped dielectrics[48] and gates.[49,50]

A. Tight-binding model of a bipolar array in graphene

In a similar fashion to the splitting of atomic energy levels in the formation of a crystal, the bringing together of N bipolar waveguides results in each energy level of the well and barrier splitting into N sub-levels. Each sub-level corresponds to a particular quantized k_x. In the limit that N becomes large, k_x can be treated as a continuous parameter on an equal footing with k_y, the wavevector along the guiding potentials.

The basis functions of the superlattice can be expressed as a linear combination of individual well and barrier wave functions, i.e., Bloch sums,

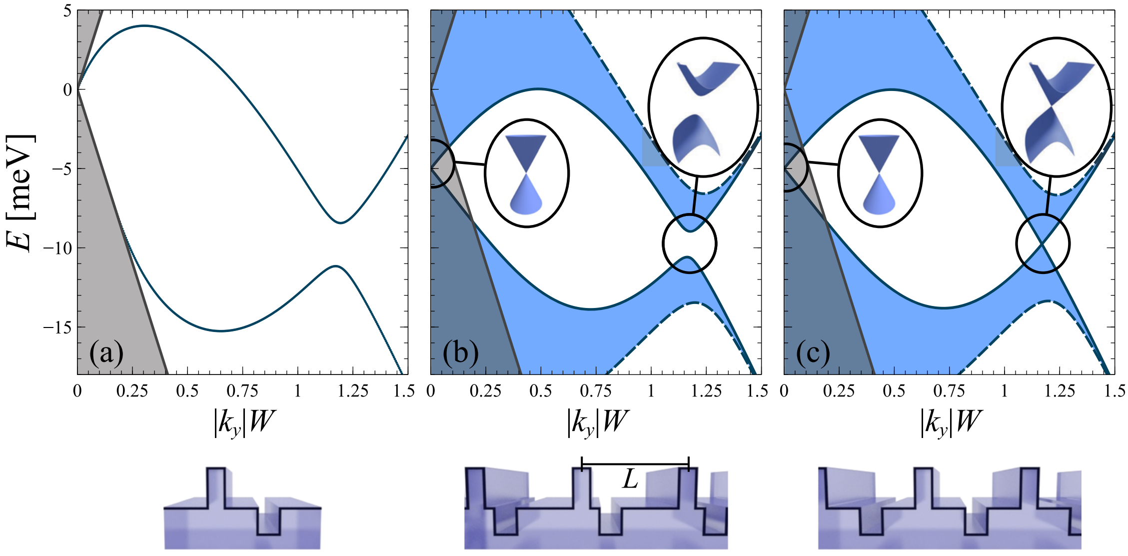

FIG. 3. Band structure and schematics of (a) single bipolar waveguide, (b) bipolar array without reflection symmetry, and (c) bipolar array with reflection symmetry. The bipolar array with or without reflection symmetry possesses a gapless Dirac cone at the center of the electronic band structure. In addition, the bipolar array without reflection symmetry hosts satellite gapped tilted Dirac cones, while the bipolar array with reflection symmetry hosts satellite gapless tilted Dirac cones. The band structures are plotted in terms of energy (E) in units of millielectron volts (meV) and wavevector along the potentials k_y normalized by the well/barrier widths $W = 15$ nm. In all cases, the applied barrier and well potentials are $U_b = 90$ meV and $U_w = -120$ meV, respectively. For the bipolar array, the unit cell width is $L = 90$ nm and the position of the well within the unit cell is determined by the parameter $a = 48$ nm in panel (b) and $a = 45$ nm in panel (c). The gray areas correspond to energies and wavevectors that support plane wave solutions across the entire potential. The periodicity of the superlattice yields an additional wavevector $|k_x| \leq \pi/L$, where L is the size of the unit cell. The band structures in panels (b) and (c) were calculated using a transfer matrix model. These panels display orthographic projections of the band structures as viewed along the k_x axis. The band edges are depicted by solid lines ($k_x = 0$) or dashed lines ($k_x = \pm\pi/L$), with intermediate values shaded in blue.

$$|\Phi_b\rangle = \frac{1}{\sqrt{N}} \sum_{j=1}^{N} e^{ijk_x L} |\psi_b(x - x_j)\rangle, \tag{4}$$

$$|\Phi_w\rangle = \frac{e^{ik_x a}}{\sqrt{N}} \sum_{j=1}^{N} e^{ijk_x L} |\psi_w(x - x_j - a)\rangle, \tag{5}$$

where $|k_x| \le \pi/L$ is the superlattice wavevector and the well and barrier functions $|\psi_w(x)\rangle$ and $|\psi_b(x)\rangle$ are the solutions to Eq. (1) with potentials $U_w(x)$ and $U_b(x)$, respectively, for a given wavevector along the guiding potentials k_y. Here, we have utilized the so-called atom gauge, where the orbital center of the well and barrier states are encoded in the phase of the Bloch sums[51] [another common choice is the cell gauge, where the $e^{ik_x a}$ term is omitted from Eq. (5)]. The eigenvalues of the superlattice as a function of k_x (the superlattice wavevector) are determined from the secular equation $\det(\mathscr{H} - E\mathbb{I}) = 0$, where the elements of the Bloch Hamiltonian are defined as $\mathscr{H}_{\alpha\beta} = \int \langle \Phi_\alpha | \hat{H} | \Phi_\beta \rangle \mathrm{d}x$, where $\alpha, \beta = w$ or b.

We intend to model the electronic dispersion of a superlattice in the vicinity of the original band crossings of the first well and barrier modes (see Fig. 2). These crossings occur at wavevectors $k_y = K_y = s|K_y|$, where $s = 1$ or -1. To determine the diagonal elements of the Bloch Hamiltonian, we approximate the well and barrier band dispersion with linear functions, i.e.,

$$\int_{-\infty}^{\infty} \langle \psi_b(x) | \hat{H} | \psi_b(x) \rangle \,\mathrm{d}x \approx s\hbar v_b (k_y - K_y) \tag{6}$$

and

$$\int_{-\infty}^{\infty} \langle \psi_w(x) | \hat{H} | \psi_w(x) \rangle \,\mathrm{d}x \approx s\hbar v_w (k_y - K_y), \tag{7}$$

where $v_w > 0$ and $v_b < 0$ are the well and barrier group velocities at the crossing point (see Fig. 2). The inclusion of higher-order terms, such as an effective mass, is discussed in Sec. III. Note that the offset energy (E_{off}) of these functions has been omitted for brevity. To determine the off-diagonal elements of the Bloch Hamiltonian, we define the nearest-neighbor overlap integrals using the well and barrier wavefunctions at the crossing wavevector $k_y = K_y = s|K_y|$. We can write the intra-cell hopping integral as

$$\gamma_{\text{intra}} = \int_{-\infty}^{\infty} \langle \psi_b(x) | \hat{H} | \psi_w(x - a) \rangle \,\mathrm{d}x \tag{8}$$

and the inter-cell hopping integral as

$$\gamma_{\text{inter}} = \int_{-\infty}^{\infty} \langle \psi_b(x) | \hat{H} | \psi_w(x + L - a) \rangle \,\mathrm{d}x. \tag{9}$$

Combining Eqs. (3)–(9) and performing a nearest-neighbor tight-binding calculation yields the Bloch Hamiltonian in the vicinity of the original band crossing,

$$\mathscr{H}(\mathbf{k}) = \begin{bmatrix} s\hbar v_w (k_y - K_y) & f(k_x) \\ f^*(k_x) & s\hbar v_b (k_y - K_y) \end{bmatrix}, \tag{10}$$

where

$$f(k_x) = \gamma_{\text{intra}} e^{-ik_x a} + \gamma_{\text{inter}} e^{ik_x (L-a)}. \tag{11}$$

We note that along the superlattice wavevector (k_x) axis, the Bloch Hamiltonian resembles the Su–Schrieffer–Heeger (SSH) model—the tight-binding model used to describe dimerized atomic chains, e.g., polyacetylene.[52]

As is standard in tight-binding methods, the model parameters (i.e., v_w, v_b, γ_{intra}, and γ_{inter}) can be fit to data, e.g., a numerical calculation of the band structure [see Fig. 3(b)] computed via a transfer matrix (see Appendix B for methods). While the magnitude of the hopping parameters is determined by intra- and inter-cell well and barrier separation, the presence of a band minima at $k_x = 0$ dictates that γ_{intra} and γ_{inter} have opposite signs. Furthermore, it can be shown that switching the sign of the wavevector along the guiding potentials (s) or the graphene valley index (s_{K}) flips the sign of the hopping parameters (see Appendix C). Combining these conditions, we can define $\gamma_{\text{intra}} = s_{\text{K}} s \gamma_1$ and $\gamma_{\text{inter}} = s_{\text{K}} s \gamma_2$, where $\gamma_1 > 0$ and $\gamma_2 < 0$.

B. Emergence of gapped and tilted Dirac cones

We now demonstrate the existence of gapped and tilted Dirac cones within the electronic band structure. These Dirac cones can be found at the local band minima, i.e., $k_y = s|K_y|$ and $k_x = 0$. To capture the quadratic band dispersion of the gapped and tilted Dirac cone, we must expand the Bloch Hamiltonian to the second-order in the wavevector. By performing a specific unitary transformation, we can eliminate second-order terms from the Hamiltonian and determine the Dirac cone velocity parameters. We perform the following unitary transformation: $\mathscr{H}'(\mathbf{k}) = \mathscr{U}(k_x)\mathscr{H}(\mathbf{k})\mathscr{U}^\dagger(k_x)$, where

$$\mathscr{U}(k_x) = \frac{1}{\sqrt{2}} \begin{bmatrix} e^{ik_x(a-l)} & e^{ik_x l} \\ ie^{ik_x(a-l)} & -ie^{ik_x l} \end{bmatrix}, \tag{12}$$

with $l = \left[\left(\gamma_2 + \sqrt{|\gamma_1 \gamma_2|}\right)/2(\gamma_1 + \gamma_2)\right] L$. This wavevector-dependent unitary transformation moves our Bloch sums out of the atom gauge [originally defined in Eqs. (4) and (5)]. This unitary transformation does not affect the electronic band structure but can affect the calculation of optical transitions—we discuss this point further in Sec. IV. Performing an expansion in terms of $q_x = k_x$ now reveals an effective Bloch Hamiltonian with no second-order wavevector terms,

$$\mathscr{H}'(\mathbf{q}) = s_{\text{K}} s \frac{E_g}{2} \sigma_z + s\hbar v (t q_y \mathbb{I} + q_y \sigma_y + s_{\text{K}} T q_x \sigma_x), \tag{13}$$

where v is the modified Fermi velocity, t is a tilt parameter, T is a Fermi velocity anisotropy factor, E_g is the local bandgap, and $\mathbf{q} = (q_x, q_y)$ is the deviation in wavevector from the Dirac point where $q_y = k_y - K_y$. We note that the offset energy has been omitted for brevity. The effective velocity, tilt, and anisotropy parameters can be expressed through $v = (v_w - v_b)/2$, $t = (v_w + v_b)/2v$, and $T = \sqrt{|\gamma_1 \gamma_2|} L/\hbar v$, respectively. Furthermore, the gap parameter can be defined through the nearest-neighbor tight-binding hopping integrals $|E_g| = 2|\gamma_1 + \gamma_2|$. Indeed, Eq. (13) is the well-known Dirac cone Hamiltonian possessing a tilted dispersion along the q_y axis, a non-tilted dispersion along the q_x axis, and a local bandgap. In contrast to tilted Dirac cone materials formed by crystalline lattices, features such as Dirac cone tilt (t) and bandgap (E_g) can be tuned by varying the applied gate voltages of the bipolar array. Throughout the rest of this paper, we will investigate how varying the voltage profiles of the bipolar array results in gate-tunable phenomena stemming from Dirac cone engineering.

It should be noted that previous studies of graphene superlattices have been limited to periodic wells/barriers,[53–56] sinusoidal[57,58] periodic even/odd potentials,[59] or electromagnetic potentials[60] that had reflection symmetry and, thus, did not open a gap in the Dirac cone. Indeed, we can recover these results by considering the specific case $a = L/2$, where the bipolar potential possesses a reflection plane and the bandgap of the tilted cones vanishes ($\gamma_1 = -\gamma_2$ and $E_g = 0$) [see Fig. 3(c)].

Although we have discussed the role of superlattice geometry in opening bandgaps in Dirac cones, we emphasize that the full band structure of the bipolar array remains gapless. This is due to gapless Dirac cones that exist at $\mathbf{k} = \mathbf{0}$ for all superlattice geometries[53,54,59] (see Fig. 3). In this respect, the previously discussed tilted and gapped Dirac cones are satellites to a central gapless Dirac cone. This central Dirac cone is not tilted and has elliptical isoenergy contours, which can be fitted by the phenomenological Fermi velocities along the k_x ($v_{c,x} \le v_{\mathrm{F}}$) and k_y ($v_{c,y} \le v_{\mathrm{F}}$) wavevector axes. The energy offset of the central Dirac cone is equal to the average potential of the bipolar array $W(U_b + U_w)/L$.

C. Details on the nearest-neighbor tight-binding model

When applied to crystalline materials, the standard nearest-neighbor tight-binding assumes that each atomic orbital is well-localized to its respective lattice site. In the context of this work, our analytic theory most closely matches the numerical transfer matrix calculations when the individual well and barrier states are sufficiently localized to the confining potential. Outside of the confining well and barrier potentials, the wavefunctions corresponding to the crossing wavevector $k_y = K_y$ and crossing energy E_{off} are proportional to $e^{\widetilde{\kappa} x}$ (to the left of the potential) or $e^{-\widetilde{\kappa} x}$ (to the right of the potential), where $\widetilde{\kappa} = (1/\hbar v_{\mathrm{F}})\sqrt{(\hbar v_{\mathrm{F}} K_y)^2 - E_{\mathrm{off}}^2}$. Provided that each wavefunction is sufficiently localized within a single superlattice unit cell ($\widetilde{\kappa} L \gg 1$), we need not consider additional next nearest-neighbor hopping terms. For example, in Fig. 3, where $|K_y|W \approx 1.2$ and $E_{\mathrm{off}} \approx -10$ meV, it can be checked that $\widetilde{\kappa} L \approx 7$, thereby justifying the use of the nearest-neighbor tight-binding model. It should also be noted that the boundary conditions of finite and infinite bipolar arrays are different. Namely, in finite arrays, the wavefunction must decay outside of the outermost wells, whereas for the infinite case, the system is subject to the Born–von Karman boundary conditions. Consequently, in finite systems, no guided modes exist in the region where $|E| > \hbar v_{\mathrm{F}} |k_y|$ (gray regions of Fig. 3). Conversely, in the infinite case, guided modes are supported in this region.

III. GAPPED DIRAC CONES WITH GATE-TUNABLE TILT

Gapped and tilted Dirac cones have been a topic of intense research. As previously discussed, modifying the degree of tilt leads to drastically different emergent system behavior. As was demonstrated in the context of isolated well and barrier band crossings, the tilt t of Dirac cones in a bipolar array can be modified by tuning the applied gate voltages. For example, as shown in Fig. 4, varying the barrier height or well depth tunes the tilt parameter. Interchanging the well depth and barrier height flips the sign of the tilt parameter of the gapped satellite Dirac cones. The experimental ability to continually change the tilt parameter across a broad range of values means that it can be viewed as an additional degree of freedom in device applications. As an example of this, in Sec. V, we explore how varying the tilt of gapped Dirac cones within the electronic band structure will lead to gate-tunable Landau level spectra.

The tilted and gapped Dirac cones in Fig. 4 correspond to sub-critically tilted type-I ($|t| < 1$) gapped Dirac cones. We note that it is possible to increase the tilt parameter further toward critically tilted type-III ($|t| = 1$) and super-critically tilted type-II ($|t| > 1$) Dirac cones. We note that for over-tilted Dirac cones (particularly the critically tilted type-III case), one branch of the electronic band dispersion appears quadratic rather than linear (see Fig. 2). When lacking a bandgap, these cones are known as three-quarter Dirac points and possess interesting properties such as Landau levels with energy that scales to the four-fifth power of magnetic field strength

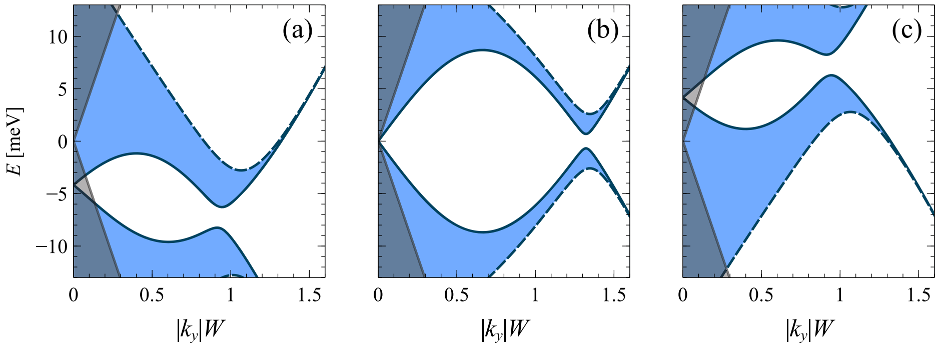

FIG. 4. Orthographic projections of the band structures of three bipolar arrays as viewed along the superlattice wavevector. In each plot, the location of the well within the unit cell is $a = 48$ nm, the well and barrier widths are $W = 15$ nm, and the superlattice unit cell width is $L = 90$ nm. The well and barrier potentials in each panel are $U_b = 85$ meV and $U_w = -110$ meV in panel (a), $U_b = 110$ meV and $U_w = -110$ meV in panel (b), and $U_b = 110$ meV and $U_w = -85$ meV in panel (c). Varying the well and barrier potentials can be seen to change the tilt of the satellite gapped and tilted Dirac cones within the electronic band structure. The band structures were calculated using a transfer matrix and are plotted in terms of energy E in units of millielectron volts (meV), wavevector along the guiding potentials k_y, and superlattice wavevector k_x. In the orthographic projection, the band edges are depicted by solid lines ($k_x = 0$) or dashed lines ($k_x = \pm\pi/L$), with intermediate values shaded in blue. The gray areas correspond to energies and wavevectors that support plane wave solutions across the entire potential.

TABLE I. Tight-binding model parameters for a bipolar array characterized by two voltage profiles: $U_b = -U_w = U_0 = 210$ meV (model A) and $U_0 = 175$ meV (model B). In each case, the well and barrier widths are $W = 10$ nm, the superlattice unit cell is $L = 50$ nm, and the well is centered at $a = 27.5$ nm within the superlattice cell.

Model	U_0/meV	$\lvert K_y\rvert W$	$v_0/v_{\rm F}$	γ_1/meV	γ_2/meV
A	210	2.18	0.68	0.52	−1.56
B	175	1.52	0.57	1.86	−3.99

B and Landau level index n, i.e., $E_n \propto (nB)^{4/5}$.[61,62] The properties of these three-quarter Dirac fermions (with and without a bandgap) could be accounted for in our model by adding an effective mass (m^*) to either the well or barrier modes. For example, amending the well dispersion, $s\hbar v_w q_y + \hbar^2 q_y^2/2m^*$, which was originally defined in Eq. (7), adds a quadratic term $(\hbar^2 q_y^2/4m^*)(\mathbb{I} + \sigma_y)$ to the gapped Dirac cone Hamiltonian given in Eq. (13). Therefore, in realistic critical (type-III) and super-critical (type-II) tilted Dirac cone materials, the gapped and tilted Dirac cone Hamiltonian may possess an additional quadratic term. This addition to the tilted Dirac cone Hamiltonian goes beyond the standard model used to predict the emergent physics of tilted Dirac cone materials and, thus, constitutes an interesting avenue for future study.

IV. TUNABLE DIRAC CONE GAP AND TERAHERTZ TRANSITIONS

In traditional tight-binding models, the atomic orbital wavefunctions are not known; as a result, model parameters such as hopping integrals are fit to experiment. For the case of equal well and barrier strengths $(U_b = -U_w = U_0)$, the band crossing occurs at zero-energy, resulting in non-tilted $(v_w = -v_b = v_0$ and $t = 0)$ Dirac cones in the electronic band structure. In this case, the well and barrier wavefunctions can be found analytically. These wavefunctions yield a transcendental equation for the crossing wavevector K_y, analytic expressions for the well and barrier group velocities v_0, as well as the hopping parameters γ_1 and γ_2 (see Appendixes A and C). For example, let us consider a bipolar array characterized by the geometry parameters $W = 10$ nm, $L = 50$ nm, and $a = 27.5$ nm. We consider realistic potential strengths,[45] e.g., $U_0 = 210$ meV and $U_0 = 175$ meV in models A and B, respectively. For these two models, we can derive values for the tight-binding parameters (see Table I). Substituting these parameters into the effective Bloch Hamiltonian [see Eq. (10)] provides an accurate match to the electronic band structure obtained via a transfer matrix [see Figs. 5(a) and 5(d)].

Using expressions for the tight-binding hopping parameters, we can derive an expression that directly determines the Dirac cone bandgap from the bipolar array geometry,

$$|E_g| = E_0 \sinh\left(\frac{|K_y||L-2a|}{2}\right) e^{-|K_y|L/2}, \tag{14}$$

where $E_0 = 4\hbar^3 v_{\rm F}^3 |K_y| \widetilde{K}^2 e^{|K_y|W} / U_0^2 (1 + |K_y|W)$, and $|K_y|$ satisfies the transcendental equation $\widetilde{K} = -|K_y| \tan(\widetilde{K}W)$ with $\widetilde{K} = (1/\hbar v_{\rm F})\sqrt{U_0^2 - (\hbar v_{\rm F} K_y)^2}$ (see Appendix C). By varying the voltage profile of a bipolar array, we can tune the Dirac cone bandgap within the THz regime: $E_g = 0.50$ THz for model A and $E_g = 1.03$ THz for model B.

The possibility of tuning the local bandgap of the Dirac cones into the THz regime provides a route to THz applications arising from interband transitions. We assume that the offset gate voltage of the superlattice places the Fermi level within the bandgap of the gapped Dirac cones. Upon illumination of light, a photon of energy $h\nu$ can excite an electron from the valence band up to an empty state in the conduction band provided that the photon energy is equal to the energy separation of the states $h\nu = E_+(\mathbf{k}) - E_-(\mathbf{k})$. The probability of optical transitions between some state at some wavevector $\mathbf{k}$ is determined by the absolute value square of the velocity matrix element (VME) $|v_{\rm cv}(\mathbf{k})|^2$, where

$$v_{\rm cv}(\mathbf{k}) = \langle \Psi_\mp(\mathbf{k}) | \hat{\mathbf{e}} \cdot \mathbf{v}(\mathbf{k}) | \Psi_\pm(\mathbf{k}) \rangle. \tag{15}$$

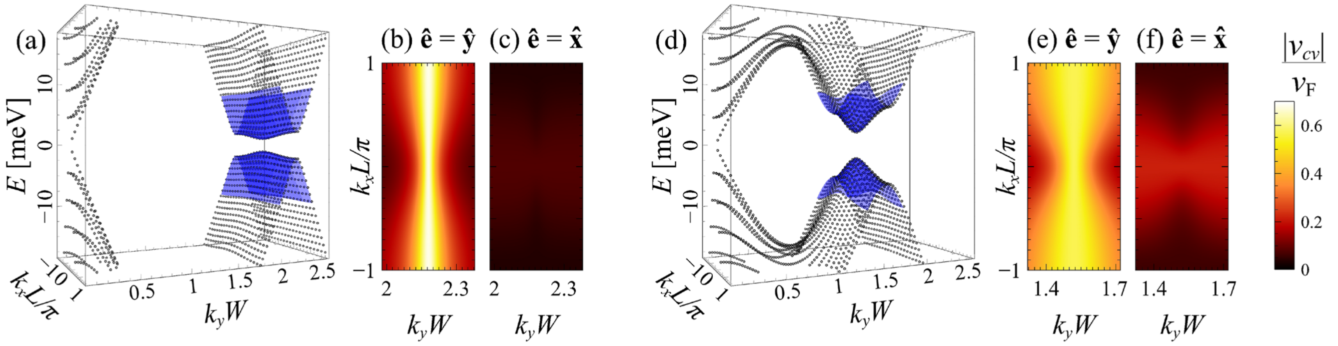

FIG. 5. Electronic band dispersions and velocity matrix elements for two bipolar array geometries with well and barrier heights: (a)–(c) $U_b = -U_w = 210$ meV and (d)–(f) $U_b = -U_w = 175$ meV. In both cases, the superlattice unit cell width is $L = 50$ nm, well, and barrier width is $W = 10$ nm, and the separation between the well and barrier within one unit cell is $a = 27.5$ nm. In panels (a) and (d), the full electronic band structure (black dots) is obtained via a transfer matrix calculation and is plotted over a finite range of wavevectors along the guiding potentials $(0 \le k_yW \le 2.6)$, and the full Brillouin zone along the superlattice axis $(|k_x|L \le \pi/L)$. In the vicinity of the gapped Dirac cones, we plot the analytic approximation to the full band structure (blue surface) obtained via the superlattice tight-binding model. Using this analytic approximation to the band structure, we plot the absolute value of the velocity matrix element $|v_{\rm cv}(\mathbf{k})|$ for light polarized along ($\hat{\mathbf{y}}$ axis) and perpendicular ($\hat{\mathbf{x}}$ axis) to the guiding potentials for both cases.

Here, $|\Psi_{\pm}(\mathbf{k})\rangle$ are the conduction $(+)$ and valence $(-)$ states of the low-energy Bloch Hamiltonian given in Eq. (10), $\mathbf{v}(\mathbf{k})$ is the velocity operator, and $\hat{\mathbf{e}} = e_x\hat{\mathbf{x}} + e_y\hat{\mathbf{y}}$ is the polarization vector of light. We note that we utilize the eigenstates $|\Psi_{\pm}(\mathbf{k})\rangle$ and velocity operator $\mathbf{v}(\mathbf{k})$ defined in the basis of well and barrier Bloch sums $|\Phi_w\rangle$ and $|\Phi_b\rangle$. Considering that this Bloch Hamiltonian is in the so-called atom gauge, the velocity operator can be conveniently determined through the gradient approximation $\mathbf{v}(\mathbf{k}) = (1/\hbar)\nabla_{\mathbf{k}}\mathscr{H}(\mathbf{k})$.[51]

In Fig. 5, we plot the absolute value of the VME for a range of wavevectors in the vicinity of the gapped Dirac cones. Here, we consider a single bipolar array with two different voltage profiles, i.e., models A and B with parameters given in Table I. Optical transitions are supported in the vicinity of the gapped Dirac cones for all polarizations of light. For light polarized along the guiding potentials $(\hat{\mathbf{e}} = \hat{\mathbf{y}})$, the max value of the VME is v_0 (for $k_y = K_y$), while for light polarized along the array axis $(\hat{\mathbf{e}} = \hat{\mathbf{x}})$, the max value of the VME is $|(L-a)\gamma_2 - a\gamma_1|/\hbar$ (for $k_x = 0$). For light polarized along the guiding potentials $(\hat{\mathbf{e}} = \hat{\mathbf{y}})$, we see that optical transitions are guaranteed for photons with energies spanning $2|\gamma_1 + \gamma_2|$ to $2|\gamma_1 - \gamma_2|$. Varying the voltage profile of the bipolar array allows for convenient control over this bandwidth after device fabrication. In this frequency regime, there appears to be a preference to absorb photons polarized along the $\hat{\mathbf{y}}$ axis; thus, a bipolar array in graphene could be used as a component in a tunable thin-film THz polarizer.

In Fig. 5, we clearly observe the optical momentum alignment phenomenon in which photoexcited electrons are aligned with wavevectors perpendicular to the plane of polarizing light. Combining this momentum alignment phenomenon with the tilt[63] or warping[64] of the satellite Dirac cones could result in the spatial separation of photoexcited carriers belonging to different satellite cones (differentiated by the index s). The optical properties of gapless and gapped tilted Dirac cones are discussed in detail within Refs. 8, 10, and 65, respectively.

We can also investigate the absorption of right-handed $\hat{\mathbf{e}}_{\circlearrowright} = (\hat{\mathbf{x}} + i\hat{\mathbf{y}})/\sqrt{2}$ and left-handed $\hat{\mathbf{e}}_{\circlearrowleft} = (\hat{\mathbf{x}} - i\hat{\mathbf{y}})/\sqrt{2}$ circularly polarized light. For demonstrative purposes, we evaluate the absolute value of the VME for right-handed circularly polarized light at the apex of the gapped Dirac cones $\mathbf{k} = (0, K_y)$, obtaining $|a\gamma_1 - (L-a)\gamma_2 + s\hbar v_0|/\sqrt{2}\hbar$. In this case, illumination from right-handed polarized light will generate more photoexcited carriers in satellite Dirac cones with index $s = 1$. If the well depth and barrier heights are not equal, these gapped Dirac cones will be tilted in a direction dictated by the sign of s [see Fig. 3(c)]. The group velocities resulting from the tilted band structures will result in a photocurrent along the waveguide axis. The direction of the photocurrent will be determined by the handedness of the circularly polarized light. This phenomenon is somewhat similar to the ratchet photocurrent predicted for graphene superlattices formed by periodic strain.[66]

It is noted that while the gapped satellite Dirac cones do not support the absorption of photons with energy less than the bandgap $(2|\gamma_1 + \gamma_2|)$, the central gapless Dirac cone will support the absorption of photons with arbitrarily low photon energies. Having an actual metallic interface or manipulating the individual atoms instead of creating a superlattice potential by remote gates leads to more drastic changes in the band structure near the central Dirac cone, as shown in the *ab initio* studies for 8-*Pmmn* borophene in Refs. 39 and 67.

V. DESIGNER LANDAU LEVEL SPECTRA

In this section, we consider a typical bipolar array geometry with an electronic band structure containing central gapless Dirac cones and gapped satellite tilted Dirac cones. We assume that the voltage profile of the superlattice has been selected so that the satellite cones are sub-critically tilted (type-I, $|t| < 1$); see Fig. 4. In the presence of an external magnetic field oriented normal to a graphene sheet (with field strength B), the energy levels of the charge carriers become quantized into Landau levels (LLs). For the gapless central Dirac cones, it is well-known that the LLs take on the energy spectra,

$$E_{n_c} = \operatorname{sign}(n_c)\sqrt{2\hbar\bar{v}_c^2 eB|n_c|}, \tag{16}$$

where $\bar{v}_c = \sqrt{v_{c,x}v_{c,y}}$ is the effective Fermi velocity of the central Dirac cone, n_c is a LL index, and e is the elementary charge. Each LL has a 4-fold degeneracy arising from each graphene valley ($s_{\mathrm{K}} = \pm 1$) and electron spin.

Assuming that the applied gate voltages are selected such that the gapped satellite Dirac cones are of type-I, the LL spectra of the tilted gapped satellite Dirac cones, described by the Hamiltonian given in Eq. (13), take the form

$$E_n = \operatorname{sign}(n)\sqrt{2\hbar\bar{v}^2 e\lambda^3 B|n| + \left(\frac{\lambda E_g}{2}\right)^2} \tag{17}$$

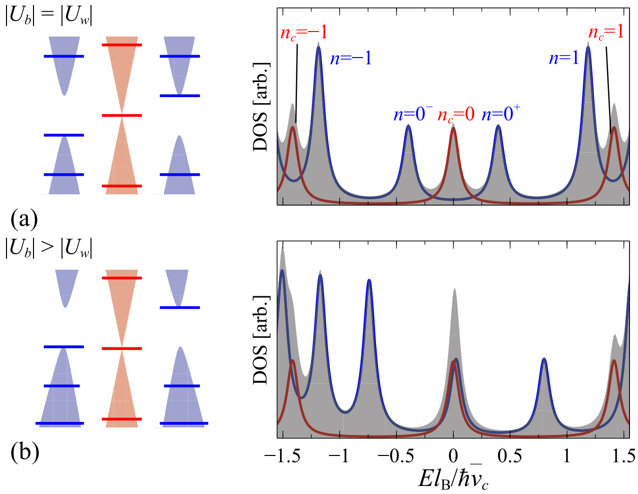

FIG. 6. Schematic of the Landau level spectra of a bipolar array in graphene under an external magnetic field for equal well and barrier heights $(|U_b| = |U_w|)$ in panel (a) and unequal well and barrier heights $(|U_b| > |U_w|)$ in panel (b). The total density of states has been sketched in gray, which is the sum of the contributions from the massive (blue, Landau level index n) and massless (red, Landau level index n_c) Dirac cones. The energy axis is normalized according to the effective Fermi velocity of the central massless Dirac cone $(\bar{v}_c)$ so that the $n_c = -1, 0,$ and 1 Landau level energies take on the values $-\sqrt{2}\ \hbar\bar{v}_c/l_B, 0,$ and $\sqrt{2}\ \hbar\bar{v}_c/l_B$, where $l_B = \sqrt{\hbar/eB}$ is the magnetic length. In panel (a), the satellite Dirac cones are non-tilted at $t = 0$ and have the same offset energy as the central cone, while in panel (b), the satellite cones are tilted and are offset from the central cone, causing overlap of LLs. This figure has been plotted for arbitrary field strength and Dirac cone parameters, and each Landau level has been modeled as a Lorentzian with a finite width.

for LL index $|n| \geq 1$,[68] where for the bipolar array $\bar{\nu} = \nu\sqrt{T}$ and $\lambda = \sqrt{1 - t^2}$ with each LL having 8-fold degeneracy from each graphene valley ($s_K = \pm 1$), satellite ($s = \pm 1$), and spin. It should be noted that in the presence of a gap, the zeroth LL splits into sub-levels at the band edges $E_{0^+} = \lambda E_g/2$ (when $s = 1$) or $E_{0^-} = -\lambda E_g/2$ (when $s = -1$) such that the degeneracy of each sub-level is half the other LLs (see Appendix D). We note that we have thus far assumed an infinitely repeating superlattice in a magnetic field. However, realistic systems are finite, resulting in edge states (for 8-*Pmmn* borophene, see, e.g., Ref. 69). Although we do not explore termination effects in this paper, we comment that it is an interesting avenue of future study. It is also noted that much like polyacetylene (treated via the Su–Schrieffer–Heeger model[70]), one could consider terminating the superlattice on or through the middle of a unit cell (leaving an isolated well/barrier at either edge of the system).

By modifying the applied voltages of the electrostatic superlattice, the tilt (t) and bandgap (E_g) of the gapped satellite Dirac cones can be tuned. We note that the offset energy of the satellite Dirac cones is different from the offset energy of the central Dirac cone. Varying the applied gate voltages of the bipolar array tunes the offset energies between the gapless and gapped LL spectra; this is illustrated schematically in Fig. 6. These theoretical results are consistent with a previous numerical study into the formation of Landau levels in graphene superlattices (see Ref. 55). In turn, this allows designer LL spectra via Dirac cone engineering, which would be measurable in magneto-resistance experiments or through magneto-optic transitions.

VI. CONCLUSION

Research into the physics of gapless and gapped tilted Dirac cone materials[6–22] is in its infancy, having been inspired by the prediction of tilted Dirac cones in 8-*Pmmn* borophene, a boron monolayer. In each of these works, the tilt parameter takes on a fixed value that is assumed to be predetermined by rigid lattice geometries. In this work, we propose a feasible method to engineer gapped and tilted Dirac cones in a lateral graphene superlattice. In stark contrast to crystalline atomic monolayers, the electronic band structure of a graphene superlattice can be modified by varying the applied voltage profile—this provides a practical means to control the tilt parameter and bandgap of Dirac cones.

While this work has been focused on the study of one-dimensional lateral superlattices in graphene, we note that two-dimensional graphene superlattices[59] may also provide a viable platform to realize designer gapped and tilted Dirac cones. It is also noted that although in this section we have considered lateral superlattices applied to graphene, it may also be possible to consider other superlattice geometries made possible through strain,[66,71–73] doping,[74] or electromagnetic fields.[60,75] Furthermore, we need not limit our substrate to graphene; superlattices could also be considered for other two-dimensional systems such as bilayer graphene,[76] silicene,[77] or eventually, two-dimensional materials that already host tilted Dirac cones in the electronic band structure, i.e., 8-*Pmmn* borophene.[78,79] It should also be noted that applying strain to the underlying crystallographic lattice, e.g., graphene,[80] gapped Dirac cone materials,[81] or 8-*Pmmn* borophene,[82,83] would add further tools to modify the electronic band structure.

The tilted and gapped Dirac cones within a lateral graphene superlattice can be engineered to give desirable device characteristics—as examples of this, we discussed tunable THz applications and designer Landau level spectra. It was shown that a lateral graphene superlattice can be engineered to absorb THz photons within a narrow bandwidth. This bandwidth can be tuned post-fabrication by varying the voltage profile of the superlattice. We hope that this work will encourage the use of lateral graphene bipolar superlattices in the design of novel THz devices.

ACKNOWLEDGMENTS

This work was supported by the EU H2020-MSCA-RISE projects TERASSE (Project No. 823878) and CHARTIST (Project No. 101007896). A.W. was supported by a UK EPSRC Ph.D. Studentship (Ref. 2239575) and by the NATO Science for Peace and Security Project No. NATO.SPS.MYP.G5860. E.M. acknowledges the financial support from the Royal Society International Exchanges Grant No. IEC/R2/192166. M.E.P. acknowledges the support from UK EPSRC (Grant No. EP/Y021339/1).

AUTHOR DECLARATIONS

Conflict of Interest

The authors have no conflicts to disclose.

Author Contributions

A. Wild: Conceptualization (equal); Formal analysis (lead); Investigation (lead); Methodology (lead); Software (lead); Visualization (lead); Writing – original draft (lead). **R. R. Hartmann**: Conceptualization (equal); Methodology (equal); Validation (equal); Writing – review & editing (equal). **E. Mariani**: Conceptualization (equal); Supervision (equal); Writing – review & editing (equal). **M. E. Portnoi**: Conceptualization (lead); Project administration (lead); Supervision (equal); Writing – review & editing (equal).

DATA AVAILABILITY

The data that support the findings of this study are available within the article.

APPENDIX A: ZERO-ENERGY STATES OF QUANTUM WELLS AND BARRIERS IN GRAPHENE

In this appendix, we present expressions for zero-energy states for quantum wells and barriers in graphene. Owing to the symmetry of the confining potential $U(x) = U(-x)$, it is convenient to rewrite Eq. (1) in the symmetrized basis, i.e., $|\psi(x)\rangle = [\psi_1(x), \psi_2(x)]^{\mathrm{T}}$, where $\psi_1(x) = [\psi_A(x) + i\psi_B(x)]/\sqrt{2}$ and $\psi_2(x) = [\psi_A(x) - i\psi_B(x)]/\sqrt{2}$. The spinor components satisfy the following simultaneous equations:

$$\left[\frac{U(x) - E}{\hbar v_{\mathrm{F}}} - s_{\mathrm{K}} k_y\right]\psi_1(x) + \partial_x \psi_2(x) = 0 \tag{A1}$$

and

$$-\partial_x\psi_1(x)+\left[\frac{U(x)-E}{\hbar v_{\mathrm{F}}}+s_{\mathrm{K}}k_y\right]\psi_2(x)=0. \tag{A2}$$

In conjunction with Eq. (2), we define three regions of the square potential: I ($x < -W/2$), II ($-W/2 \le x \le W/2$), and III ($x > W/2$). The total wavefunction is obtained by solving Eqs. (A1) and (A2) in each region of the potential and matching the spinor components at the boundaries. We note that for the case of graphene, in contrast to traditional free-electron quantum well problems, it is not necessary to match the derivative of the spinor components.

For a quantum barrier with height $\pi/2 < U_0W/\hbar v_{\mathrm{F}} < 3\pi/2$, there are two zero-energy solutions in each graphene valley ($s_{\mathrm{K}} = \pm1$)—one has a positive wavevector and the other has a negative wavevector $k_y = s|K_y|$ with $s = \pm1$. It can be seen from Eqs. (A1) and (A2) that interchanging the graphene valley index is mathematically equivalent to changing the sign of the wavevector along the guiding potential. We first solve for a quantum barrier in graphene for the case $s_{\mathrm{K}}s = 1$, where the zero-energy wavefunction takes the form

$$|\psi_b^{\mathrm{I}}(x)\rangle=\frac{1}{N}e^{|K_y|W/2}\sin(\widetilde{K}W/2)\begin{pmatrix}1\\1\end{pmatrix}e^{|K_y|x}, \tag{A3}$$

$$|\psi_b^{\mathrm{II}}(x)\rangle=\frac{1}{N}\begin{bmatrix}\tan(\widetilde{K}W/2)\cos(\widetilde{K}x)\\ -\sin(\widetilde{K}x)\end{bmatrix}, \tag{A4}$$

and

$$|\psi_b^{\mathrm{III}}(x)\rangle=\frac{1}{N}e^{|K_y|W/2}\sin(\widetilde{K}W/2)\begin{pmatrix}1\\-1\end{pmatrix}e^{-|K_y|x}, \tag{A5}$$

where the effective wavevector in the barrier is

$$\widetilde{K}=\frac{1}{\hbar v_{\mathrm{F}}}\sqrt{U_0^2-(\hbar v_{\mathrm{F}}K_y)^2} \tag{A6}$$

and the normalization factor is

$$N=\sqrt{\frac{(|K_y|W+1)}{2|K_y|}}\sec(\widetilde{K}W/2). \tag{A7}$$

The zero-energy states occur at wavevector $s|K_y|$, where $|K_y|$ is the solution to the transcendental equation,

$$\widetilde{K}=-|K_y|\tan(\widetilde{K}W). \tag{A8}$$

Here, we have centered the barrier at the coordinate $x = 0$; however, the barrier can be offset by setting $x \to x - x_0$. We can see from Eqs. (A1) and (A2) that a wavefunction for the case $s_{\mathrm{K}}s = -1$ can be obtained from the $s_{\mathrm{K}}s = 1$ wavefunction through the operation $\sigma_x|\psi_{w/b}(-x)\rangle$. It can also be seen from Eqs. (A1) and (A2) that the zero-energy ($E = 0$) wavefunction for a well can be related to that of a barrier $|\psi_w(x)\rangle = \sigma_x|\psi_b(x)\rangle$ provided the well depth is equal to the barrier height $U_b = -U_w = U_0$.

We can obtain the group velocity of the well and barrier dispersions at the crossing point by calculating the expectation of the velocity operator $v_{w/b} = \int\langle\psi_{w/b}(x)|\hat{v}|\psi_{w/b}(x)\rangle\mathrm{d}x$, where in the symmetrized basis the velocity operator is defined as $\hat{v} = -s_{\mathrm{K}}v_{\mathrm{F}}\sigma_z$, where σ_z is the third Pauli matrix. Performing this calculation yields the barrier and well group velocities $v_w = -v_b = v_0$, where

$$v_0=\frac{s\hbar v_{\mathrm{F}}^2|K_y|}{U_0}. \tag{A9}$$

APPENDIX B: TRANSFER MATRIX METHOD FOR THE BIPOLAR ARRAY IN GRAPHENE

To support the theoretical predictions of our work, we provide a transfer matrix model that can be used to calculate the electronic band structure of the bipolar array in graphene numerically. The employed transfer matrix model is based on earlier works used to derive the electronic band structure of simpler graphene superlattices.[53,54] The general theory of the transfer matrix method for Dirac systems is discussed in Ref. 84.

The bipolar array has a superlattice unit cell consisting of four regions ($n = 1$ to 4) with potential (U_n) between the coordinates $x_{n-1} \le x \le x_n$. For consistency with the theoretical model, the potentials take the values $U_1 = U_b$, $U_3 = U_w$, and $U_2 = U_4 = 0$, while the boundaries take the values $x_0 = -W/2$, $x_1 = W/2$, $x_2 = a - W/2$, $x_3 = a + W/2$, and $x_4 = L - W/2$. The wavefunction in region n in unit cell j can be found by solving Eq. (1) for a constant potential U_n yielding $|\psi_n(x)\rangle = \mathbf{\Omega}_n(x)\left(\alpha_n^{(j)},\beta_n^{(j)}\right)^{\mathrm{T}}$, where $\alpha_n^{(j)}$ and $\beta_n^{(j)}$ are the wavefunction components and T is the transpose operator. For the case $|U_n - E| \ge \hbar v_{\mathrm{F}}|k_y|$, we obtain guided mode solutions encoded by the matrix,

$$\mathbf{\Omega}_n(x)=\begin{pmatrix}e^{i\widetilde{k}_nx} & e^{-i\widetilde{k}_nx}\\ \Lambda_{n,+}e^{i\widetilde{k}_nx} & \Lambda_{n,-}e^{-i\widetilde{k}_nx}\end{pmatrix}, \tag{B1}$$

where the effective wavevector is

$$\widetilde{k}_n=\frac{1}{\hbar v_{\mathrm{F}}}\sqrt{(U_n-E)^2-(\hbar v_{\mathrm{F}}k_y)^2} \tag{B2}$$

and

$$\Lambda_{n,\pm}=\frac{E-U_n}{\hbar v_{\mathrm{F}}\left(\pm\widetilde{k}_n-ik_y\right)}, \tag{B3}$$

which are defined for a single graphene valley ($s_{\mathrm{K}} = 1$) up to a normalization factor. We note that for the case $|U_n - E| < \hbar v_{\mathrm{F}}|k_y|$, the wavefunction decays—this is achieved by replacing $\widetilde{k}_n$ with $i\widetilde{\kappa}_n$ in Eqs. (B1)–(B3), where

$$\widetilde{\kappa}_n=\frac{1}{\hbar v_{\mathrm{F}}}\sqrt{(\hbar v_{\mathrm{F}}k_y)^2-(U_n-E)^2}. \tag{B4}$$

To obtain the total wavefunction of the bipolar array, we sequentially satisfy each boundary condition in the superlattice potential. By matching all boundary conditions within a single unit cell, we can relate the wavefunction in unit cell j to the wavefunction in the neighboring unit cell $j + 1$,

$$\begin{pmatrix}\alpha_1^{(j)}\\ \beta_1^{(j)}\end{pmatrix}=\mathbf{T}\begin{pmatrix}\alpha_1^{(j+1)}\\ \beta_1^{(j+1)}\end{pmatrix}, \tag{B5}$$

where the transfer matrix is defined as

$$\mathbf{T} = \left[\prod_{n=1}^{3} \mathbf{\Omega}_n^{-1}(x_n)\mathbf{\Omega}_{n+1}(x_n)\right]\mathbf{\Omega}_4^{-1}(x_4)\mathbf{\Omega}_1(x_0). \tag{B6}$$

In conjunction with the theoretical model [see Eq. (3)], this superlattice unit cell is repeated N times, leading to the expression,

$$\begin{pmatrix}\alpha_1^{(j)}\\ \beta_1^{(j)}\end{pmatrix} = \mathbf{T}^N \begin{pmatrix}\alpha_1^{(j+N)}\\ \beta_1^{(j+N)}\end{pmatrix}. \tag{B7}$$

Due to the translational invariance of the superlattice, the spinor components $\alpha_1^{(j)}$ and $\beta_1^{(j)}$ are equivalent to $\alpha_1^{(j+N)}$ and $\beta_1^{(j+N)}$, respectively. This places a constraint on the transfer matrix $(\mathbf{T}^N = 1)$, yielding the eigenvalues $e^{\pm 2ij\pi/N}$. For the case of an infinite superlattice $(N \to \infty)$, we label the continuum of eigenvalues $e^{\pm ik_x L}$ with the superlattice wavevector $(k_x = 2\pi j/NL)$. As discussed in Ref. 84, the electronic band structure is found by searching for energy (E) and wavevector $(\mathbf{k} = (k_x, k_y))$ values that satisfy the condition

$$2\cos(k_x L) = \mathrm{Tr}(\mathbf{T}). \tag{B8}$$

APPENDIX C: TIGHT-BINDING HOPPING PARAMETERS AND ESTIMATION OF DIRAC CONE BANDGAP

In the case of the bipolar array that lacks a reflection plane in the superlattice, gapped Dirac cones appear. The bandgap of these Dirac cones is given by twice the magnitude of the sum of the intra- and inter-cell hopping integrals. For the case of equal well depth and barrier height $(U_b = -U_w = U_0)$, the well and barrier dispersions cross at zero-energy. In this case, we can obtain analytic expressions for γ_{intra} and γ_{inter} by utilizing the analytic zero-energy solutions to the square well and barrier in graphene provided in Appendix A.

We will begin by calculating the intra-cell hopping parameter for the specific case of $s_{\mathrm{K}}s = 1$. Without loss of generality, we specify the unit cell $(j = 0)$ and substitute the superlattice Hamiltonian $\hat{H}$ [see Eq. (3)] into Eq. (8). Removing all negligible terms yields

$$\gamma_{\text{intra}} = \int_{-\infty}^{\infty} \langle \psi_b(x)|U_b(x)|\psi_w(x-a)\rangle \,\mathrm{d}x + \int_{-\infty}^{\infty} \langle \psi_b(x)|\hat{H}_{\mathrm{G}} + U_w(x-a)|\psi_w(x-a)\rangle \,\mathrm{d}x. \tag{C1}$$

We note that the term $[\hat{H}_{\mathrm{G}} + U_w(x-a)]|\psi_w(x-a)\rangle$ is the eigenvalue problem given in Eq. (1). As the wavefunction $|\psi_w(x-a)\rangle$ corresponds to a zero-energy state, this term vanishes. Inputting the definition for a quantum barrier [defined through Eq. (2)] yields the simplified expression for the hopping parameter,

$$\gamma_{\text{intra}} = U_0 \int_{-W/2}^{W/2} \langle \psi_b(x)||\psi_w(x-a)\rangle \,\mathrm{d}x. \tag{C2}$$

Inputting the analytic solutions for the zero-energy states [see Eqs. (A3)–(A8) and $|\psi_w(x)\rangle = \sigma_x|\psi_b(x)\rangle$] into Eq. (C2) and solving the resultant integral yields an expression for the intra-cell hopping parameter $\gamma_{\text{intra}} = \gamma_1$ (when $s_{\mathrm{K}}s = 1$), where

$$\gamma_1 = \frac{\hbar^3 v_{\mathrm{F}}^3 |K_y| \widetilde{K}^2}{U_0^2(1 + |K_y|W)} e^{|K_y|(W-a)}. \tag{C3}$$

Carrying out the same procedure for the inter-cell hopping parameter yields $\gamma_{\text{inter}} = \gamma_2$ (when $s_{\mathrm{K}}s = 1$), where $\gamma_2 = -\gamma_1 \exp[|K_y|(2a - L)]$. For the alternate case $s_{\mathrm{K}}s = -1$, the well and barrier wavefunctions are modified as $\sigma_x|\psi_{w/b}(-x)\rangle$ (see Appendix A). Substituting this transformation into Eqs. (8) and (9) reveals that flipping the sign of $s_{\mathrm{K}}s$ is mathematically equivalent to switching the well and barrier positions. Thus, for the symmetric case $(a = L/2)$, switching the sign of $s_{\mathrm{K}}s$ simply interchanges the inter- and intra-cell hopping parameters. In general, when $a \neq L/2$, we obtain $\gamma_{\text{intra}} = s_{\mathrm{K}}s\gamma_1$ and $\gamma_{\text{inter}} = s_{\mathrm{K}}s\gamma_2$. We can then obtain the local bandgap of the gapped Dirac cones through $|E_{\mathrm{g}}| = 2|\gamma_1 + \gamma_2|$, which yields the solution given in Eq. (14) of the main text.

APPENDIX D: LANDAU LEVEL WAVEFUNCTIONS IN MASSIVE TILTED DIRAC CONES

In the presence of a magnetic field, we substitute the vector potential into the Hamiltonian given in Eq. (13) using the identity $\hat{\mathbf{q}} \to \hat{\mathbf{q}} + e\mathbf{A}/\hbar$. Here, the wavevector operators take on the value $\hat{q}_{x,y} = -i\partial_{x,y}$, while the vector potential $\mathbf{A} = -Bx\hat{\mathbf{y}}$ describes a magnetic field normally incident on the system. In this gauge, the Hamiltonian is solved by the wavefunction $|\Psi_n(x,y)\rangle = e^{iq_y y}|\Psi_n(x)\rangle$, resulting in the eigenvalue problem $\hat{\mathscr{H}}_B|\Psi_n(x)\rangle = E_n|\Psi_n(x)\rangle$ with

$$\hat{\mathscr{H}}_B = s_{\mathrm{K}}s\frac{E_g}{2}\sigma_z + sv(\hbar q_y - eBx)(t\mathbb{I} + \sigma_y) - is_{\mathrm{K}}s\hbar vT\frac{\partial}{\partial x}\sigma_x, \tag{D1}$$

where n is the LL index, E_n is the Landau level energy, and $|\Psi_n(x)\rangle$ is the associated LL wavefunction.

While this problem can be solved using a generalized chiral operator,[68] we solve it using an approach previously outlined for gapless tilted Dirac cones in Ref. 85, which we have adapted for the gapped case. For LLs with index $|n| \geq 1$, the energy spectra are defined in Eq. (17), while the wavefunctions take the form

$$|\Psi_n(x)\rangle = \frac{e^{-X_n^2/2}}{N_n}\left[(2s\varepsilon_n + \lambda\varepsilon_g)\begin{pmatrix}1+\lambda\\ -it\end{pmatrix}h_{|n|}(X_n) - 2i\sqrt{2\lambda^3|n|}\begin{pmatrix}it\\ 1+\lambda\end{pmatrix}h_{|n|-1}(X_n)\right] \tag{D2}$$

for $s_{\mathrm{K}} = 1$. In these expressions, for brevity, we have utilized dimensionless variables for the energy spectra $\varepsilon_n = E_n l_B/\hbar\bar{v}$ and bandgap $\varepsilon_g = E_g l_B/\hbar\bar{v}$, which are defined through the magnetic length $l_B = \sqrt{\hbar/eB}$. In addition, we have utilized the scaled and translated coordinates,

$$X_n = \sqrt{\lambda}\left(\frac{x}{l_B\sqrt{T}} - \frac{q_y l_B}{\sqrt{T}} - \frac{s\varepsilon_n t}{\lambda^2}\right), \tag{D3}$$

the normalization factor,

$$N_n = \sqrt{2(1+\lambda)}\sqrt{(2s\varepsilon_n + \lambda\varepsilon_g)^2 + 8\lambda^3|n|}, \tag{D4}$$

and the normalized Hermite polynomials,

$$h_m(X_n) = \left(\frac{\lambda}{\pi T}\right)^{\frac{1}{4}} \frac{1}{\sqrt{2^m l_B m!}} H_m(X_n), \tag{D5}$$

where $H_m()$ are the Hermite polynomials. For the second graphene valley ($s_K = -1$), the LL wavefunction takes the form $-i\sigma_y|\Psi_n\rangle$. As discussed in the main text, each LL with index $|n| \geq 1$ has 8-fold degeneracy arising from spin, graphene valley ($s_K = \pm 1$), and satellite Dirac cones ($s = \pm 1$).

As discussed in the main text, there are two zeroth LLs that sit at the band edge ($E_{0^\pm} = \pm E_g \lambda/2$). The $n = 0^+$ LL only exists in satellite Dirac cones at positive wavevectors along the guiding potential ($s = 1$), while the $n = 0^-$ LL only exists at negative wavevectors ($s = -1$). As a consequence, these zeroth LLs have half the degeneracy of the other levels, meaning that if the gap were to close, they would combine into a single zero-energy LL with degeneracy equal to all other levels. The wavefunctions of the zeroth LL can be written as

$$|\Psi_{0^\pm}(x)\rangle = \frac{1}{\sqrt{2(1+\lambda)l_B}} \left(\frac{\lambda}{\pi T}\right)^{\frac{1}{4}} \begin{pmatrix} 1+\lambda \\ -it \end{pmatrix} e^{-X_{0^\pm}^2/2} \tag{D6}$$

for $s_K = 1$ or $-i\sigma_y|\Psi_{0^\pm}\rangle$ in the other graphene valley $s_K = -1$.

REFERENCES

[1] A. H. Castro Neto, F. Guinea, N. M. R. Peres, K. S. Novoselov, and A. K. Geim, "The electronic properties of graphene," Rev. Mod. Phys. **81**, 109–162 (2009).

[2] R. R. Nair, P. Blake, A. N. Grigorenko, K. S. Novoselov, T. J. Booth, T. Stauber, N. M. R. Peres, and A. K. Geim, "Fine structure constant defines visual transparency of graphene," Science **320**, 1308 (2008).

[3] X.-F. Zhou, X. Dong, A. R. Oganov, Q. Zhu, Y. Tian, and H.-T. Wang, "Semimetallic two-dimensional boron allotrope with massless Dirac fermions," Phys. Rev. Lett. **112**, 085502 (2014).

[4] A. A. Soluyanov, D. Gresch, Z. Wang, Q. Wu, M. Troyer, X. Dai, and B. A. Bernevig, "Type-II Weyl semimetals," Nature **527**, 495–498 (2015).

[5] M. Milićević, G. Montambaux, T. Ozawa, O. Jamadi, B. Real, I. Sagnes, A. Lemaître, L. Le Gratiet, A. Harouri, J. Bloch, and A. Amo, "Type-III and tilted Dirac cones emerging from flat bands in photonic orbital graphene," Phys. Rev. X **9**, 031010 (2019).

[6] T. Nishine, A. Kobayashi, and Y. Suzumura, "Tilted-cone induced cusps and nonmonotonic structures in dynamical polarization function of massless Dirac fermions," J. Phys. Soc. Jpn. **79**, 114715 (2010).

[7] S. Verma, A. Mawrie, and T. K. Ghosh, "Effect of electron-hole asymmetry on optical conductivity in 8-*Pmmn* borophene," Phys. Rev. B **96**, 155418 (2017).

[8] M. A. Mojarro, R. Carrillo-Bastos, and J. A. Maytorena, "Optical properties of massive anisotropic tilted Dirac systems," Phys. Rev. B **103**, 165415 (2021).

[9] C.-Y. Tan, C.-X. Yan, Y.-H. Zhao, H. Guo, and H.-R. Chang, "Anisotropic longitudinal optical conductivities of tilted Dirac bands in $1T'$-MoS$_2$," Phys. Rev. B **103**, 125425 (2021).

[10] A. Wild, E. Mariani, and M. E. Portnoi, "Optical absorption in two-dimensional materials with tilted Dirac cones," Phys. Rev. B **105**, 205306 (2022).

[11] T. Cheng, H. Lang, Z. Li, Z. Liu, and Z. Liu, "Anisotropic carrier mobility in two-dimensional materials with tilted Dirac cones: Theory and application," Phys. Chem. Chem. Phys. **19**, 23942–23950 (2017).

[12] V. H. Nguyen and J.-C. Charlier, "Klein tunneling and electron optics in Dirac-Weyl fermion systems with tilted energy dispersion," Phys. Rev. B **97**, 235113 (2018).

[13] S.-H. Zhang and W. Yang, "Oblique Klein tunneling in 8-*Pmmn* borophene *p*–*n* junctions," Phys. Rev. B **97**, 235440 (2018).

[14] P. Sengupta, Y. Tan, E. Bellotti, and J. Shi, "Anomalous heat flow in 8-*Pmmn* borophene with tilted Dirac cones," J. Phys.: Condens. Matter **30**, 435701 (2018).

[15] M. Zare, "Thermoelectric transport properties of borophane," Phys. Rev. B **99**, 235413 (2019).

[16] P. Kapri, B. Dey, and T. K. Ghosh, "Valley caloritronics in a photodriven heterojunction of Dirac materials," Phys. Rev. B **102**, 045417 (2020).

[17] A. Kobayashi, Y. Suzumura, and H. Fukuyama, "Hall effect and orbital diamagnetism in zerogap state of molecular conductor α-(BEDT-TTF)$_2$I$_3$," J. Phys. Soc. Jpn. **77**, 064718 (2008).

[18] I. Proskurin, M. Ogata, and Y. Suzumura, "Longitudinal conductivity of massless fermions with tilted Dirac cone in magnetic field," Phys. Rev. B **91**, 195413 (2015).

[19] S. F. Islam and A. M. Jayannavar, "Signature of tilted Dirac cones in Weiss oscillations of 8-*Pmmn* borophene," Phys. Rev. B **96**, 235405 (2017).

[20] Z. Jalali-Mola and S. A. Jafari, "Tilt-induced kink in the plasmon dispersion of two-dimensional Dirac electrons," Phys. Rev. B **98**, 195415 (2018).

[21] A. E. Champo and G. G. Naumis, "Metal-insulator transition in 8-*Pmmn* borophene under normal incidence of electromagnetic radiation," Phys. Rev. B **99**, 035415 (2019).

[22] R. A. Ng, A. Wild, M. E. Portnoi, and R. R. Hartmann, "Quasi-exact solutions for guided modes in two-dimensional materials with tilted Dirac cones," Sci. Rep. **12**, 7688 (2022).

[23] F.-Y. Liu, S.-J. Zhang, Y. Zhang, and K.-H. Ding, "Localized magnetic states in a tilted Dirac cone system," Europhys. Lett. **143**, 46002 (2023).

[24] M. A. Mojarro, R. Carrillo-Bastos, and J. A. Maytorena, "Hyperbolic plasmons in massive tilted two-dimensional Dirac materials," Phys. Rev. B **105**, L201408 (2022).

[25] S. Katayama, A. Kobayashi, and Y. Suzumura, "Pressure-induced zero-gap semiconducting state in organic conductor α-(BEDT-TTF)$_2$I$_3$ salt," J. Phys. Soc. Jpn. **75**, 054705 (2006).

[26] M. O. Goerbig, J.-N. Fuchs, G. Montambaux, and F. Piéchon, "Tilted anisotropic Dirac cones in quinoid-type graphene and α-(BEDT-TTF)$_2$I$_3$," Phys. Rev. B **78**, 045415 (2008).

[27] T. Morinari, E. Kaneshita, and T. Tohyama, "Topological and transport properties of Dirac fermions in an antiferromagnetic metallic phase of iron-based superconductors," Phys. Rev. Lett. **105**, 037203 (2010).

[28] X. Qian, J. Liu, L. Fu, and J. Li, "Quantum spin Hall effect in two-dimensional transition metal dichalcogenides," Science **346**, 1344–1347 (2014).

[29] L. Muechler, A. Alexandradinata, T. Neupert, and R. Car, "Topological nonsymmorphic metals from band inversion," Phys. Rev. X **6**, 041069 (2016).

[30] H.-Y. Lu, A. S. Cuamba, S.-Y. Lin, L. Hao, R. Wang, H. Li, Y. Zhao, and C. S. Ting, "Tilted anisotropic Dirac cones in partially hydrogenated graphene," Phys. Rev. B **94**, 195423 (2016).

[31] Y. Ma, L. Kou, X. Li, Y. Dai, and T. Heine, "Room temperature quantum spin Hall states in two-dimensional crystals composed of pentagonal rings and their quantum wells," NPG Asia Mater. **8**, 264 (2016).

[32] C.-K. Chiu, Y.-H. Chan, X. Li, Y. Nohara, and A. P. Schnyder, "Type-II Dirac surface states in topological crystalline insulators," Phys. Rev. B **95**, 035151 (2017).

[33] A. Varykhalov, D. Marchenko, J. Sánchez-Barriga, E. Golias, O. Rader, and G. Bihlmayer, "Tilted Dirac cone on W(110) protected by mirror symmetry," Phys. Rev. B **95**, 245421 (2017).

[34] R. M. Geilhufe, B. Commeau, and G. W. Fernando, "Chemical-strain induced tilted Dirac nodes in (BEDT-TTF)$_2$X$_3$ (X = I, Cl, Br, F) based charge-transfer salts," Phys. Status Solidi RRL **12**, 1800081 (2018).

[35] L. L. Tao and E. Y. Tsymbal, "Two-dimensional type-II Dirac fermions in a LaAlO$_3$/LaNiO$_3$/LaAlO$_3$ quantum well," Phys. Rev. B **98**, 121102 (2018).

[36] R. G. Polozkov, N. Y. Senkevich, S. Morina, P. Kuzhir, M. E. Portnoi, and I. A. Shelykh, "Carbon nanotube array as a van der Waals two-dimensional hyperbolic material," Phys. Rev. B **100**, 235401 (2019).

[37] S. Li, Y. Liu, Z.-M. Yu, Y. Jiao, S. Guan, X.-L. Sheng, Y. Yao, and S. A. Yang, "Two-dimensional antiferromagnetic Dirac fermions in monolayer TaCoTe$_2$," Phys. Rev. B **100**, 205102 (2019).

[38] P.-J. Guo, X.-Q. Lu, W. Ji, K. Liu, and Z.-Y. Lu, "Quantum spin Hall effect in monolayer and bilayer TaIrTe$_4$," Phys. Rev. B **102**, 041109 (2020).

[39] Y. Yekta, H. Hadipour, and S. A. Jafari, "Tunning the tilt of the Dirac cone by atomic manipulations in 8Pmmn borophene," Commun. Phys. **6**, 46 (2023).

[40] N. Yu and F. Capasso, "Flat optics with designer metasurfaces," Nat. Mater. **13**, 139–150 (2014).

[41] R. R. Hartmann and M. E. Portnoi, "Quasi-exact solution to the Dirac equation for the hyperbolic-secant potential," Phys. Rev. A **89**, 012101 (2014).

[42] R. R. Hartmann, N. J. Robinson, and M. E. Portnoi, "Smooth electron waveguides in graphene," Phys. Rev. B **81**, 245431 (2010).

[43] R. R. Hartmann and M. E. Portnoi, "Two-dimensional Dirac particles in a Pöschl-Teller waveguide," Sci. Rep. **7**, 11599 (2017).

[44] J. M. Pereira, V. Mlinar, F. M. Peeters, and P. Vasilopoulos, "Confined states and direction-dependent transmission in graphene quantum wells," Phys. Rev. B **74**, 045424 (2006).

[45] A. Cheng, T. Taniguchi, K. Watanabe, P. Kim, and J.-D. Pillet, "Guiding Dirac fermions in graphene with a carbon nanotube," Phys. Rev. Lett. **123**, 216804 (2019).

[46] R. R. Hartmann and M. E. Portnoi, "Bipolar electron waveguides in graphene," Phys. Rev. B **102**, 155421 (2020).

[47] R. R. Hartmann and M. E. Portnoi, "Guided modes and terahertz transitions for two-dimensional Dirac fermions in a smooth double-well potential," Phys. Rev. A **102**, 052229 (2020).

[48] Y. Li, S. Dietrich, C. Forsythe, T. Taniguchi, K. Watanabe, P. Moon, and C. R. Dean, "Anisotropic band flattening in graphene with one-dimensional superlattices," Nat. Nanotechnol. **16**, 525–530 (2021).

[49] M. Drienovsky, F.-X. Schrettenbrunner, A. Sandner, D. Weiss, J. Eroms, M.-H. Liu, F. Tkatschenko, and K. Richter, "Towards superlattices: Lateral bipolar multibarriers in graphene," Phys. Rev. B **89**, 115421 (2014).

[50] S. Dubey, V. Singh, A. K. Bhat, P. Parikh, S. Grover, R. Sensarma, V. Tripathi, K. Sengupta, and M. M. Deshmukh, "Tunable superlattice in graphene to control the number of Dirac points," Nano Lett. **13**, 3990–3995 (2013).

[51] J. J. Esteve-Paredes and J. J. Palacios, "A comprehensive study of the velocity, momentum and position matrix elements for Bloch states: Application to a local orbital basis," SciPost Phys. Core **6**, 002 (2023).

[52] N. R. Cooper, J. Dalibard, and I. B. Spielman, "Topological bands for ultracold atoms," Rev. Mod. Phys. **91**, 015005 (2019).

[53] M. Barbier, F. M. Peeters, P. Vasilopoulos, and J. M. Pereira, "Dirac and Klein-Gordon particles in one-dimensional periodic potentials," Phys. Rev. B **77**, 115446 (2008).

[54] M. Barbier, P. Vasilopoulos, and F. M. Peeters, "Extra Dirac points in the energy spectrum for superlattices on single-layer graphene," Phys. Rev. B **81**, 075438 (2010).

[55] C.-H. Park, Y.-W. Son, L. Yang, M. L. Cohen, and S. G. Louie, "Landau levels and quantum Hall effect in graphene superlattices," Phys. Rev. Lett. **103**, 046808 (2009).

[56] J. R. F. Lima, "Engineering the electronic structure of graphene superlattices via Fermi velocity modulation," Eur. Phys. J. B **90**, 5 (2017).

[57] L. Brey and H. A. Fertig, "Emerging zero modes for graphene in a periodic potential," Phys. Rev. Lett. **103**, 046809 (2009).

[58] J. H. Ho, Y. H. Chiu, S. J. Tsai, and M. F. Lin, "Semimetallic graphene in a modulated electric potential," Phys. Rev. B **79**, 115427 (2009).

[59] C.-H. Park, L. Yang, Y.-W. Son, M. L. Cohen, and S. G. Louie, "New generation of massless Dirac fermions in graphene under external periodic potentials," Phys. Rev. Lett. **101**, 126804 (2008).

[60] P. Somroob, T. Sutthibutpong, S. Tangwancharoen, and W. Liewrian, "Tunable tilted anisotropy of massless Dirac fermion in magnetic Kronig-Penney-type graphene," Physica E **127**, 114501 (2021).

[61] K. Kishigi and Y. Hasegawa, "Three-quarter Dirac points, Landau levels, and magnetization in α-(BEDT-TTF)$_2$I$_3$," Phys. Rev. B **96**, 085430 (2017).

[62] Y. Hasegawa and K. Kishigi, "Energy quantization at the three-quarter Dirac point in a magnetic field," Phys. Rev. B **99**, 045409 (2019).

[63] A. Wild, E. Mariani, and M. E. Portnoi, "Optical valley separation in two-dimensional semimetals with tilted Dirac cones," Sci. Rep. **13**, 19211 (2023).

[64] V. A. Saroka, R. R. Hartmann, and M. E. Portnoi, "Momentum alignment and the optical valley Hall effect in low-dimensional Dirac materials," J. Exp. Theor. Phys. **135**, 513–530 (2022).

[65] C.-Y. Tan, J.-T. Hou, C.-X. Yan, H. Guo, and H.-R. Chang, "Signatures of Lifshitz transition in the optical conductivity of two-dimensional tilted Dirac materials," Phys. Rev. B **106**, 165404 (2022).

[66] Y. Y. Kiselev and L. E. Golub, "Optical and photogalvanic properties of graphene superlattices formed by periodic strain," Phys. Rev. B **84**, 235440 (2011).

[67] V. Vishnubhotla, S. Mitra, and S. Mahapatra, "First-principles based study of 8-*Pmmn* borophene and metal interface," J. Appl. Phys. **134**, 034301 (2023).

[68] Y. Hatsugai, T. Kawarabayashi, and H. Aoki, "Survival of sharp $n = 0$ Landau levels in massive tilted Dirac fermions: Role of the generalized chiral operator," Phys. Rev. B **91**, 085112 (2015).

[69] N. Deily Nazar, F. M. Peeters, R. N. C. Filho, and T. Vazifehshenas, "8-*Pmmn* borophene: Edge states in competition with Landau levels and local vacancy states," Phys. Chem. Chem. Phys. **26**, 16153–16159 (2024).

[70] W. P. Su, J. R. Schrieffer, and A. J. Heeger, "Solitons in polyacetylene," Phys. Rev. Lett. **42**, 1698–1701 (1979).

[71] S. Gattenlöhner, W. Belzig, and M. Titov, "Dirac-Kronig-Penney model for strain-engineered graphene," Phys. Rev. B **82**, 155417 (2010).

[72] Z. Wu, F. Zhai, F. M. Peeters, H. Q. Xu, and K. Chang, "Valley-dependent Brewster angles and goos-hänchen effect in strained graphene," Phys. Rev. Lett. **106**, 176802 (2011).

[73] R. Banerjee, V.-H. Nguyen, T. Granzier-Nakajima, L. Pabbi, A. Lherbier, A. R. Binion, J.-C. Charlier, M. Terrones, and E. W. Hudson, "Strain modulated superlattices in graphene," Nano Lett. **20**, 3113–3121 (2020).

[74] C. Wang, K. Wang, H. Wang, Q. Tian, J. Zong, X. Qiu, W. Ren, L. Wang, F.-S. Li, W.-B. Zhang, H. Zhang, and Y. Zhang, "Observation of a folded Dirac cone in heavily doped graphene," J. Phys. Chem. Lett. **14**, 7149–7156 (2023).

[75] P. Somroob and W. Liewrian, "Electrical manipulation of spin-dependent anisotropy of a Dirac cone in a graphene superlattice with alternating periodic electrostatic and exchange fields," Condens. Matter **8**, 28 (2023).

[76] M. Barbier, P. Vasilopoulos, and F. M. Peeters, "Single-layer and bilayer graphene superlattices: Collimation, additional Dirac points and Dirac lines," Philos. Trans. R. Soc., A **368**, 5499–5524 (2010).

[77] K. Shakouri, P. Vasilopoulos, V. Vargiamidis, and F. M. Peeters, "Spin- and valley-dependent magnetotransport in periodically modulated silicene," Phys. Rev. B **90**, 125444 (2014).

[78] Y. Xu, Y. Fang, and G. Jin, "Valley-polarized and supercollimated electronic transport in an 8-*Pmmn* borophene superlattice," New J. Phys. **25**, 013020 (2023).

[79] M.-Q. Jiao and Y.-X. Li, "Transport properties and electron filter in 8-*Pmmn* borophene superlattice," Phys. Lett. A **497**, 129343 (2024).

[80] G. G. Naumis, S. Barraza-Lopez, M. Oliva-Leyva, and H. Terrones, "Electronic and optical properties of strained graphene and other strained 2D materials: A review," Rep. Prog. Phys. **80**, 096501 (2017).

[81] A. V. Snegirev, V. M. Kovalev, and M. V. Entin, "Photogalvanic effect induced by intervalley relaxation in a strained two-dimensional Dirac monolayer," Phys. Rev. B **109**, 085422 (2024).

[82] A. Lopez-Bezanilla and P. B. Littlewood, "Electronic properties of 8-*Pmmn* borophene," Phys. Rev. B **93**, 241405 (2016).

[83] J. Yuan, N. Yu, K. Xue, and X. Miao, "Ideal strength and elastic instability in single-layer 8-*Pmmn* borophene," RSC Adv. **7**, 8654–8660 (2017).

[84] B. H. J. McKellar and G. J. Stephenson, "Relativistic quarks in one-dimensional periodic structures," Phys. Rev. C **35**, 2262–2271 (1987).

[85] T. Morinari and T. Tohyama, "Crossover from positive to negative interlayer magnetoresistance in multilayer massless Dirac fermion system with non-vertical interlayer tunneling," J. Phys. Soc. Jpn. **79**, 044708 (2010).

APL Quantum

RESEARCH ARTICLE | FEBRUARY 14 2025

Electronic structure of YV_6Sn_6 probed by de Haas–van Alphen oscillations and density functional theory

Special Collection: Quantum Dynamics in Theory, Numerics and in Experimental Research

Kyryl Shtefiienko ; Cole Phillips; Shirin Mozaffari ; Richa P. Madhogaria; William R. Meier ; David G. Mandrus ; David E. Graf; Keshav Shrestha ✉

APL Quantum 2, 016118 (2025)
https://doi.org/10.1063/5.0252563

AIP Publishing

APL Quantum ARTICLE pubs.aip.org/aip/apq

Electronic structure of YV_6Sn_6 probed by de Haas–van Alphen oscillations and density functional theory

Cite as: APL Quantum 2, 016118 (2025); doi: 10.1063/5.0252563
Submitted: 10 December 2024 • Accepted: 27 January 2025 •
Published Online: 14 February 2025

Kyryl Shtefiienko,[1] **Cole Phillips,**[1] **Shirin Mozaffari,**[2] **Richa P. Madhogaria,**[2] **William R. Meier,**[2] **David G. Mandrus,**[2,3] **David E. Graf,**[4,5] **and Keshav Shrestha**[1,a)]

AFFILIATIONS

[1] Department of Chemistry and Physics, West Texas A&M University, Canyon, Texas 79016, USA
[2] Department of Materials Sciences and Engineering, University of Tennessee, Knoxville, Tennessee 37996, USA
[3] Materials Science & Technology Division, Oak Ridge National Laboratory, Oak Ridge, TN 37831, USA
[4] Department of Physics, Florida State University, Tallahassee, Florida 32306, USA
[5] National High Magnetic Field Laboratory, Tallahassee, Florida 32310, USA

Note: This paper is part of the APL Quantum Special Topic on Quantum Dynamics in Theory, Numerics and in Experimental Research.

[a)] **Author to whom correspondence should be addressed:** kshrestha@wtamu.edu or drkeshavshrestha@gmail.com

ABSTRACT

This study investigates the electronic structure of the vanadium-based kagome metal YV_6Sn_6 using magnetoresistance (MR) and torque magnetometry. The MR exhibits a nearly linear, non-saturating behavior, increasing by up to 55% at 35 T but shows no evidence of Shubnikov–de Haas oscillations. In contrast, the torque signal, measured up to 41.5 T, reveals clear de Haas–van Alphen (dHvA) oscillations over a wide frequency range, from a low frequency of $F_\alpha \sim 20$ T to high frequencies between 8 and 10 kT. Angular and temperature-dependent dHvA measurements were performed to probe the Fermi surface parameters of YV_6Sn_6. The dHvA frequencies display weak angular dependence, and the effective mass, determined by fitting the temperature-dependent data to the Lifshitz–Kosevich formula, is 0.097 m_o, where m_o represents the free electron mass. To complement the experimental findings, we computed the electronic band structure and Fermi surface using density functional theory. The calculations reveal several notable features, including multiple Dirac points near the Fermi level, flatbands, and Van Hove singularities. Two bands cross the Fermi level, contributing to the Fermi surface, with theoretical frequencies matching well with the observed dHvA frequencies. These combined experimental and theoretical insights enhance our understanding of the electronic structure of YV_6Sn_6 and provide a valuable framework for studying other vanadium- and titanium-based kagome materials.

I. INTRODUCTION

Recently, kagome materials, with atomic arrangements resembling a corner-sharing kagome lattice, have attracted significant attention in condensed matter physics due to their fascinating properties, such as non-trivial topology, flatbands, charge-density wave (CDW), and superconductivity.[1–3] A prototypical example is AV_3Sb_5 (A = K, Rb, and Cs), also known as the "135" family, which forms a hexagonal lattice of V atoms coordinated by Sb atoms.[4–6] AV_3Sb_5 exhibits superconductivity with T_c ranging from ~0.3–3 K, CDW order near T_{CDW} ~80–110 K, and a Van Hove singularity, among other intriguing features.[7–10] Electronic band structure calculations reveal several remarkable properties, including the presence of flatbands, Van Hove singularity points, Dirac points near the Fermi level, and non-trivial $\mathbb{Z}_2$ topological invariants. Recent quantum oscillation studies[11–21] on AV_3Sb_5 have confirmed the non-trivial band topology and uncovered significant reconstruction of the Fermi surface in the CDW phase.

Another class of kagome compounds, RM_6X_6, known as the 166 family, has been discovered, where R represents alkali, alkaline earth, or rare earth metals (e.g., Li, Mg, Yb, Sm, Gd, etc.); *M* represents transition metals (e.g., Co, Cr, Mn, V, Ni, etc.); and *X* represents Si, Ge, or Sn.[22–27] This family crystallizes in the $MgFe_6Ge_6$ prototype structure, exhibits significant chemical diversity, and, therefore, offers a wide range of functionalities. Several interesting physical phenomena have already been observed in this family, for example, a large anomalous Hall effect in $LiMn_6Sn_6$, non-trivial topological properties in GdV_6Sn_6,[24,28] Chern topological magnetism in $TbMn_6Sn_6$,[2] competing magnetic phases in YMn_6Sn_6,[29] and more. Notably, within this family, ScV_6Sn_6 is the only member to exhibit a CDW transition at T_{CDW} = 92 K.[30,31] However, no superconductivity has been observed in ScV_6Sn_6 under either ambient conditions or high pressures up to 11 GPa.[32] We recently reported on the electronic structure of ScV_6Sn_6, studied using high-field torque measurements[33] and density functional theory (DFT), which probed its electronic bands and Fermi surface, uncovering its non-trivial topology.

This work focuses on YV_6Sn_6, a member of the 166 kagome family. Figure 1(a) shows the unit cell (upper panel) and the kagome lattice (bottom panel) of vanadium atoms in YV_6Sn_6. Previous electrical transport and magnetic studies by Pokharel *et al.*[22] have shown that YV_6Sn_6 does not exhibit a magnetic transition or CDW order down to 2 K. Recent studies[34] suggest that the CDW phase in ScV_6Sn_6 originates from a structural instability caused by tin–tin bond modulation in the rare-earth–tin chains. This instability appears to be driven by the undersized scandium atoms, which allow the scandium–tin chains to rattle within the larger V–Sn framework. In contrast, yttrium is too large, preventing the rattling of the rare-earth–tin chain and inhibiting the development of a CDW phase in YV_6Sn_6. DFT studies[22] on this material have revealed a non-trivial band topology, confirmed by calculating the $\mathbb{Z}_2$ topological invariants. Here, we have investigated the electronic structure of YV_6Sn_6 by employing high-field torque measurements and DFT calculations. Torque measurements under applied fields of 41.5 T revealed well-defined de Haas–van Alphen (dHvA) oscillations with frequencies reaching up to 10 kT. DFT calculations of the electronic band structure show multiple Dirac points, Van Hove singularities, and flatbands near the Fermi level. A comparison of the theoretical frequencies derived from DFT with the experimental frequencies demonstrates good agreement.

II. EXPERIMENTAL AND COMPUTATIONAL DETAILS

High-quality single crystals of YV_6Sn_6 were synthesized via the tin flux method following the recipe in Refs. 34 and 35. Elemental Y (Alfa Aesar, 99.9%), V (Alfa Aesar, 99.8%), and Sn (Alfa Aesar, 99.9999%) were put in an alumina Canfield crucible set and then sealed in silica ampoules filled with about 0.2 atm argon. The ampoules were heated to 1150 °C over 12 h, held for 15 h, and cooled to 780 °C over 300 h. To remove the tin flux, the ampoules were centrifuged at 780 °C. To remove the remaining tin on the surface, the crystals were etched in an aqueous 10 wt. % HCl solution for 12–36 h. Temperature-dependent resistivity measurements were carried out in a physical property measurement system (Quantum Design) using the four-probe technique. Magnetoresistance (MR) and torque measurements with maximum applied magnetic fields up to 35 and 41.5 T, respectively, were carried out at the National High Magnetic Field Laboratory (NHMFL), Tallahassee, FL. Torque measurements were conducted using a miniature piezoresistive cantilever. A tiny single crystal of YV_6Sn_6 was selected and attached to the cantilever arm using vacuum grease and then mounted on a rotating platform of the measurement probe. The probe was slowly cooled down to a base temperature of 0.5 K. Two resistive elements on the cantilever were balanced at the base temperature before taking the field dependent and temperature dependent torque measurements. Magnetic fields were swept at each fixed temperature at a rate of 1.5 T/min.

Electronic structures were calculated using density functional theory (DFT) with the full-potential linearized augmented plane wave (FP-LAPW) method, as implemented in the WIEN2k code.[36] The exchange-correlation energies were treated using the standard generalized gradient approximation (PBE-GGA).[37] Internal atomic coordinates were optimized in the scalar relativistic mode until the forces on individual atoms were reduced to below 20 meV/Å. Spin–orbit coupling (SOC) was incorporated through the second variational step.[38] The energy convergence criterion for self-consistent calculations was set to 10^{-4} Ry. The atomic sphere radii (RMT) were chosen as 2.50 bohrs for Y, V, and Sn. Self-consistent calculations utilized a grid of 800 *k*-points across the full Brillouin zone, while a denser *k*-point mesh of 5000 points was employed for Fermi surface computations.

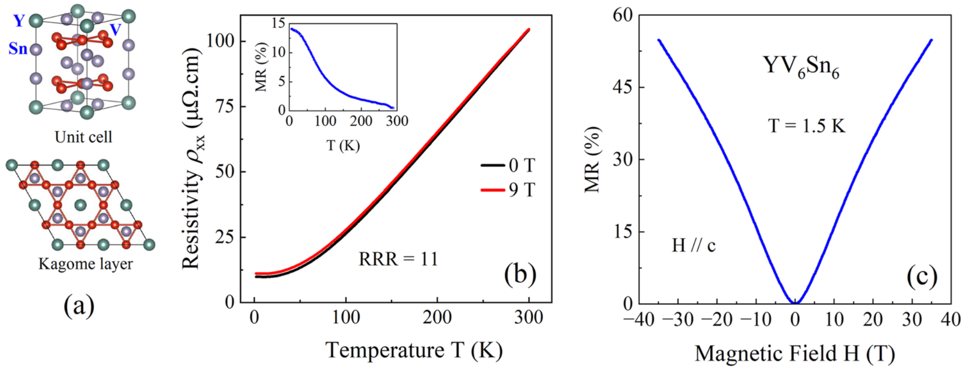

FIG. 1. (a) Unit cell (upper panel) and the top view (lower panel) of YV_6Sn_6, illustrating the kagome network formed by V atoms. (b) Temperature dependence of resistivity for a YV_6Sn_6 single crystal at 0 and 9 T. Inset: Magnetoresistance (MR) vs temperature plot. (c) MR plot for a YV_6Sn_6 single crystal with the magnetic field applied along the c-axis at T = 1.5 K. The MR reaches up to 55%, with no sign of quantum oscillations.

III. RESULTS AND DISCUSSION

Figure 1(b) shows the electrical resistivity, ρ_{xx}, as a function of temperature. As seen in the graph, the resistivity decreases with temperature, indicating typical metallic behavior. The residual resistivity ratio (RRR), calculated by dividing ρ_{xx} at 300 K by its value at 2 K, is 11, indicating the high quality of our YV_6Sn_6 crystals. Upon applying a magnetic field of 9 T, the resistivity increases, as shown by the red curve. The $\rho_{xx}(T)$ exhibits a similar behavior to that observed in another 166 family member, LuV_6Sn_6.[35] The inset displays the magnetoresistance (MR), defined as MR = $[\rho_{xx}\ (9\ \mathrm{T}) - \rho_{xx}(0)]/\rho_{xx}(0)$, where $\rho_{xx}(9\ \mathrm{T})$ and $\rho_{xx}(0)$ represent the resistivity values at 9 and 0 T, respectively. As shown in the inset, the MR reaches as high as 15% at 2 K and decreases to nearly zero at 300 K. In order to understand the effect of a magnetic field on electrical transport, we measured the electrical resistance as a function of the magnetic field. Figure 1(c) shows the MR for YV_6Sn_6 with the magnetic field applied along the c-axis at $T = 1.5$ K. As seen in the graph, the MR increases nearly linearly with the applied field, without any indication of saturation. At 35 T, the MR reaches 55%, but no Shubnikov–de Haas oscillations are observed. However, observing quantum oscillations is essential to probe the Fermi surface of YV_6Sn_6. Therefore, we proceed with an alternative measurement technique: torque magnetometry.

Figure 2(a) shows the τ vs field plot at two different tilt angles, $\theta = -7^\circ$ and -21°. Here, θ is defined as the angle between the magnetic field and the c-axis of the sample, as depicted in the upper inset of Fig. 2(a). The dHvA oscillations are clearly observed at both angles above 5 T. In addition to the low-frequency signal, there is an additional high-frequency signal at high magnetic fields above 30 T. The high-frequency signal is more prominent at $\theta = -7^\circ$ compared to $\theta = -21^\circ$, as indicated by the dotted circle. This is clearer in the zoomed-in plot of the high-field region, shown in the lower inset. To extract the oscillation frequencies, we subtracted a smooth polynomial background from the torque data and then performed a fast Fourier transform (FFT). Figure 2(b) shows the Fourier transform of the torque data presented in Fig. 2(a). The low-frequency component, F_α = 25 T, is present at both angles, as shown in the inset. The torque signal at $\theta = -7^\circ$ exhibits additional frequencies at 180, 1400, and 8800 T. In contrast, at $\theta = -21^\circ$, these frequencies are completely overshadowed by the dominant lower frequency, F_α. Due to the low resolution of the high-frequency signal, it is difficult to extract from the torque data at some θ values. However, the lower frequency F_α is consistently observed at all measured angles. We observed a similar behavior in torque measurements[33] of another 166 compound, ScV_6Sn_6, where low frequencies are dominant and present at all θ values, while high frequencies are weak and only emerge at very high magnetic fields. This will be discussed in detail later.

In order to calculate the effective mass of charge carriers, we carried out the torque measurement at different temperatures. Figure 3(a) shows the temperature dependent torque data measured at $\theta = 28^\circ$. As seen in the graph, the dHvA oscillations are pronounced at low temperatures and gradually disappear at higher temperatures. At 35 K, the quantum oscillations are not visible. At this tilt angle, the lower frequency F_α changes to 18 T, and there is no interference from the high frequency signals, as seen in the frequency spectrum in Fig. 3(b). The amplitude of the frequency decreases at higher temperatures, and this behavior can be described by the Lifshitz–Kosevich (LK) theory.[39] According to the LK theory, the temperature dependent quantum oscillations in torque is given by

$$\Delta\tau(T,H) \propto e^{-\lambda_D}\frac{\lambda(T/H)}{\sin h[\lambda(T/H)]}, \qquad (1)$$

with $\lambda_D(H) = \frac{2\pi^2 k_B}{\hbar e} m^* \frac{T_D}{H}$ and $\lambda(T/H) = \frac{2\pi^2 k_B}{\hbar e} m^* \frac{T}{H}$. Here, T_D, k_B, and m^* represent the Dingle temperature, Boltzmann's constant, and effective mass of the charge carriers, respectively. The first term is the Dingle factor, which describes the attenuation of the oscillations with decreasing field H. The second term explains the weakening of the oscillations at higher temperatures.

The inset in Fig. 3(b) shows the FFT amplitude at different temperatures. The scattered squares represent the FFT amplitude,

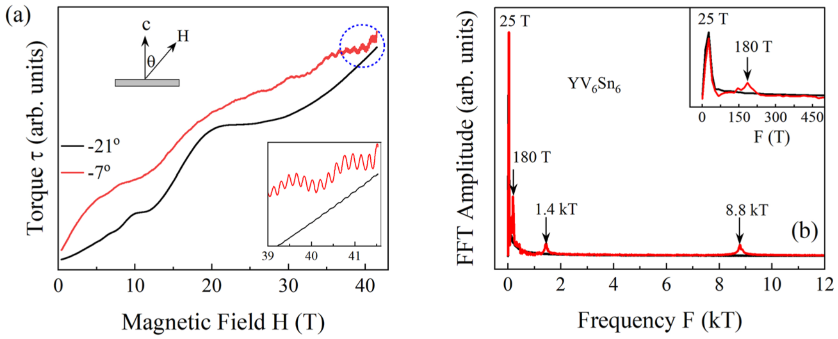

FIG. 2. (a) Torque (τ) of a YV_6Sn_6 single crystal measured up to 41.5 T at $\theta = -7^\circ$ and -21° and $T = 0.5$ K. The de Haas–van Alphen (dHvA) oscillations are observed at both angles above 5 T. A high-frequency signal is apparent at $\theta = -7^\circ$, as indicated by the dotted circle. Upper inset: A schematic diagram defining the tilt angle, θ. Lower inset: Zoomed-in torque data in the high-field region. The high-frequency signal is prominent at $\theta = -7^\circ$, although it is observed at both angles, -7° and -21°. (b) Frequency spectrum of the dHvA oscillations shown in (a). The low-frequency peak at F_α = 25 T is present at both angles, while three additional frequencies, 180, 1400, and 8800 T, are observed only at $\theta = -7^\circ$. Inset: A zoomed-in view of the frequency spectrum highlighting the lower frequencies.

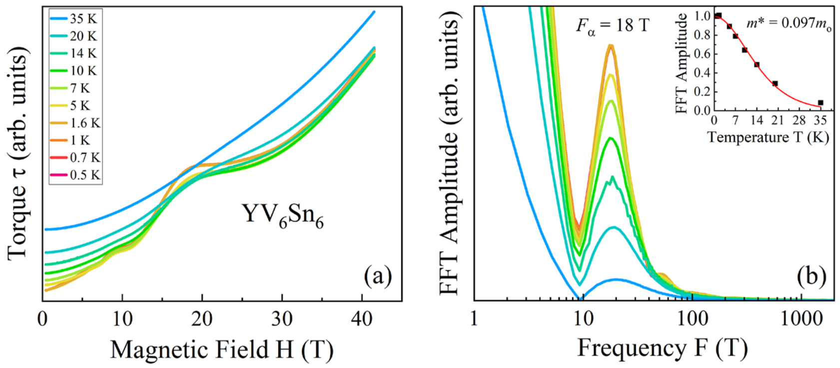

FIG. 3. Torque data of YV_6Sn6 at different temperatures. The de Haas–van Alphen (dHvA) oscillations are visible at low temperatures and gradually diminish at higher temperatures. (b) Frequency spectrum of the torque data shown in (a). A prominent peak is observed at $F_\alpha = 18$ T in the frequency spectrum. Inset: temperature dependence of the frequency peak. The squares represent the data points, and the solid curve is the best fit using the Lifshitz–Kosevich formula.

while the solid red curve represents the best-fit curve to the data using the LK formula [Eq. (1)]. As shown in the graph, the LK formula explains the temperature-dependent behavior of the frequency. From the best fit, we determined $m^* = 0.097\ m_o$, where m_o is the rest mass of an electron. This m^* is comparable to the effective mass of other kagome systems[40,43–45] reported previously.

The angular dependence of quantum oscillations provides information about the shape, size, and dimensionality of the Fermi surface.[39,42–44] To explore this, we conducted torque measurements at various tilt angles. In Fig. 4(a), the torque data for YV_6Sn_6 measured at different θ values are shown. As shown in Fig. 4(a), there are clearly more than two periods, representing multiple quantum oscillation frequencies, and they seem to vary with θ values. Furthermore, the dHvA oscillations are present even if the magnetic field is perpendicular to the sample surface, indicating the three-dimensional nature of the Fermi surface. We have carried out background subtraction from the torque signal and determined the frequency values at different θ points, as presented in Fig. 4(b). For comparison purposes, we have also included possible theoretical frequencies computed by using DFT. We will discuss it in detail later.

From our high-field data, we observed a prominent peak at F_α, which appears to remain nearly constant while rotating the sample. In order to understand its topological feature, we calculated the Berry phase (Φ_B) of the Fermi pocket of F_α using the Landau level (LL) fan plot, as shown in Fig. S1 of the supplementary material. For a topologically non-trivial (or trivial) system, the Φ_B value is π (or zero).[42,45] To avoid possible interference from other frequency signals, we employed the FFT bandpass filter approach[21,40,46,47] to extract the oscillations corresponding to the particular frequency. When constructing this diagram, we assigned the LL index to the minima and maxima positions as $(N - \frac{1}{4})$ and $(N + \frac{1}{4})$, respectively.[46–48] By performing a linear extrapolation of the data, represented by the dashed line, we derived an intercept $N_0 = 0.18 \pm 0.02$, corresponding to $\Phi_B = (0.36 \pm 0.04)\pi$. Although Φ_B is not exactly π, its non-zero value indicates the non-trivial topology of the α pocket. Furthermore, the slope value (18.1 ± 0.3) T closely matches the F_α value of 18 T in Fig. 3(b), validating the precision of the linear extrapolation in determining the intercept (and consequently the Φ_B value). Furthermore, the bandpass filter's effectiveness in retaining the original dHvA oscillation signal without significant error is affirmed. A non-trivial Φ_B has been reported for the sister compound ScV_6Sn_6 using quantum oscillation studies.[33,49]

To better understand the experimental observations, we computed the electronic band structure and Fermi surface of YV_6Sn_6. Figure 5 illustrates the electronic band structures of YV_6Sn_6 (a) with-

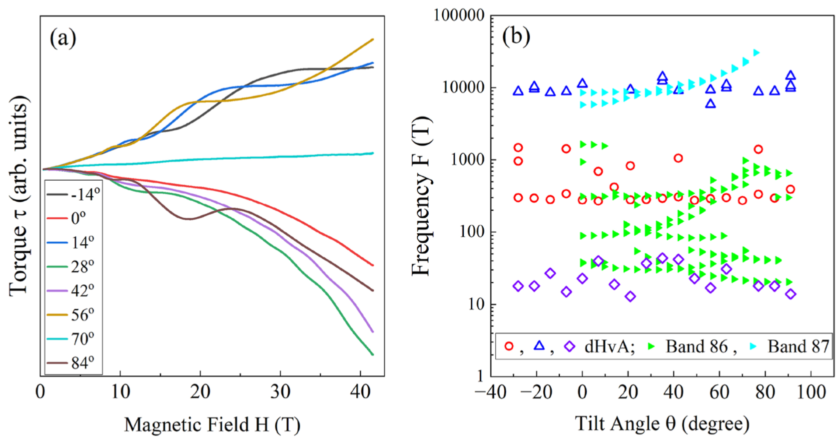

FIG. 4. (a) Angle-dependent torque signal for YV_6Sn_6. The period, and thus the frequency, of quantum oscillations varies with the tilt angle θ. (b) Comparison of theoretical frequencies from **band 86** and **band 87** with experimental quantum oscillation frequencies. **Band 86** frequencies align well with experimental values below 1000 T, while higher frequencies, around 10 kT, correspond closely to those from **band 87**.

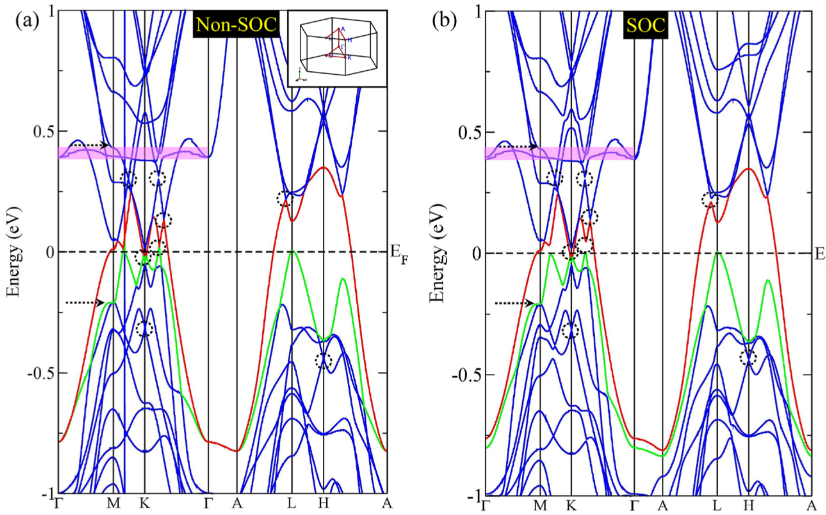

FIG. 5. Electronic band structure of pristine YV$_6$Sn$_6$ with (a) non-SOC and (b) SOC. The SOC is oriented along the [001] direction, corresponding to the out-of-plane axis of the material. The flatband is denoted by the shaded purple area, and the Dirac points near the Fermi level are indicated by the dotted circles. Two bands, indicated by red and green colors, cross the Fermi level. The dashed arrows represent the Van Hove singularities. Inset: first Brillouin zone showing high-symmetry points.

out and (b) with the inclusion of spin–orbit coupling (SOC). The inset in Fig. 5(a) shows the high-symmetry points in the first Brillouin zone. As shown in Fig. 5(a), the electronic bands exhibit several intriguing features, including multiple Dirac points near the Fermi level (highlighted by the dotted circles), a flatband (shaded area), and multiple Van Hove singularities (indicated by the dashed arrows). Orbital-resolved electronic band structure provides detailed insights into the contributions of specific atomic orbitals to the electronic bands in a material. This information is critical for understanding the electronic, magnetic, and optical properties of materials. Therefore, we computed the orbital-resolved electronic bands of YV$_6$Sn$_6$, as presented in Fig. S2 of the supplementary material. As shown in the graph, the electronic bands near the Fermi level are primarily dominated by the vanadium 3*d* orbitals. Moreover, features such as Dirac points, Van Hove singularities, and flatbands arise from the vanadium 3*d* and tin 5*p* orbitals. Notably, there appears to be no contribution from the yttrium 4*d* orbitals to the electronic bands of YV$_6$Sn$_6$.

Here, we have aligned the SOC along the [001] direction, corresponding to the out-of-plane axis of the material. To investigate the magnetic anisotropy, we calculated the effect of SOC along various directions, including [001], [100], [110], and [111]. Our analysis revealed that [110] is the easy axis for magnetization, while [001] is the hard axis. By computing the total energy differences between magnetization orientations along different crystallographic directions, we determined the magnetic anisotropy energy to be 0.23 meV for YV$_6$Sn$_6$.

Our electronic band structure is consistent with those calculated for other 166 kagome families.[22,33,41,50,51] With the inclusion of SOC, the electronic bands slightly shift (either up or down), as shown in Fig. 5(b). Here, the SOC is oriented along the [001] direction, corresponding to the out-of-plane axis of the material. While some of the Dirac points develop gaps due to the inclusion of SOC, the flatbands and Van Hove singularity points remain nearly intact. For example, the previously gapless Dirac point along the K–Γ and A–L directions develops a gap as high as ~50 meV in the presence of SOC. There are two bands: **band 86** and **band 87** cross the Fermi level, as indicated by the green and red colors, respectively. These bands contribute to the Fermi surface of YV$_6$Sn$_6$.

Figure 6 shows the band-resolved Fermi surface of YV$_6$Sn$_6$. The Fermi surface of **band 86** exhibits a chain-like feature at the Brillouin zone boundary, along with small pockets at the edge of the Brillouin zone. For **band 87**, there is a deformed, cylinder-like feature with a belly in the middle. The final inset represents the combined Fermi surface sheets from both bands. To understand the effect of SOC, we computed the Fermi surface of YV$_6$Sn$_6$ including the SOC effect, as shown in Fig. S3 of the supplementary material. It is found that the Fermi surface remains nearly unchanged. According to Onsager's relation,[39,42,52,53] the frequency (F) of quantum oscillations is directly proportional to the cross-sectional area (A_F) of the Fermi surface as $F = \hbar/(2\pi e)A_F{}^2$, where $\hbar$ is the reduced Planck constant and e is the charge of an electron. Therefore, we can calculate possible theoretical frequencies by measuring the cross-sectional area of the Fermi surface.

We employed the SKEAF code[54] for computing possible theoretical frequencies from the Fermi pockets derived from **band 86** and **band 87**. The calculated angular dependence of frequencies from different bands is plotted in Fig. 4(b) alongside the experimental data. As observed in the figure, frequencies derived from

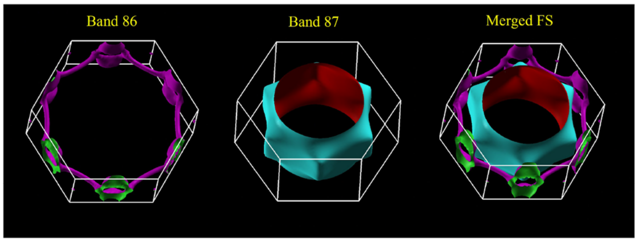

FIG. 6. Band resolved Fermi surface (FS) of YV$_6$Sn$_6$. Two bands: **band 86** and **band 87** contribute to the FS. The last inset is the combined FS sheets from both bands.

both **bands 86** and **87** describe the behavior of F_α. Low frequencies below 1000 T, observed in dHvA oscillations, are in good agreement with the theoretical frequencies computed from **band 86**. Similarly, the high-frequency signal near 10 kT is in good agreement with those computed from **band 87**. It is important to note that, although the frequency values are comparable, the angular dependence of the theoretical frequency derived from **band 87** shows an upward trend, especially above 60°, which is not clearly observed in the experimental data. The high frequency signal appears in very high fields (around 35 T) and is dominated by the low frequency signal, reducing its resolution [Figs. 4(a) and 2(a) and 2(b)]. This makes it challenging to track the angular dependence precisely. However, the angular dependence of the low frequencies is well captured by the frequencies derived from **band 86**. There are also possible frequencies below 100 T, but we did not observe these frequencies in our dHvA oscillation data. However, quantum oscillation experiments are not uncommon to miss higher frequencies.[55,56]

IV. SUMMARY

Despite the chemical diversity of 166 compounds, there are limited studies[33,41,49,50,57,58] that use quantum oscillations to understand their electronic properties. Moreover, most of these studies report the presence of low-frequency signals (below 100 T).[49,57,58] For instance, Ma *et al.* performed Shubnikov–de Haas (SdH) oscillations in RMn_6Sn_6 (R = Gd–Tm, Lu) and observed frequencies below 100 T. This paper focuses on the detailed electrical transport, magnetotransport, and torque magnetometry studies of YV_6Sn_6 with applied fields up to 41.5 T. Our electrical transport measurement shows that this material demonstrates a good metallic behavior. To investigate the magnetotransport properties, we measured magnetoresistance (MR) with the applied fields up to 35 T. We found nearly a linearly varying and non-saturating MR with the value reaching as high as 55%; however, there is no clear sign of SdH oscillations in MR data. Therefore, we proceeded with another measurement technique: torque magnetometry. Our torque data, measured up to 41.5 T, show clear de Haas–van Alphen (dHvA) oscillations with the major frequency near 20 T, along with a high frequency signal as high as 10 kT.

To probe the Fermi surface properties, we performed both angular and temperature-dependent torque measurements. To complement the experimental results, we calculated the electronic band structure and the Fermi surface of YV_6Sn_6 using density functional theory (DFT). The calculations reveal several Dirac points near the Fermi level, along with notable features such as flatbands and Van Hove singularities. Two electronic bands cross the Fermi level, contributing to the Fermi surface. Unlike other kagome materials, the Fermi surface consists of a deformed cylindrical pocket at the center and chain-like features along the boundary of the Brillouin zone. By analyzing the cross-sectional areas of these Fermi pockets, we computed theoretical dHvA frequencies, which show good agreement with the experimentally observed values.

We did not observe SdH oscillations in YV_6Sn_6 even at a maximum applied magnetic field of 35 T [Fig. 1(c)]. This is likely due to the sensitivity of resistivity-based SdH measurements to various damping effects, including electron–phonon interactions and scattering from defects and impurities within the crystal, which can suppress quantum oscillations. In contrast, torque magnetometry, which detects changes in magnetization, offers a higher signal-to-noise ratio and can amplify even subtle oscillations. Notably, torque measurements can resolve tiny high-frequency signals embedded within larger, low-frequency oscillations [Fig. 2(a)]. The proximity of multiple Dirac points near the Fermi level results in charge carriers behaving like massless Dirac fermions, characterized by exceptionally high mobility and unique quantum mechanical properties. As shown in Fig. 5, the flatband resides near the Fermi level (~0.4 eV above) and can be tuned closer through doping or application of external pressure. Furthermore, the presence of Van Hove singularities, or saddle points in the band structure where the density of states (DOS) diverges, significantly enhances electronic interactions, increasing the likelihood of emergent phenomena, such as magnetism, charge-density waves, and superconductivity. These combined experimental and computational insights presented here for YV_6Sn_6 provide a valuable foundation for understanding the electronic properties of other titanium- and vanadium-based kagome systems.

SUPPLEMENTARY MATERIAL

The supplementary material provides details on the Berry phase calculations (Fig. S1), orbital-resolved electronic band structures (Fig. S2), and band-resolved Fermi surfaces (Fig. S3) of YV_6Sn_6.

ACKNOWLEDGMENTS

The work at West Texas A&M University (WTAMU) was supported by the Killgore Undergraduate and Graduate Student Research Grants, the Welch Foundation (Grant No. AE-0025), and the National Science Foundation (Award No. 2336011). DFT calculations were performed in the WTAMU HPC cluster, which was funded by the National Science Foundation (NSF CC* GROWTH 2018841). S.M. and D.G.M. acknowledge the support from AFOSR MURI (Grant No. FA9550-20-1-0322) and the support from the Gordon and Betty Moore Foundation (Grant No. GBMF9069). A portion of this work was performed at the National High Magnetic Field Laboratory, which is supported by National Science Foundation Cooperative Agreement No. DMR-2128556 and the State of Florida.

AUTHOR DECLARATIONS

Conflict of Interest

The authors have no conflicts to disclose.

Author Contributions

K.S. and C.P. contributed equally to this work.

Kyryl Shtefiienko: Conceptualization (equal); Investigation (equal). **Cole Phillips**: Conceptualization (equal); Investigation (equal). **Shirin Mozaffari**: Conceptualization (equal); Investigation (equal). **Richa P. Madhogaria**: Conceptualization (equal); Investigation (equal). **William R. Meier**: Conceptualization (equal); Investigation (equal). **David G. Mandrus**: Conceptualization (equal); Investigation (equal). **David E. Graf**: Conceptualization (equal); Investigation (equal). **Keshav Shrestha**: Conceptualization (lead); Formal analysis (equal); Investigation (lead); Writing – original draft (lead); Writing – review & editing (lead).

DATA AVAILABILITY

The data that support the findings of this study are available within the article.

REFERENCES

[1] L. Ye, M. Kang, J. Liu, F. von Cube, C. R. Wicker, T. Suzuki, C. Jozwiak, A. Bostwick, E. Rotenberg, D. C. Bell, L. Fu, R. Comin, and J. G. Checkelsky, Nature **555**, 638 (2018).

[2] J.-X. Yin, W. Ma, T. A. Cochran, X. Xu, S. S. Zhang, H.-J. Tien, N. Shumiya, G. Cheng, K. Jiang, B. Lian *et al.*, Nature **583**, 533 (2020).

[3] K. Jiang, T. Wu, J.-X. Yin, Z. Wang, M. Z. Hasan, S. D. Wilson, X. Chen, and J. Hu, Natl. Sci. Rev. **10**, nwac199 (2022).

[4] B. R. Ortiz, L. C. Gomes, J. R. Morey, M. Winiarski, M. Bordelon, J. S. Mangum, I. W. H. Oswald, J. A. Rodriguez-Rivera, J. R. Neilson, S. D. Wilson, E. Ertekin, T. M. McQueen, and E. S. Toberer, Phys. Rev. Mater. **3**, 094407 (2019).

[5] B. R. Ortiz, P. M. Sarte, E. M. Kenney, M. J. Graf, S. M. L. Teicher, R. Seshadri, and S. D. Wilson, Phys. Rev. Mater. **5**, 034801 (2021).

[6] B. R. Ortiz, S. M. Teicher, Y. Hu, J. L. Zuo, P. M. Sarte, E. C. Schueller, A. M. Abeykoon, M. J. Krogstad, S. Rosenkranz, R. Osborn, R. Seshadri, L. Balents, J. He, and S. D. Wilson, Phys. Rev. Lett. **125**, 247002 (2020).

[7] F. H. Yu, D. H. Ma, W. Z. Zhuo, S. Q. Liu, X. K. Wen, B. Lei, J. J. Ying, and X. H. Chen, Nat. Commun. **12**, 3645 (2021).

[8] K. Y. Chen, N. N. Wang, Q. W. Yin, Y. H. Gu, K. Jiang, Z. J. Tu, C. S. Gong, Y. Uwatoko, J. P. Sun, H. C. Lei, J. P. Hu, and J. Cheng, Phys. Rev. Lett. **126**, 247001 (2021).

[9] N. N. Wang, K. Y. Chen, Q. W. Yin, Y. N. N. Ma, B. Y. Pan, X. Yang, X. Y. Ji, S. L. Wu, P. F. Shan, S. X. Xu, Z. J. Tu, C. S. Gong, G. T. Liu, G. Li, Y. Uwatoko, X. L. Dong, H. C. Lei, J. P. Sun, and J.-G. Cheng, Phys. Rev. Res. **3**, 043018 (2021).

[10] M. Kang, S. Fang, J.-K. Kim, B. R. Ortiz, S. H. Ryu, J. Kim, J. Yoo, G. Sangiovanni, D. D. Sante, B.-G. Park, C. Jozwiak, A. Bostwick, E. Rotenberg, E. Kaxiras, S. D. Wilson, J.-H. Park, and R. Comin, Nat. Phys. **18**, 301 (2022).

[11] F. H. Yu, T. Wu, Z. Y. Wang, B. Lei, W. Z. Zhuo, J. J. Ying, and X. H. Chen, Phys. Rev. B **104**, 041103 (2021).

[12] Q. Yin, Z. Tu, C. Gong, Y. Fu, S. Yan, and H. Lei, Chin. Phys. Lett. **38**, 037403 (2021).

[13] S.-Y. Yang, Y. Wang, B. R. Ortiz, D. Liu, J. Gayles, E. Derunova, R. Gonzalez-Hernandez, L. Šmejkal, Y. Chen, S. S. P. Parkin, S. D. Wilson, E. S. Toberer, T. McQueen, and M. N. Ali, Sci. Adv. **6**, eabb6003 (2020).

[14] K. Nakayama, L. Yongkai, T. Kato, M. Liu, Z. Wang, T. Takahashi, Y. Yao, and T. Sato, Phys. Rev. X **12**, 011001 (2022).

[15] B. R. Ortiz, S. M. L. Teicher, L. K. abd Paul, M. Sarte, J. P. C. Ruff, R. Seshadri, and S. D. Wilson, Phys. Rev. X **11**, 041030 (2021).

[16] H. Luo, Q. Gao, H. Liu, Y. Gu, D. Wu, C. Yi, J. Jia, S. Wu, X. Luo, Y. Xu *et al.*, Nat. Commun. **13**, 273 (2022).

[17] Y. Fu, N. Zhao, Z. Chen, Q. Yin, Z. Tu, C. Gong, C. Xi, X. Zhu, Y. Sun, K. Liu, and H. Lei, Phys. Rev. Lett. **127**, 207002 (2021).

[18] W. Zhang, L. Wang, C. W. Tsang, X. Liu, J. Xie, W. C. Yu, K. T. Lai, and S. K. Goh, Phys. Rev. B **106**, 195103 (2022).

[19] C. Broyles, D. Graf, H. Yang, X. Dong, H. Gao, and S. Ran, Phys. Rev. Lett. **129**, 157001 (2022).

[20] K. Shrestha, M. Shi, T. Nguyen, D. Miertschin, K. Fan, L. Deng, D. E. Graf, X. Chen, and C.-W. Chu, Phys. Rev. B **107**, 075120 (2023).

[21] K. Shrestha, R. Chapai, B. K. Pokharel, D. Miertschin, T. Nguyen, X. Zhou, D. Y. Chung, M. G. Kanatzidis, J. F. Mitchell, U. Welp, D. Popović, D. E. Graf, B. Lorenz, and W. K. Kwok, Phys. Rev. B **105**, 024508 (2022).

[22] G. Pokharel, S. M. L. Teicher, B. R. Ortiz, P. M. Sarte, G. Wu, S. Peng, J. He, R. Seshadri, and S. D. Wilson, Phys. Rev. B **104**, 235139 (2021).

[23] J. Lee and E. Mun, Phys. Rev. Mater. **6**, 083401 (2022).

[24] S. Peng, Y. Han, G. Pokharel, J. Shen, Z. Li, M. Hashimoto, D. Lu, B. R. Ortiz, Y. Luo, H. Li, M. Guo, B. Wang, S. Cui, Z. Sun, Z. Qiao, S. D. Wilson, and J. He, Phys. Rev. Lett. **127**, 266401 (2021).

[25] E. Rosenberg, J. M. DeStefano, Y. Guo, J. S. Oh, M. Hashimoto, D. Lu, R. J. Birgeneau, Y. Lee, L. Ke, M. Yi, and J.-H. Chu, Phys. Rev. B **106**, 115139 (2022).

[26] X. Zhang, Z. Liu, Q. Cui, Q. Guo, N. Wang, L. Shi, H. Zhang, W. Wang, X. Dong, J. Sun, Z. Dun, and J. Cheng, Phys. Rev. Mater. **6**, 105001 (2022).

[27] G. Pokharel, B. Ortiz, J. Chamorro, P. Sarte, L. Kautzsch, G. Wu, J. Ruff, and S. D. Wilson, Phys. Rev. Mater. **6**, 104202 (2022).

[28] Y. Hu, X. Wu, Y. Yang, S. Gao, N. C. Plumb, A. P. Schnyder, W. Xie, J. Ma, and M. Shi, Sci. Adv. **8**, eadd2024 (2022).

[29] N. J. Ghimire, R. L. Dally, L. Poudel, D. Jones, D. Michel, N. T. Magar, M. Bleuel, M. A. McGuire, J. Jiang, J. Mitchell *et al.*, Sci. Adv. **6**, eabe2680 (2020).

[30] H. W. S. Arachchige, W. R. Meier, M. Marshall, T. Matsuoka, R. Xue, M. A. McGuire, R. P. Hermann, H. Cao, and D. Mandrus, Phys. Rev. Lett. **129**, 216402 (2022).

[31] T. Hu, H. Pi, S. Xu, L. Yue, Q. Wu, Q. Liu, S. Zhang, R. Li, X. Zhou, J. Yuan, D. Wu, T. Dong, H. Weng, and N. Wang, Phys. Rev. B **107**, 165119 (2023).

[32] X. Zhang, J. Hou, W. Xia, Z. Xu, P. Yang, A. Wang, Z. Liu, J. Shen, H. Zhang, X. Dong, Y. Uwatoko, J. Sun, B. Wang, Y. Guo, and J. Cheng, Materials **15**, 7372 (2022).

[33] K. Shrestha, B. Regmi, G. Pokharel, S.-G. Kim, S. D. Wilson, D. E. Graf, B. A. Magar, C. Phillips, and T. Nguyen, Phys. Rev. B **108**, 245119 (2023).

[34] W. R. Meier, R. P. Madhogaria, S. Mozaffari, M. Marshall, D. E. Graf, M. A. McGuire, H. W. S. Arachchige, C. L. Allen, J. Driver, H. Cao, and D. Mandrus, J. Am. Chem. Soc. **145**, 20943 (2023).

[35] S. Mozaffari, W. R. Meier, R. P. Madhogaria, N. Peshcherenko, S.-H. Kang, J. W. Villanova, H. W. S. Arachchige, G. Zheng, Y. Zhu, K.-W. Chen, K. Jenkins, D. Zhang, A. Chan, L. Li, M. Yoon, Y. Zhang, and D. G. Mandrus, Phys. Rev. B **110**, 035135 (2024).

[36] P. Blaha, K. Schwarz, G. K. Madsen, D. Kvasnicka, and J. Luitz, *An Augmented Plane Wave Plus Local Orbitals Program for Calculating Crystal Properties* (Schwarz, Vienna University of Technology, Austria, 2001), Vol. 60.

[37] J. P. Perdew, K. Burke, and M. Ernzerhof, Phys. Rev. Lett. **77**, 3865 (1996).

[38] K. Koepernik and H. Eschrig, Phys. Rev. B **59**, 1743 (1999).

[39] D. Shoenberg, *Magnetic Oscillations in Metals* (Cambridge University Press, 1984).

[40] C. Phillips, K. Shtefiienko, T. Nguyen, A. N. Capa Salinas, B. A. Magar, G. Pokharel, S. D. Wilson, D. E. Graf, and K. Shrestha, Phys. Rev. B **110**, 205135 (2024).

[41] C. Dhital, G. Pokharel, B. Wilson, I. Kendrick, M. M. Asmar, D. Graf, J. Guerrero-Sanchez, R. Gonzalez-Hernandez, and S. D. Wilson, Phys. Rev. B **109**, 235145 (2024).

[42] B. R. Ortiz, P. M. Sarte, E. M. Kenney, M. J. Graf, S. M. L. Teicher, R. Seshadri, and S. D. Wilson, Phys. Rev. Mater. **5**, 034801 (2021).

[43] K. Shrestha, V. Marinova, D. Graf, B. Lorenz, and C. W. Chu, Phys. Rev. B **95**, 075102 (2017).

[44] K. Shrestha, D. Graf, V. Marinova, B. Lorenz, and C. W. Chu, J. Appl. Phys. **122**, 125901 (2017).

[45] K. Shrestha, "Magnetotransport studies on topological insulators," Doctoral dissertation, University of Houston (2015), see https://hdl.handle.net/10657/4881.

[46] T. Nguyen, N. Aryal, B. K. Pokharel, L. Harnagea, D. Mierstchin, D. Popović, D. E. Graf, and K. Shrestha, Phys. Rev. B **106**, 075154 (2022).

[47] K. Shrestha, M. Shi, B. Regmi, T. Nguyen, D. Miertschin, K. Fan, L. Z. Deng, N. Aryal, S.-G. Kim, D. E. Graf, X. Chen, and C. W. Chu, Phys. Rev. B **107**, 155128 (2023).

[48] K. Shrestha, D. Miertschin, R. Sankar, B. Lorenz, and C. W. Chu, J. Phys.: Condens. Matter **33**, 335501 (2021).

[49] G. Zheng, Y. Zhu, S. Mozaffari, N. Mao, K.-W. Chen, K. Jenkins, D. Zhang, A. Chan, H. W. S. Arachchige, R. P. Madhogaria *et al.*, J. Phys.: Condens. Matter **36**, 215501 (2024).

[50] E. Rosenberg, J. M. DeStefano, Y. Lee, C. Hu, Y. Shi, D. Graf, S. M. Benjamin, L. Ke, and J.-H. Chu, Phys. Rev. B **110**, 035119 (2024).

[51] S. R. Bhandari, M. Zeeshan, V. Gusain, K. Shrestha, and D. Rai, APL Quantum **1**, 046118 (2024).

[52] K. Shrestha, V. Marinova, B. Lorenz, and P. C. W. Chu, Phys. Rev. B **90**, 241111 (2014).

[53] K. Shrestha, V. Marinova, B. Lorenz, and C. W. Chu, J. Phys.: Condens. Matter **30**, 185601 (2018).

[54] P. Rourke and S. Julian, Comput. Phys. Commun. **183**, 324 (2012).

[55] W. Zheng, R. Schönemann, S. Mozaffari, Y.-C. Chiu, Z. B. Goraum, N. Aryal, E. Manousakis, T. M. Siegrist, K. Wei, and L. Balicas, Phys. Rev. B **102**, 125103 (2020).

[56] D. Rhodes, R. Schönemann, N. Aryal, Q. Zhou, Q. R. Zhang, E. Kampert, Y.-C. Chiu, Y. Lai, Y. Shimura, G. T. McCandless, J. Y. Chan, D. W. Paley, J. Lee, A. D. Finke, J. P. C. Ruff, S. Das, E. Manousakis, and L. Balicas, Phys. Rev. B **96**, 165134 (2017).

[57] W. Ma, X. Xu, J.-X. Yin, H. Yang, H. Zhou, Z.-J. Cheng, Y. Huang, Z. Qu, F. Wang, M. Z. Hasan, and S. Jia, Phys. Rev. Lett. **126**, 246602 (2021).

[58] M. He, X. Xu, D. Li, Q. Zeng, Y. Liu, H. Zhao, S. Zhou, J. Zhou, and Z. Qu, Phys. Rev. B **109**, 155117 (2024).

APL Quantum

RESEARCH ARTICLE | DECEMBER 10 2024

Electron beam-splitting effect with crossed zigzag graphene nanoribbons in high-spin metallic states

Special Collection: Quantum Dynamics in Theory, Numerics and in Experimental Research

Sofia Sanz ✉ ; Géza Giedke ; Daniel Sánchez-Portal ; Thomas Frederiksen

APL Quantum 1, 046122 (2024)
https://doi.org/10.1063/5.0233722

APL Quantum ARTICLE pubs.aip.org/aip/apq

Electron beam-splitting effect with crossed zigzag graphene nanoribbons in high-spin metallic states

Cite as: APL Quantum 1, 046122 (2024); doi: 10.1063/5.0233722
Submitted: 16 August 2024 • Accepted: 13 November 2024 •
Published Online: 10 December 2024

Sofia Sanz,[1,2,a)] **Géza Giedke,**[1,3] **Daniel Sánchez-Portal,**[2] **and Thomas Frederiksen**[1,3]

AFFILIATIONS

[1] Donostia International Physics Center (DIPC), E-20018 Donostia-San Sebastián, Spain
[2] Centro de Física de Materiales (CFM) CSIC-UPV/EHU, E-20018 Donostia-San Sebastián, Spain
[3] IKERBASQUE, Basque Foundation for Science, E-48013 Bilbao, Spain

Note: This paper is part of the APL Quantum Special Topic on Quantum Dynamics in Theory, Numerics and in Experimental Research.

[a)] **Author to whom correspondence should be addressed:** sofia.sanzwuhl@ehu.eus

ABSTRACT

Here, we analyze the electron transport properties of a device formed of two crossed graphene nanoribbons with zigzag edges (ZGNRs) in a spin state with total magnetization different from zero. While the ground state of ZGNRs has been shown to display antiferromagnetic ordering between the electrons at the edges, for wide ZGNRs—where the localized spin states at the edges are decoupled and the exchange interaction is close to zero—in the presence of relatively small magnetic fields, the ferromagnetic (FM) spin configuration can become the state of lowest energy due to the Zeeman effect. In these terms, by comparing the total energy of a periodic ZGNR as a function of the magnetization per unit cell, we obtain the FM-like solution of the lowest energy for the perfect ribbon, the corresponding FM-like configuration of the lowest energy for the four-terminal device formed of crossed ZGNRs, and the critical magnetic field needed to excite the system to this spin configuration. By performing transport calculations, we analyze the role of the distance between layers and the crossing angle of this device in the electrical conductance, at small gate voltages. The problem is approached employing the mean-field Hubbard Hamiltonian in combination with non-equilibrium Green's functions. We find that ZGNR devices subject to transverse magnetic fields may acquire a high-spin configuration that ensures a metallic response and tunable beam-splitting properties, making this setting promising for studying electron quantum optics with single-electron excitations.

I. INTRODUCTION

The increasing interest in graphene nanoribbons (GNRs) for molecular-scale electronic and spintronic devices has emerged because it is well known that they inherit some of the exceptional properties of graphene while having tunable electronic properties, such as the dependence of the bandgap on their width and edge topology,[1] and the appearance of π-magnetism,[2] absent in pure two-dimensional (2D) graphene. Moreover, these systems are a remarkable platform for electron quantum optics, where the electrons propagating coherently in these ballistic conductors resemble photons propagating in optical waveguides.[3] On the one hand, it has been shown that electrons can propagate without scattering over large distances of the order of ~100 nm in GNRs.[4–6] On the other hand, ballistic transport in ZGNRs can be fairly insusceptible to edge defects as a consequence of the prevailing Dirac-like behavior, which makes the electronic current flow maximally through the central region of the ribbon.[7] Furthermore, with the advent of bottom-up fabrication techniques, long samples of GNRs free of defects can now be chemically realized via on-surface synthesis, as demonstrated in the seminal works by Cai *et al.* for armchair GNRs[8] and by Ruffieux *et al.* for ZGNRs.[9]

It is known that the ground state of ZGNRs corresponds to a ferromagnetic (FM) ordering of spins along the edges and antiferromagnetic (AFM) ordering between the edges,[10,11] i.e., with total spin projection per unit cell equal to zero, $S_z = 0$. In this configuration, the magnetic instabilities of the states localized at the edges coming from the flat bands of ZGNRs open a bandgap due to the Coulomb repulsion in the otherwise metallic ribbons.[12] The opening of the bandgap and the edge states associated with the AFM coupling in ZGNRs have been confirmed by experiments, where the magnetic order has been shown to be stable up to room temperature.[13,14] The spin-polarized states localized at the edges are coupled such that there is an energy penalty to excite the AFM ground state to the FM state (exchange interaction). In the case of wider ZGNRs, the AFM and FM solutions are close in energy (small exchange interaction) due to the decoupling of the localized edge states, as they decay exponentially toward the center of the ribbon.[10,15–18] In this case, the FM solution can be favored due to the Zeeman energy under a relatively small magnetic field. The presence of a net spin-polarization, in the absence of transition metals or heavy atoms, makes these structures privileged for spintronics due to the weak spin scattering in pure carbon-based systems.[2,19] For instance, the intrinsically weak spin-orbit and hyperfine couplings in graphene lead to long spin coherence and relaxation times[20] and a large spin-diffusion length that is expected to reach ~10 μm even at room temperature.[21]

Recently, devices formed of crossed GNRs have been predicted to behave as perfect beam splitters, where the injected electron beam is divided into two of the four arms with near 50–50 probability and zero backscattering.[22–24] Furthermore, the particular case of devices formed of crossed ZGNRs is even more interesting, since they can create a spin-polarizing scattering potential[25] where the device can work as a spin-polarizing beam splitter. Following these ideas for electron quantum optics applications, a Mach–Zehnder-like interferometer in a GNRs network has recently been proposed.[26] In terms of their feasibility, manipulation of GNRs in STMs[27,28] has opened the possibility of building 2D multi-terminal GNR-based electronic circuits.[29] The spin properties of such devices can be addressed by measuring with spin-polarized STMs[30,31] and probed by shot-noise measurements.[32] For instance, a device formed of two crossed ZGNRs has been experimentally realized with the control over the crossing angle reaching a precision of 5°.[33]

While, in previous studies, only the AFM regime has been explored, other spin configurations can appear and show interesting spin-polarized transport properties. For instance, in contrast to the AFM case, the FM band structure of periodic ZGNRs does not show a bandgap around the Fermi level, which makes this regime interesting since there is conduction of electrons at the Fermi level. Given the metallic character of the FM-like spin configuration, one can envision to generate a minimal excitation in the device with only one particle and no hole (a leviton)[34–37] by applying a Lorentzian-like voltage pulse of specific amplitude and duration, enabling the generation of a single-electron excitation.[38]

Here, we analyze the functioning of an electronic beam splitter built with two crossed ZGNRs (of width 30 carbon atoms across) in an FM-like configuration, i.e., where the total magnetization of the device is different from zero. To describe the spin physics of the system, we employ the Hubbard Hamiltonian in the mean-field approximation (MFH).[39] The main complexity of the modeling lies in the description of the coupling between ZGNRs at the crossing, for which we use a Slater–Koster parameterization[40] that has shown to be in good agreement with other more accurate descriptions, such as density functional theory.[24] By employing this simple, yet powerful description based on single-electron physics, we can explore large systems composed of ~8000 atoms.

The manuscript is structured as follows: In Sec. II, we explain in detail the theoretical methods employed in this work (MFH Hamiltonian and NEGF formalism). In Sec. III, we present the obtained results for a device formed of two crossed-wide ZGNRs in its FM-like configuration, and finally, the conclusions are provided in Sec. IV.

II. METHODS

The system of study is composed of two infinite crossed ZGNRs placed one on top of the other separated by an inter-ribbon distance d, with a relative crossing angle of around $\theta = 60°$, as shown in Fig. 1. Here, the semi-infinite electrodes are indicated by red squares numbered 1–4.

To describe the π-electrons, responsible for the spin polarization and the transport phenomena in the system in the presence of Coulomb repulsion, we employ the MFH Hamiltonian[39] with a single p_z orbital per site,

$$H_{\mathrm{MFH}} = \sum_{ij,\sigma} t_{ij} c^{\dagger}_{i\sigma} c_{j\sigma} + U \sum_{i,\sigma} n_{i\sigma} \langle n_{i\bar{\sigma}} \rangle. \tag{1}$$

Here, $c_{i\sigma}$ ($c^{\dagger}_{i\sigma}$) is the annihilation (creation) operator of an electron at site i with spin $\sigma = \{\uparrow, \downarrow\}$ and $n_{i\sigma} = c^{\dagger}_{i\sigma} c_{i\sigma}$ is the corresponding number operator. The tight-binding parameters t_{ij} are described by Slater–Koster two-center σ- and π-type integrals between two p_z

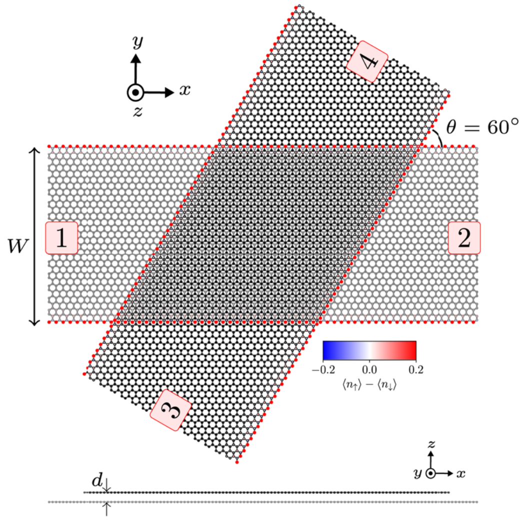

FIG. 1. Top and side views of the device geometry with spin density distribution. The size of the blobs is proportional to the magnitude of the spin polarization, $\langle n_{\uparrow} \rangle - \langle n_{\downarrow} \rangle$, and the color depicts the sign of the spin polarization as indicated by the color bar placed as an inset figure. The four numbered electrodes are indicated in red squares. The crossing angle between the ribbons in this geometry is $\theta = 60°$. The layers are separated by a distance d. The width (W) of the ribbons is 30 atoms across.

atomic orbitals[40] as used previously for twisted-bilayer graphene[41] and crossed GNRs.[24–26] U accounts for the Coulomb interaction between two electrons occupying the same p_z orbital. The total Hamiltonian H_T is the composition of the device Hamiltonian H_D, the electrodes Hamiltonian for the periodic leads H_α, and the coupling between these two $H_{\alpha D}$, i.e., $H_T = H_D + \sum_\alpha (H_\alpha + H_{\alpha D})$. More details for the implementation can be found in Refs. 25, 26, and 42.

As the junction between the ribbons breaks the translational invariance of the perfect ZGNRs, we use Green's function[43,44] formalism to solve the Schrödinger equation for the open quantum system. Details of the implemented MFH model with open boundary conditions[42] can be found in the supplementary material of Ref. 25.

The transport properties are analyzed by computing the transmission probabilities per spin index $\sigma = \{\uparrow, \downarrow\}$, between the different pairs of terminals as a function of the electron energy E from the Landauer–Büttiker formula,[45,46]

$$T^{\sigma}_{\alpha\beta}(E) = \mathrm{Tr}\left[\boldsymbol{\Gamma}^{\sigma}_{\alpha}\mathbf{G}^{\sigma}\boldsymbol{\Gamma}^{\sigma}_{\beta}\mathbf{G}^{\sigma\dagger}\right], \tag{2}$$

where $\mathbf{G}$ is the retarded Green's function and $\boldsymbol{\Gamma}_\alpha$ is the broadening matrix of lead α, due to the coupling of the device to this lead. See Ref. 26 for further details on the implementation. From the transmission probability, one can obtain the zero-bias conductance, calculated as

$$\mathrm{G}^{\sigma}_{\alpha\beta} = \mathrm{G}_0 \sum_n T^{\sigma n}_{\alpha\beta}(E_F), \tag{3}$$

where G_0 is the conductance quantum and $T^{\sigma n}_{\alpha\beta}(E_F)$ is the transmission of the nth available channel at the Fermi level E_F, which is related to Eq. (2) by $T_{\alpha\beta}(E) = \sum_n T^{\sigma n}_{\alpha\beta}(E)$. Note that, around E_F, there is only one single transverse mode (channel) available, and therefore, $T^{\sigma n}_{\alpha\beta}(E) = T^{\sigma}_{\alpha\beta}(E)$. To compute the transmission probabilities, we use the open-source code TBTRANS[47] and the Python package SISL for post-processing.[48]

III. RESULTS

In this section, we analyze the transport properties for a device formed of two crossed ZGNRs of $W = 30$ carbon atoms across (30-ZGNR) as a function of the inter-layer separation d for values close to the typical distance between layers in graphite ($d = 3.34$ Å), and the intersecting angle θ for values close to the commensurate case where $\theta = 60°$. To understand the spin states of ZGNRs, we performed different spin-polarized calculations changing the total mean value of the spin operator $\hat{S}_z$ per unit cell, $\langle \hat{S}_z \rangle = \frac{1}{2}\sum_i (\langle n_{i\uparrow}\rangle - \langle n_{i\downarrow}\rangle) \equiv S_z$, where the summation goes over the sites i within the unit cell of the periodic ZGNR.

In Fig. 2(a), we show the total energy per unit cell as a function of S_z relative to the case of $S_z = 0$ (the AFM case) for a periodic ZGNR of $W = 30$ carbons across. As can be seen here, there is a local minimum at $S_z = 0.317$, corresponding to the solution of the lowest energy for $S_z \neq 0$. The fact that the solution of minimum energy appears at such total S_z can be understood from the fact that, in the AFM case, the local spin projection summed over the bottom (or top) half of the unit cell of the ZGNR is $|S_z^{\mathrm{half}}| = 0.159$. This means that the total S_z per unit cell in the FM case needs to reach twice this value to flip the local magnetic moment at one edge. Note that the magnetic moment associated with S_z is $\mu = g_S \mu_B S_z$, where $g_S \approx 2$ is the electron spin g-factor and μ_B is the Bohr magneton. To see to what extent the ribbon width affects these results, we compare $E(S_z)$ for $W = 10, 20, 30, 40$-ZGNRs in Fig. S1 in the supplementary material, where we observe two main features: While the qualitative behavior is the same for all of them, the value of S_z at which the minimum of energy appears is larger for wider ribbons, and, as expected, the minimum value of $E(S_z > 0)$ diminishes with the width.

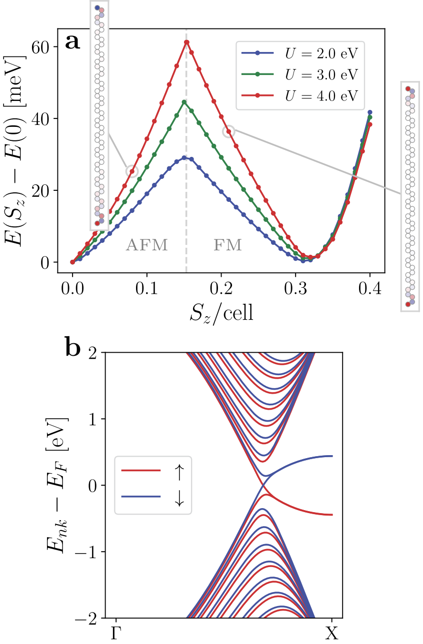

FIG. 2. (a) Energy differences between MFH solutions calculated with $U = 2$ eV (blue line), $U = 3$ eV (green line), and $U = 4$ eV (red line), obtained by imposing different spin projections S_z per unit cell. The dashed line separates the two phases depending on S_z (AFM and FM). The inset figures show examples of the spin polarization for the AFM and FM configurations, calculated with $S_z = 0.08$ and $S_z = 0.21$, respectively, where the red color indicates the up-spin majority, while the blue color indicates the down-spin majority. (b) Band structure of the periodic 30-ZGNR calculated with $U = 3.0$ eV for $S_z = 0.317$. Red and blue lines represent the up- and down-spin components, respectively.

For each S_z, we plot the energy corresponding to the spin configuration of the lowest energy in Fig. 2(a). Here, we distinguish between two phases depending on S_z: AFM character (for $S_z < 0.15$), where the spin polarization shows opposite spin majorities at the edges, and FM character (for $S_z > 0.15$), where the spin polarization shows the spin majority of equal spin index. The two insets to Fig. 2(a) show the spin polarization for a 30-ZGNR: one in the AFM-like spin configuration (calculated with $S_z = 0.08$), where it can be seen that the colors at the edges are different (red and blue), and another one in the FM-like spin configuration (calculated with $S_z = 0.21$), where it can be seen that the same color appears at both edges (red). In the case of the AFM-like spin configuration for $S_z \neq 0$, not only the sign of the local magnetic moments at the bottom and top edges of the unit cell is different but also the magnitude, as a consequence of the existing spin imbalance. Whereas when the FM character is achieved, both the magnitude and sign of the local magnetic moments at the bottom and top edges of the unit cell are equal.

In Fig. 2(b), we plot the band structure for the FM solution of the lowest energy for the 30-ZGNR, obtained with $S_z = 0.317$, for spin $\sigma = \uparrow$ (red lines) and $\sigma = \downarrow$ (blue lines). Here, we can observe the metallic character of the FM configuration for the ZGNR, as there are states available at the Fermi level, E_F, for both up and down spins.

As mentioned above, although the ground state corresponds to the configuration with $S_z = 0$, the presence of a magnetic field B in the z-direction (cf. Fig. 1) can stabilize a high-spin configuration due to the Zeeman energy $\Delta E = \mu B = g_S \mu_B S_z B$. For instance, the corresponding electronic energy $E(S_z)$ for the FM-like configuration of the lowest energy is $E(S_z = 0.317) = 0.97$ meV/cell above the ground state, implying that a critical magnetic field of the order $B_c = 26.6$ T (parallel to the z-axis in this case) is needed to make the two spin states degenerate. In Fig. 3(a), we study the zero-bias conductance $G_{\alpha\beta}(V)$ with $(\alpha, \beta) \in \{(1,2),(1,3)\}$ (black and green lines, respectively) for a device formed of two crossed 30-ZGNRs as a function of the inter-layer separation d. Here, V represents a rigid shift of the Fermi level E_F. We consider inter-layer distances close to the typical van der Waals distance between graphene layers in graphite ($d = 3.34$ Å).[23,49,50] In the first place, we can infer that the total spin-averaged conductance (sum of intra- and inter-layer conductances) is 1 since the values for $\overline{G}_{12}$ and $\overline{G}_{13}$ are symmetric with respect to $0.5G_0$, which means that there is no backscattering for an incoming electron at the Fermi level in these devices at least for these ranges of d and θ. In the second place, we observe an oscillating behavior of $\overline{G}_{\alpha\beta}$ with respect to this varying parameter. For instance, the inter-/intra-layer conductance ratio reaches its maximum for $d = 3.34$ Å. While one would expect that for smaller inter-layer distances d the interlayer ($\overline{G}_{13}$) conductance would increase, as the interlayer hopping integral depends exponentially on the distance between the ribbons, we observe a decrease (and increase in $\overline{G}_{12}$) for smaller d in Fig. 3(a), as a consequence of an interference process due to the scattering potential created by the crossing. We also observe that, for d between 3.44 and 3.49 Å, there is a crossing between $\overline{G}_{12}$ and $\overline{G}_{13}$, implying that, for that inter-layer separation, the device behaves as a perfect 50:50 beam splitter where the incoming electron beam is equally separated in the two possible outgoing directions with $\overline{G}_{\alpha\beta} = 0.5G_0$ for low gate voltages V.

Similarly, in Fig. 3(b), we study $G_{\alpha\beta}(V)$ for different crossing angles close to the commensurate configuration with $\theta = 60^\circ$. We apply the rotation around the center of the scattering region (crossing) that is obtained for the case with $\theta = 60^\circ$ and accounts for the effect of different possible stackings by averaging over the in-plane translations of one ribbon with respect to the other. By doing so, we aim to provide a comprehensive overview of the results, accounting for the variability in stacking configurations that might occur in practical scenarios. The in-plane unit cell is determined by the graphene lattice vectors. We obtain the conductance for a mesh of four points along each lattice vector within the unit cell. The error bars are calculated as the standard deviation of the spin-averaged conductance $\overline{G}_{\alpha\beta}$ at each point, averaging over the in-plane translations. The observed variance of approximately ∼10%–20% reflects the variations across different translational configurations, showing the inherent differences sampled by these translations. However, not all the stackings are equivalent. For instance, the most energetically favorable (and therefore most likely) configuration is the AB-stacking (see the supplementary material of Ref. 25). By analyzing the transport properties relative to this varying parameter in Fig. 3(b), we observe, on the one hand, that the inter-/intra-layer conductance ratio reaches its maximum for $\theta = 55^\circ, 65^\circ$. On the other hand, the sum of the total spin-averaged conductance is 1 as in panel (a), since the values for $\overline{G}_{12}$ and $\overline{G}_{13}$ are symmetric with respect to $0.5G_0$ as well, meaning that the variation of θ does not introduce backscattering. We can see that the oscillatory dependence of the conductance on the crossing angle is less smooth than the one seen in Fig. 3(a). This occurs due to a more complicated dependence of the σ- and π-type hopping integrals on θ.

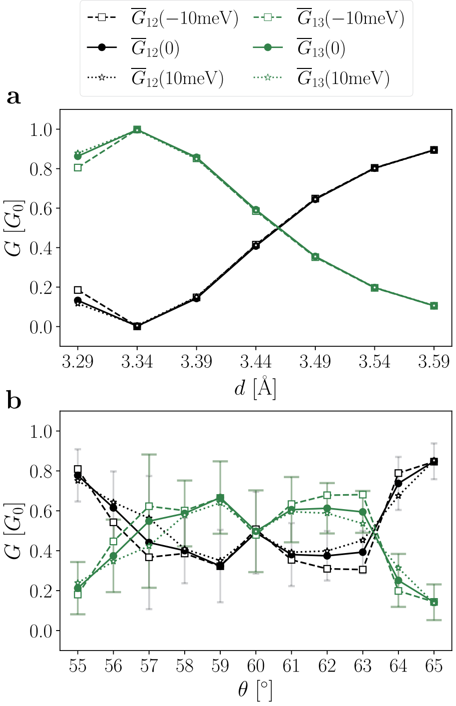

FIG. 3. Spin-averaged conductance $\overline{G}_{\alpha\beta}(V)$ between incoming electrode $\alpha = 1$ and outgoing electrodes $\beta = 2$ (black lines) and $\beta = 3$ (green lines) in units of the conductance quantum G_0, as a function of (a) the inter-layer separation d, with fixed crossing angle $\theta = 60^\circ$ and stacking as shown in Fig. 1, and (b) the crossing angle θ averaged over the in-plane translations of one ribbon with respect to the other, with fixed $d = 3.34$ Å, for a device formed of crossed 30-ZGNRs obtained with $U = 3.0$ eV in the FM configuration. The error bars in (b) are calculated as the standard deviation of $\overline{G}_{\alpha\beta}(0)$ at each θ by averaging over the different displacements. We obtain this conductance at different gate voltages $V = -10$ meV (dashed lines with open squares), $V = 0$ (solid lines with filled circles), and $V = 10$ meV (dotted lines with open stars). The legend placed on top is common to both panels (a) and (b).

To see the effect of the width on the transport properties as a function of these two varying parameters, we performed a similar analysis for a 20-ZGNR device in the supplementary material (see Fig. S2), where we observe that, qualitatively, the behavior is maintained. For further detail, we plot the energy-resolved transmission probabilities for the 30-ZGNR device as a function of d and θ in the supplementary material (see Figs. S3 and S4).

Finally, we note that it has been previously shown that the symmetries associated with the spatial distribution of the spin densities are crucial for the transport properties of the device.[24,25] In this case, since the FM character implies that $\langle n_\uparrow \rangle \neq \langle n_\downarrow \rangle$, there will not be a symmetric behavior for the existing spin channels. However, the spin-density distribution possesses a symmetry axis at $y = \sin(-60^\circ)x$ that maps the device geometry to itself through mirror operations, and applies to each spin component individually (conserves the spin index). As it has been shown in Refs. 24 and 25, certain symmetrical combinations of electrodes lead to equal transmission probabilities $T^{\sigma}_{\alpha\beta} = T^{\sigma}_{\gamma\delta}$. In this case, the symmetrical electrode mapping corresponds to $(1,2,3,4) \leftrightarrow (4,3,2,1)$.

IV. CONCLUSIONS

We have analyzed the electron transport properties for a device formed of two crossed infinite ZGNRs of $W = 30$ carbon atoms across (30-ZGNRs) as a function of the spin configuration by fixing different values for the total spin per unit cell S_z. In the first place, by computing the total energy associated with these configurations $E(S_z)$, we have shown that there is a local minimum for the solution with $S_z > 0$, with $E(S_z > 0)$ close to 1 meV/cell above the ground state $[E(0)]$. We have also seen that, depending on S_z, there are two possible phases: AFM-character, where the edges of the ZGNR unit cell are populated by opposite spin majorities, and FM-character, where the two edges of the ribbon are populated by the same spin majority. These two phases appear for $S_z < 0.15$ and $S_z > 0.15$, respectively. We also computed the band structure for the FM-like configuration of the lowest energy, where we observe that this system in such a spin state shows a metallic character. We estimate that the critical magnetic field needed to make this FM-like solution degenerate with the AFM ground state is $B_c = 26.6$ T for this particular case, although this value will further decrease for wider ribbons.

We have also calculated the inter- and intra-layer electrical conductances for different gatings varying the inter-layer distances, for distances close to the van der Waals distance between graphene layers in graphite ($d = 3.34$ Å), and crossing angles close to the commensurate stacking where $\theta = 60^\circ$ for this four-terminal device. We have shown that the (spin- and displacement-averaged) electrical conductance displays an oscillatory behavior with respect to these varying parameters at low gate voltages ($-10\text{ meV} \leq V \leq 10\text{ meV}$) while maintaining the sum $\overline{G}_{12} + \overline{G}_{13} = 1$, which means that there is no backscattering for the devices for different values of d and θ within the shown ranges nor conductance into terminal 4. The maximum value for the inter-/intra-layer spin-averaged conductance ratio $(\overline{G}_{13}/\overline{G}_{12})$ for this device is found for $d = 3.34$ Å and $\theta = 55^\circ, 65^\circ$. In addition, to show that these results are not exclusive to the chosen ZGNR width, we performed a similar analysis for a 20-ZGNR device (see supplementary material), where we show that it possesses similar qualitative behavior.

The results presented here add to the vision of using GNR-based devices for spintronics and quantum technologies. On top of the already discussed properties and applications of spin-polarized GNR-based beam splitters for electron quantum optics,[24–26] this device in its FM-like spin configuration can be a promising candidate due to its metallic nature, which facilitates electron injection through the generation of a minimal excitation. This can be achieved by applying a Lorentzian-like voltage pulse with a specific amplitude and duration to produce a single-electron excitation within the device.[34–37] In fact, performing time-dependent quantum transport calculations for levitonic excitations[34–37] could offer critical insights into the nonequilibrium dynamics of the proposed devices, and further elucidate the role of minimal excitation states in transport phenomena of the charges injected by the pulse.[51–53]

SUPPLEMENTARY MATERIAL

See the supplementary material for additional calculations, including transport calculations for devices with other ribbon widths and transmission curves as a function of electronic energy for the device discussed in the main text.

ACKNOWLEDGMENTS

This work was funded by the Spanish Grant No. MCIN/AEI/10.13039/501100011033 (Grant Nos. PID2020-115406GB-I00, TED2021-132388B-C44, PID2022-140845OB-C66, and JDC2022-048665-I), the Basque Department of Education (Grant No. PIBA-2023-1-0021), the University of the Basque Country (UPV/EHU) through Grant No. IT-1569-22, and the European Union's Horizon 2020 (FET-Open project SPRING Grant No. 863098).

AUTHOR DECLARATIONS

Conflict of Interest

The authors have no conflicts to disclose.

Author Contributions

Sofia Sanz: Conceptualization (equal); Data curation (equal); Formal analysis (equal); Funding acquisition (equal); Investigation (equal); Software (equal); Visualization (equal); Writing – original draft (equal); Writing – review & editing (equal). **Géza Giedke**: Formal analysis (supporting); Funding acquisition (equal); Investigation (equal); Supervision (supporting); Writing – original draft (supporting); Writing – review & editing (equal). **Daniel Sánchez-Portal**: Formal analysis (supporting); Funding acquisition (equal); Investigation (equal); Supervision (supporting); Writing – original draft (supporting); Writing – review & editing (equal). **Thomas Frederiksen**: Data curation (supporting); Formal analysis (equal); Funding acquisition (lead); Investigation (equal); Resources (equal); Software (equal); Supervision (equal); Visualization (equal); Writing – original draft (supporting); Writing – review & editing (equal).

DATA AVAILABILITY

The dataset that supports the findings of this study is publicly available on Zenodo, https://doi.org/10.5281/zenodo.14224593.

REFERENCES

[1] Y.-W. Son, M. L. Cohen, and S. G. Louie, "Half-metallic graphene nanoribbons," Nature **444**, 347 (2006).

[2] D. G. de Oteyza and T. Frederiksen, “Carbon-based nanostructures as a versatile platform for tunable π-magnetism,” J. Phys.: Condens. Matter **34**, 443001 (2022).

[3] H. Chakraborti, C. Gorini, A. Knothe, M.-H. Liu, P. Makk, F. D. Parmentier, D. Perconte, K. Richter, P. Roulleau, B. Sacépé, C. Schönenberger, and W. Yang, “Electron wave and quantum optics in graphene,” J. Phys.: Condens. Matter **36**, 393001 (2024).

[4] S. Minke, J. Bundesmann, D. Weiss, and J. Eroms, “Phase coherent transport in graphene nanoribbons and graphene nanoribbon arrays,” Phys. Rev. B **86**, 155403 (2012).

[5] J. Baringhaus, M. Ruan, F. Edler, A. Tejeda, M. Sicot, A. Taleb-Ibrahimi, A.-P. Li, Z. Jiang, E. H. Conrad, C. Berger, C. Tegenkamp, and W. A. de Heer, “Exceptional ballistic transport in epitaxial graphene nanoribbons,” Nature **506**, 349 (2014).

[6] J. Aprojanz, S. R. Power, P. Bampoulis, S. Roche, A.-P. Jauho, H. J. W. Zandvliet, A. A. Zakharov, and C. Tegenkamp, “Ballistic tracks in graphene nanoribbons,” Nat. Commun. **9**, 4426 (2018).

[7] L. P. Zârbo and B. K. Nikolić, “Spatial distribution of local currents of massless Dirac fermions in quantum transport through graphene nanoribbons,” Europhys. Lett. **80**, 47001 (2007).

[8] J. Cai, P. Ruffieux, R. Jaafar, M. Bieri, T. Braun, S. Blankenburg, M. Muoth, A. P. Seitsonen, M. Saleh, X. Feng, K. Müllen, and R. Fasel, “Atomically precise bottom-up fabrication of graphene nanoribbons,” Nature **466**, 470 (2010).

[9] P. Ruffieux, S. Wang, B. Yang, C. Sánchez-Sánchez, J. Liu, T. Dienel, L. Talirz, P. Shinde, C. A. Pignedoli, D. Passerone, T. Dumslaff, X. Feng, K. Müllen, and R. Fasel, “On-surface synthesis of graphene nanoribbons with zigzag edge topology,” Nature **531**, 489 (2016).

[10] M. Fujita, K. Wakabayashi, K. Nakada, and K. Kusakabe, “Peculiar localized state at zigzag graphite edge,” J. Phys. Soc. Jpn. **65**, 1920 (1996).

[11] H. Lee, Y.-W. Son, N. Park, S. Han, and J. Yu, “Magnetic ordering at the edges of graphitic fragments: Magnetic tail interactions between the edge-localized states,” Phys. Rev. B **72**, 174431 (2005).

[12] Y.-W. Son, M. L. Cohen, and S. G. Louie, “Energy gaps in graphene nanoribbons,” Phys. Rev. Lett. **97**, 216803 (2006).

[13] G. Z. Magda, X. Jin, I. Hagymási, P. Vancsó, Z. Osváth, P. Nemes-Incze, C. Hwang, L. P. Biró, and L. Tapasztó, “Room-temperature magnetic order on zigzag edges of narrow graphene nanoribbons,” Nature **514**, 608–611 (2014).

[14] Y. Y. Li, M. X. Chen, M. Weinert, and L. Li, “Direct experimental determination of onset of electron-electron interactions in gap opening of zigzag graphene nanoribbons,” Nat. Commun. **5**, 4311 (2014).

[15] K. Nakada, M. Fujita, G. Dresselhaus, and M. S. Dresselhaus, “Edge state in graphene ribbons: Nanometer size effect and edge shape dependence,” Phys. Rev. B **54**, 17954 (1996).

[16] K. Wakabayashi, M. Fujita, H. Ajiki, and M. Sigrist, “Electronic and magnetic properties of nanographite ribbons,” Phys. Rev. B **59**, 8271 (1999).

[17] Y. Miyamoto, K. Nakada, and M. Fujita, “First-principles study of edge states of H-terminated graphitic ribbons,” Phys. Rev. B **59**, 9858 (1999).

[18] J. Jung, T. Pereg-Barnea, and A. H. MacDonald, “Theory of interedge superexchange in zigzag edge magnetism,” Phys. Rev. Lett. **102**, 227205 (2009).

[19] A. R. Rocha, V. M. García-suárez, S. W. Bailey, C. J. Lambert, J. Ferrer, and S. Sanvito, “Towards molecular spintronics,” Nat. Mater. **4**, 335 (2005).

[20] W. Han and R. K. Kawakami, “Spin relaxation in single-layer and bilayer graphene,” Phys. Rev. Lett. **107**, 047207 (2011).

[21] N. Tombros, C. Jozsa, M. Popinciuc, H. T. Jonkman, and B. J. van Wees, “Electronic spin transport and spin precession in single graphene layers at room temperature,” Nature **448**, 571 (2007).

[22] L. R. F. Lima, A. R. Hernández, F. A. Pinheiro, and C. Lewenkopf, “A 50/50 electronic beam splitter in graphene nanoribbons as a building block for electron optics,” J. Phys.: Condens. Matter **28**, 505303 (2016).

[23] P. Brandimarte, M. Engelund, N. Papior, A. Garcia-Lekue, T. Frederiksen, and D. Sánchez-Portal, “A tunable electronic beam splitter realized with crossed graphene nanoribbons,” J. Chem. Phys. **146**, 092318 (2017).

[24] S. Sanz, P. Brandimarte, G. Giedke, D. Sánchez-Portal, and T. Frederiksen, “Crossed graphene nanoribbons as beam splitters and mirrors for electron quantum optics,” Phys. Rev. B **102**, 035436 (2020).

[25] S. Sanz, N. Papior, G. Giedke, D. Sánchez-Portal, M. Brandbyge, and T. Frederiksen, “Spin-polarizing electron beam splitter from crossed graphene nanoribbons,” Phys. Rev. Lett. **129**, 037701 (2022).

[26] S. Sanz, N. Papior, G. Giedke, D. Sánchez-Portal, M. Brandbyge, and T. Frederiksen, “Mach–Zehnder-like interferometry with graphene nanoribbon networks,” J. Phys.: Condens. Matter **35**, 374001 (2023).

[27] M. Koch, F. Ample, C. Joachim, and L. Grill, “Voltage-dependent conductance of a single graphene nanoribbon,” Nat. Nanotechnol. **7**, 713 (2012).

[28] S. Kawai, A. Benassi, E. Gnecco, H. Söde, R. Pawlak, X. Feng, K. Müllen, D. Passerone, C. A. Pignedoli, P. Ruffieux, R. Fasel, and E. Meyer, “Superlubricity of graphene nanoribbons on gold surfaces,” Science **351**, 957 (2016).

[29] L. Jiao, L. Zhang, L. Ding, J. Liu, and H. Dai, “Aligned graphene nanoribbons and crossbars from unzipped carbon nanotubes,” Nano Res. **3**, 387 (2010).

[30] D. Wortmann, S. Heinze, P. Kurz, G. Bihlmayer, and S. Blügel, “Resolving complex atomic-scale spin structures by spin-polarized scanning tunneling microscopy,” Phys. Rev. Lett. **86**, 4132 (2001).

[31] J. Brede, N. Merino-Díez, A. Berdonces-Layunta, S. Sanz, A. Domínguez-Celorrio, J. Lobo-Checa, M. Vilas-Varela, D. Peña, T. Frederiksen, J. I. Pascual, D. G. de Oteyza, and D. Serrate, “Detecting the spin-polarization of edge states in graphene nanoribbons,” Nat. Commun. **14**, 6677 (2023).

[32] A. Burtzlaff, A. Weismann, M. Brandbyge, and R. Berndt, “Shot noise as a probe of spin-polarized transport through single atoms,” Phys. Rev. Lett. **114**, 016602 (2015).

[33] D. Wang, D.-L. Bao, Q. Zheng, C.-T. Wang, S. Wang, P. Fan, S. Mishra, L. Tao, Y. Xiao, L. Huang, X. Feng, K. Müllen, Y.-Y. Zhang, R. Fasel, P. Ruffieux, S. Du, and H.-J. Gao, “Twisted bilayer zigzag-graphene nanoribbon junctions with tunable edge states,” Nat. Commun. **14**, 1018 (2023).

[34] L. S. Levitov, H. Lee, and G. B. Lesovik, “Electron counting statistics and coherent states of electric current,” J. Math. Phys. **37**, 4845 (1996).

[35] D. A. Ivanov, H. W. Lee, and L. S. Levitov, “Coherent states of alternating current,” Phys. Rev. B **56**, 6839 (1997).

[36] J. Keeling, I. Klich, and L. S. Levitov, “Minimal excitation states of electrons in one-dimensional wires,” Phys. Rev. Lett. **97**, 116403 (2006).

[37] J. Dubois, T. Jullien, F. Portier, P. Roche, A. Cavanna, Y. Jin, W. Wegscheider, P. Roulleau, and D. C. Glattli, “Minimal-excitation states for electron quantum optics using levitons,” Nature **502**, 659 (2013).

[38] A. Assouline, L. Pugliese, H. Chakraborti, S. Lee, L. Bernabeu, M. Jo, K. Watanabe, T. Taniguchi, D. C. Glattli, N. Kumada, H.-S. Sim, F. D. Parmentier, and P. Roulleau, “Emission and coherent control of levitons in graphene,” Science **382**, 1260 (2023).

[39] J. Hubbard, “Electron correlations in narrow energy bands,” Proc. R. Soc. A **276**, 238 (1963).

[40] J. C. Slater and G. F. Koster, “Simplified LCAO method for the periodic potential problem,” Phys. Rev. **94**, 1498 (1954).

[41] G. Trambly de Laissardière, D. Mayou, and L. Magaud, “Localization of Dirac electrons in rotated graphene bilayers,” Nano Lett. **10**, 804 (2010).

[42] S. Sanz, N. Papior, M. Brandbyge, and T. Frederiksen (2022), Hubbard, v0.2.0

[43] L. V. Keldysh, “Diagram technique for nonequilibrium processes,” Sov. Phys. JETP **20**, 1018 (1965).

[44] L. Kadanoff and G. Baym, *Quantum Statistical Mechanics: Green’s Function Methods in Equilibrium and Nonequilibrium Problems, Frontiers in Physics: A Lecture Note and Reprint Series* (W. A. Benjamin, 1962).

[45] M. Büttiker, Y. Imry, R. Landauer, and S. Pinhas, “Generalized many-channel conductance formula with application to small rings,” Phys. Rev. B **31**, 6207 (1985).

[46] M. Büttiker, “Scattering theory of thermal and excess noise in open conductors,” Phys. Rev. Lett. **65**, 2901 (1990).

[47] N. Papior, N. Lorente, T. Frederiksen, A. García, and M. Brandbyge, “Improvements on non-equilibrium and transport Green function techniques: The next-generation TRANSIESTA,” Comput. Phys. Commun. **212**, 8 (2017).

[48] N. Papior (2021), SISL, v0.11.0, https://doi.org/10.5281/zenodo.13745302.

[49] Y. Baskin and L. Meyer, “Lattice constants of graphite at low temperatures,” Phys. Rev. **100**, 544 (1955).

[50] Y. X. Zhao and I. L. Spain, “X-ray diffraction data for graphite to 20 GPa,” Phys. Rev. B **40**, 993 (1989).

[51] B. Gaury and X. Waintal, "Dynamical control of interference using voltage pulses in the quantum regime," Nat. Commun. **5**, 3844 (2014).
[52] B. S. Popescu and A. Croy, "Efficient auxiliary-mode approach for time-dependent nanoelectronics," New J. Phys. **18**, 093044 (2016).
[53] A. Suresh, U. Bajpai, and B. K. Nikolić, "Magnon-driven chiral charge and spin pumping and electron–magnon scattering from time-dependent quantum transport combined with classical atomistic spin dynamics," Phys. Rev. B **101**, 214412 (2020).